Final Technical Report

Project Title: Effect of Casting Conditions and Composition on Microstructural Gradients in Roll Cast Aluminum Alloys

Covering Period: September 15, 2002 through September 14, 2007

Date of Report: April 30, 2007

Recipient: University of Alabama at Birmingham
1530 3rd Ave. South
Birmingham, AL 35294-4461

Award Number: DE-FC36-02ID14401

Subcontractors: None

Other Partners: Alcoa Technical Center
100 Technical Drive
Alcoa Center, PA 15069
Dr. Hasso Weiland
(724) 337-3133

Project Director: Dr. Burton R. Patterson, (205) 934-8454, patters@uab.edu

Industrial Partner: Dr. Hasso Weiland, Alcoa Technical Center

No Disclosure Limitations

Project Objective: This project will investigate roll casting of highly alloyed aluminum. The studies will determine the relationships between roll casting process parameters and the resulting microstructure, annealing response and properties. In particular, the microstructural analysis will investigate the nature of the microstructural gradients that occur in these materials and the influence of these structures on recrystallization response, crystallographic texture, and formation of cracks during forming. The combined effects of alloying level and casting parameters on the resultant materials will be modeled. Development of a basis of knowledge about roll casting of these highly alloyed materials will be of great technological, economic and environmental benefit to the U.S. aluminum industry.

Background: The proposed program is a comprehensive investigation of the effect of roll casting process conditions on the microstructure and properties of relatively highly alloyed aluminum. Use of this innovative and energy efficient process is currently restricted to low alloy or unalloyed products, such as AA1050, for relatively low technology applications. It would be of great technological and economic benefit to the U.S. aluminum industry to extend roll casting capability to higher alloy systems of greater value. Highly alloyed roll cast aluminum exhibits significant differences from conventional DC cast material, through the presence of microstructural gradients from the casting process. These gradients, resulting from solute segregation, result in different annealing response and increased cracking during forming operations. Use of the roll casting process for these higher alloy series will be based on understanding the relationships between the roll casting process variables and the resulting

gradient microstructure, the nature of its crystallographic texturing and the response to annealing and cracking during forming.

The proposed research will greatly benefit the application of the roll casting process in production of aluminum sheet products for higher alloy contents than are presently possible. Providing a scientific basis of understanding of the effects of composition (alloy level) and roll casting variables on microstructure, texture and cracking tendency during subsequent forming will result in greater product quality and yield, and enable realization of the potential energy and cost efficiencies of this novel process.

Executive Summary

This program has investigated the effect of roll casting conditions, composition and post-roll cast homogenization and annealling heat treatments on the microstructure of roll cast aluminum alloy AA3105. Roll cast A3105 suffers from a very coarse recrystallized grain size that results in reduced formability and an “orange peel” surface. These problems restrict the suitable products for this material to those with H-temper, disallowing many possible O-temper products.

The coarse recrystallized grain size results from the roll casting process itself, in which rapid solidification and subsequent rapid cooling retains a high level of manganese in supersaturation. The O-temper annealing treatment precipitates many fine dispersoid particles from this supersaturated matrix that inhibit recrystallization, allowing nucleation of only a few grains, which grow to an excessive size. The present program developed means for producing a fine grain size in roll cast AA3105, to enable it’s use for O-temper products.

The principal findings were that the problems with the dispersoid particles could be avoided and a fine annealed grain size achieved by either of two means: (a) rapid heating to the annealing temperature, as by continuous annealing of uncoiled strip passing through a furnace, or (b) a several hour homogenization treatment of the roll cast material prior to conventional annealing.

Both of these means were shown to achieve grain sizes as fine as conventional DC cast AA3105 and are attainable commercially. The rapid heating method above is likely preferable to the longer homogenization treat treatment from an energy standpoint and from the more complete avoidance of moderately coarse surface grains that sometimes form during annealing of the homogenized material if not given a suitably extensive hold at high temperature. Rapid heating produces annealed material with a uniformly fine recrystallized grain size. The rapid heating is presently limited to fewer plant locations that have continuous annealing furnaces.

Goals / Accomplishments

The primary goals fo the program were to:

(a) Understand the effects of TRC on the compositional gradients, annealing response, microstructure (dispersoid distribution, annealed grain size and gradient) of roll cast AA3105 aluminum alloy.

(b) Develop means for overcoming problems associated with compositional and microstructural gradients

(c) Facilitate the use of TRC for production of AA3105 and other roll cast aluminum alloys

The program was able to meet these goals very well. A significant portion of the program was spent on the topics in (a), *understanding the origin of the microstructural problems originating from the roll casting process*. In particular, numerous heat treating studies were performed for extensive times over a wide range of temperatures to understand the rate of formation of the detrimental dispersoid precipitates, and how to avoid their formation prior to recrystallization .

Time-temperature-transformation curves were determined experimentally and the relationship of the dispersoid size and volume fraction to the recrystallization rate and the resulting grain size was determined. These studies were extremely comprehensive, have been published in the scientific literature and have provided a very sound groundwork for solving problems that may occur with AA3105 and other roll cast aluminum alloys. The selected alloy, AA3105, proved to be an ideal model material to examine several other fundamental metalluirgical processes not limited to roll cast material, namely particle inhibited grain growth (Zener pinning) and abnormal grain growth. Significant new progress was made in these areas and these results have been published or are near completion for publication.

Under the topics in section (b), *develop means to overcome the above problems*, considerable progress was made. It was found that the coarse grain problem can be completely eliminated by homogenization treatments prior to cold rolling and annealing, or, by continuous annealing after cold rolling, with no homogenization treatment required. Thus, it can be stated that the problem is solvable by appropriate industrial practices, as available in particular plants.

Section (c), *facilitate the use of twin roll casting for AA3105 and other aluminum alloys*, has been accomplished through successes in goals (a) and (b). The problems that previously appeared to be inherent in roll cast alloys can now be overcome by any of several means mentioned above.

Summary of Project Activities

The project activities followed a logical progression, each successive one following the findings of the previous activities, as summarized below. The experimental details, plots and findings are provided in the nine publications and the dissertation attached in the Appendix.

Hypothesis

The original hypothesis was that the sharp gradient in temperature from the cooled rolls through the solidifying metal led to the coarse recrystallized grain size and surface-to-center gradients in grain size and particle size. Although this general connection was very likely true, the detailed effects of the temperature gradient on the material were not known at the onset of the study and became known only throughout its long term performance.

Approaches employed

The principal approaches used throughout the program involved short and long term anneals and homogenization treatments. The short time anneals were performed to understand how the dispersoid precipitation could be avoided by rapid heating. These experiments were performed through lead bath anneals and controlled infrared heating at Oak Ridge National Lab. The longer time anneals and homogenization treatments were performed in conventional air furnaces.

TTT plots were used to characterize precipitation and recrystallization kinetics, to understand the relationship of heating rate to recrystallized grain size.

Amount of transformation was determined through electrical conductivity measurements and high resolution FEG-SEM measurement. The latter was used to determine the location of precipitation, e.g., on subgrain boundaries, and for particle size distribution analysis of the constituent particles.

Grain size and shape measurements and determination of general microstructural state were performed by optical microscopy.

Products Developed

Publications

The research from this program has resulted in a total of eight published papers, including three in high level refereed journals, and one Ph.D. dissertation. The citations for these publications are listed below and the papers and dissertation are attached in the Appendices of this report.

N. Sun, B.R. Patterson, H. Weiland, E. Simielli and M. Li, "Roll Casting of Aluminum Alloy 3105," Aluminum 2003, TMS, pp. 187-191, 2003.

B.R. Patterson, Naiyu Sun, Jaakko Suni, Hasso Weiland and Eider Simielli, "Effect of Homogenization on Recrystallization of Roll Cast AA3105," Metallurgical Modeling for Aluminum Alloys, Eds.M. Tiryakioğlu and L.A. Lalli, ASM International, pp.209-212, 2004.

Naiyu Sun, Burton Patterson, Jaakko Suni, Eider Simielli, Hasso Weiland, Puja Kadolkar, Craig Blue, and Gregory Thompson, "Heating Rate Effect on Microstructure Evolution during Annealing of Twin Roll Cast AA3105," in Aluminum Wrought Products for Automotive, Packaging, and other Applications, Eds. S. Das, G. Jha, Z. Li, T. Zhai, and J. Liu, pp.119-124,TMS, 2006.

B.R. Patterson, Naiyu Sun, Jaakko Suni, Eider Simielli, Hasso Weiland and Larry Allard, "Microstructural Evolution during Annealing of Twin Roll Cast AA3105," TMS Letters, Vol. 1, Issue 8, pp. 173-174, 2004.

Naiyu Sun, Burton R. Patterson, Jaakko P. Suni, Eider A. Simielli, Hasso Weiland and Larry Allard, "Microstructural Gradients in Twin Roll Cast AA3105," TMS Letters, Vol. 2, Issue 2. pp. 33-34, 2005.

Naiyu Sun, Burton R. Patterson, Jaakko P. Suni, Eider A. Simielli, Hasso Weiland and Lawrence F. Allard, "Microstructural Evolution in Twin Roll Cast AA3105 during Homogenization," Materials Science and Engineering A, Vol. 416, pp. 232-239, 2005.

Naiyu Sun, Burton R. Patterson, Jaakko P. Suni, Hasso Weiland and Lawrence F. Allard, "Characterization of Particle Pinning Potential," Acta Materialia, 2006, Vol.54, pp. 4091-4099.

Naiyu Sun, Burton R. Patterson, Jaakko P. Suni, Roger D. Doherty, Hasso Weiland, Puja Kadolkar, Craig A. Blue, Gregory B. Thompson, "Effect of Heating Rate on Recrystallization of Twin Roll Cast Aluminum," Metall. Mater. Trans. A, 2008, Vol.39A, No.1, pp.165-170.

Naiyu Sun, Microstructure Evolution in Twin Roll Cast AA3105, Ph.D dissertation , University of Alabama at Birmingham, 2006.

Collaborations developed

This program has helped develop several excellent collaborations that have continued. The UAB/Alcoa interaction has continued in a variety of areas throughout the program and ever since. The UAB and Alcoa researchers made numerous visits and seminars at both locations

and the UAB Ph.D. student had the opportunity to work for Alcoa after graduation. Dr. R.D. Doherty of Drexel University became intimately involved in the DOE program work and co-authored several publications form the program, in print and near completion.

Appendix
Publications from the Program

A. N. Sun, B.R. Patterson, H. Weiland, E. Simielli and M. Li, “Roll Casting of Aluminum Alloy 3105,” Aluminum 2003, TMS, pp. 187-191, 2003.

B. B.R. Patterson, Naiyu Sun, Jaakko Suni, Hasso Weiland and Eider Simielli, “Effect of Homogenization on Recrystallization of Roll Cast AA3105,” Metallurgical Modeling for Aluminum Alloys, Eds.M. Tiryakioğlu and L.A. Lalli, ASM International, pp.209-212, 2004.

C. Naiyu Sun, Burton Patterson, Jaakko Suni, Eider Simielli, Hasso Weiland, Puja Kadolkar, Craig Blue, and Gregory Thompson, “Heating Rate Effect on Microstructure Evolution during Annealing of Twin Roll Cast AA3105,” in Aluminum Wrought Products for Automotive, Packaging, and other Applications, Eds. S. Das, G. Jha, Z. Li, T. Zhai, and J. Liu, pp.119-124,TMS, 2006.

D. B.R. Patterson, Naiyu Sun, Jaakko Suni, Eider Simielli, Hasso Weiland and Larry Allard, “Microstructural Evolution during Annealing of Twin Roll Cast AA3105,” TMS Letters, Vol. 1, Issue 8, pp. 173-174, 2004.

E. Naiyu Sun, Burton R. Patterson, Jaakko P. Suni, Eider A. Simielli, Hasso Weiland and Larry Allard, “Microstructural Gradients in Twin Roll Cast AA3105,” TMS Letters, Vol. 2, Issue 2. pp. 33-34, 2005.

F. Naiyu Sun, Burton R. Patterson, Jaakko P. Suni, Eider A. Simielli, Hasso Weiland and Lawrence F. Allard, “Microstructural Evolution in Twin Roll Cast AA3105 during Homogenization,” Materials Science and Engineering A, Vol. 416, pp. 232-239, 2005.

G. Naiyu Sun, Burton R. Patterson, Jaakko P. Suni, Hasso Weiland and Lawrence F. Allard, “Characterization of Particle Pinning Potential,” Acta Materialia, 2006, Vol.54, pp. 4091-4099.

H. Naiyu Sun, Burton R. Patterson, Jaakko P. Suni, Roger D. Doherty, Hasso Weiland, Puja Kadolkar, Craig A. Blue, Gregory B. Thompson, “Effect of Heating Rate on Recrystallization of Twin Roll Cast Aluminum,” Metall. Mater. Trans. A, 2008, Vol.39A, No.1, pp.165-170.

I. Naiyu Sun, Microstructure Evolution in Twin Roll Cast AA3105, Ph.D dissertation, University of Alabama at Birmingham, 2006.

Roll Casting of Aluminum Alloy 3105

B. R. Patterson and Naiyu Sun
University of Alabama at Birmingham, Birmingham, AL 35294

Hasso Weiland, Eider Simielli and Ming Li
Alcoa Technical Center, Alcoa Ctr., PA 15069

Abstract

Roll cast aluminum alloy exhibits apparent microstructural gradients from the casting surface to the center of the strip. These gradients, resulting from solute segregation, result in different annealing responses. In this paper, the homogenization and recrystallization responses of AA3105 alloy are studied. The influences of casting conditions (casting speed) and the thermo-mechanical processing on Particle Size Distribution (PSD) are revealed. The corresponding relation between PSD and the recrystallized grain structure is presented.

Introduction

In the past five decades or so, twin roll casting has been well established as an economical and efficient method for producing many types of aluminum sheet and foil [1-5]. The properties of the final aluminum products mainly depend on the processing variables. Among them, heat treatment is one of the most important factors. It is very important to understand the relationships between the resulting gradient microstructure, the nature of its crystallographic texturing, the response to annealing and the casting variables.

Experimental Procedure

AA3105 alloy was cast with two casting speeds. Homogenization was carried out at 550^{o}C for 5 hours. Prior to recrystallization, 90% cold work was achieved by cold roll. Four different recrystallization temperatures were used, 250 ^{o}C, 300 ^{o}C, 350 ^{o}C and 400^{o}C.

Results and Discussion

Fig. 1 and 2 are the micrographs of as-cast samples with different casting speeds. We can see that the fast casting speed causes severe Center-Line Segregation (CLS), which is undesirable to the following deformation processing steps and to the application of final products.
Fig. 3 and 4 are similar micrographs except that samples are cold rolled by 90% and recrystallized. We can still see the CLS. But the coarse constituent phases are broken down into fine dispersoids due to the cold roll processing.

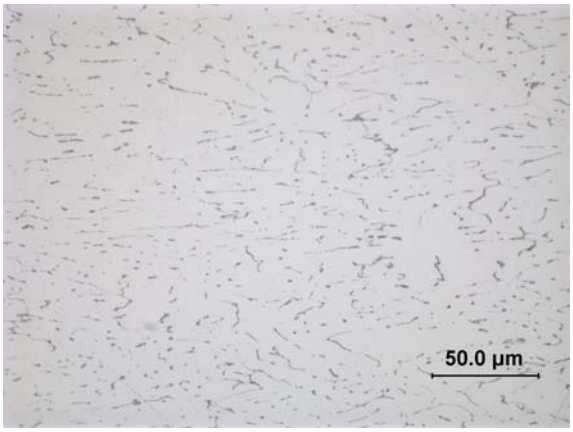

Fig. 1 Slow casting speed

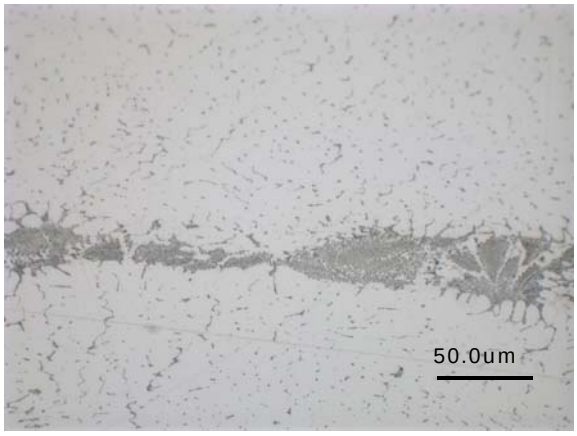

Fig. 2 Fast casting speed

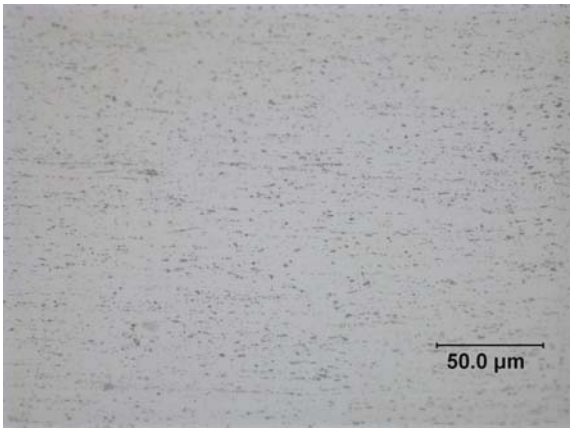

Fig. 3 Slow (after 90% CR and Rex)

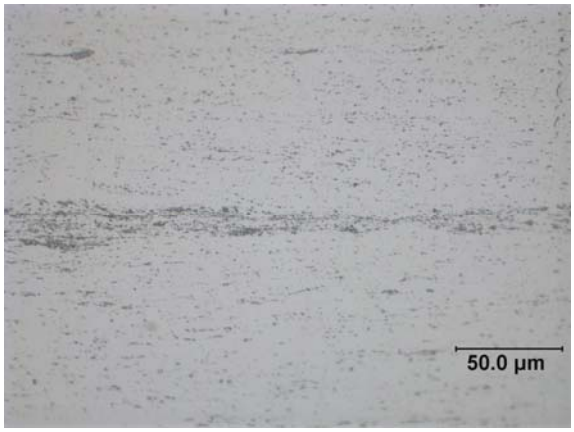

Fig. 4 Fast (after 90% CR and Rex)

Fig. 5 shows the gradient of PSD from the edge to the center of the strip. The particles near the edge are finer and denser than those in the center area of the strip. To further verify this phenomenon, the SEM micrographs were taken, as shown in fig. 6 for non-homogenized samples and in fig. 7 for homogenized samples. The same PSD gradient is shown better in the SEM shots. The mean free path of particles in the center area, as shown in fig. 6 (b) and fig. 7 (b), is larger that those in the edge area, as shown in fig. 6 (a) and fig. 7 (a). This difference in PSD brings a significant grain structure variation across the thickness of the strip, as shown later in fig. 8 through fig. 12.

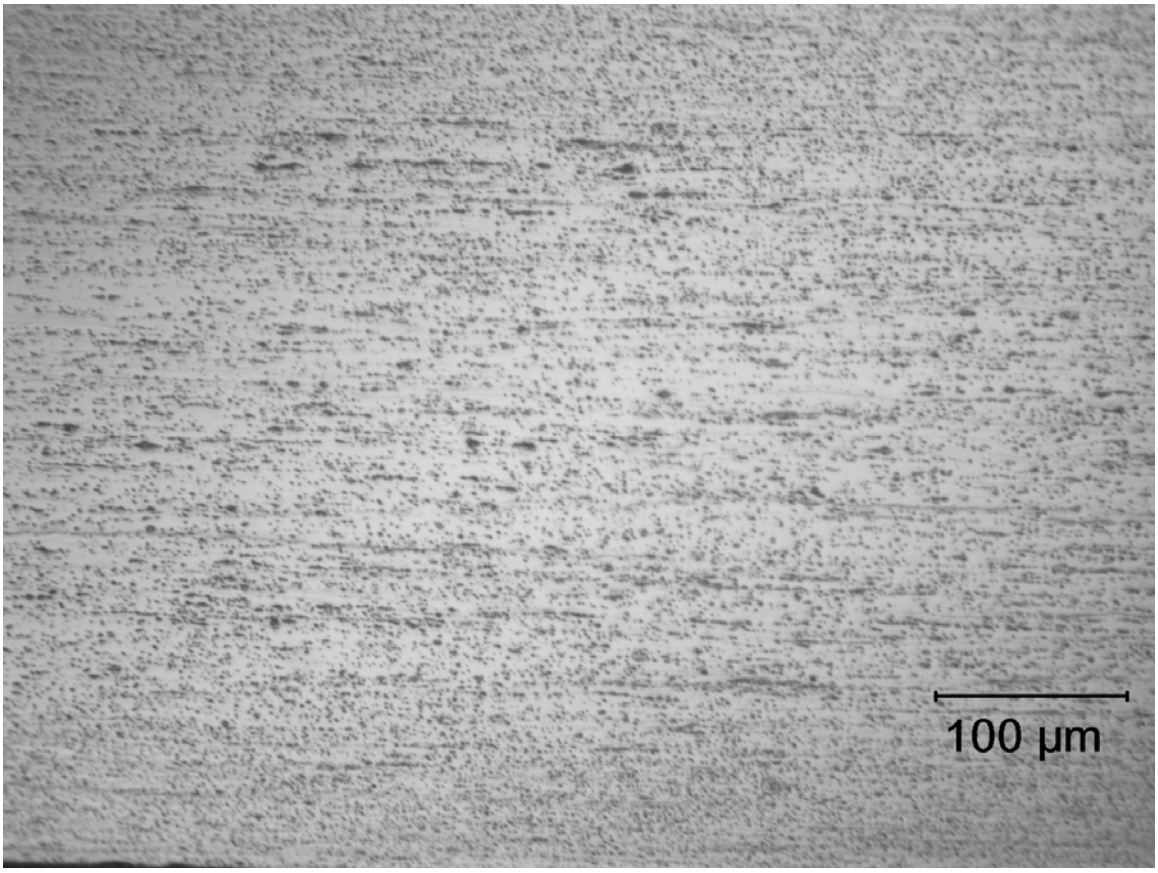

Fig. 5 The strip cross section after 90% CR and Rex

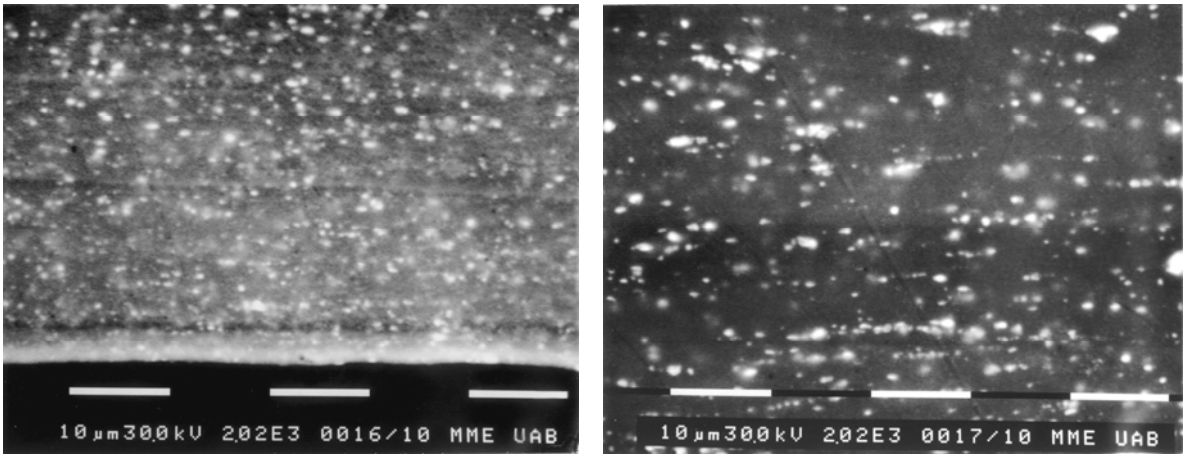

(a) (b)

Fig. 6 SEM images of Non-homogenized recrystallized strips: (a) edge, (b) center

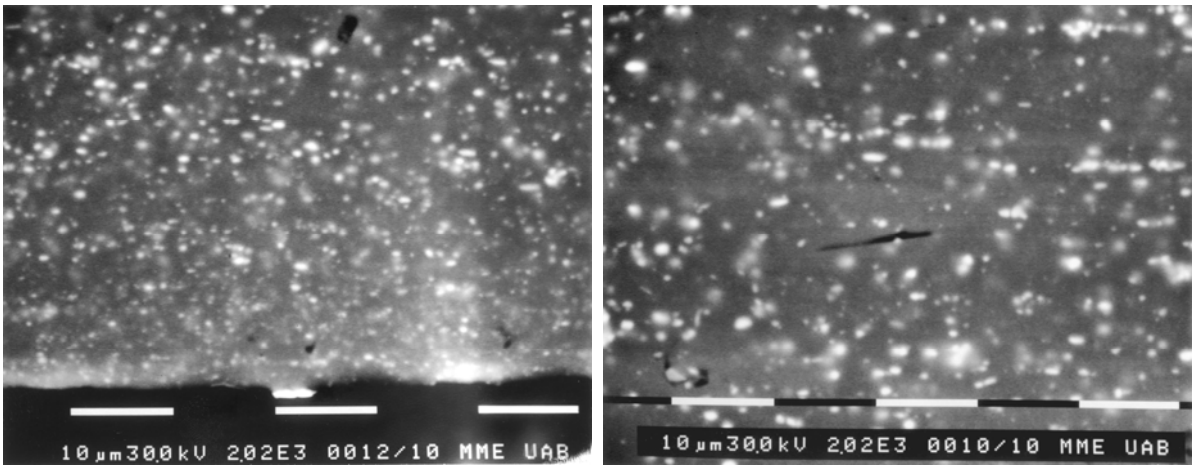

(a) (b)

Fig. 7 SEM images of homogenized recrystallized strips: (a) edge, (b) center

Fig. 8 (a) and (b) are the recrystallized grain structure micrographs of non-homogenized samples with slow casting speed. Fig. 9 (a) and (b) are grain structure micrographs of non-homogenized samples with fast casting speed. It is shown that under 350 ^{o}C, both samples have little recrystallization. At 400 ^{o}C, samples with both casting speeds show recrystallized grain structure in the strip center. But on the edge, there are non-recrystallized areas. This character can be attributed to the very fine and dense precipitate particles near the edge. Some researchers [6] believe that particles can either stimulate or inhibit recrystallization depending on their size. Large particles (>um's) favor recrystallization, while small particles impede it. Also, the sample with slow casting speed has higher recrystallization tendency than sample with fast casting speed, as shown in fig. 8 (b) and fig. 9 (b).

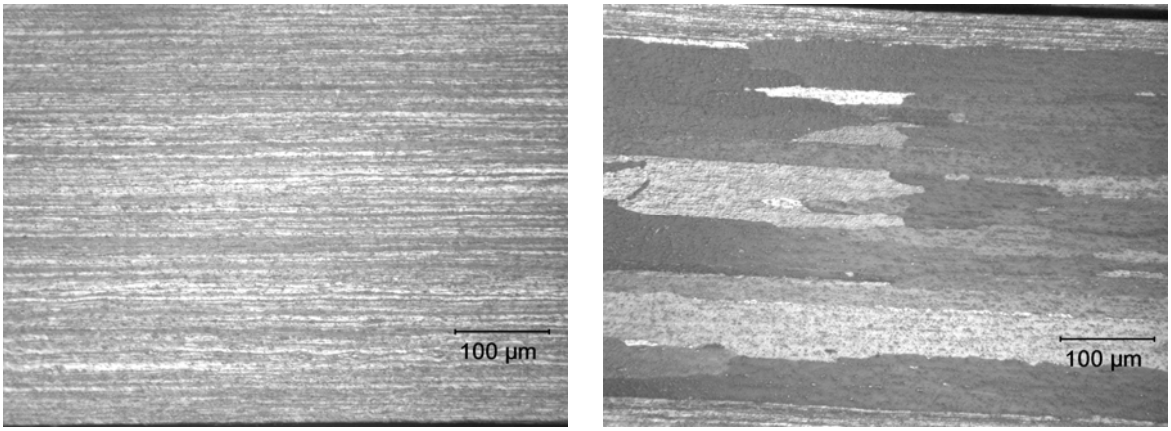

(a) (b)

Fig. 8 Grain structure of samples with slow casting speed: (a) 350 ^{o}C, (b) 400 ^{o}C

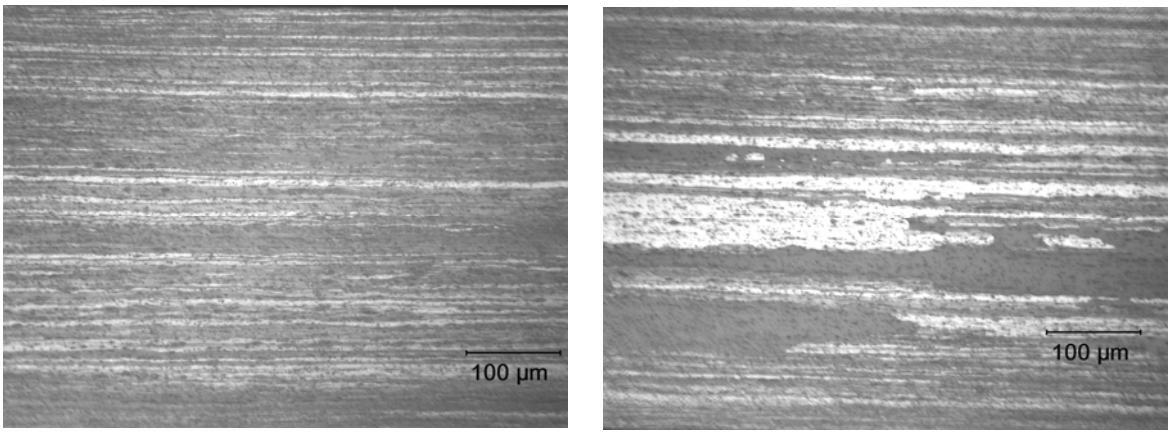

(a) (b)

Fig. 9 Grain structure of samples with fast casting speed: (a) 350 ^{o}C, (b) 400 ^{o}C

Fig.10 and fig.11 are micrographs of grain structures of homogenized samples. Compared with non-homogenized ones, the homogenized samples show lower recrystallization temperature (300 ^{o}C instead of 350 ^{o}C). Moreover, the grain structure after homogenization is finer, as shown in Fig. 10 (c), (d) and fig. 11 (c), (d). But it seems that the grain structure inherits the gradient character from the precipitate particles. This, to some degree, verifies the validity of the Particle Stimulated Nucleation (PSN) theory [6].

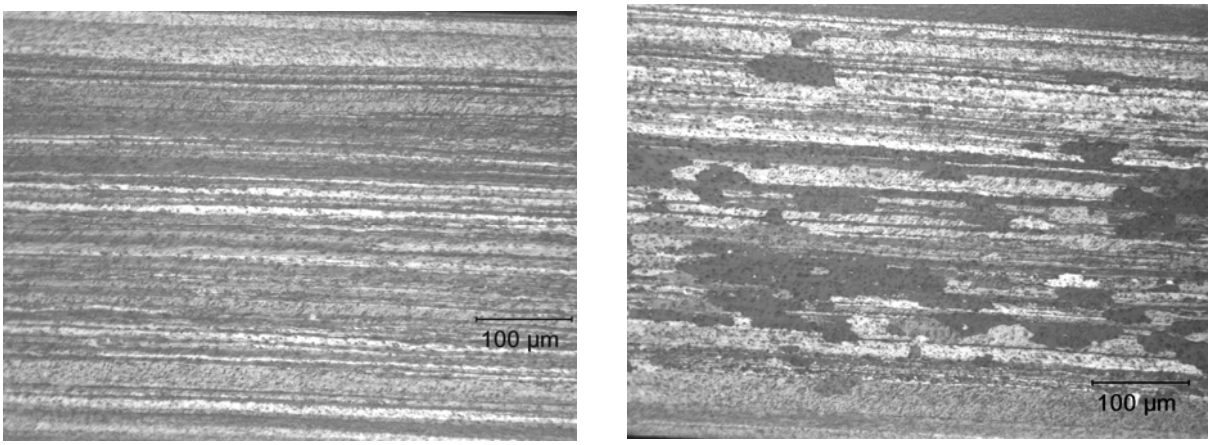

(a) (b)

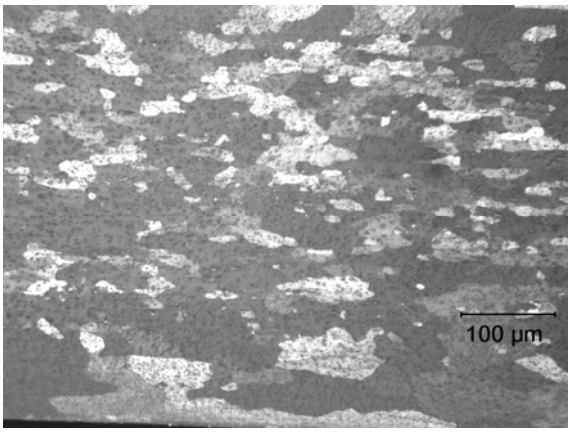

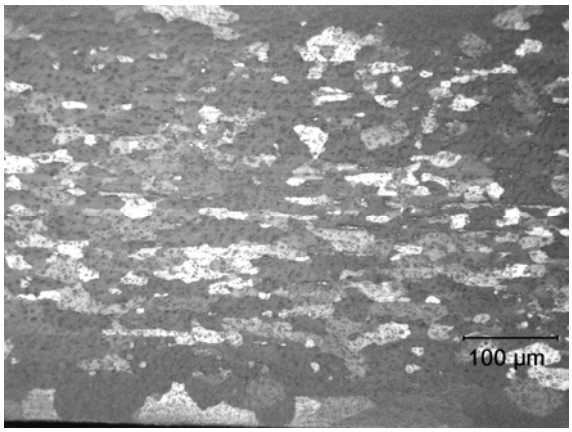

(c) (d)

Fig. 10 Grain structure of homogenized samples with fast casting speed: (a) 250 °C Rex, (b) 300 °C Rex, (c) 350 °C Rex, (d) 400 °C Rex.

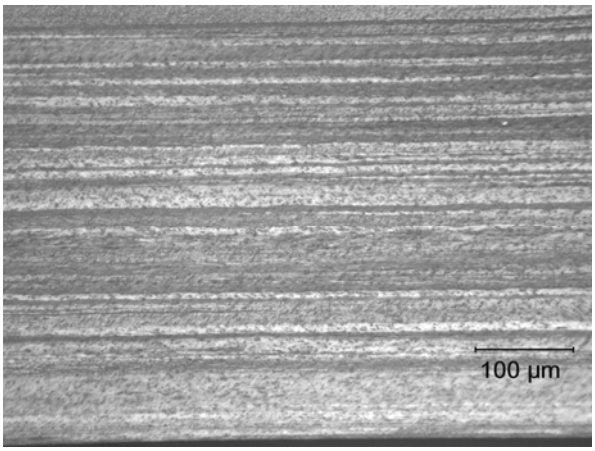

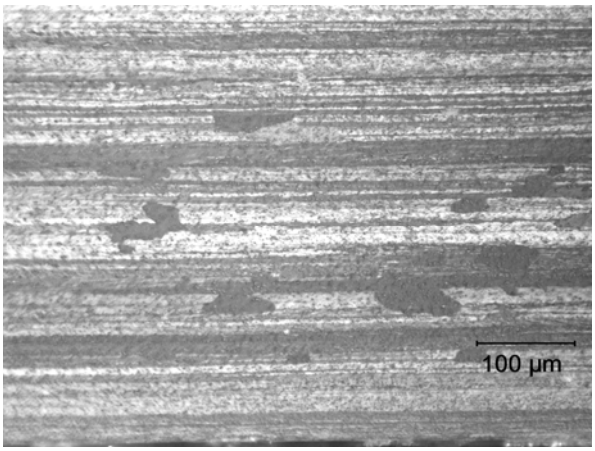

(a) (b)

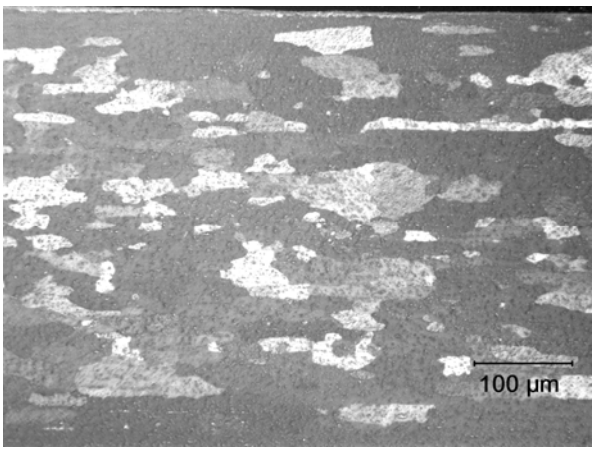

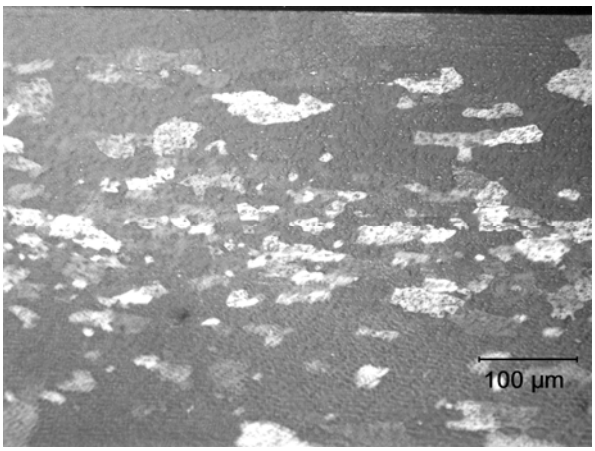

(c) (d)

Fig. 11 Grain structure of homogenized samples with slow casting speed: (a) 250 °C Rex, (b) 300 °C Rex, (c) 350 °C Rex, (d) 400 °C Rex.

Fig. 12 shows the corresponding relation between the recrystallized grain structure and the PSD. As pointed out above, this relation may be one of the major reasons of microstructure gradient across the thickness of strips.

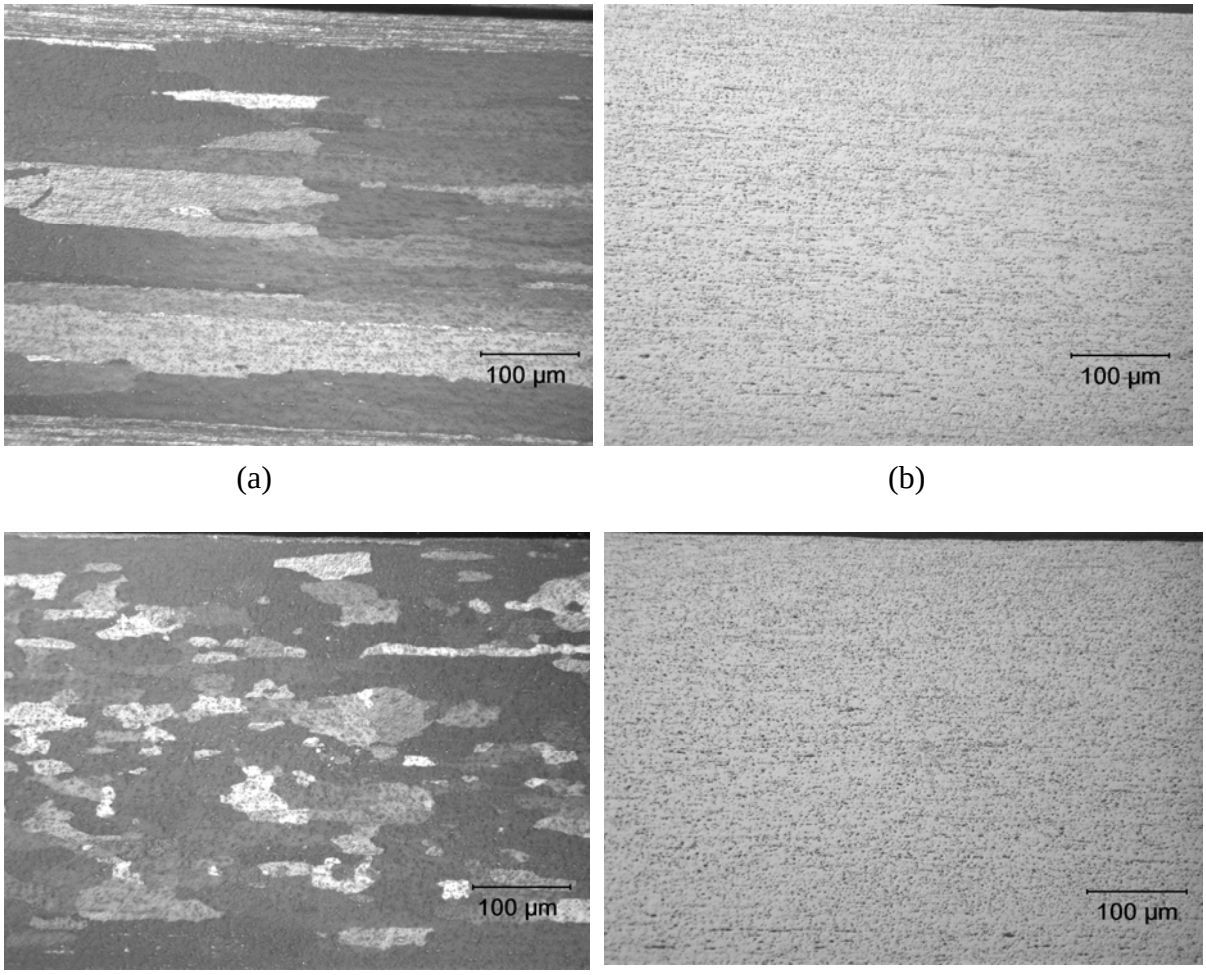

Fig. 12 Micrographs of grain structure and corresponding particle distribution: (a) 80% rex and coarse grain, (b) corresponding micrograph of particles, (c) full rex, (d) corresponding micrograph of particles.

Table 1 summarizes the recrystallization results of this research. The variables involved in the experiment are: 90% cold roll, with or without homogenization, casting speed and different recrystallization temperatures (250 ^{o}C, 300 ^{o}C, 350 ^{o}C and 400 ^{o}C).

		250 °C	300 °C	350 °C	400 °C
Non-homog.	Fast casting speed	Non-Rex	Non-Rex	Non-Rex	20% Rex Coarse
	Slow casting speed	Non-Rex	Non-Rex	Non-Rex	80% Rex Coarse, Edge not rex
Homog.	Fast casting speed	Non-Rex	50% Rex in center	Full rex Center-fine Edge-coarse	Full rex Center-fine Edge-coarse
	Slow casting speed	Non-Rex	25% Rex in center	Full rex Center-fine Edge-coarse	Full rex Center-very fine Edge-coarse

Table 1 Summary of recrystallization results (after 90% CR)

Conclusion

1.Strong PSD gradient near cast surface.
2. Rexld grain structure strongly influenced by particles and PSD gradient. Small particle tends to inhibit nucleation of rexln. Moreover, small particle tends to delay rexln. This happens mainly at cast surface. As a result, small particle causes coarse grains.
3. Homogenization promotes rexln. Homogenization coarsens the otherwise fine particle. Coarse particle lowers rexln temperature. Also, large particle favors nucleation. As a result, large particle results in finer grains. But the grains near the surface are still coarser than those at the strip center. So, further research is needed to refine the surface grains.
4. Casting speed influences rexld grain structure. Without homogenization, rexln is promoted by *slow* speed. With homogenization, rexln is promoted by *fast* speed. But the casting speed has less influence than homogenization.

Reference

1. M. Yun, S. Lokyer, J. D. Hunt, Twin roll casting of aluminum alloy, Materials Science and Engineering A280, 2000, pp. 116-123.
2. M. Karlik, J. Siegl, M. Slamova, Cracking of AA 8006 thin sheets during forming of heat exchanger fins, Physical Metallurgy and Fracture of Materials, 1999, pp. 113-116.
3. M. Slamova, V. Ocenasek, M. Cieslar, B. Chalupa and P. Merle, Differences in structure evolution of twin-roll cast AA8006 and AA8011 alloys during annealing, Materials Science Forum Vols 331-337, 2000, pp. 829-834
4. Sir H. Bessemer, British Patent No. 11317, 1846.
5. R. Cook, P.G. Grocok, P.M. Thomas, D.V. Edmonds and J. D. Hunt, Journal of Materials Processing Technology, 55, 1995, pp. 76-84.
6. F. J. Humphreys and M. Hatherly, Recrystalization and related annealing phenomena, Pergamon, 1995.

Effect of Homogenization on Recrystallization of Roll Cast AA3105

B.R. Patterson, Naiyu Sun
The University of Alabama at Birmingham
Jaakko Suni, Hasso Weiland, and Eider Simielli
Alcoa Technical Center

Abstract

Studies of the effects of thermomechanical treatments on ease of recrystallization and recrystallized grain size of roll cast AA3105 show beneficial effects of a high temperature homogenization treatment prior to final cold rolling and annealing. Recrystallized grain size was markedly decreased with decreased cooling rate from homogenization. Lesser but beneficial effects were also found from increased homogenization temperature and addition of a pre-homogenization cold roll. The metallographic observations were supported qualitatively by electrical conductivity based estimates and computer modeling of volume fraction of manganese bearing phase precipitated during homogenization and annealing.

Introduction

Roll casting is an efficient means for producing aluminum sheet, requiring fewer roll passes than direct chill casting since the roll cast material is typically cast to a thickness of several mm.[1-5] In alloy AA3105 the high solidification rate associated with roll casting causes the problem of an excessively large recrystallized grain size, reducing the formability of the material. It is believed that this large recrystallized grain size results from inhibition of recrystallization by the fine manganese bearing dispersoids that result from casting, especially near the surface.

It has been found that high temperature homogenization treatments prior to the final cold roll and recrystallization anneal alleviate this problem to some degree, most likely due to some or all of the following effects- dissolution of the as cast dispersoids, re-precipitation of manganese onto the coarser constituent particles and as dispersoids in the matrix, and finally, possible coarsening of any of these dispersoids formed on cooling. This paper describes the results of modeling and experimental studies of the effects of (a) homogenization temperature, (b) cooling rate after homogenization and (c) cold rolling prior to homogenization. The model predictions of the volume fraction of manganese bearing second phase present were compared to the amounts of precipitation calculated from electrical conductivity measurements and to the final grain structures obtained after recrystallization.

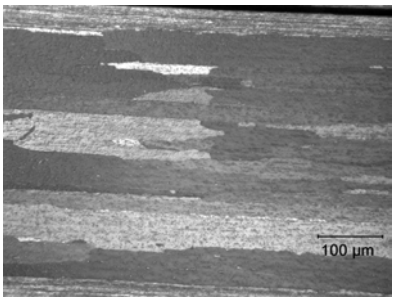

(a)

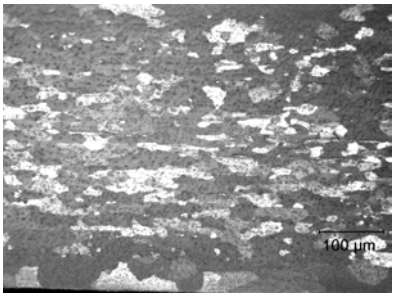

(b)

Figure 1. Microstructure of roll cast AA3105 (a) without and (b) with, homogenization treatment prior to cold roll and anneal.

The strip cross sections, top to bottom, shown in Fig. 1 illustrate the above mentioned problem experienced with roll cast AA3105. Figure 1(a) shows the material after cold rolling to 90% reduction and annealing at 400°C for 30 min. The recrystallized grain size is extremely large and the surface material is resistant to nucleation and has not yet recrystallized. Figure 1(b) shows the recrystallized grain structure after the same cold roll and anneal treatment but with a 5hr homogenization hold at 550°C followed by furnace cooling (~10°C/min) to room temperature prior to the cold roll. Here the recrystallized grain size is significantly finer and the surface has

recrystallized, although with a coarser grain size than in the interior of the strip.

The above recrystallization behavior is best explained in terms of particle inhibited nucleation. [6] Without the high temperature treatment the as-cast particle structure, finest at the surface of the strip, pins subgrain boundaries and prevents their growth into viable recrystallization nuclei. This inhibition is greatest at the surface where the particle size is finest and is still significant within the strip interior. The high temperature homogenization treatment serves to dissolve, reprecipitate, and coarsen the manganese bearing dispersoids, reducing the pinning effect and the inhibition of nucleation.

After establishing the benefit of the homogenization treatment prior to cold rolling, it was desired to optimize the pre-cold roll treatments by investigating several variables, including (a) homogenization temperature, (b) cooling rate after homogenization, and (c) cold rolling prior to homogenization. These effects were modeled using a code developed at Alcoa Technical Center, tuned to hot rolling of AA3004. The model was used here to predict volume fractions of constituent and dispersoid phase and manganese level in solution after roll casting, homogenization and after the recrystallization anneal. These factors are strongly related to particle inhibition of nucleation and therefore recrystallized grain size. Model predictions were tested via resistivity measurements and metallography after laboratory scale thermomechanical processing.

A major goal of this study was to evaluate the ability of the model to guide the design of heat treatments to promote recrystallization nucleation for refining the grain size in roll cast AA3105. The model is now being used to explore the effects of other homogenization cycles and further reduction in cooling rate on recrystallized grain size.

Experimental Procedures

The material used in the investigation was roll cast AA3105, produced by Alcoa, with composition Al-0.59Mn, 0.44Mg, 0.55Fe, 0.28Si, 0.04Cu. The material was supplied as-roll cast to 5mm thickness. Specimens were cut from the strip and given further processing to evaluate the different homogenization variables. To evaluate the effect of homogenization temperature, treatments were performed at either 575 or 600°C for 5hr. The effect of cooling rate from the homogenization temperature was investigated by cooling from the above two temperatures either by shutting down the furnace, roughly 10°C/min, or with a programmed cooling rate of 0.3°C/min. The effect of cold work prior to homogenization was examined by giving the material 50% reduction by rolling at room temperature prior to the above treatments. All combinations of the above treatments were examined in a 2x2x2 matrix, yielding 8 treatments. All specimens were then rolled at room temperature to 90% reduction and given a recrystallization anneal at 300°C for 60min.

Electrical resistivity was measured before and after the final anneals to evaluate the manganese solute level and estimate the volume fractions of constituent and dispersoid phases after homogenization and the amount of precipitation of manganese bearing dispersoid during annealing.

Specimens were sectioned longitudinally and polished to show the extent of recrystallization and the recrystallized grain size.

Results

Cooling rate. Figure 2(a) shows the microstructure of the material homogenized at 600°C for 5hr and slow cooled at 0.3°C/min prior to the 90% cold roll and 60min. anneal at 300°C The entire cross section of the strip is recrystallized with the surface having much coarser grains, as was also evident in Fig. 1(b). By comparison, Fig. 2(b) shows the material receiving the same 600°C homogenization treatment but with a faster cooling rate of 10°C/min. The more rapidly cooled material had just begun to recrystallize after 60min at 300°C, i.e., nucleation was much more inhibited, presumably by fine dispersoids that precipitated during the more rapid cooling.

Prior deformation. Figure 2(c) shows the material receiving a 50% cold reduction prior to the 600°C homogenization and slow cool, followed by the standard 90% cold roll and 60min. anneal at 300°C. This strip, half the thickness of the others due to the prior cold work, is fully recrystallized and appears possibly to have a finer grain size than in Fig. 2(a) that had the same treatment except without the pre-homogenization cold roll. This effect of improved nucleation with the prior cold roll is not apparent in all cases and will be investigated further to better understand the conditions under which it occurs.

Homogenization temperature. Comparison of Figs. 2(a) and (d) shows the effect of homogenization temperature on recrystallized grain size, again, after 90% cold roll and 60min anneal at 300°C. There is possibly a small effect of better nucleation and finer recrystallized grain size with higher homogenization temperature, although, again, this is not readily apparent in all cases.

Conductivity measurements and modeling. Electrical conductivity was measured on specimens with all combinations of thermomechanical processing, before and after both homogenization and annealing to determine the effect of the treatments on precipitation of second phase as either constituent or dispersoids. The changes in conductivity values during the different treatments were calibrated to the volume fraction of second phase precipitated. It was desired to have a large amount of precipitation during the homogenization treatments to remove manganese from solution and prevent later precipitation of manganese bearing dispersoids during annealing, possibly hindering nucleation.

The computed volume fractions of manganese bearing phase precipitated during homogenization and annealing are shown in Figs. 3 and 4, respectively. In Fig. 3 it is apparent that the slow cool from homogenization produces a noticeably greater precipitation than the faster cool, as expected. Correspondingly, Fig. 4 shows the slow cooled materials to have less dispersoid precipitation during annealing. It is expected that the slow cool from homogenization should also aid coarsening of the particles, reducing their number and increasing their

spacing, both of which would reduce the dispersoid drag effect on nucleation and result in faster recrystallization and a finer grain size.

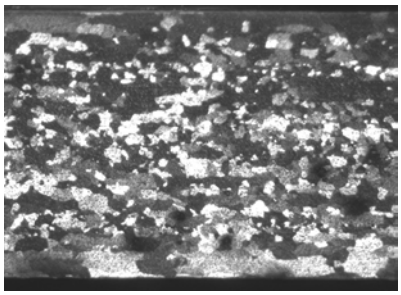

(a)

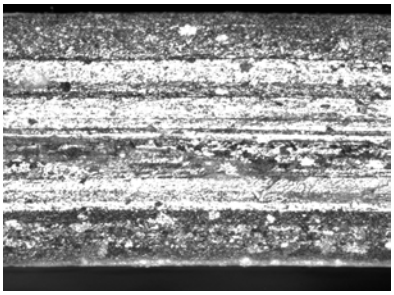

(b)

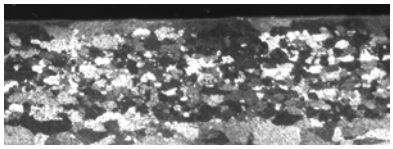

(c)

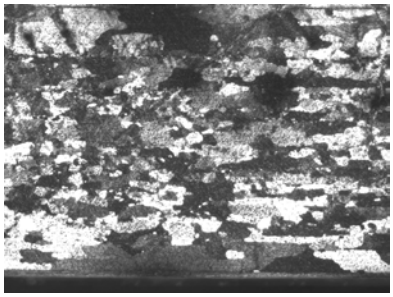

(d)

Figure 2. Microstructure of roll cast AA3105 after homogenization, cold roll and anneal. (a) 600 °C, slow cool, (b) 600 °C, fast cool, (c) 600°C, slow cool, with prior cold roll, and (d) 575°C, slow cool.

The above precipitation results, inferred from the conductivity measurements, are consistent with the metallographic indications of Figs. 2(a) and (b), where the slow cooled material was fully recrystallized, with a relatively fine grain size, while the faster cooled material was in the early stages of recrystallization. The model, which at this point only addressed precipitation during annealing, also predicted markedly less precipitation than the faster cooled material. The greater amount of precipitation that actually occurred relative to the model prediction is due to the model not addressing precipitation enhancement effects from deformation.

The conductivity measurements and modeling both showed very little effect of pre-homogenization cold work and homogenization temperature on precipitation during homogenization or annealing. These effects, shown metallographically by comparing Figs. 2(a) vs. (c) and 2(a) vs. (d), were relatively less and more inconsistent than the significant effect of post-homogenization cooling rate. It is planned to further explore these treatments to better understand the conditions under which they affect final grain size. The results of this study also point to further studies of the cooling rate effect, especially with slower and faster rates than studied here.

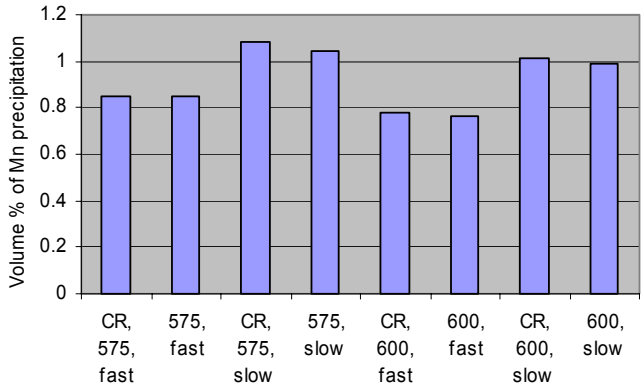

Figure 3. Volume fraction of Mn precipitated during homogenization

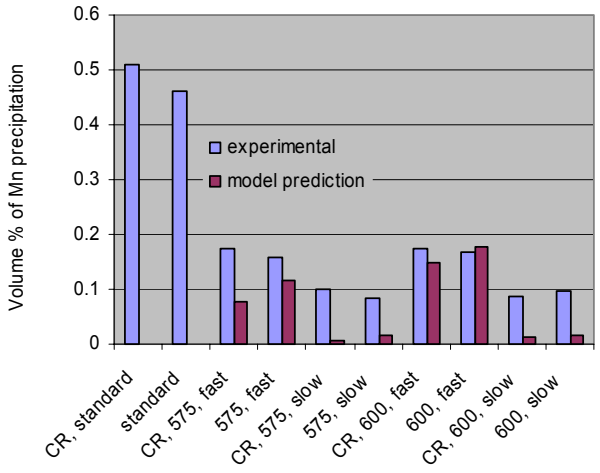

Figure 4. Volume fraction of Mn precipitated during anneal

Summary and Conclusions

This study explored the effects of several thermomechanical treatments prior to the final cold roll and anneal, on ease of recrystallization and recrystallized grain size of roll cast AA3105.

In all cases, addition of a homogenization treatment prior to cold rolling and annealing resulted in a marked reduction in recrystallized grain size. The grain size at the surface of the sheet was typically much coarser than in the center. Reducing the cooling rate from the homogenization treatment resulted in a marked increase in recrystallization rate. Increased homogenization temperature and addition of a prior cold roll prior to homogenization both showed a small and less consistent effect on reducing recrystallized grain size, i.e., increasing the ease of nucleation. The metallographic results were qualitatively consistent with electrical conductivity based estimates of volume fractions of manganese bearing phase precipitated during homogenization and annealing. Computer modeling of these amounts of precipitates were qualitatively consistent with the conductivity measurements and metallographic observations of the recrystallized grain structure.

Acknowledgements

The authors would like to acknowledge financial and other support from the Department of Energy Office of Industrial Technology, grant no. DE-FC07-02ID14401.

References

[1] M. Yun, S. Lokyer, J. D. Hunt, *Materials Science and Engineering*, A280, 116-123 (2000)
[2] M. Karlik, J. Siegl, M. Slamova, *Physical Metallurgy and Fracture of Materials*, 113-116 (1999)
[3] M. Slamova, V. Ocenasek, M. Cieslar, B. Chalupa and P. Merle, *Materials Science Forum*, 331, 829-834 (2000)
[4] Sir H. Bessemer, British Patent 11317
[5] R. Cook, P.G. Grocok, P.M. Thomas, D.V. Edmonds and J. D. Hunt, *Journal of Materials Processing Technology*, 55, 76-84 (1995)
[6] F. J. Humphreys and M. Hatherly, *Recrystallization and related annealing phenomena*, Pergamon (1995).

Aluminum Wrought Products for Automotive, Packaging, and Other Applications -The James Morris Honorary Symposium
Edited by S.K. Das, G. Jha, Z. Li, T. Zhai, and J. Liu TMS (The Minerals, Metals & Materials Society), 2006

HEATING RATE EFFECT ON MICROSTRUCTURE EVOLUTION DURING ANNEALING OF TWIN ROLL CAST AA3105

Naiyu Sun[1], Burton Patterson[1], Jaakko Suni[2], Eider Simielli[2], Hasso Weiland[2], Puja Kadolkar[3], Craig Blue[3], Gregory Thompson[4]

[1]University of Alabama at Birmingham; 1530 3rd Avenue South; Birmingham, AL, 35294, USA
[2]Alcoa Technical Center; 100 Technical Drive; Alcoa Center, PA, 15069, USA
[3]Oak Ridge National Laboratory; 1 Bethel Valley Road; Oak Ridge, TN, 37831, USA
[4]University of Alabama; 2765 3rd Street; Tuscaloosa, AL, 35487, USA

Keywords: Aluminum alloy, Recrystallization, Infrared heating, Twin roll cast

Abstract

The effect of heating rate on precipitation and recrystallization behavior in twin roll cast (TRC) AA3105 has been investigated using controlled infrared heating. Experimental results show that as-recrystallized grain size decreases as heating rate increases. Time-temperature-transformation curves for both precipitation and recrystallization were obtained. At a heating rate of 50°C/s, the material undergoes grain growth after recrystallization at 500°C. No sign of grain growth was observed in materials heated with lower heating rates, 3, 0.5 and 0.01°C/s.

Introduction

Rapid solidification and cooling during twin roll casting of AA3105 retains manganese supersaturation that precipitates as fine $Al_{12}(Mn,Fe)_3Si$ dispersoids during annealing. These particles inhibit recrystallization by Zener pinning of subgrain boundaries, resulting in a coarse, elongated grain structure [1, 2]. Prior studies have shown that a higher annealing temperature produces a finer recrystallized grain structure [3]. However, the heating rate of material placed in a conventional air furnace at temperature varies with both furnace temperature and time, as shown in Figure 1(a). As a result, in a conventional air furnace, the effect of annealing temperature on recrystallization is combined with the effect of heating rate, i.e., higher furnace temperatures produce higher workpiece heating rates and the two effects on recrystallization are difficult to separate.

Infrared (IR) heating provides an excellent means for investigating the effect of heating rate on precipitation and recrystallization in a material with supersaturated matrix. The IR furnace employs a high intensity tungsten filament to transfer radiant energy to the part. The extremely high source temperature of the tungsten filament leads to high thermal transfer and extremely fast heating [4, 5]. The low thermal mass of the tungsten filament gives good control of the heat output and process temperature. Full output can be obtained within seconds of applying power. Also, power can be turned off almost immediately at the end of the process. Thus, workpiece heating rate can be well controlled and is independent of temperature, as shown in Figure 1(b).

Experimental Procedure

TRC AA3105 was produced by Alcoa, with the chemical composition given in Table I. The material was cold rolled 90% prior to annealing. The three highest constant heating rates, 50, 3 and 0.5°C/s, were achieved in an electric IR furnace at the ORNL Materials Processing Lab,

while the slowest constant heating rate, 0.01°C/s, was obtained with a conventional programmable air furnace. For comparison, some material was also annealed at different temperatures in a conventional air furnace. Optical microscopy was used to examine the recrystallized grain structure. Solute precipitation during annealing was monitored via electrical conductivity measurement.

Table I. Chemical Composition of TRC AA3105					
Element	Mn	Mg	Fe	Si	Cu
Wt %	0.59	0.44	0.55	0.28	0.04

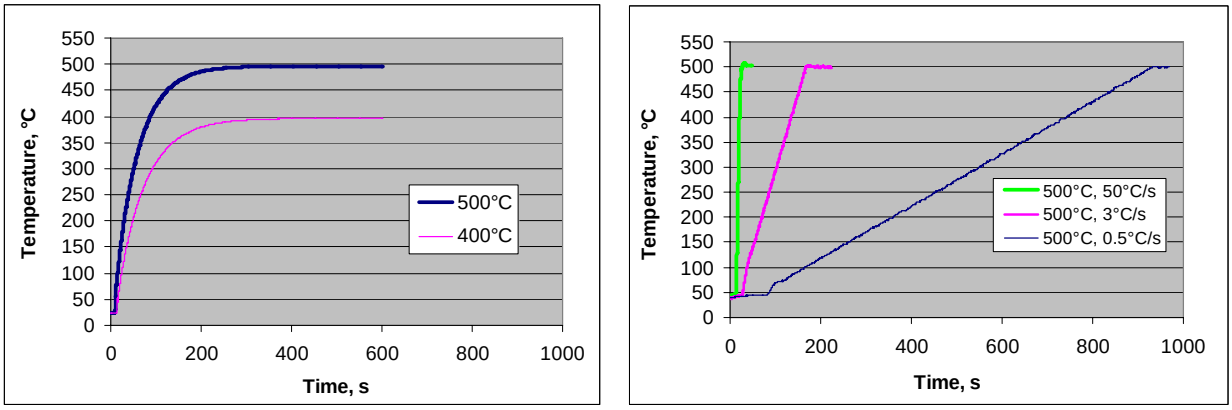

(a) (b)

Figure 1, Heating curves for TRC AA3105: (a) conventional air furnace, (b) IR furnace.

Results and Discussion

Figure 2 shows recrystallized grain structure for TRC AA3105 annealed in an air furnace at different temperatures, 500°C and 400°C. Material annealed at 500°C shows finer recrystallized grain structure than at 400°C, as shown in Figures 2 (a) and (b). This apparent effect of recrystallization temperature on grain size is actually a combined effect of both annealing temperature and heating rate. Dispersoid particles precipitating during heating and at the annealing temperature are known to interact with subgrains that form the nuclei for recrystallization [2, 6-8]. Slower heating allows more dispersoid precipitation on subgrain boundaries, preventing nucleation of recrystallizing grains, resulting in a coarser recrystallized grain size.

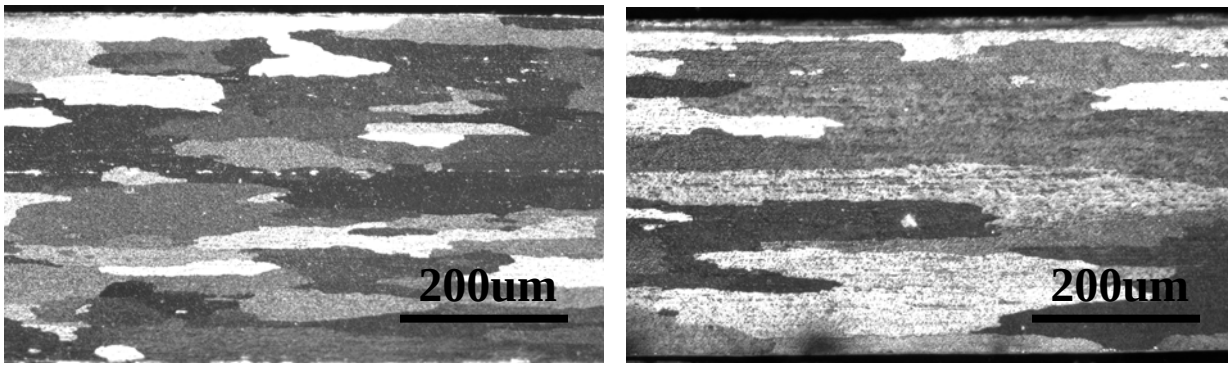

(a) (b)

Figure 2, As-recrystallized grain structure for material annealed in an air furnace at different temperatures: (a) 500°C, and (b) 400°C.

Figure 3 shows the TTT diagram determined for TRC AA3105, overlaying the start and finish of recrystallization with the times for different amounts of dispersoid precipitation at different temperatures, the latter determined from electrical conductivity measurements. It is apparent that high heating rates to high temperatures should allow rapid recrystallization prior to formation of nucleation inhibiting dispersoids, and should result in a fine recrystallized grain size. Also, slower heating rates should allow significant dispersoid precipitation prior to the start of recrystallization, greatly hindering nucleation and resulting in a much coarser grain size. The following study was designed to explore this predicted effect of heating rate on recrystallized grain size.

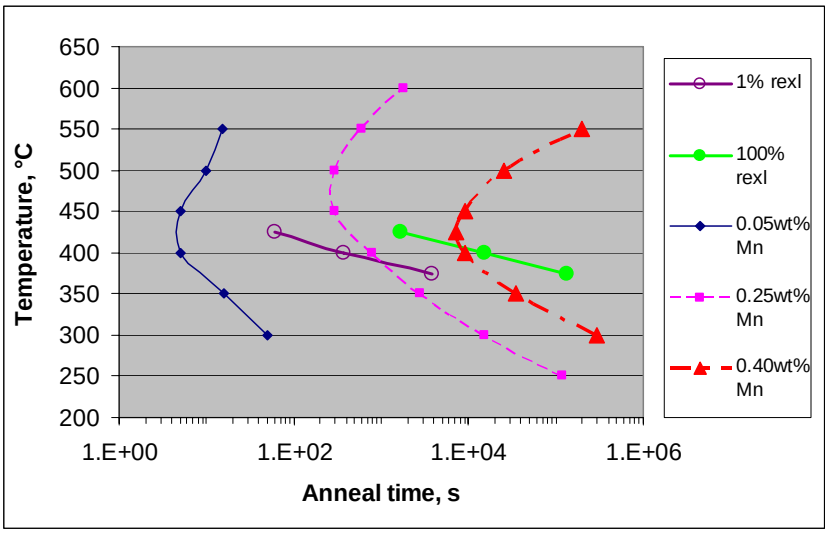

Figure 3, Recrystallization and precipitation TTT curves for TRC AA3105

The rapid, controlled heating rate of the IR furnace enables separation of the effects of heating rate and annealing temperature on recrystallization. Figure 4 shows as-recrystallized grain structure, i.e., prior to any grain growth, for materials annealed with different IR heating rates. It is apparent that, the average recrystallized grain size increases as the heating rate decreases. For the fastest heating rate, 50°C/s, the material was heated up to target temperature within approximately 10 seconds from room temperature. As a result, very little manganese precipitation occurred, less than 0.05 wt%, as shown in Figure 3. As heating rate decreases, materials require a longer heating time to temperature, resulting in greater precipitation. In a previous study [2], the authors showed that precipitates tend to pin subgrain boundaries and inhibit nucleation process during recrystallization. Thus, material with fewer precipitates can form more nuclei during recrystallization, and obtain a finer recrystallized grain structure.

Figure 5 shows material annealed at 500°C with a 50°C/s heating rate. It is apparent that the material underwent grain growth after holding at temperature for a short period of time, from 5 seconds to 5 minutes. However, grain growth was not observed in material annealed at the lower heating rates, 3, 0.5 and 0.01°C/s. This observation suggests that the grain growth at 500°C may due to the absence of precipitates during recrystallization in the most rapidly heated material. At lower heating rates, the material had more time to precipitate a large amount of dispersoids that pin the grain boundaries. As a result, the as-recrystallized grain structure is stable in material annealed with the slower heating rates, as shown in Figure 6.

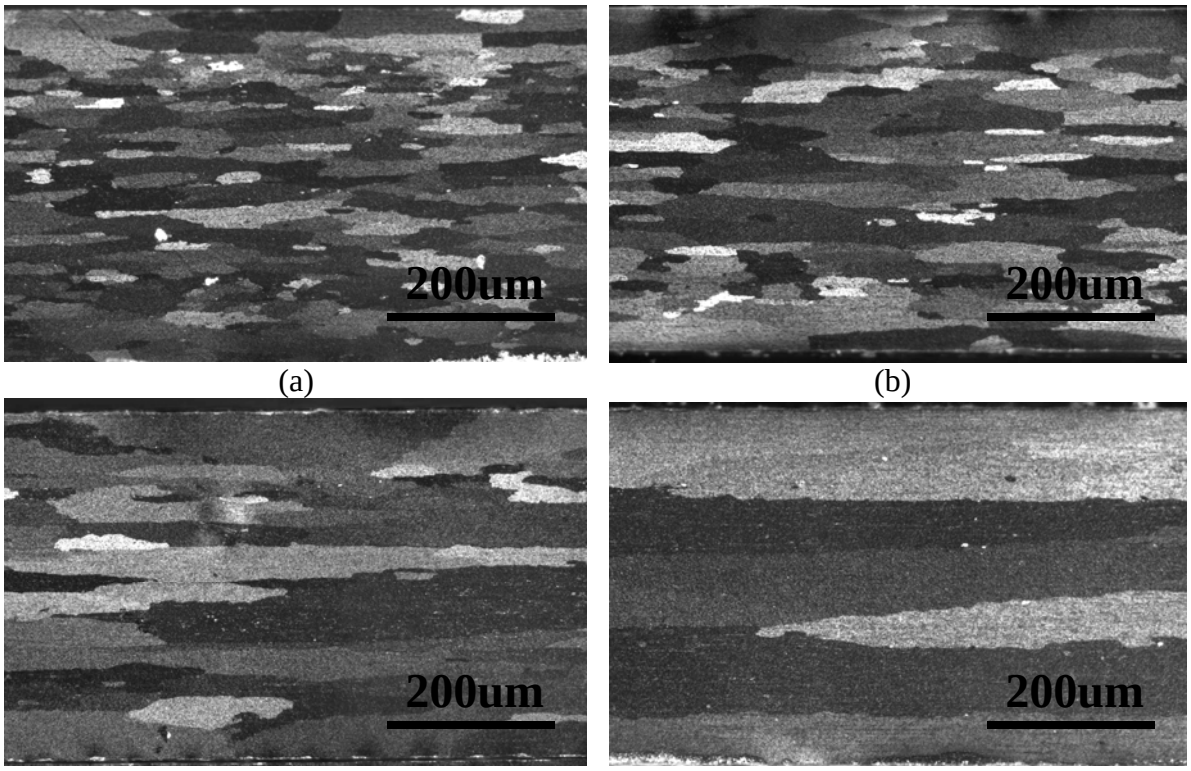

(a) (b)

(c) (d)

Figure 4, As-recrystallized grain structure for materials annealed at 500°C with different heating rates: (a) 50, (b) 3, (c) 0.5, and (d) 0.01°C/s

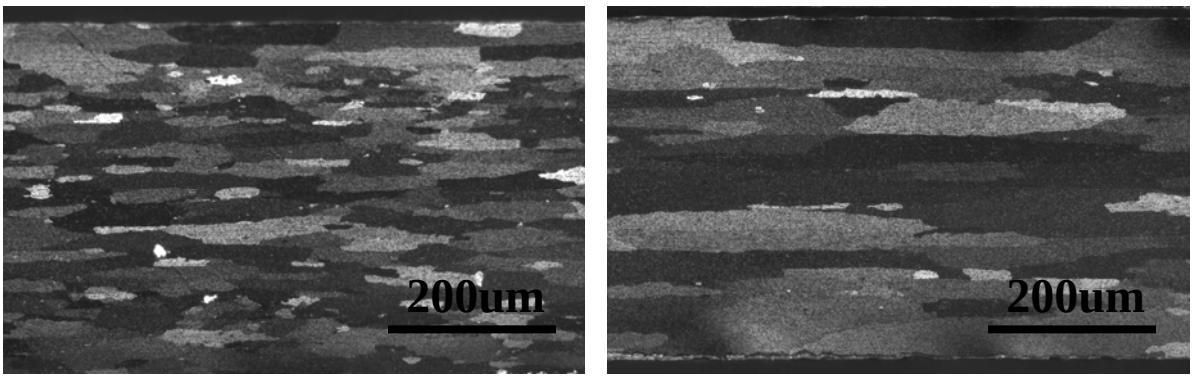

(a) (b)

Figure 5, Material annealed at 500°C with 50°C/s heating rate: (a) 5s hold at temperature, (b) 5min at temperature.

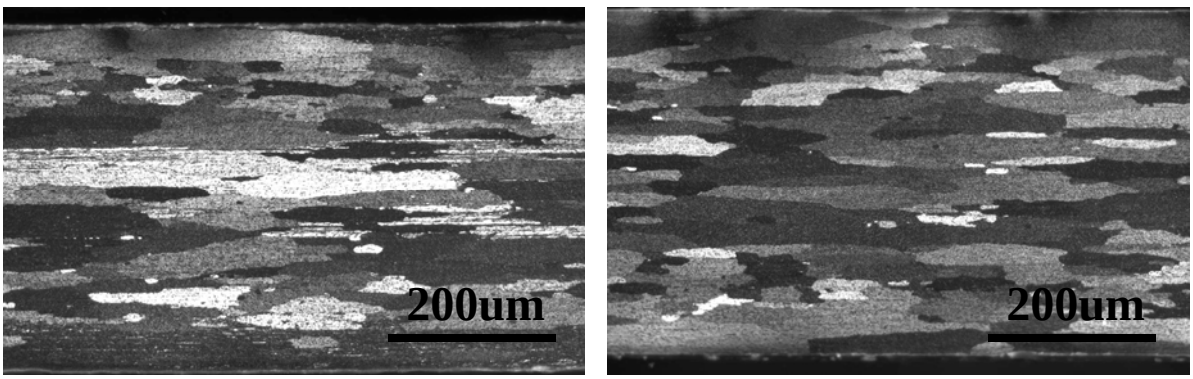

(a) (b)

Figure 6, Material annealed at 500°C with 3°C/s heating rate: (a) 5s hold at temperature, (b) 5minute at temperature. Note: material has not fully recrystallized yet after 5 seconds.

Conclusions

The following conclusions can be drawn from this study on TRC AA3105:

1. For conventional air furnace, annealing at a higher temperature results in a finer recrystallized grain structure.
2. Faster anneal heating rate results in a finer recrystallized grain structure.
3. Grain growth is observed after recrystallization at 500°C with the fastest 50°C/s heating.
4. No grain growth is found in material annealed at the slower heating rates, 3, 0.5 and 0.01°C/s.

Acknowledgments

The authors gratefully acknowledge research funding by Department of Energy grant no. DE-FC36-02ID14401 and the support from the Assistant Secretary for Energy Efficiency and Renewable Energy, Office of Industrial Technologies, Advanced Industrial Materials Program, under contract DE-AC05-00OR22725 with UT-Battelle, LLC.

References

1. N. Sun, B. R. Patterson, J. P. Suni, E. A. Simielli, H. Weiland and L. F. Allard, TMS letters, 2, 33-34 (2005)
2. N. Sun, B. R. Patterson, J. P. Suni, E. A. Simielli, H. Weiland and L. F. Allard, Materials Science and Engineering A, in press, (2005)
3. B. R. Patterson, N. Sun, J. P. Suni, E. A. Simielli, H. Weiland and L. F. Allard, TMS letters, 8, 173-174 (2004)
4. Craig A. Blue, Vinod K. Sikka, Randall A. Blue, and Ray Y. Lin, Metallurgical and Materials Transactions A, 27A, 1-8 (1996)
5. C. A. Blue, V. K. Sikka, E. K. Ohriner, P. G. Engleman, D. C. Harper, JOM-e, 52, (2000)
6. R. D. Doherty and J. W. Martin, Journal of the Institute of Metals, 91, 332-338 (1962)
7. Erik Nes, Acta Metallurgica, 24, 391-398 (1976)
8. F. J. Humphreys and M. Hatherly, Recrystallization and related annealing phenomena, first ed., Pergamon, Oxford, 1995

Microstructural Evolution During Annealing Of Twin Roll Cast AA3105

Burton R. Patterson[1], Naiyu Sun[1], Jaakko P. Suni[2], Eider A. Simielli[2], Hasso Weiland[2], Larry Allard[3]

[1]University of Alabama at Birmingham; 1530 3rd Avenue South; Birmingham, AL 35294, USA
[2]Alcoa Technical Center; 100 Technical Drive; Alcoa Center, PA 15069, USA
[3]Oak Ridge National Laboratory; 1 Bethel Valley Road; Oak Ridge, TN 37831, USA

Subject Categories: Advanced Processing, Aluminum, Characterization

Abstract

This study examined the effects of preheat and annealing temperature on the annealing response of twin roll cast AA3105. TTT curves for dispersoid precipitation and recrystallization were developed. Variations in recrystallization kinetics and grain size were explained in terms of dispersoid influence on recrystallization.

Introduction

Twin roll casting (TRC) is an energy and cost efficient process for producing thin strip directly from molten metal, eliminating hot rolling [1-4]. With AA3105, the TRC process results in inhibited recrystallization after cold rolling and a large grain size. The goal of this study was to investigate the causes of these problems, believed to be dispersoid precipitation from the rapidly solidified manganese supersaturated material.

Experimental Procedure

TRC AA3105 material was produced by Alcoa, with the chemical composition given in Table I. Annealing response was investigated for both preheated and as-cast materials. Preheating involved holding at 600°C for 5 hours followed by cooling at 0.3°C/min to room temperature. Both materials were cold rolled 90% before annealing at different temperatures and times.

Table I. Chemical Composition of TRC AA3105

Element	Mn	Mg	Si	Fe	Cu
wt%	0.59	0.44	0.28	0.55	0.04

Results and Discussion

Figure 1 shows non-preheated materials annealed at 550°C and 400°C. Material annealed at higher temperature, Figure 1a, exhibits a finer recrystallized grain size than that at lower temperature, Figure 1b. Figure 2, showing recrystallization and precipitation TTT curves for non-preheated material, helps explain the interaction of recrystallization and precipitation during annealing. At higher temperatures, recrystallization begins and finishes earlier with less concurrent precipitation, resulting in a finer grain size.

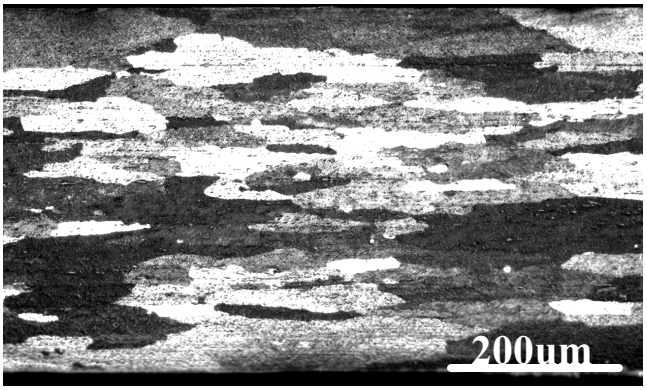

(a) 550°C air furnace anneal for 5minutes

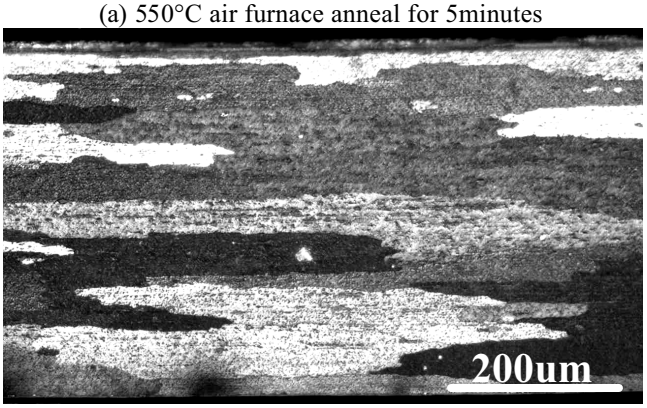

(b) 400°C air furnace anneal for 8 hours

Figure 1 Non-preheated materials annealed at (a) 550°C, and (b) 400°C.

Figure 3 shows the duplex particle structure of non-preheated material, with coarse constituents and fine dispersoids. Material annealed at lower temperatures precipitates more dispersoids, pinning sub-grain boundaries, increasing recrystallization time and final grain size [5]. High temperature preheating with slow cooling coarsens constituent and removes supersaturated manganese solute from solution. These changes reduce dispersoid formation, Figure 4, resulting in a much finer

recrystallized grain size, Figure 5 and faster recrystallization kinetics. Even at a higher temperature, non-preheated material recrystallized more slowly than that of the preheated, as shown in Figure 6.

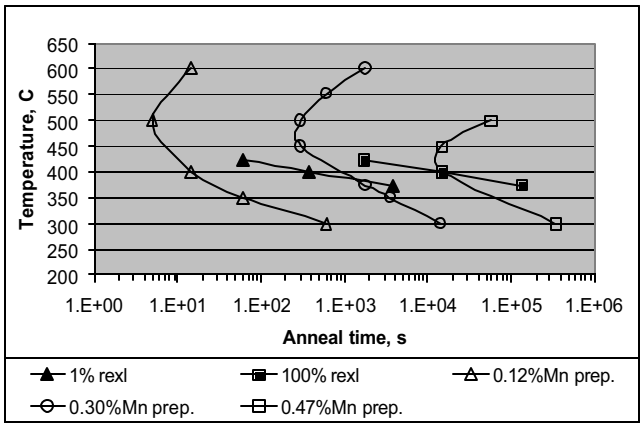

Figure 2 Recrystallization and precipitation TTT curves for non-preheated material.

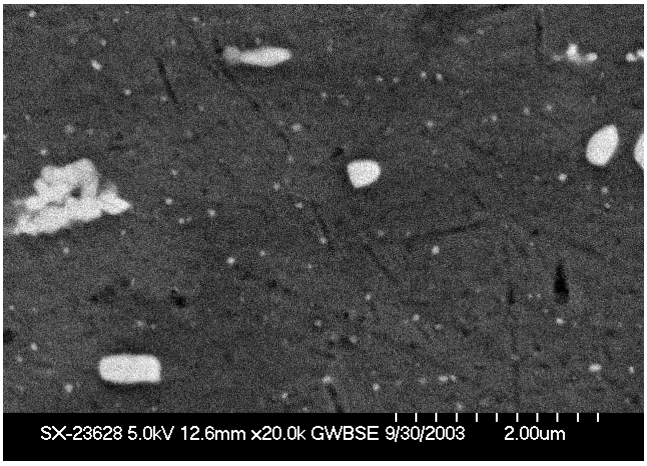

Figure 3 Constituent and dispersoid particle structure in non-preheated material after annealing at 450°C.

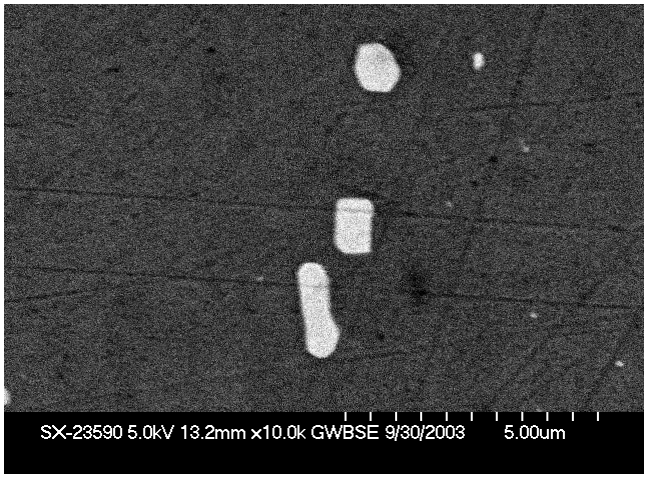

Figure 4 Coarsened constituent particle structure in preheated material, lower magnification.

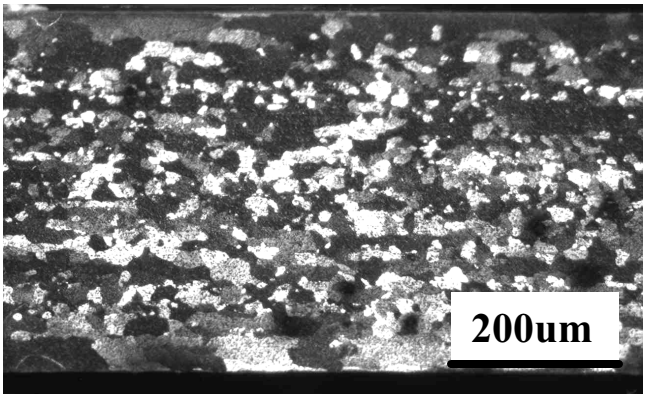

Figure 5 Preheated materials annealed at 300C for 1 hour.

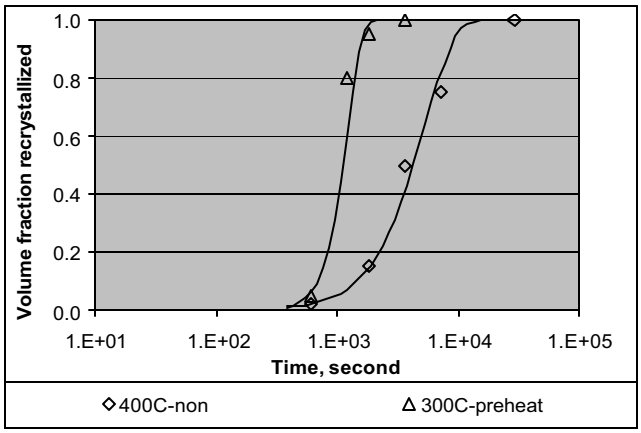

Figure 6 Recrystallization kinetics for preheated and non-preheated materials.

Acknowledgements

The authors gratefully acknowledge research support from Department of Energy grant no. DE-FC36-02ID14401 and the Assistant Secretary for Energy Efficiency and Renewable Energy, Office of Transportation Technologies, as part of the High Temperature Materials Laboratory User Program, Oak Ridge National Laboratory, managed by UT-Battelle, LLC, for the U.S. Department of Energy under contract number DE-AC05-00OR22725.

References

[1] M. Yun, S. Lokyer and J. D. Hunt, *Materials Science and Engineering*, A280, 116-123 (2000)

[2] M. Karlik, J. Siegl and M. Slamova, *Physical Metallurgy and Fracture of Materials*, 113-116 (1999)

[3] M. Slamova, V. Ocenasek, M. Cieslar, B. Chalupa and P. Merle, *Materials Science Forum*, 331, 829-834 (2000)

[4] R. Cook, P.G. Grocok, P.M. Thomas, D.V. Edmonds and J. D. Hunt, *Journal of Materials Processing Technology*, 55, 76-84 (1995)

[5] R. D. Doherty and J. W. Martin, *Journal of the Institute of Metals*, 91, 332-338 (1962)

TMS Letters **TMS (The Minerals, Metals & Materials Society), 2005**

Microstructural gradients in Twin Roll Cast AA3105

Naiyu Sun[1], Burton R. Patterson[1], Jaakko P. Suni[2], Eider A. Simielli[2], Hasso Weiland[2], Larry Allard[3]

[1]University of Alabama at Birmingham; 1530 3rd Avenue South; Birmingham, AL 35294, USA
[2]Alcoa Technical Center; 100 Technical Drive; Alcoa Center, PA 15069, USA
[3]Oak Ridge National Laboratory; 1 Bethel Valley Road; Oak Ridge, TN 37831, USA

Subject Categories: Advanced Processing, Aluminum, Characterization

Abstract

Twin roll cast (TRC) AA3105 exhibits a marked constituent particle size gradient and coarse grain size after cold rolling and annealing. Traditional homogenization treatments refine the recrystallized grain size but still result in relatively coarse grains at the strip surface. This paper examines the effects of different homogenization treatments on the particle and grain structure in the above alloy. A new homogenization procedure to eliminate the particle and grain size gradients is proposed.

Introduction

TRC is an energy and cost efficient process for producing thin strip directly from molten metal, eliminating hot rolling [1-4]. With AA3105, the TRC process results in inhibited recrystallization and a coarse recrystallized grain structure elongated in the rolling direction, Fig.1.[5] Homogenization prior to rolling has been found to refine the recrystallized grain structure, somewhat, although a relatively coarse grain size at the strip surface often results. The goal of this study is to determine the cause of the grain size gradient and propose a new procedure to overcome it.

Experimental Procedure

TRC AA3105 was produced by Alcoa, with the chemical composition given in Table I. Annealing response was investigated for both homogenized and non-homogenized materials. The homogenization procedures are given in Table II. Materials were cold rolled 90% prior to annealing.

Table I. Chemical Composition of TRC AA3105					
Element	Mn	Mg	Fe	Si	Cu
wt%	0.59	0.44	0.55	0.28	0.04

Table II. Homogenization parameters			
Designation	H1	H3	H5
Temperature, ºC	500	600	620/450
Duration, hr	5	5	5
Cooling rate, ºC/min	0.3	0.3	0.3
Heating cycles	1	1	10

Results and Discussion

Figure 1 shows recrystallized grain structures for both homogenized (H) and non-homogenized (NH) material. The NH material, Fig.1(a), exhibits a very coarse and elongated grain structure. The homogenized materials all show finer grain sizes, mostly due to the removal of manganese from solution and less dispersoid precipitation during annealing. The H3 homogenization, 600ºC/5hr, Fig.1(c), shows a finer grain size than H1 at lower temperature), 500ºC/5hr, Fig.1(b). However, both H1 and H3 treatments exhibit a grain size gradient, with coarse grains near the strip surface. With H3, Fig.1(c), the average grain size is approximately 70um at the surface and 20um at the center. H5 homogenization, involving 10 cycles

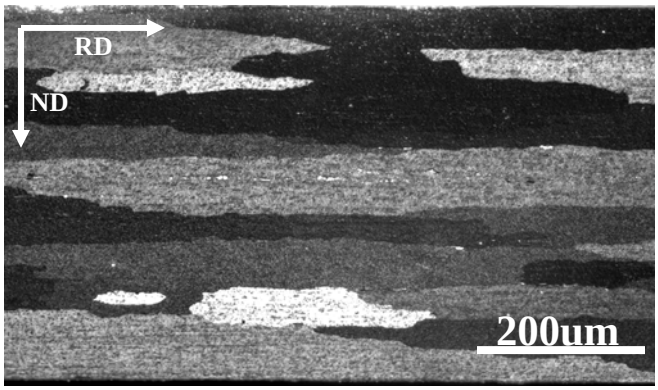

(a)

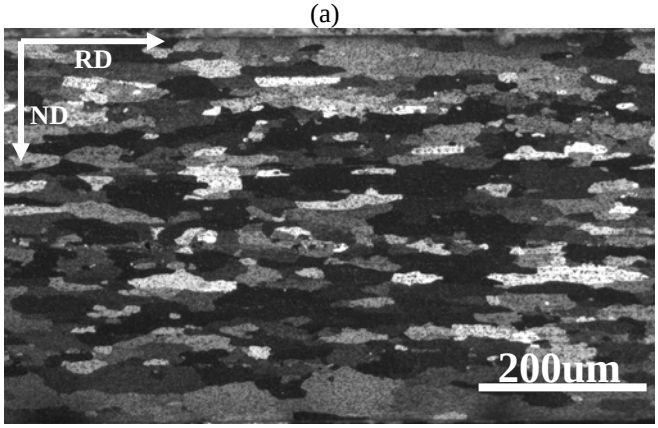

(b)

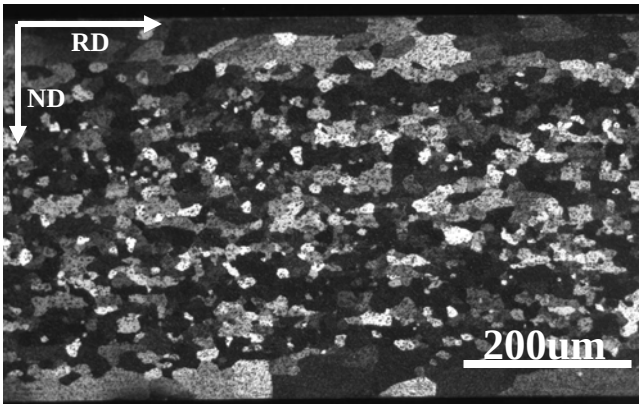

(c)

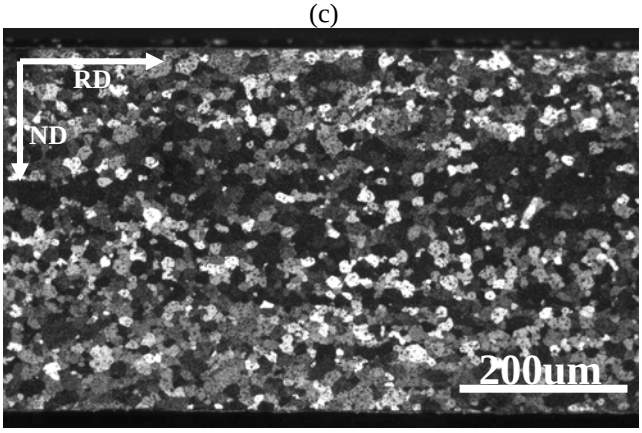

(d)

Figure 1 Micrographs of cold rolled and annealed TRC AA3105 (a) non-homogenized, (b) H1, (c) H3 and (d) H5 homogenized. All photos show entire strip cross-section.

between 450 and 620ºC, Fig.1(d), eliminated the grain size gradient and produced a uniform fine grain size of 15um.Figure 2 shows the particle number distribution from strip surface to the center in H3 homogenized material. The overall number per unit area, N_A, of particle sections decreases rapidly from approximately $1.8x10^5$ to $5x10^4$ mm^{-2}. The number density of just the larger particles, >1um, increases rapidly from approximately $4x10^4$ to $1.3x10^5$ within the first 50um from the surface. After H5

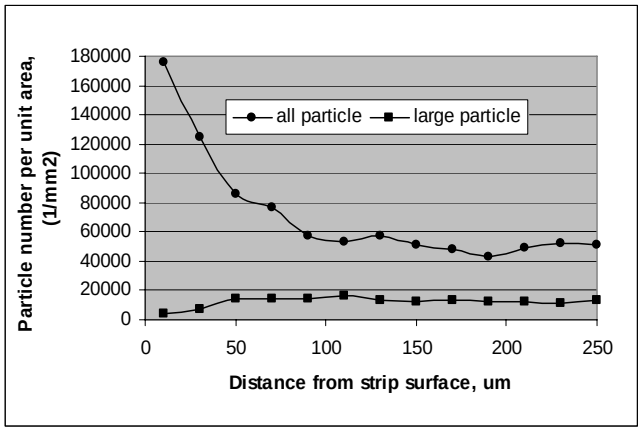

Figure 2 Second phase particle number distribution from strip surface to center after H3 homogenization.

homogenization the overall particle number density and gradient are both greatly reduced, Fig.3, while the large particle number density stays unchanged at about $1.3x10^4$. It is evident that increased homogenization temperature and time promote particle coarsening, with (a)dissolution of the fine constituent particles, especially at the strip surface, increasing the mean interparticle spacing and reducing inhibition[6], and (b)growth of the coarse particles that stimulate nucleation[7], whose numbers remain relatively constant. Together, these processes reduce recrystallized grain size and avoid formation of large surface grains.

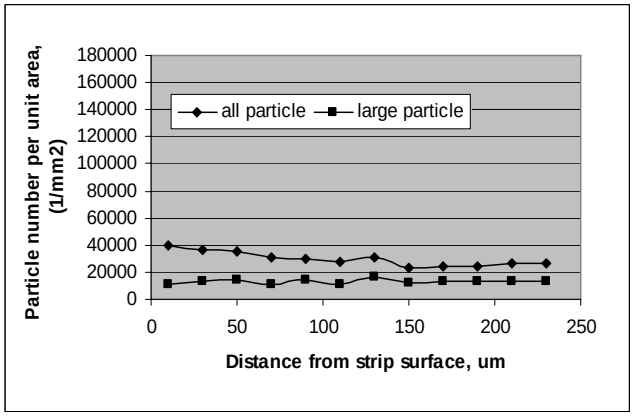

Figure 3 Second phase particle number distribution from strip surface to center after H5 homogenization.

Acknowledgements

The authors gratefully acknowledge research funding by Department of Energy grant no. DE-FC36-02ID14401 and the support from the Assistant Secretary for Energy Efficiency and Renewable Energy, Office of Transportation Technologies, as part of the High Temperature Materials Laboratory User Program, Oak Ridge National Laboratory, managed by UT-Battelle, LLC, for the U.S. Department of Energy under contract number DE-AC05-00OR22725.

References

[1] M. Yun, S. Lokyer and J. D. Hunt, *Materials Science and Engineering*, A280, 116-123 (2000)

[2] Toshio Haga, Kenta Tkahashi, Masaaki Ikawaand and Hisaki Watari, *Journal of Materials Processing Technology*, 153, 42-47 (2004)

[3] M. Slamova, V. Ocenasek, M. Cieslar, B. Chalupa and P. Merle, *Materials Science Forum*, 331, 829-834 (2000)

[4] R. Cook, P.G. Grocok, P.M. Thomas, D.V. Edmonds and J. D. Hunt, *Journal of Materials Processing Technology*, 55, 76-84 (1995)

[5] B. R. Patterson, N. Sun, J. P. Suni, E. A. Simielli, H. Weiland and L. F. Allard, *TMS letters*, 8, 173-174 (2004)

[6] R. D. Doherty and J. W. Martin, *Journal of the Institute of Metals*, 91, 332-338 (1962)

[7] F. J. Humphreys and M. Hatherly, Recrystallization and Related Annealing Phenomena, Pergamon (1995)

Materials Science and Engineering A 416 (2006) 232–239

www.elsevier.com/locate/msea

Microstructural evolution in twin roll cast AA3105 during homogenization

Naiyu Sun [a,*], Burton R. Patterson [a], Jaakko P. Suni [b], Eider A. Simielli [b], Hasso Weiland [b], Lawrence F. Allard [c]

[a] *Department of Materials Science and Engineering, University of Alabama at Birmingham, 1530 3rd Avenue South, Birmingham, AL 35294, USA*
[b] *Alcoa Technical Center, 100 Technical Drive, Alcoa Center, PA 15069, USA*
[c] *Oak Ridge National Laboratory, 1 Bethel Valley Road, Oak Ridge, TN 37831, USA*

Received in revised form 28 September 2005; accepted 5 October 2005

Abstract

In twin roll cast (TRC) AA3105, high solidification and post-solidification cooling rates lead to high manganese supersaturation throughout the strip and very fine constituent particles near the surface. Rolled and annealed TRC material shows sluggish recrystallization kinetics and a very coarse grain structure, due to concurrent dispersoid precipitation that inhibits formation of recrystallization nuclei. Homogenization from 5 to 120 h at 600 °C reduced solute supersaturation and coarsened constituent particles, reducing but not eliminating the particle size gradient. The resulting grain structure was fine throughout most of the strip, but with larger grains at the surface. More extensive cyclical homogenization up to 620 °C further coarsened the constituent particles and produced a uniform fine grain structure throughout the strip.

Keywords: Twin roll casting; Homogenization; Aluminum alloy; Microstructural evolution; Recrystallization

1. Introduction

Twin roll casting (TRC) is an energy efficient process for producing several-mm thick sheet directly from molten metal in one operation, eliminating the need for hot rolling [1–3]. Solidification in the TRC process is quite different than that in traditional direct chill (DC) casting, due to the large thermal gradient across the thickness of the strip. Fig. 1 shows the "working zone" of a twin roll caster. The molten metal is directed through a ceramic tip between two internally cooled rolls, with a higher solidification rate at the roll-strip contact surface than at the center of the strip.

To some degree, the microstructure of TRC material is controlled by the various casting parameters, such as casting rate, tip setback, strip gauge, and metal temperature. Higher casting speed increases production efficiency, but can lead to centerline segregation, as shown in Fig. 2, and macro-defects [4]. Intensive studies have been carried out to optimize the casting parameters and alloy compositions in order to achieve high production and quality in TRC materials [5–9]. However, in some aluminum alloys such as TRC AA3105, microstructural gradients and/or inhomogeneities inherently exist and cannot be eliminated by altering TRC processing parameters.

In particular, there exist gradients in constituent particle size and solute content, with high solute supersaturation throughout the material and very fine constituent particles within 50 μm of the surface. After cold rolling and annealing, the recrystallized grain size is much coarser, on the order of mm, than in DC cast AA3105. This coarse structure is detrimental to mechanical properties and surface appearance, and limits the applications for the material to lower end products. The applications for TRC AA3105 would be greatly expanded by developing means to overcome the above problems associated with the roll casting process.

The recrystallization behavior of commercial DC cast aluminum alloys has been the focus of extensive research over several decades, and numerous studies have been made of the effects of second phase particles, both constituent and finer dispersoids [10–16]. It is widely accepted that coarse constituent particles promote nucleation, by the particle-stimulated nucleation (PSN) mechanism. Finer particles, whether constituent or precipitated dispersoids, inhibit growth of subgrains into

* Corresponding author. Tel.: +1 205 934 1572; fax: +1 205 934 8485.
E-mail address: nysun@uab.edu (N. Sun).

0921-5093/$ – see front matter © 2005 Elsevier B.V. All rights reserved.
doi:10.1016/j.msea.2005.10.018

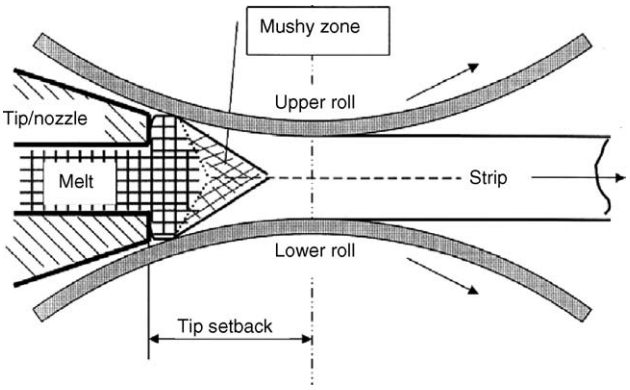

Fig. 1. Illustration of the solidification and rolling process during TRC.

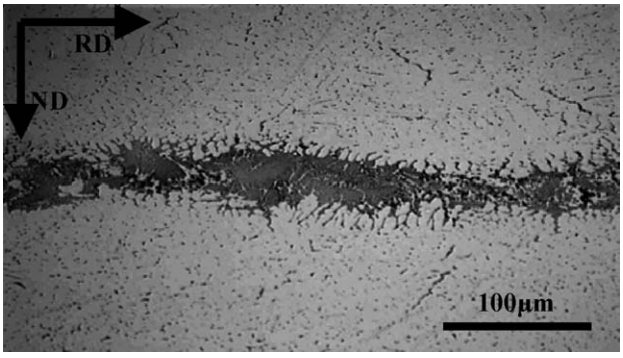

Fig. 2. Optical micrograph of centerline segregation in an as-cast AA3105 strip.

viable nuclei by boundary pinning, and can restrict growth of nucleated grains. These basic processes and understandings provide insight into the recrystallization problems with TRC AA3105, with inherent constituent particle size gradients and the high solute supersaturation promoting dispersoid formation.

Few detailed recrystallization studies have been performed on TRC aluminum [17,18]. The above characteristics of TRC AA3105, however, suggest possible solutions to the annealing problems. It is of particular interest to determine the ability of high temperature homogenization, or preheating, on refinement of the recrystallized grain size. High temperature treatment should increase the number of potential PSN nucleation sites by coarsening the overall constituent particle structure and dissolving the finest particles that could hinder formation of viable recrystallization nuclei. Slow cooling from the high temperature soak should also reduce solute supersaturation, depositing the excess manganese on constituent phase, reducing later dispersoid precipitation during annealing. Reduced dispersoid formation would enable more of the nuclei forming at constituent particles to evolve into growing grains, reducing the overall grain size. This paper presents a systematic study of the effects of different homogenization treatments on these processes and the resultant effect on recrystallization of TRC AA3105.

2. Experimental

Twin roll cast AA3105, with composition given in Table 1, was produced for this study by Alcoa, using normal commercial processing. Homogenization treatments, listed in Table 2, were conducted in a laboratory air furnace with controllable heating and cooling rates. Treatments H1–H4 involved heating to temperature at 5 °C/min, high temperature holds from 500 to 600 °C for times from 5 to 120 h and cooling to room temperature at a rate of 0.3 °C/min. Treatment H5, suggested by Doherty [19],

Table 1
Chemical composition of the experimental AA3105, wt%

Mn	0.59
Fe	0.55
Mg	0.44
Si	0.28
Cu	0.04
Al	Bal.

Table 2
Homogenization parameters

Designation	Variables			
	Temperature (°C)	Duration (h)	Cooling rate (°C/min)	Heating cycles
H1	500	5	0.3	1
H2	550	5	0.3	1
H3	600	5	0.3	1
H4	600	120	0.3	1
H5 [19]	620/450	5	0.3	10

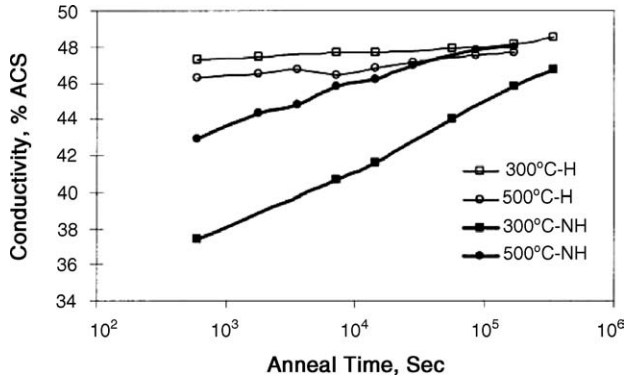

Fig. 3. Electrical conductivity of homogenized (H) and non-homogenized (NH) materials during annealing.

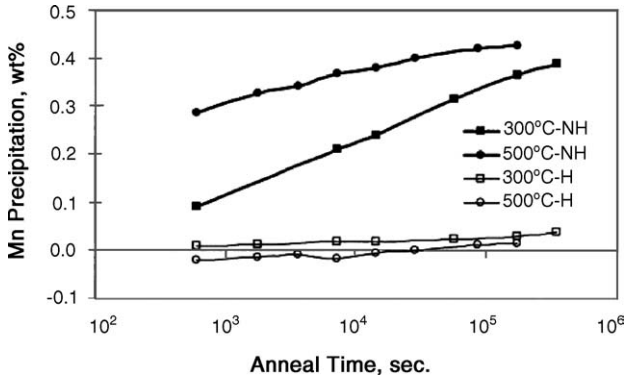

Fig. 4. Mn precipitation in H3 homogenized (H) and non-homogenized (NH) materials during annealing.

included ten cycles between 450 and 620 °C with 5 h holds at each temperature and 0.3 °C/min cooling rate from the higher to lower temperature. The single-hold treatments relied on normal particle coarsening, or Ostwald ripening, to dissolve the finer particles and diffuse the solute to the coarser particles. The cyclic H5 treatment provided accelerated dissolution and coarsening by heating to a higher temperature, 620 °C, to actively dissolve constituent, including the smallest particles, followed by slow cooling to 450 °C to re-precipitate solvent onto the remaining larger particles. All homogenization treatments were concluded by cooling to room temperature at 0.3 °C/min, to simulate the cooling rate of a commercial coil, also reducing residual solvent supersaturation. After homogenization, specimens were cold rolled to 90% reduction in thickness and annealed for recrystallization.

Samples for microstructure examination were prepared on planes parallel to the normal direction (ND) and to the rolling direction (RD). Optical microscopy was used to examine the recrystallized grain structure. Manganese solute precipitation during annealing was monitored by electrical conductivity. A Hitachi S-4700 field-emission SEM and a Hitachi HF-2000 field-emission TEM were used at Oak Ridge National Laboratory to study the constituent and dispersoid particles.

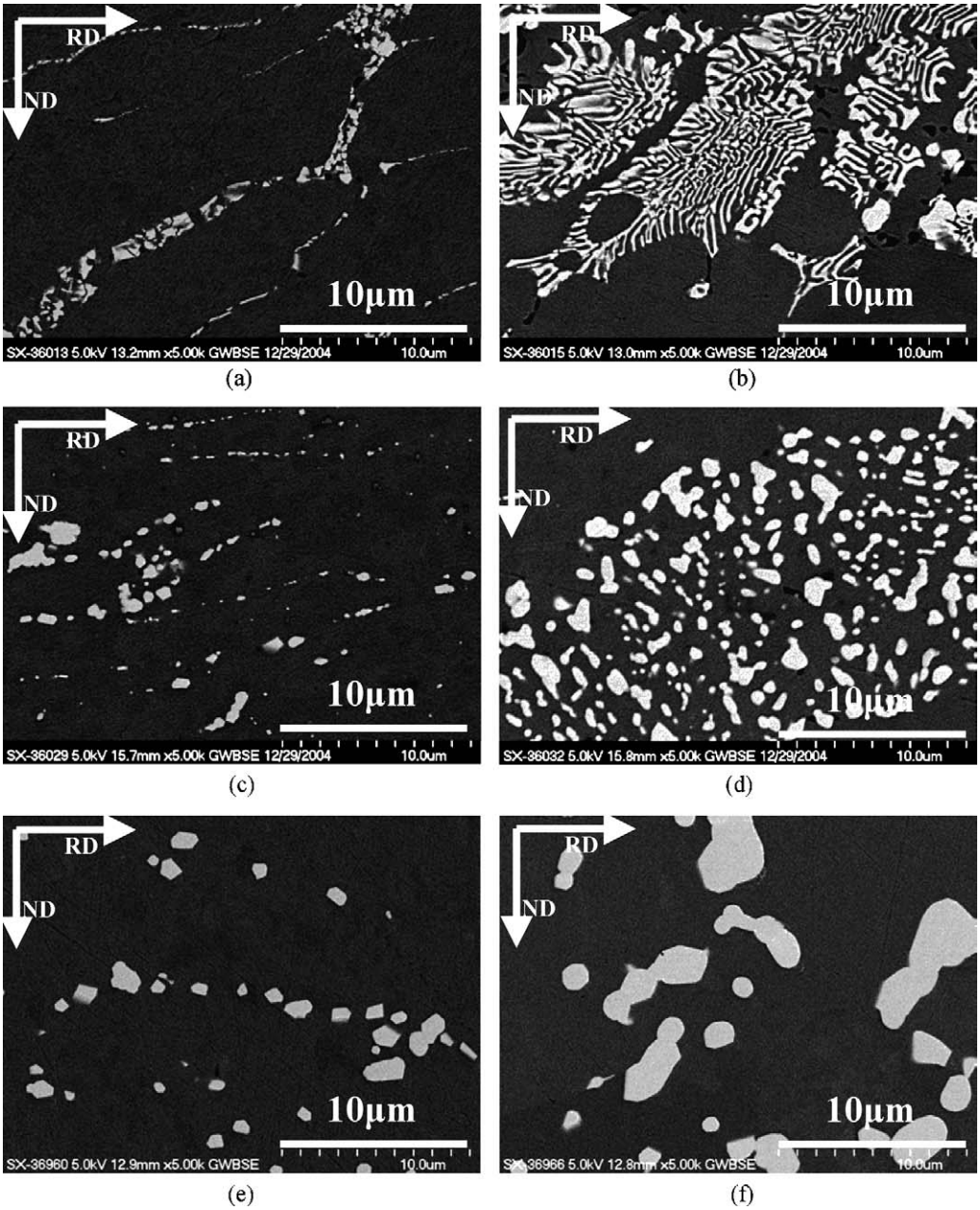

Fig. 5. Backscattered electron images showing second phase morphology of a TRC AA3105 strip before and after homogenisation: (a) as-cast, strip surface, (b) as-cast, strip center, (c) after H3, strip surface, (d) after H3, strip center, (e) after H5, strip surface and (f) after H5, strip center.

3. Results and discussion

3.1. Homogenization effect on solute precipitation

Fig. 3 shows the electrical conductivity of both homogenized (H3) and non-homogenized materials annealed at different temperatures for various times. The homogenized material showed much higher initial conductivity than non-homogenized material, with only slight change with time due to solute removal. The non-homogenized material showed a marked increase in conductivity with annealing time, from relatively low initial values. The degree of manganese removal from solution during annealing, Fig. 4, could be computed from the nearly linear relationship between manganese removal and decrease in resistivity in this material. It is apparent that there is substantial precipitation of Mn-bearing dispersoid in the non-homogenized material during annealing but little, if any, precipitation in the homogenized material. For the non-homogenized material, more than 0.4 wt% Mn left solution by precipitating as dispersoids. The H3 homogenization treatment was found to produce almost precipitate-free material after annealing, greatly increasing the recrystallization kinetics and resulting in a fine recrystallized grain structure.

3.2. Homogenization effect on constituent phase

Fig. 5 shows backscattered-electron micrographs of the constituent morphology in as-cast TRC AA3105 before and after homogenization. In the as-cast state, the constituent exists at grain boundaries with an essentially continuous network structure, as shown in Fig. 5(a). After homogenization, the second phase is broken up forming chain structures of discrete particles, as shown in Fig. 5(c). This chain structure of particles is completely replaced by well-spaced large individual particles after H5 homogenization due to more aggressive coarsening, Fig. 5(e). At the strip mid-thickness, homogenization changes the constituent from a lamellar eutectic structure, as shown in Fig. 5(b), to colonies of individual particles, as shown in Fig. 5(d), which are further coarsened during H5 homogenization, as shown in Fig. 5(f).

Fig. 6 shows the constituent particle morphology after 90% cold rolling. As shown in Fig. 6(a), the particles in the non-homogenized material tend to exist in clusters, with a size gradient from the strip surface toward the center, i.e. smaller particles at the surface, and larger particles towards the center. After H3 homogenization and cold rolling, the constituent particles do not tend to form clusters but still show the size gradient, Fig. 6(b). This distribution of more discrete particles is inherited from the homogenized structure prior to cold rolling.

With the more extensive H4 homogenization, i.e. 120 h at 600 °C, the overall particle size is coarser and the severity of size gradient is reduced, as shown in Fig. 6(c). After the higher temperature, cyclic H5 treatment, the particles are seen to be much more rounded and uniformly distributed, with a larger size and mean spacing, as shown in Fig. 6(d).

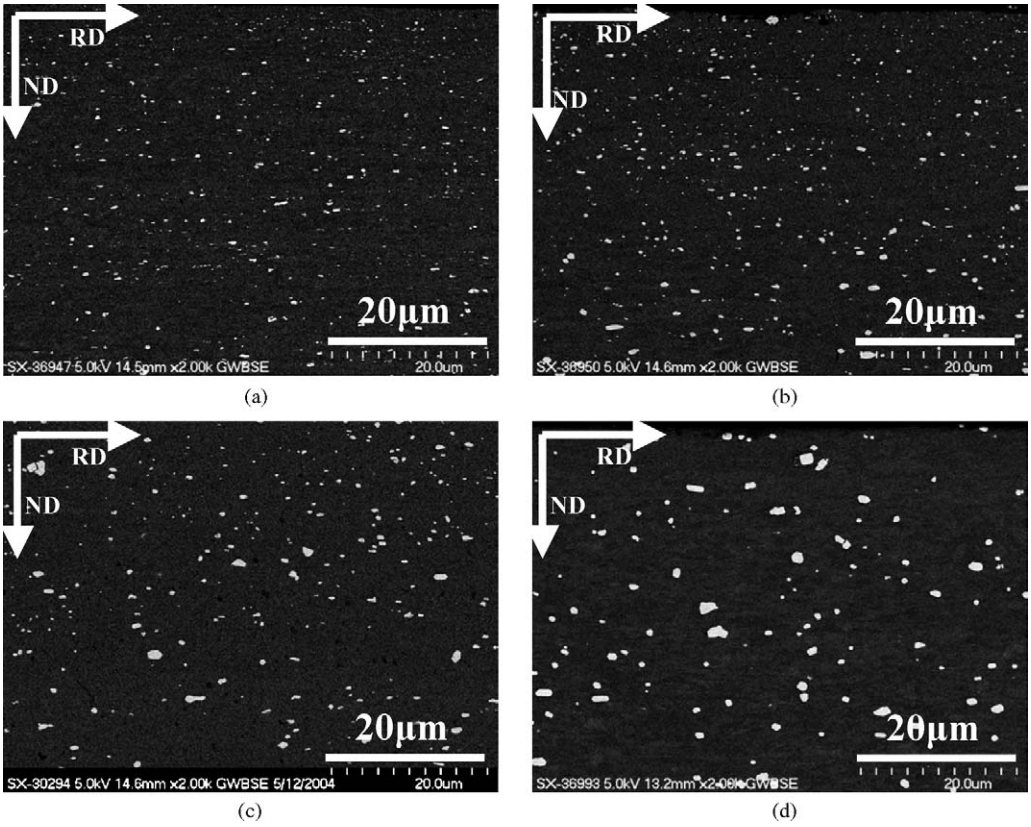

Fig. 6. Backscattered electron images showing homogenization effect on second phase particles in TRC AA3105 strip after 90% cold roll: (a) non-homogenized, and after (b) H3, (c) H4 and (d) H5 homogenization.

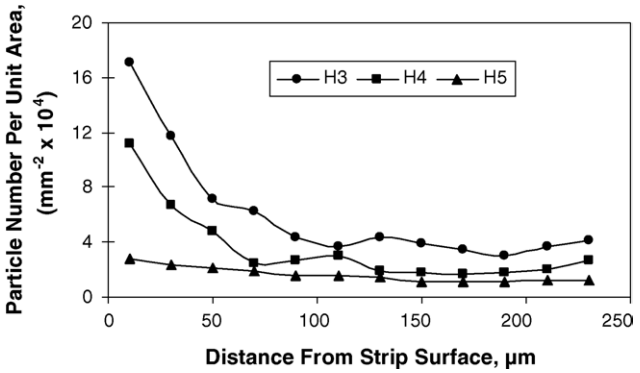

Fig. 7. Small particle (<1 μm) number distribution from strip surface to center after different homogenization treatments: H3, H4 and H5. Materials are cold rolled 90%.

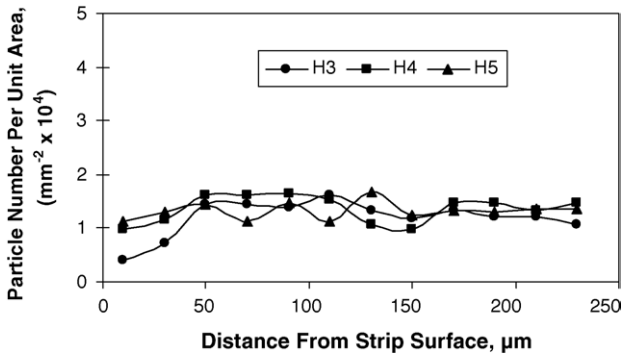

Fig. 8. Large particle (>1 μm) number distribution from strip surface to center after different homogenization treatments: H3, H4 and H5. Materials are cold rolled 90%.

3.3. Particle analysis

Particle size and distribution changes during different homogenization treatments were quantitatively characterized using particle analysis techniques. Particle sections were classified into two size groups, greater than 1 μm diameter and less than 1 μm, and quantified as particle number per area, N_A. Figs. 7 and 8 show the variation in N_A from strip surface to center.

Fig. 7 shows the small particle number density gradient from strip surface to the center for the different homogenization treatments, H3, H4 and H5. For H3 homogenized material, the particle density shows a maximum of approximately 1.7×10^5 sections/mm^2 near the surface, rapidly decreasing towards the center until reaching a stable level of $\sim 4.0 \times 10^4$ sections/mm^2 at a depth of approximately 50 μm. The maximum overall particle density for H4 homogenized material is $\sim 1.1 \times 10^5$ sections/mm^2 at strip surface, decreasing to $\sim 2.5 \times 10^4$ sections/mm^2 at approximately 50 μm below the surface. As for H5 homogenized material, the particle density shows only a small decrease from 3.0×10^4 sections/mm^2 to about 1.5×10^4 sections/mm^2 from strip surface to center.

The density of large particles shows the opposite trend, as shown in Fig. 8. For H3 homogenized material, the large particle density sees a minimum of $\sim 4 \times 10^3$ sections/mm^2 near the strip surface, increasing with depth to a stable level of $\sim 1.3 \times 10^4$ sections/mm^2 at approximately 50 μm below the

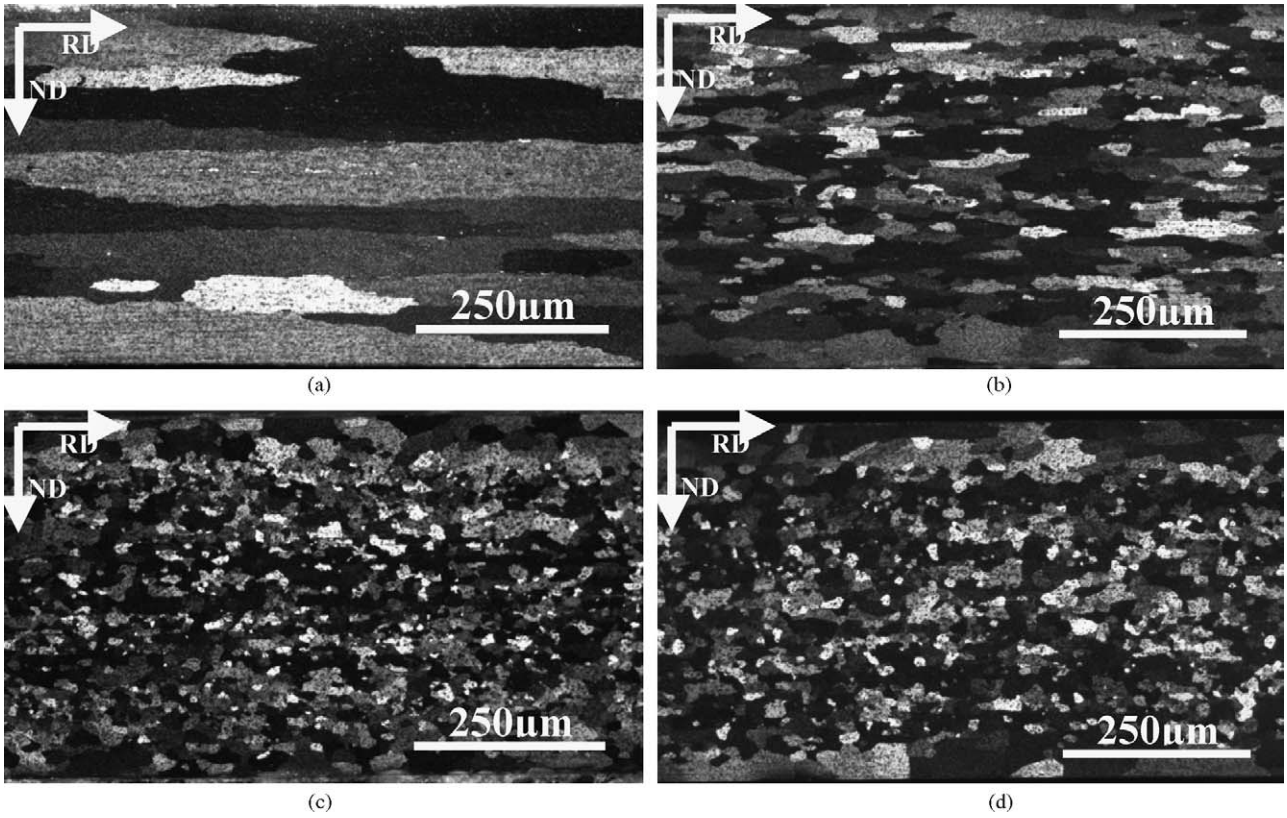

Fig. 9. Optical micrographs of cold rolled and recrystallized TRC AA3105: (a) Non-homogenized, after (b) H1, (c) H2 and (d) H3 homogenization.

strip surface. For H4 and H5 homogenized materials, the density of large particles is fairly stable at $\sim 1.3 \times 10^4$ sections/mm^2 across the strip thickness, showing only a small fluctuation with depth.

The above results show that from H3 to H5, the small particle density decreases by a factor of 6 at the strip surface and a factor of 3 at the center, while the density of large particles remains constant except for the very surface layer. It is clear that coarsening occurs during H3, H4 and H5 homogenization, with H5 giving the most extensive coarsening and reduction in particle gradient, which plays a very important role in recrystallized grain structure as shown below.

3.4. Homogenization effect on recrystallization

Fig. 9 shows the recrystallized grain structures for both non-homogenized and homogenized TRC AA3105 after 90% cold roll and annealing. In Fig. 9(a), for non-homogenized material, most grains are very coarse and elongated in the rolling direction. Although this material contains many large constituent particles, there are apparently few effective nucleation sites. As shown in Fig. 5(a), constituent tends to form a continuous network along grain boundaries during casting. The subsequent cold rolling process does not completely break up the as-cast second phase network into widely spaced discrete particles as in the case of homogenized material, forming instead colonies of particle clusters, greatly reducing the potential to be nucleation sites. Moreover, concurrent precipitation of dispersoid from the supersaturated matrix further hinders nuclei forming near large particles, which makes it even more difficult for a large constituent particle to act as a PSN site in the non-homogenized material.

Cold rolling tends to align grain boundaries longitudinally, compressed closer together in the normal direction forming a denser barrier to growth of recrystallizing grains than in the rolling direction. As a result, the boundaries of newly recrystallized grains and/or nuclei encounter less inhibition when growing in the rolling direction than in the normal direction, resulting in elongated recrystallized grains. In addition to the resulting very coarse and elongated grain structure, the recrystallization kinetics for non-homogenized material is much slower compared to homogenized material.

Fig. 9(b–d) are optical micrographs of the recrystallized grain structures resulting from the different homogenization treatments prior to cold rolling and annealing. Compared with non-homogenized material, recrystallized grain structures are much finer and more equiaxed after homogenization. Higher homogenization temperature results in a finer recrystallized grain structure, comparing Fig. 9(b and c). Note that these homogenized materials contain a grain size gradient, with a larger grain size at the strip surface and finer grains in the center. The structure in Fig. 9(d) has a mean linear grain intercept of approximately 70 μm at the surface and 20 μm at the center along the rolling direction.

The grain size gradient appears to be closely related to the second phase particle gradients in this material, as shown in Figs. 7 and 8. It is well established that finely dispersed small particles inhibit recrystallization by pinning moving boundaries while large particles promote recrystallization by acting as nucleation sites. According to Humphreys et al. [20], PSN is usually found to occur only at particles of diameter greater than approximately 1 μm. In Fig. 6(b), the density of the small particles is extremely high at the strip surface, rapidly decreasing to a stable level at a depth of 50 μm. Meanwhile, the density of potential PSN particles is very low at the surface, approximately 4×10^3 sections/mm^2, increasing rapidly to about 1.3×10^4 sections/mm^2 at a depth of 50 μm from the

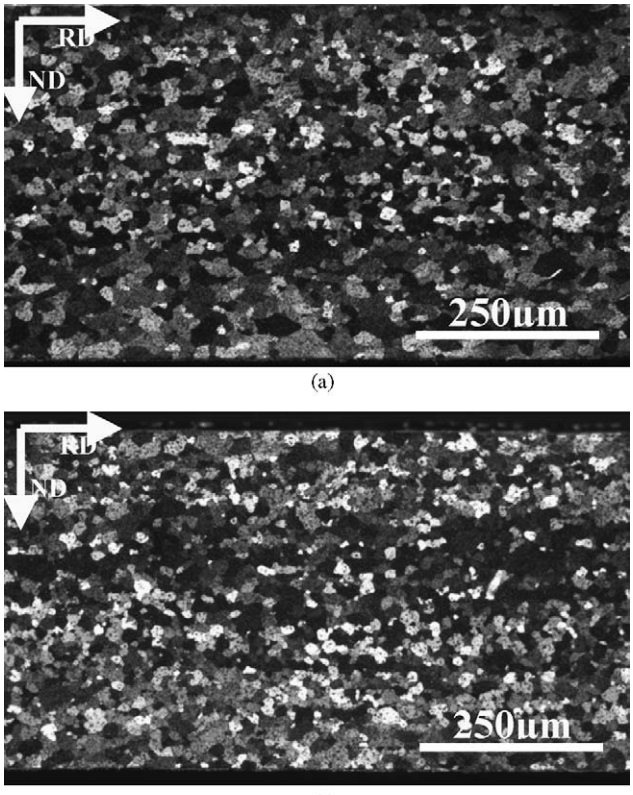

Fig. 10. Optical micrographs of cold rolled and recrystallized material after (a) H4 and (b) H5 homogenization.

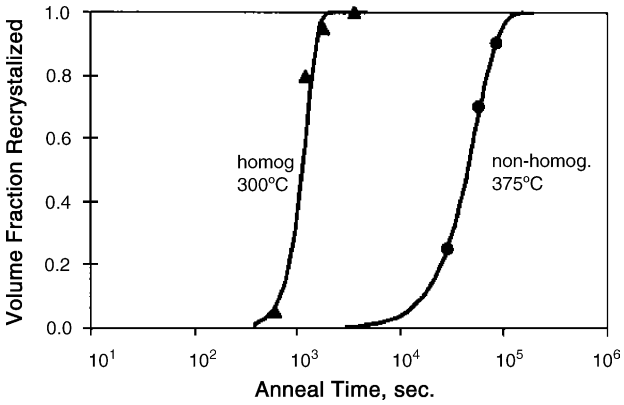

Fig. 11. Recrystallization kinetics for H3 homogenized and non-homogenized (NH) materials. Notice that homogenized material exhibits faster recrystallization kinetics than non-homogenized material.

surface, which is approximately the thickness of large grain size layer in recrystallized material, as shown in Fig. 9(c and d).

In order to eliminate the grain size gradient in recrystallized material, more aggressive homogenization treatments, H4 and H5, were investigated. The recrystallized grain structures of these are shown in Fig. 10. The grain size gradient is greatly reduced in the H4 material, as shown in Fig. 10(a). This improvement can be understood by examining the data shown in Figs. 7 and 8, showing reduced particle density gradients for both small and PSN particles. No grain size gradient exists in H5 material, which also shows a very fine grain size of approximately 15 μm across the strip thickness, as shown in Fig. 10(b). As seen in Fig. 7, H5 greatly reduces the density of overall particles and essentially eliminating the gradients. These factors all contribute the fine and uniform recrystallized grain structure in this material.

Fig. 11 shows the effect of H3 homogenization on recrystallization kinetics in TRC AA3105. It is clear that homogenized material has much faster recrystallization kinetics than that of non-homogenized material, where the non-homogenized material was annealed at even a higher temperature. The sluggish recrystallization kinetics of non-homogenized material is due to the concurrent precipitation of large quantities of dispersoids on subgrain boundaries, greatly hindering their motion and preventing formation of viable recrystallization nuclei at potential PSN sites, as shown in Fig. 12(a). However, homogenization removes surplus manganese solute, resulting in larger constituent particles and no further precipitation, as shown in Fig. 12(b).

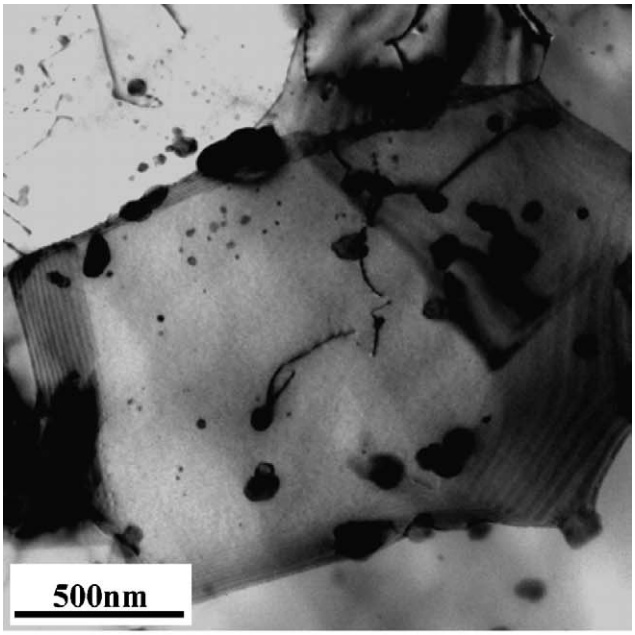

Fig. 12. Bright-field TEM images of early recrystallization: (a) non-homogenized material, note particle pinning at subgrain boundaries, and (b) H3 homogenized material, note absence of small particles in matrix, B, only large constituent particles present, such as A.

4. Conclusions

The following conclusions can be made from this study:

1. TRC AA3105 has a marked gradient in constituent particle size, with very fine, closely spaced particles within approximately 50 μm of the 90% cold rolled strip surface and larger particles with greater spacing toward the strip center.
2. As roll cast, AA3105 has a high manganese supersaturation, capable of precipitating many fine dispersoids during annealing.
3. Non-homogenized material shows a very coarse recrystallized grain structure, suggesting that nucleation is hindered by fine constituent and dispersoid pinning.
4. Homogenization reduces the supersaturation, coarsens constituent particles and reduces the total number of particles in TRC AA3105.
5. Homogenization prior to cold rolling and annealing results in marked reduction in recrystallized grain size and faster recrystallization kinetics in TRC AA3105.
6. Extensive isothermal homogenization treatments result in a recrystallized grain size gradient zone at the strip surface with a thickness of approximately 50 μm.
7. More extensive cyclic homogenization treatments greatly coarsen constituent particles, producing a uniform fine grain structure.

Acknowledgements

The authors gratefully acknowledge funding of this research by the Department of Energy, award number: DE-FC36-021D14401. The electron microscopy studies were sponsored by the Assistant Secretary for Energy Efficiency and Renewable Energy, Office of Transportation Technologies, as part of the High Temperature Materials Laboratory User Program, Oak Ridge National Laboratory, managed by UT-Battelle, LLC,

for the U.S. Department of Energy under contract number DE-AC05-00OR22725.

The authors also thank Dr. R. D. Doherty for his very helpful discussions and suggestions.

References

[1] H. Bessemer, British Patent 11317.
[2] M. Yun, S. Lokyer, J.D. Hunt, Mater. Sci. Eng. A280 (2000) 116–123.
[3] R. Cook, P.G. Grocok, P.M. Thomas, D.V. Edmonds, J.D. Hunt, J. Mater. Process. Technol. 55 (1995) 76–84.
[4] S.A. Lockyer, Ming Yun, J.D. Hunt, D.V. Edmonds, Mater. Character. 37 (1996) 301–310.
[5] A.V. Kuznetsov, Int. J. Heat Mass Transfer 40 (1997) 2949–2961.
[6] M. Slamova, P. Dvorak, Z. Juricek, Microstruct. Sci. 27 (2000) 20–28.
[7] Toshio Haga, Shinsuke Suzuki, J. Mater. Process. Technol. 118 (2001) 165–168.
[8] T. Haga, J. Mater. Process. Technol. 111 (2001) 64–68.
[9] M. Slamova, Z. Juricek, V. Ocenasek, Mater. Sci. Forum 331 (2000) 161–186.
[10] E. Nes, Acta Metall. 24 (1976) 391–398.
[11] P. Furrer, H. Warlimont, Aluminum 54 (1978) 135–142.
[12] N. Hansen, B. Bay, J. Mater. Sci. 7 (1972) 1351–1362.
[13] P. Furrer, G. Hausch, Met. Sci. 13 (1979) 155–162.
[14] U. Koster, Met. Sci. 8 (1974) 151–160.
[15] R.D. Doherty, J.W. Martin, J. Inst. Met. 91 (1962) 332–338.
[16] Y.J. Li, L. Arnberg, Acta Mater. 51 (2003) 3415–3428.
[17] B.R. Patterson, N. Sun, J.P. Suni, E.A. Simielli, H. Weiland, L.F. Allard, TMS Lett. 8 (2004) 173–174.
[18] B. Patterson, N. Sun, J. Suni, E. Simielli, H. Weiland, Proceedings of Materials Solutions Conference 2003: First International Symposium on Metallurgical Modeling for Aluminum Alloys, 2003, pp. 209–212.
[19] R.D. Doherty, Private communication, November, 2004.
[20] F.J. Humphreys, M. Hatherly, Recrystallization and Related Annealing Phenomena, first ed., Pergamon, Oxford, 1995.

Available online at www.sciencedirect.com
SCIENCE DIRECT
Acta Materialia 54 (2006) 4091–4099
Acta MATERIALIA
www.actamat-journals.com

Characterization of particle pinning potential

Naiyu Sun [a,*], Burton R. Patterson [a], Jaakko P. Suni [b], Hasso Weiland [b], Lawrence F. Allard [c]

[a] Department of Materials Science and Engineering, University of Alabama at Birmingham, 1530 3rd Avenue South, Birmingham, AL 35294, USA
[b] Alcoa Technical Center, 100 Technical Drive, Alcoa Center, PA 15069, USA
[c] Oak Ridge National Laboratory, 1 Bethel Valley Road, Oak Ridge, TN 37831, USA

Received 24 February 2006; received in revised form 1 May 2006; accepted 3 May 2006
Available online 17 July 2006

Abstract

Five methods for characterizing second-phase particle pinning potential in twin roll cast AA 3105 have been evaluated experimentally and analytically. A stereological expression, $S_V/4$, has been demonstrated as a robust means for characterizing the degree of particle pinning in real material systems with neither the assumption of particle shape nor size distribution and without the experimental difficulty of unfolding the size distribution.

Keywords: Zener pinning; Particle size distribution; Aluminum alloy; Stereology

1. Introduction

The grain growth behavior of particle-containing materials is dependent on the volume fraction, size, shape and spatial distribution of second-phase particles. Many models, beginning with that of Zener [1], have been developed to describe these effects on grain growth inhibition [2–20]. Although these models differ in various aspects, essentially all contain the ratio of the particle volume fraction, f, to some measure of particle size, typically radius, r. This well-known ratio f/r, often referred to as Z, the Zener pinning factor, results from a variety of descriptions of restraining pressure or energy dissipated during grain boundary motion and includes the computation of the number of particles interacting with the boundary.

The fact that most models of grain growth inhibition are based on the assumption of monosized spherical particles of radius r presents a problem with model testing due to the unrealistic nature of the assumption. Not only are particles often non-spherical but the presence of a size distribution leads to the ambiguity of which size parameter to employ. Different characterization methods measure different averages of the mean size, such as by number or volume weighting. The relative ease of some measurements may favor those that are not necessarily the most appropriate. Difficult and time-consuming methods that appear theoretically sound may be employed when easier measurements give equivalent results.

Based on an energy model of describing particle pinning in grain growth, Rios [18] first introduced a stereological parameter, S_V, the surface area of particles per unit volume, to characterize the energy dissipated when a grain boundary moves across particles. Liu and Patterson later employed this parameter in their study [12] of grain growth inhibition by porosity. More recently, Rios and Fonseca developed this idea further by relating S_V to grain boundary curvature and validated their models in a high-purity Al–1 wt.% Mn alloy [19,20]. From the fundamental stereological relationships [21]

$$\bar{\lambda} = \frac{4f}{S_V} \tag{1}$$

* Corresponding author. Tel.: +1 205 240 8271.
E-mail address: nysun@uab.edu (N. Sun).

1359-6454/$30.00
doi:10.1016/j.actamat.2006.05.008

it is clear that S_V has similar properties as f/r in that it includes the ratio of volume fraction to a length scale, $\bar{\lambda}$, which is the mean linear intercept of second phase. To compare the different approaches for determining Z, it is necessary to use a single basic definition, Eq. (2), consisting of the simplest core common to all such models – the ratio of particle volume fraction to a length scale, the shape-independent $\bar{\lambda}$:

$$Z = \frac{f}{\bar{\lambda}} \tag{2}$$

Use of the common format of Eq. (2) enables a fundamental comparison of the different measures without confounding effects from other constants or components of the different models. Understanding the differences in this component of the pinning force gives a better understanding of the biases present in the different methods.

This study will compare values of Z computed from S_V with four other more common approaches employing f and r, experimentally and analytically. It will be shown that the different experimental methods for obtaining Z result in different averages of the particle size that are not necessarily apparent from the measurement. The various measures and their expressions for Z will then be analyzed with respect to these differences.

2. Experimental

Twin roll cast (TRC) aluminum alloy AA3105 was employed for the measurements of the Zener pinning factor in this study. The composition of this material, provided by Alcoa, is given in Table 1. This alloy contains aluminum–manganese constituent particles that are typically much finer near the rapidly solidified surface than in the interior, and that coarsen during homogenization or high-temperature annealing. These particles impart considerable influence on recrystallization and grain growth and this material has been the subject of extensive studies of the effects of homogenization, annealing temperature and heating rate on recrystallization, and the transition between the pinned state and normal and abnormal grain growth [22–25].

The experimental material was roll cast as 5 mm thick sheet and given different thermomechanical treatments for recrystallization and grain growth. Homogenization treatments, given to some specimens prior to rolling, involved ten cycles between 450 and 620 °C with 5 h holds at each temperature and 0.3 °C/min cooling from the higher to lower temperature [26]. Both as-cast and homogenized materials were cold rolled to 90% reduction and annealed for 19 different temperature/time combinations, ranging from 500 to 640 °C and 5 min to 3 weeks. The variety of thermal treatments provided a wide range of particle structures for evaluating the different measures of the Zener pinning factor. Specimens for microstructural examination were prepared on the longitudinal cross section, parallel to the normal direction (ND) and rolling direction (RD).

Table 1
Chemical composition of the experimental TRC AA3105 (wt.%)

Mn	Mg	Fe	Si	Cu	Al
0.40	0.51	0.52	0.14	0.15	Balance

Figs. 1 and 2 show typical variations in particle size and morphology among different locations and materials. Fig. 1(a) and (b) show the typically finer particle structure at the strip surface than in the center that often leads to gradients in recrystallized grain size and strong pinning during grain growth. Fig. 2(a) shows still coarser constituent typically present after annealing at higher temperature. Fig. 2(b) shows the coarsest constituent particles that result from the extensive homogenization treatment. The volume fraction of constituent particles resulting from the variety of heat treatments varied from approximately 1.0% to 2.0% among the specimens, as shown in Table 2.

Considerable particle characterization, including volume fraction, length of particle boundary, and distribution of three-dimensional (3D) particle size, computed from two-dimensional (2D) particle section area, Fig. 3, was performed by automated image analysis of field-emission scanning electron microscopy (SEM) images taken at ×2000 magnification. A very low accelerating voltage, 5 kV, was employed to minimize the electron–specimen interaction volume effect. Measurements were performed at six randomly selected locations along the strip length, in both the surface and interior regions of the strip cross section. Measurements typically included a total of 250–1500 particle sections from the six fields. The relative errors associated with the measurements in this study were evaluated by the coefficient of variation of the measurements, which ranged from 0.03 to 0.09, typically 0.06.

Five different approaches, described below, were used to determine experimentally the particle pinning potential in the specimens described above. Analytical descriptions for the five methods, illustrating the effect of the particle size distribution width on the measured Z values, are also presented for comparison. It should be noted that the methods described in this paper are general and apply to any material with second-phase particles.

3. Computation of particle pinning potential, Z

3.1. Monosized sphere assumption

The simplest, although unrealistic, assumption of particle structure is that of monosized spheres. For this case, Fullman [27] developed stereological relationships between the 3D particle radius, r, and the mean linear intercept, $\bar{\lambda}$, and mean particle section area, $\overline{A}$:

$$\bar{\lambda} = \frac{4}{3}r \tag{3}$$

$$\overline{A} = \frac{2}{3}\pi r^2 \tag{4}$$

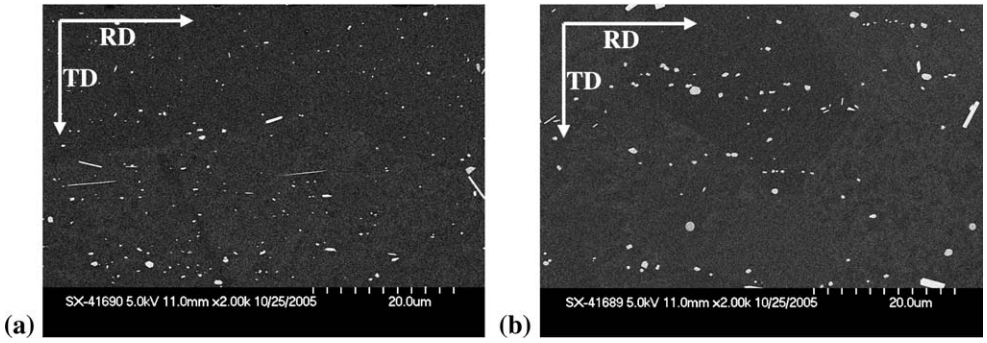

Fig. 1. Backscattered electron (BSE) images showing second-phase particles of a TRC AA3105 strip annealed at 630 °C for 12 h. (a) Strip surface, (b) strip interior. Note that particles are finer near the strip surface, with some acicular shapes present.

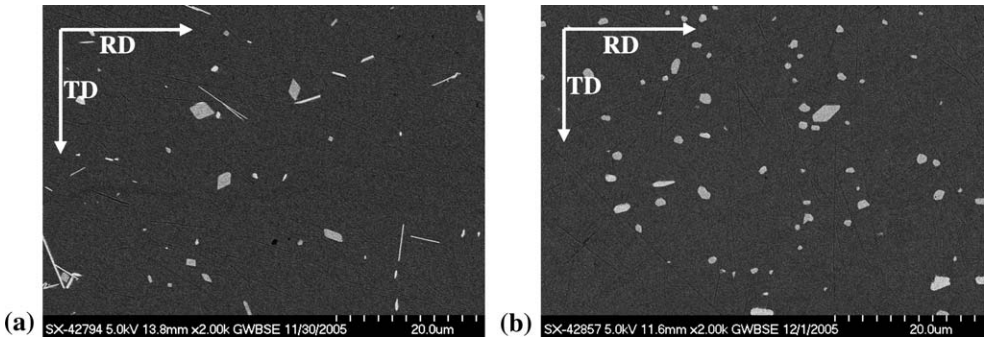

Fig. 2. BSE images showing particles in the interior region of the annealed strip. (a) Non-homogenized material annealed at 650 °C for 2 h, (b) homogenized material annealed at 550 °C for 24 h.

Table 2
Particle volume fraction and pinning potential, Z ($\times 10^{-2}$ μm^{-1})

Treatment (°C/h)	f (vol.%)	Z_m Sur./Cen.	Z_n Sur./Cen.	Z_v Sur./Cen.	Z_s Sur./Cen.	Z_{st} Sur./Cen.
620/504	1.4	2.6/2.2	4.7/4.3	1.6/1.5	2.4/2.0	1.9/1.8
630/1.5	1.4	5.3/3.1	6.7/4.9	2.3/1.9	4.1/2.7	3.9/2.7
630/12	1.3	3.7/2.6	5.1/3.5	1.8/1.6	2.9/2.3	3.2/2.4
630/132	1.3	2.6/1.7	4.8/2.9	1.4/1.2	2.2/1.7	2.0/1.5
630/168	1.3	2.5/2.1	3.7/3.3	1.5/1.4	2.3/1.9	2.2/1.8
640/8	1.2	2.8/2.2	3.9/3.1	1.6/1.4	2.4/2.0	2.6/2.1
640/16	1.1	2.6/1.9	4.1/2.7	1.4/1.2	2.1/1.7	2.3/1.9
650/0.5	1.3	5.0/3.1	6.4/4.7	2.2/1.7	3.8/2.5	3.9/2.9
650/2	1.2	2.1/1.1	4.4/2.3	1.5/0.9	2.0/1.1	2.1/1.2
500/2 (H)	1.4	2.6/1.6	4.5/3.0	1.8/1.3	2.3/1.6	2.3/1.5
550/0.5 (H)	1.5	2.4/1.7	4.7/3.6	1.8/1.4	2.3/1.6	2.0/1.5
550/24 (H)	2.0	2.8/2.2	4.8/4.8	2.1/1.8	2.5/2.1	2.5/1.9
600/0.1 (H)	1.5	2.5/1.6	3.7/2.4	1.9/1.3	2.4/1.6	2.4/1.5
600/0.2 (H)	1.5	2.3/1.8	3.5/3.8	1.8/1.5	2.3/1.8	2.1/1.6
600/1 (H)	1.4	2.1/1.4	3.0/3.0	1.7/1.2	2.1/1.4	2.0/1.2
620/0.2 (H)	1.4	2.0/1.6	2.8/2.4	1.5/1.4	1.9/1.7	1.9/1.5
620/2 (H)	1.6	2.3/1.7	2.9/2.2	1.8/1.5	2.2/1.8	2.3/1.6
640/0.2 (H)	1.4	2.2/1.4	3.4/2.7	1.7/1.2	2.1/1.4	2.1/1.4
640/2 (H)	1.2	1.8/1.2	2.7/1.9	1.4/1.0	1.8/1.1	1.8/1.2

(H) = Homogenized.

Combining Eqs. (2)–(4) yields the particle pinning potential for the monosized sphere assumption, Z_m, in terms of $\overline{A}$, the number weighted mean section area:

$$Z_m = \frac{3f}{\sqrt{\left(\frac{24}{\pi}\right)\overline{A}}} \tag{5}$$

This approach computes the pinning potential equivalent to Eq. (2), with the assumption that the relationship between the mean section area and the mean intercept is that for monosized spheres, which is often not the case in real materials. Table 2 tabulates values of Z_m measured for the matrix of specimens. Fig. 4 compares these values with those computed by the other four methods.

To understand the relationship between this measure of Z and others it is necessary to re-express Z_m in terms of particle, rather than section, size. Also, since there is generally a distribution of particle sizes in real materials, it is useful to examine the effect of the width of the particle size distribution on the experimentally measured Zener pinning factor. In the following analysis, Z_m is then re-formulated using the coefficient of variation (CV) of the distribution of particle radii.

From Eq. (4), the average section area from particles of the ith 3D particle size class given by

$$\overline{A}_i = \frac{2}{3}\pi r_i^2 \tag{6}$$

The average section area contributed from all particle classes is

$$\overline{A} = \sum_i \left[(\overline{A}_i) \cdot \left(\frac{(N_A)_i}{N_A} \right) \right] \tag{7}$$

where $(N_A)_i$ is the number of sections from the ith particle class per unit area of examination plane, and is related to the number of particles per unit volume, $(N_V)_i$, and their size, r_i. In turn, $(N_V)_i$ can be expressed as the ratio of the volume fraction of particles in the ith class to their individual volumes, V_i:

$$(N_A)_i = 2r_i(N_V)_i = 2r_i\left(\frac{f_i}{V_i}\right) = \frac{2r_i f_i}{4\pi r_i^3/3} = \frac{3f_i}{2\pi r_i^2} \tag{8}$$

Combining Eqs. (6)–(8) yields the expression for the mean section area in terms of particle radii:

$$\overline{A} = \frac{2\pi}{3}\left[\frac{f}{\sum_i (f_i/r_i^2)}\right] = \frac{2\pi}{3}\left[\frac{1}{\overline{(r^{-2})}_v}\right] \tag{9}$$

where $\overline{(r^{-2})}_v$ is the volume weighted average of the inverse square of 3D particle size, defined as

$$\overline{(r^{-2})}_v = \frac{\sum_i (f_i/r_i^2)}{f} \tag{10}$$

Inserting Eq. (9) for $\overline{A}$ into Eq. (5) yields

$$Z_m = \left(\frac{3f}{4}\right)\overline{(r^{-2})}_v^{1/2} \tag{11}$$

Expressing S_V and f in terms of moments of the distribution:

$$S_V = N_V \cdot (4\pi\mu_2^n) \tag{12}$$

$$f = N_V \cdot \left(\frac{4}{3}\pi\mu_3^n\right) \tag{13}$$

yields

$$f = \left(\frac{S_V}{3}\right)\left(\frac{\mu_3^n}{\mu_2^n}\right) \tag{14}$$

where μ_2^n and μ_3^n are the second and third number weighted moments of the particle radius, about the origin. Inserting Eq. (14) into Eq. (11) and re-writing $\overline{(r^{-2})}_v$ as the moment μ_{-2}^v yields

$$Z_m = \left(\frac{S_V}{4}\right)\left(\frac{\mu_3^n}{\mu_2^n}\right)\left(\mu_{-2}^v\right)^{1/2} \tag{15}$$

where, μ_{-2}^v is the volume weighted second moment of the inverse particle size, about the origin.

The following Eqs. (16)–(19) give the basic relationships for the moments of the lognormal distribution [28,29]:

$$\mu_k^n = \exp[k \cdot \overline{(\ln D)}_n + \frac{k^2}{2}(\ln^2\sigma_D)] \tag{16}$$

$$\mu_k^v = \exp\left[k \cdot \overline{(\ln D)}_v + \frac{k^2}{2}(\ln^2\sigma_D)\right] \tag{17}$$

$$\mathrm{CV}^2 + 1 = \exp(\ln^2\sigma_D) \tag{18}$$

$$\overline{(\ln D)}_v = \overline{(\ln D)}_n + 3\ln^2\sigma_D \tag{19}$$

where, μ_k^n and μ_k^v are the kth number weighted and volume weighted moments of the particle size about the origin, $\overline{(\ln D)}_n$ and $\overline{(\ln D)}_v$ are the number and volume weighted geometric means of the particle diameters, and $\ln\sigma_D$ is the geometric standard deviation of the particle diameters. Employing Eqs. (16)–(19) with Eq. (15) yields

$$Z_m = \left(\frac{S_V}{4}\right)(\mathrm{CV}^2 + 1)^{1/2} \tag{20}$$

In Eq. (20), Z_m consists of two components, a stereological core, $S_V/4$, which will be shown to be the unbiased Zener pinning potential, and a particle size distribution term, $(\mathrm{CV}^2+1)^{1/2}$, that biases the experimental measurement to higher apparent values. As will be shown below, the analytical formulae of all the five methods for computing Z contain the same fundamentally correct core, but some measures also contain these variations of the size distribution term that bias them above or below the actual pinning potential. Here, for the case of monosized particles, $\mathrm{CV} = 0$ and the size distribution term is unity, leaving Z_m equal to the basic term, $S_V/4$. Wider distributions with $\mathrm{CV} > 0$ have size distribution terms greater than unity, with larger computed values of Z_m. A compilation of all of the analytical Z expressions is shown in Table 3.

3.2. Unfolding 3D size distribution

Several approaches for computing the pinning factor involve determining the 3D particle size distribution from measurements on the 2D plane. Unfolding methods, requiring measurement of particle section size distribution and assumption of constant geometric shape, can be experimentally difficult and prone to error, especially with micrometer- or submicrometer-sized particles. The obtained size distribution information can be incorporated into Z by either (a) directly inserting number or volume weighted average values of r, or (b) summing values of Z_i, obtained from r_i and the computed f_i for each size class, over all classes. The appropriateness of the former method depends on the weighting of the average particle

Table 3
Expressions for particle pinning potential, Z, for different methods

Z	Experimental	Analytical
Z_m	$\frac{3f}{\sqrt{(24/\pi)\bar{A}}}$ (5)	$\left(\frac{S_V}{4}\right)(CV^2+1)^{1/2}$ (20)
Z_n	$\frac{3f}{4\bar{r}_n}$ (23)	$\left(\frac{S_V}{4}\right)(CV^2+1)^{2}$ (25)
Z_v	$\frac{3f}{4\bar{r}_v}$ (27)	$\left(\frac{S_V}{4}\right)(CV^2+1)^{-1}$ (29)
Z_s	$\frac{3}{4}\sum_i\left(\frac{f_i}{r_i}\right)$ (31)	$\frac{S_V}{4}$ (34)
Z_{st}	$\frac{L_A}{\pi}$ (36)	$\frac{S_V}{4}$ (36)

size. The latter method is a logical extension of the basic Zener derivation. With the assumption of constant geometric shape, in this case spherical particles, the summation method is analytically equivalent to the stereological approach, $S_V/4$, which relies upon no assumptions in computing the Zener pinning potential, as will be shown below.

Other methods for estimating r include the number or volume weighted mean particle volume, which can be obtained without unfolding and independent of shape [30,31]. Assuming spherical particles enables computation of radii of these mean volumes. Obtaining the number weighted mean volume requires serial sectioning [32], potentially difficult for fine particles. Obtaining volume weighted mean volume requires selected 2D chord measurements and is more feasible, but, again, would be difficult with the usual case of fine particles. These experimental methods are not included in this study.

3.2.1. Unfolding method

For the Schwartz–Saltykov method used here, the distribution of section areas obtained by image analysis was converted to equivalent section diameters, classified into ten size groups and unfolded to the distribution of 3D diameters using Eq. (21):

$$N_V(j)=\frac{\alpha(i)N_A(i)-\alpha(i+1)N_A(i+1)-\alpha(i+2)N_A(i+2)-\cdots-\alpha(k)N_A(k)}{\Delta} \tag{21}$$

where $N_V(j)$ and $N_A(i)$ are the number of 3D particles per unit volume and number of 2D sections per unit area, respectively, in size classes j and i, which vary from 1 to k, the total number of classes, Δ is defined as the ratio of the maximum diameter $D_{\max}$ to the number of size classes. The values of the coefficients $\alpha(i)$, $\alpha(i+1),\ldots,\alpha(k)$ have been tabulated by Saltykov [21].

Fig. 3 illustrates 3D particle size distributions computed by this technique, demonstrating the wide range in particle size in both the surface and center regions of rolled AA3105 strip annealed at 630 °C for 12 h.

3.2.2. Number weighted average radius

The simplest use of the unfolded 3D particle size distribution involves computation of the average particle radius, specifically the number weighted mean radius, $\bar{r}_n$:

$$\bar{r}_n=\sum_{i=1}\left[r_i\cdot\left(\frac{(N_V)_i}{N_V}\right)\right] \tag{22}$$

where the number per volume ratio is the number frequency of 3D particles in the ith size class. The equivalent particle pinning potential is then obtained from Eqs. (2) and (3), as Z_n, indicating that this Z is weighted by number fraction of particles:

$$Z_n=\frac{3f}{4\bar{r}_n}=\left(\frac{3f}{4}\right)(\bar{r}_n)^{-1} \tag{23}$$

Use of the number weighted mean radius in Z_n biases the averaged r towards relatively smaller values, resulting in a relatively larger computed pinning factor than with Z_m. The experimental values for Z_n are, in fact, markedly higher than those from any of the other methods, as predicted. The values of Z_n determined from the experimental materials with a wide range of particle sizes are listed in Table 2 and included in the comparison plots of Fig. 4.

The effect of the particle size distribution on Z_n can be determined by inserting Eq. (14) into Eq. (23) and substituting the first number weighted moment of particle radius about the origin, μ_1^n, for $\bar{r}_n$:

$$Z_n=\left(\frac{S_V}{4}\right)\left(\frac{\mu_3^n}{\mu_2^n}\right)(\mu_1^n)^{-1} \tag{24}$$

Again, restating these distribution terms using relationships for the moments of the lognormal distribution, Eqs. (16) and (18), one obtains

$$Z_n=\left(\frac{S_V}{4}\right)(\mathrm{CV}^2+1)^2 \tag{25}$$

Comparing this expression to Eq. (20) it is apparent that both are of the same form except for the size distribution term. Here, the distribution term is again unity for monosized particles and increases with increasing distribution width, biasing Z_n to higher values than the fundamental term, $S_V/4$.

3.2.3. Volume weighted average radius

As an alternative to the above number weighted particle size, the volume weighted mean particle radius, $\bar{r}_v$, can also be determined from the unfolded 3D size distribution:

$$\bar{r}_v = \sum_{i=1} \left[r_i \cdot \left(\frac{f_i}{f} \right) \right] \tag{26}$$

where the volume fraction ratio is the volume frequency of 3D particles in the ith size class. The pinning potential is then obtained from Eqs. (2) and (3), as Z_v, indicating the weighting by particle volume:

$$Z_v = \frac{3f}{4\bar{r}_v} = \left(\frac{3f}{4} \right) (\bar{r}_v)^{-1} \tag{27}$$

The volume weighting biases the averaged r towards larger sizes, resulting in a relatively smaller computed pinning factor than with Z_m or Z_n. The values of Z_v determined from the specimens are given in Table 2 and plotted in Fig. 4. The experimental values for Z_v are, in fact, markedly smaller than those from any of the other methods, as predicted.

Inserting Eq. (14) into Eq. (27) and substituting μ_1^v for $\bar{r}_v$ yields

$$Z_v = \left(\frac{S_V}{4} \right) \left(\frac{\mu_3^n}{\mu_2^n} \right) (\mu_1^v)^{-1} \tag{28}$$

Employing Eqs. (16)–(19) with Eq. (28) yields

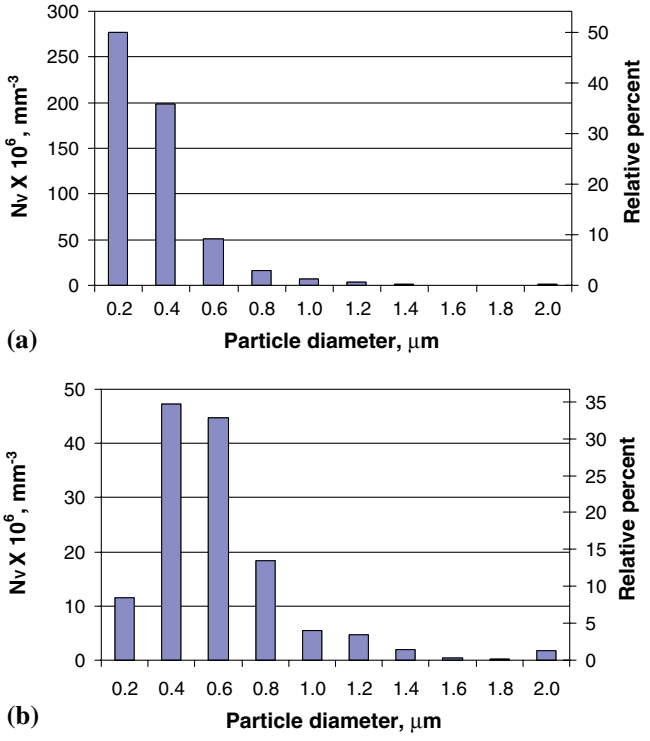

Fig. 3. Distribution of 3 D particle diameter computed by the Schwartz–Saltykov method in TRC AA3105 after 12 h at 630 °C, at (a) surface and (b) interior region of the strip. Typical micrographs of these areas are shown in Fig. 1(a) and (b).

$$Z_v = \left(\frac{S_V}{4} \right) (\mathrm{CV}^2 + 1)^{-1} \tag{29}$$

This expression is again similar in structure to Eqs. (20) and (25) except for the size distribution term, $(\mathrm{CV}^2 + 1)^{-1}$. Note that this term decreases below unity for wider distributions, decreasing Z_v below the fundamental pinning term. It is apparent that using different averages of r (Z_n and Z_v) or assuming monosized spherical particles (Z_m) introduces variable biases into the experimentally measured values of Z. If the particles were actually monosized spheres all of the above measures would yield the same correct value of the pinning factor, $S_V/4$. The analytical descriptions of the experimental equations show that the distribution of particle size, that is inevitably present in real materials, increases the magnitude of bias in the measured Z values.

3.2.4. Summation method

A more fundamentally sound method of computing Z from the unfolded 3D size distribution determines the pinning potential for each size class, Z_i, and computes the overall potential as the sum of the effects from each size class.

Combining Eqs. (2) and (3) gives the pinning potential of particles in size group i as

$$Z_i = \frac{3f_i}{4r_i} \tag{30}$$

The pining potential of the overall particle distribution is the sum of Z_i over all size groups, here termed Z_s:

$$Z_s = \frac{3}{4} \sum_i \left(\frac{f_i}{r_i} \right) = \left(\frac{3f}{4} \right) \overline{(r^{-1})}_v \tag{31}$$

where $\overline{(r^{-1})}_v$ is the volume weighted average of the inverse of particle size:

$$\overline{(r^{-1})}_v = \frac{\sum_i \left[f_i \cdot (r_i^{-1}) \right]}{f} \tag{32}$$

The values of Z_s for all experimental materials, computed from the summation of Z_i, are tabulated in Table 2 and used as the abscissa against which the other Z computations are plotted in Fig. 4.

Inserting Eq. (14) into Eq. (31) and substituting μ_{-1}^v for $\overline{(r^{-1})}_v$ yields

$$Z_s = \left(\frac{S_V}{4} \right) \left(\frac{\mu_3^n}{\mu_2^n} \right) (\mu_{-1}^v) \tag{33}$$

Again, using the moments of the lognormal distribution and converting the volume weighted moment to number weighted moment, Eq. (33) reduces to

$$Z_s = \frac{S_V}{4} \tag{34}$$

Compared to Eqs. (20), (25) and (29), (34) consists of only the stereological core, $S_V/4$. The size distribution term is lost because Eq. (31) already sums the pinning effect from

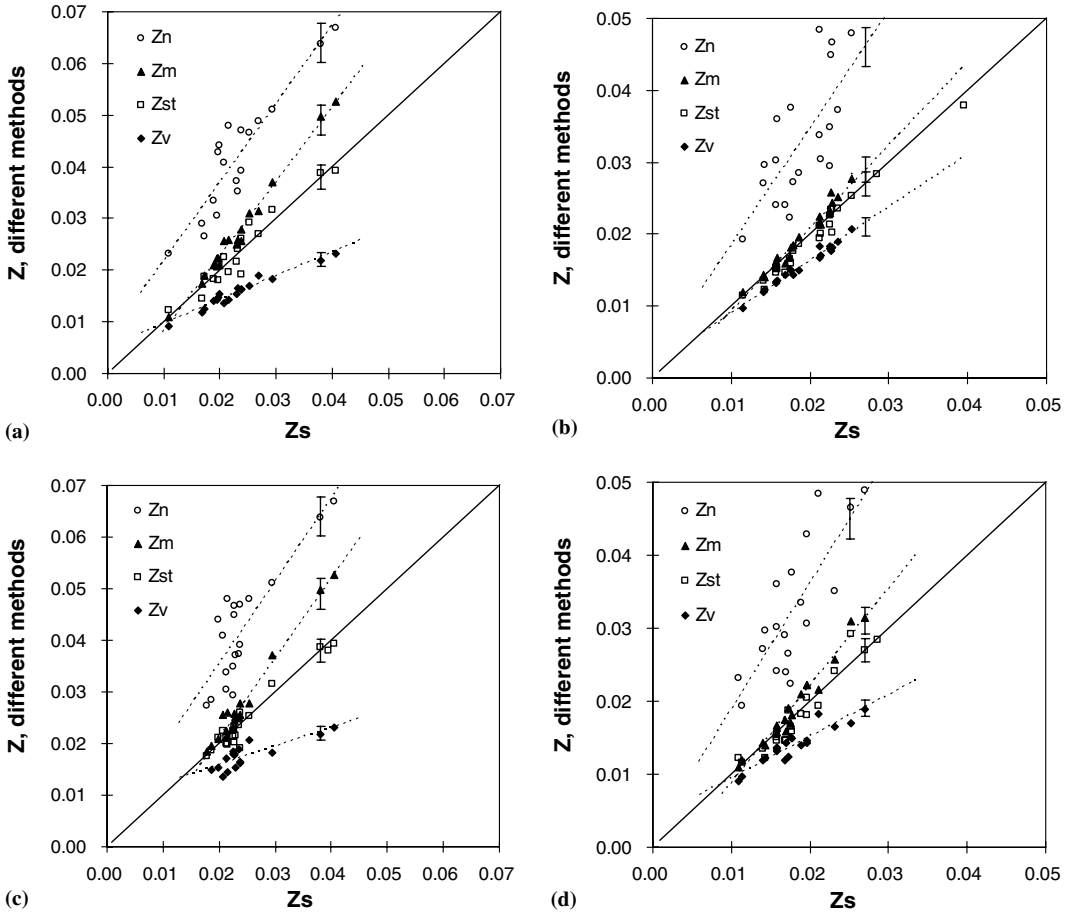

Fig. 4. Experimental results of particle pinning potential, Z, measured by different methods: (a) non-homogenized, (b) homogenized, (c) strip surface, and (d) strip interior. Error bars for each data set indicate ±1 SE.

all particle classes, and is, thus, independent of the size distribution. It will be shown that for constant geometric shape this result is analytically equivalent to that obtained from the stereological measurement of S_V.

3.3. Stereological method, S_V

This method involves measuring only the surface area of particles per unit volume, S_V, which is easily obtained from direct measurement of the length of boundary between the particles and matrix per unit area, L_A, by automated means, or can be obtained easily from manual line intercept measurement, P_L. The basic stereological equations [21] give the following relationships:

$$S_V = 2P_L = \frac{4}{\pi} L_A \tag{35}$$

Recalling Eqs. (1) and (2) and combining them with Eq. (35) yields

$$Z_{st} = \frac{S_V}{4} = \frac{L_A}{\pi} \tag{36}$$

where the stereological pinning factor, Z_{st}, contains only the particle surface area per unit volume, S_V. Eq. (36), identical to Eq. (34), inherently contains the particle size, shape and volume fraction information, regardless of size distribution, and is valid for particles with complex morphology in real material systems.

The measurements required for Eq. (36) are much simpler and more accurately obtainable than the unfolding measurements for Z_s. The particle pinning potential calculated from Eq. (36) employs direct image analysis measurements of L_A, with no post-measurement processing. Measured values of Z_{st} for the different specimens, shown in Table 2, are in very good agreement with those from Z_s. In Fig. 4 these values are plotted versus Z_s with a slope of unity, illustrating their equivalence.

4. Discussion

Fig. 4 shows the experimentally determined relationships among the five methods for computing Z. The data, listed in Table 2, were obtained from specimens with a wide range of particle structures covering a four-fold range of Z. It should be noted that Z_m, Z_n, Z_v and Z_s were computed from the basic experimental expressions for each method, Eqs. 5, 23, 27 and 31, compiled in Table 3, rather than the respective analytical descriptors containing the size

distribution term. For Z_{st}, the experimental and analytical expressions are identical since there is no shape or size distribution assumption involved in the basic definition. The non-homogenized specimens in Fig. 4(a) and surface regions of the strip, Fig. 4(c), had relatively finer particles and high Z values while the homogenized specimens, Fig. 4(b), and strip interior regions, Fig. 4(d), had relatively coarser particles and lower Z. In each plot, the values of Z_m, Z_n, Z_v and Z_{st} were plotted versus Z_s, chosen here as the most basic and recognizable descriptor of Z. As shown in these figures, Z_{st}, the pinning potential calculated from S_V was in excellent agreement with Z_s, especially the homogenized specimens with more equiaxed particles. The number weighted term, Z_n, showed much higher values than Z_s, by a factor of two, due to the bias towards finer particles. Conversely, the volume weighted term, Z_v, showed much smaller values than Z_s, falling well below the comparison line. The Z_m values were generally close to Z_s, but slightly higher, and again closer for homogenized specimens.

The trends of the data in Fig. 4 can be explained through the analytical expressions for the different measures, Eqs. 20, 25, 29, 34 and 36, condensed in Table 3. Fig. 5 shows the effect of particle size distribution on the Zener pining factor, Z, computed by these five methods, with CV varying from 0 to 1. Here the ordinate represents the size distribution term, that multiplied by $S_V/4$ yields the total Z. It is clear that the number weighting in Z_n produces the greatest positive bias, by a factor of $(\mathrm{CV}^2+1)^2$ relative to the unbiased values of Z_s or Z_{st}. The volume weighting in Z_v results in a negative bias, by a factor of $(\mathrm{CV}^2+1)^{-1}$. The monosized sphere assumption, Z_m, exhibits a slight positive bias, by a factor of $(\mathrm{CV}^2+1)^{1/2}$. The Z_s and Z_{st} terms are analytically equivalent, as described above, and are not influenced beyond their basic expression by CV. The degree of bias of the different expressions increases with particle size distribution width. Thus, for an actual material with a particle size distribution width, CV ranging from 0.5 to 0.7 for the studied specimens, Z_m, Z_n and Z_v are variably biased in computing the Zener pinning factor. For $\mathrm{CV}=0.6$, the respective values of Z_m, Z_n and Z_v are approximately 1.2, 1.8 and $0.7Z_{st}$, in general agreement with the slopes of the experimental data in Fig. 4.

The advantages of using the stereological means versus the summation method are evident when dealing with real material systems. In many materials, particles not only exhibit a size distribution but also possess different shapes. Because the summation method is reliant upon particle shape assumption, it is prone to error in description of the size distribution, while the stereological method needs no shape assumption. Secondly, the stereological means is experimentally more robust than the summation method by avoiding the considerable effort and tendency for errors in the unfolding process. Use of a single parameter obtained from simple line intercept or automated field measurements requires significantly less experimental effort than those of measuring several parameters, whose ratio increases the statistical error of the final Z term.

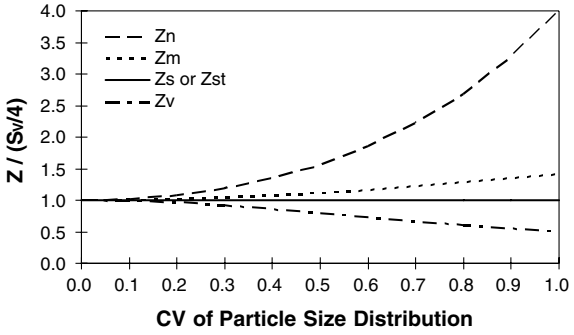

Fig. 5. Analytical prediction of particle pinning potential, Z, computed by the different methods, for different particle size distributions.

5. Summary

Five methods for characterizing the Zener pinning factor have been compared through experimental measurements on second-phase particles in TRC AA3105 and evaluated analytically. Based on a general expression for the Zener pinning potential, $Z = f/\bar{\lambda}$, the analytical expressions of the five approaches are structurally similar, with a common fundamental core, $S_V/4$, but with different size distribution terms, which biases them above or below the correct core value. The stereological method, yielding the fundamental pinning factor, $S_V/4$, is experimentally very close and analytically identical to the summation method; however, with neither the need for unfolding the 3D particle size distribution nor assumption of spherical particles. For a real material system, the stereological means is demonstrated to be the simplest experimentally and with the least error.

Acknowledgements

The authors gratefully acknowledge funding of this research by the Department of Energy, award number DE-FC36-021D14401. The electron microscopy studies were sponsored by the Assistant Secretary for Energy Efficiency and Renewable Energy, Office of Transportation Technologies, as part of the High Temperature Materials Laboratory User Program, Oak Ridge National Laboratory, managed by UT-Battelle, LLC, for the US Department of Energy under contract number DE-AC05-00OR22725. The authors especially appreciate the critical reviews and suggestions by Professors R.T. DeHoff and R.D. Doherty and extensive assistance of Mr. Larry Walker of the HTML Materials Analysis Group with the FEG–SEM operation.

References

[1] Smith CS. Trans Am Inst Min Eng 1948;175:47.

[2] Hillert M. Acta Metall 1965;13:227.
[3] Rios PR. Acta Metall 1992;40:649.
[4] Rios PR. Acta Metall 1992;40:2765.
[5] Rios PR. Acta Metall 1994;42:839.
[6] Rios PR. Acta Metall 1997;45:1785.
[7] Rollett AD, Srolovitz DJ, Anderson MP. Acta Metall 1989;37:1227.
[8] Doherty R, Hoffman E, Hovanec C, Lens A. Mater Sci Forum 2004;467:843.
[9] Rios PR. Scripta Mater 1996;34:1185.
[10] Nes E, Ryum N, Hunderi O. Acta Metall 1985;33:11.
[11] Liu Y, Patterson BR. Scripta Mater 1992;27:539.
[12] Liu Y, Patterson BR. Acta Metall 1993;41:2651.
[13] Liu Y, Patterson BR. Metall Trans A 1993;24:1497.
[14] Liu Y, Patterson BR. Scripta Mater 1993;29:1101.
[15] Liu Y, Patterson BR. Metall Trans A 1994;25:81.
[16] Liu Y, Patterson BR. Acta Metall 1996;44:4327.
[17] Couturier G, Doherty R, Maurice C, Fortunier R. Acta Mater 2005;53:977.
[18] Rios PR. Acta Metall 1987;35:2805.
[19] Rios PR, Fonseca GS. Scripta Mater 2004;50:71.
[20] Rios PR, Fonseca GS. Scripta Mater 2004;50:1373.
[21] Dehoff RT, Rhines FN, editors. Quantitative microscopy. New York (NY): McGraw-Hill; 1968.
[22] Sun N, Patterson BR, Suni JP, Simielli EA, Weiland H, Allard LF. Mater Sci Eng A 2006;416:232.
[23] Patterson BR, Sun N, Suni JP, Simielli EA, Weiland H, Allard LF. TMS Lett 2004;1:173.
[24] Sun N, Patterson BR, Suni JP, Simielli EA, Weiland H, Allard LF. TMS Lett 2005;2:33.
[25] Patterson BR, Sun N. Unpublished research, University of Alabama at Birmingham, 2006.
[26] Mould PR, Cotterill P. J Mater Sci 1967;2:241.
[27] Fullman RL. Trans AIME 1953;197:447.
[28] Aitchison J, Brown JAC. The lognormal distribution. Cambridge University Press; 1957.
[29] Goldman A, Lewis HD, Moore RH. On the proper use of transformations of log normal functions in small particle statistics. Los Alamos Scientific Laboratory, LA-3262; 1965.
[30] Howard CV, Reed MG. Unbiased stereology. Garland Science; 2005.
[31] Kurzydlowski KJ, Ralph B. The quantitative description of the microstructure of materials. CRC Press; 1995.
[32] Patterson BR, Rhines FN. Microstruct Sci 1979;7:457.

Effect of Heating Rate on Recrystallization of Twin Roll Cast Aluminum

NAIYU SUN, BURTON R. PATTERSON, JAAKKO P. SUNI, ROGER D. DOHERTY, HASSO WEILAND, PUJA KADOLKAR, CRAIG A. BLUE, and GREGORY B. THOMPSON

The effect of heating rate on precipitation and recrystallization behavior in twin roll cast (TRC) AA3105 has been investigated by three different means: conventional air furnace, controlled infrared, and lead bath heating. Experimental results showed that as-recrystallized grain size decreased and became more equiaxed as the annealing heating rate increased. These results were explained *via* time-temperature-transformation (TTT) curves for both dispersoid precipitation and recrystallization. With the faster heating rate, recrystallization could occur before precipitation of Mn present in the unhomogenized TRC samples. At a heating rate of 50 °C/s, the material underwent grain growth after recrystallization at 500 °C. No sign of grain growth was observed in materials annealed with lower heating rates, 3 °C/s, 0.5 °C/s, and 0.01 °C/s, due to greater dispersoid precipitation.

DOI: 10.1007/s11661-007-9367-3

I. INTRODUCTION

TWIN roll casting (TRC) is an efficient and economical process for producing aluminum sheets directly from molten metal.[1–3] The process involves feeding the melt directly between water-cooled rolls where solidification occurs, producing 4- to 10-mm-thick sheets that can be coiled and later cold rolled to finished thickness. Advantages of TRC over conventional direct chill (DC) casting include reduced scale of operation, avoidance of ingot scalping, homogenization, and hot rolling, with their additional costs. Although the process is predominantly used for low alloys, it can also be used for higher alloys, but with some problems. In AA3105, the rapid solidification and subsequent cooling with no homogenization retain considerable manganese supersaturation. The supersaturated manganese can form fine α-Al(Mn,Fe)Si dispersoids during the imposed annealing after cold rolling to final thickness. These particles inhibit recrystallization by Zener pinning of subgrain boundaries, resulting in a coarse, elongated grain structure[4,5] giving material with poor formability.[6–8] The object of the study was to find a way to overcome the problem of the large grain size produced by the new process of twin roll casting with its inherent Mn supersaturation.

In DC castings, the problems of heavy dispersoid precipitation on recrystallization annealing are avoided by always applying an expensive predeformation homogenization anneal lasting many hours at elevated temperatures. The TRC can potentially avoid this expensive processing step if the major problem of inhibited nucleation and, thus, a large resulting grain size on annealing cold rolled nonhomogenized metal can be avoided. The present study was designed to examine as quantitatively as possible the conditions needed to allow recrystallization to a fine grain size in such nonhomogenized material.

Prior studies have shown that a higher annealing temperature produces a finer, more desirable recrystallized grain structure.[9] However, the heating rate of material placed in a conventional air furnace at temperature varies with both furnace temperature and time, as shown in Figure 1(a). As a result, in a conventional air furnace, the effect of annealing temperature on recrystallization is combined with the effect of heating rate; *i.e.*, higher furnace temperatures produce higher workpiece heating rates and the two effects on recrystallization are thus difficult to separate.

Infrared (IR) heating provides an excellent means for investigating the effect of heating rate on precipitation and recrystallization in a material with supersaturated matrix.[10] The IR furnace employs a high intensity tungsten filament to transfer radiant energy to the part. The extremely high source temperature of the tungsten filament leads to high thermal transfer and extremely fast heating.[11] The low thermal mass of the tungsten filament gives good control of the heat output and process temperature. Full output can be obtained within seconds of applying power. Also, power can be turned

BURTON R. PATTERSON, Professor, is with the Department of Materials Science and Engineering, University of Alabama at Birmingham, Birmingham, AL, 35294, USA. NAIYU SUN, formerly with the Department of Materials Science and Engineering, University of Alabama at Birmingham, Birmingham, AL, 35294, USA, is with Citation Corporation, Browntown, WI, USA. Contact e-mail: naiyus@browntown.citation.net or nysun@uab.edu JAAKKO P. SUNI and HASSO WEILAND, Research Scientists, are with the Alcoa Technical Center, Alcoa Center, PA, 15069, USA. ROGER D. DOHERTY, Professor, is with the Department of Materials Engineering, Drexel University, Philadelphia, PA 19104, USA. PUJA KADOLKAR, Research Assistant, and CRAIG A. BLUE, Metal Process Group Leader, are with the Oak Ridge National Laboratory, Oak Ridge, TN, 37831, USA. GREGORY B. THOMPSON, Assistant Professor, is with the Department of Metallurgical and Materials Engineering, University of Alabama, Tuscaloosa, AL, 35487, USA.

Manuscript submitted August 23, 2006.
Article published online November 16, 2007

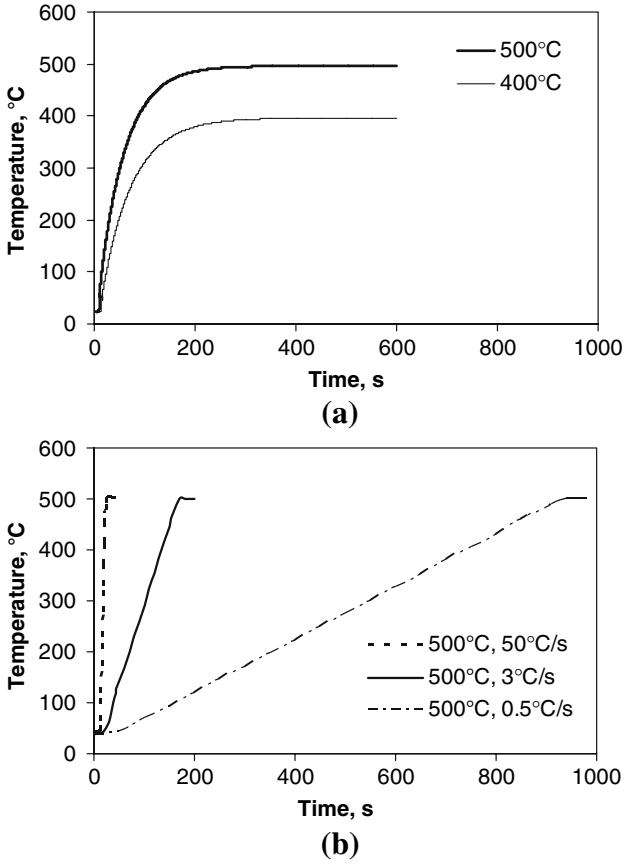

Fig. 1—Heating curves for TRC AA3105 after 90 pct cold rolling: (*a*) conventional air furnace and (*b*) infrared furnace.

off almost immediately at the end of the process. Thus, the heating rate of the studied material with a thickness of approximately 500 μm can be well controlled and is independent of temperature, as shown in Figure 1(b). In the present study, the microstructural change on annealing cold-rolled TRC AA3105 is investigated at different controlled heating rates to different annealing temperatures to determine the relative kinetics of Mn precipitation and recrystallization.

II. EXPERIMENTAL

The TRC AA3105 was produced by Alcoa (Pittsburgh, PA), with the chemical composition given in Table I. The material, in the as-TRC state of 5-mm thickness, was cold rolled 90 pct in thickness prior to annealing. Three of the highest constant heating rates, 50 °C/s, 3 °C/s, and 0.5 °C/s, were achieved in an electric IR furnace at the Materials Processing Laboratory, Oak Ridge National Laboratory. The slowest constant heating rate, 0.01 °C/s, was obtained with a conventional programmable air furnace. For comparison, materials were also annealed at different temperatures in a conventional air furnace or in a lead bath. The latter gave the highest heating rate investigated; however, the rate is not linear nor readily controlled. Optical and electron microscopy were used to examine the recrystallized grain structure and dispersoid

Table I. Chemical Composition of TRC AA3105

Element	Mn	Mg	Fe	Si	Cu
Wt pct	0.59	0.44	0.55	0.28	0.04

precipitation, respectively. Average grain size and grain aspect ratio were measured *via* the mean linear intercept length in both the longitudinal and transverse directions. All optical micrographs were taken on the longitudinal cross section, parallel to the normal direction (ND) and rolling direction (RD). Electrical conductivity (EC) was used to calculate the change of manganese in solid solution, *i.e.*, the evolution of dispersoid precipitation. The calculation procedure has been described elsewhere.[12]

III. RESULTS AND DISCUSSION

Figure 2 shows the grain structure for TRC AA3105 annealed to full recrystallization in an air furnace at 500 °C and 400 °C, respectively. At 500 °C, the material exhibits a finer recrystallized grain structure than at 400 °C, as shown in Figures 2(a) and (b). This apparent effect of recrystallization temperature on grain size is, our results suggest, mainly the effect of anneal heating rate. Figure 3 shows the as-recrystallized grain structure for material annealed in a lead bath at 500 °C for 1 second after achieving the temperature. The estimated heating rate for the lead bath anneal is approximately 100 °C/s, resulting in a much finer and more equiaxed grain structure than with the air furnace anneal, as shown in Figure 2(a).

Dispersoid particles, either pre-existing at a spacing of the subgrains or precipitating during heating or forming at the annealing temperature, are known to interact with coarsening or coalescence of subgrains that form the nuclei for recrystallization.[5,13–16] Slower heating should allow more dispersoid precipitation on subgrain boundaries, preventing nucleation of recrystallization and resulting in a coarser recrystallized grain size. Typical scanning transmission electron microscopy (STEM) (Figure 4) shows the interaction between precipitates and subgrain boundaries at the early stage of recrystallization in air-furnace-annealed TRC AA3105. It is clear that dispersoids preferentially formed along dislocations and subgrain boundaries, whose subsequent motion will be inhibited by these fine particles.

Figure 5 shows the time-temperature-transformation (TTT) diagram determined for 90 pct cold-rolled TRC AA3105, overlaying the start and finish of recrystallization with the times for different amounts of dispersoid precipitation at different temperatures, the latter determined from EC measurements. The early stage of precipitation, arbitrarily chosen as 10 pct removal of total manganese supersaturation, was obtained *via* infrared annealing with the fastest heating rate of 50 °C/s to minimize the precipitation during heating. The curve for nearly complete precipitation, *i.e.*, removal of 80 pct of manganese supersaturation, was

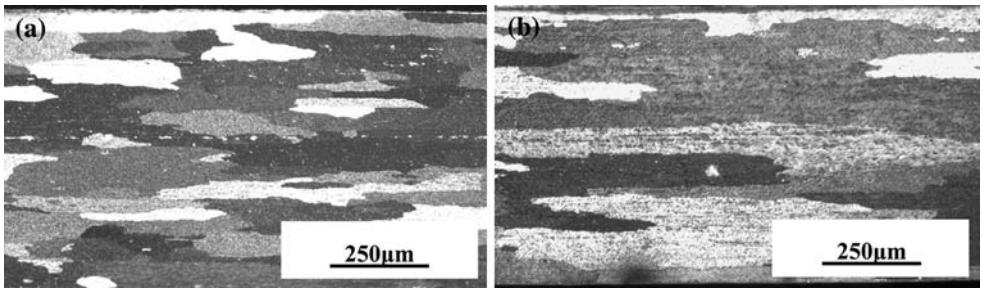

Fig. 2—As-recrystallized grain structure for material air furnace annealed at different temperatures: (*a*) 500 °C for 5 min and (*b*) 400 °C for 8 h.

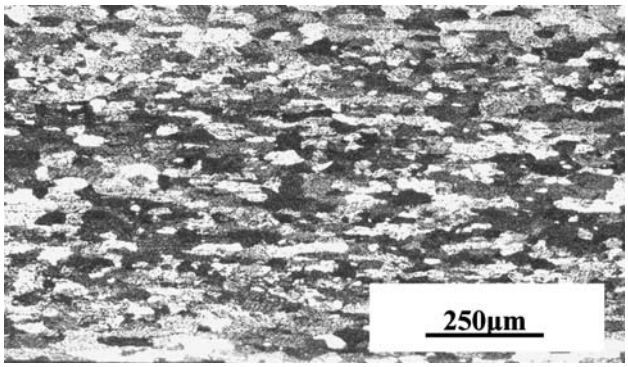

Fig. 3—As-recrystallized grain structure for material lead bath annealed at 500 °C for 1 s.

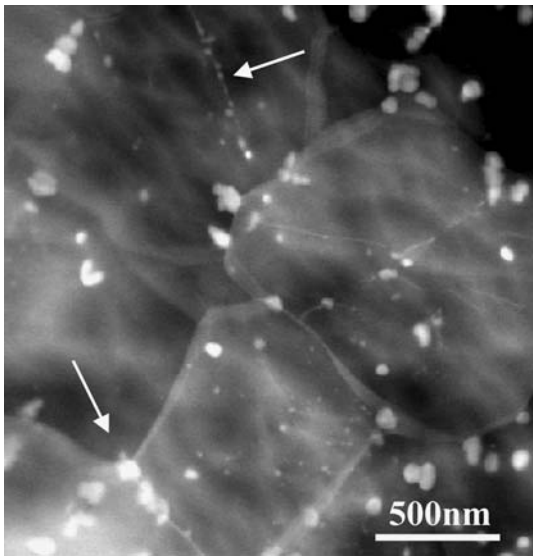

Fig. 4—STEM image of early recrystallization in TRC AA3105 air furnace annealed at 375 °C for 30 min. Note that dispersoids tend to form along subgrain boundaries and dislocations.

obtained for materials annealed in a conventional air furnace. For these air-furnace-annealed specimens, the effect of heating on the amount of precipitation is negligible, because the time spent during heating was less than 5 pct of the isothermal holding time.

The start and finish of recrystallization were followed *via* optical microscopy for both air furnace and the

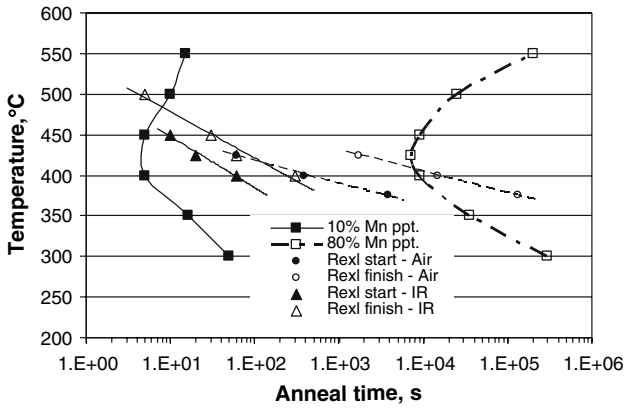

Fig. 5—Recrystallization and precipitation TTT curves for TRC AA3105 after 90 pct cold rolling. The 10 pct manganese precipitation curve was obtained *via* infrared heating of 50 °C/s. The 80 pct precipitation curve was obtained using conventional air furnace heating, because the heating time was negligible compared to the isothermal anneal time.

50 °C/s infrared anneal. A faster heating rate to temperatures allowed rapid recrystallization prior to formation of many inhibiting dispersoids and resulted in increased recrystallization kinetics and a finer recrystallized grain size. Conversely, a slower heating rate allowed significant dispersoid precipitation prior to the start of recrystallization, greatly hindering nucleation of recrystallization and resulting in slower kinetics (Figure 5) and a much coarser grain size (Figure 6). This result is most clearly seen for the samples recrystallized at 400 °C in the air furnace. These samples took over 200 seconds to reach temperature (Figure 1(a)), while the sample in the IR furnace took only 8 seconds to reach 400 °C on heating at 50 °C/s (Figure 1(b)). The IR sample started recrystallization after about 70 seconds and recrystallization was complete after about 300 seconds, at which time recrystallization in the air furnace sample, also at 400 °C, had not yet started (Figure 5). Even in the IR furnace, at 50 °C/s, some significant Mn precipitation, about 10 pct, had occurred at 400 °C after about 5 seconds. In the samples annealed at 400 °C, 80 pct Mn precipitation was achieved after about 10,000 seconds. This was about the same time as the *completion of recrystallization* in the sample annealed in the air furnace. On heating to 500 °C at 50 °C/s, recrystallization was completed in 5 seconds in the IR furnace, before even 10 pct Mn precipitation was seen.

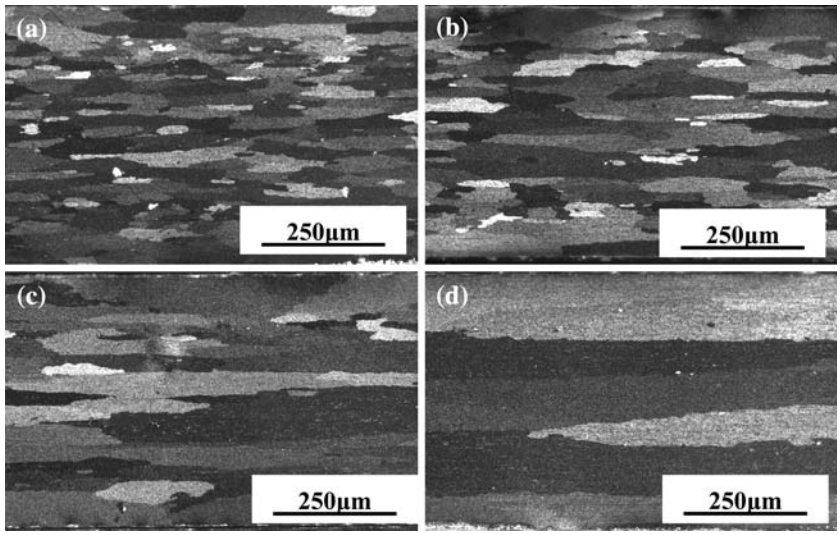

Fig. 6—As-recrystallized grain structure for material IR annealed at 500 °C with different heating rates: (*a*) 50 °C/s, (*b*) 3 °C/s, (*c*) 0.5 °C/s, and (*d*) 0.01 °C/s. Note that the grain size increases as the anneal heating rate decreases.

The displacement to the longer times for conventional heating is thus clearly due to the greater dispersoid precipitation during slow heating to temperature. The lower slope with slow heating is, as reported by Koster,[17] due to the progressively greater amount and finer dispersion of precipitates forming at lower temperatures with decreased heating rate. These finer precipitates have been shown to lead to slower recrystallization, mainly by inhibition of the nucleation of the new grains, leading to the larger recrystallized grain size.[13] Recrystallization is made even slower by the greater recovery allowed by longer times before recrystallization starts.

The rapid, controlled heating rate of IR annealing enabled separation of the effects of heating rate and annealing temperature on recrystallization. Figure 6 shows the as-recrystallized grain structure, *i.e.*, prior to any grain growth, for material IR annealed with different controlled heating rates. In these micrographs, together with Figures 2(a) and 3, the increase in grain size with decreased heating rate, even at the same annealing hold temperature, is visually apparent. Figure 7, including both the lead bath anneal and the IR treatments with different hold temperatures, illustrates these effects more clearly. It is apparent that the average recrystallized grain size markedly decreased as the heating rate increased. For the fastest heating rate, approximately 100 °C/s in the lead bath, the material was heated to target temperature within 5 seconds. As a result, very little manganese precipitation occurred, less than 0.05 wt pct Mn, *i.e.*, 10 pct removal of the total supersaturation of approximately 0.5 wt pct, as shown in Figure 5. As the heating rate decreased, the material spent a longer time heating through the lower temperatures, resulting in greater precipitation. These concurrently forming precipitates tended to pin subgrain boundaries and inhibit the nucleation process during recrystallization,[13] as shown in Figure 4.

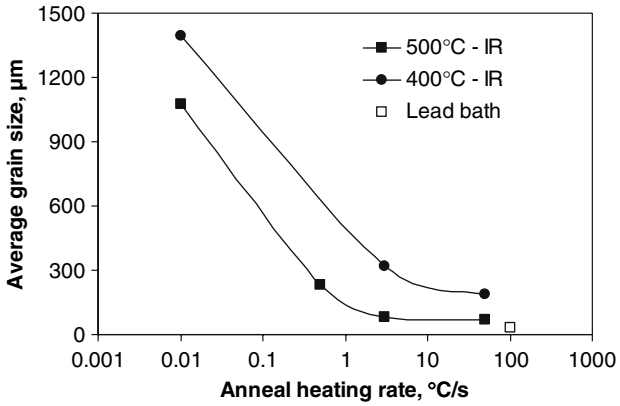

Fig. 7—Effect of anneal heating rate and temperature on recrystallized grain size. The grain size was estimated by averaging the mean linear intercept length in both the longitudinal and transverse directions of the strip shown in Figs. 3 and 6.

Figure 7 also shows that for a constant IR heating rate, a lower annealing hold temperature also resulted in coarser grain size. This effect was more predominant at the higher heating rates and relatively smaller at the lowest rates. At the highest rate of 50 °C/s, the grain size at 400 °C was a factor of 1.7 larger than that at 500 °C, while for 0.01 °C/s, the difference was only a factor of 0.3. Again, the cause of this grain size increase with decreased hold temperature, even at the same heating rate, is apparently due to the greater precipitation at the lower hold temperatures, near the nose of the precipitation transformation curve. For practical purposes, however, this effect of temperature on recrystallized grain size is secondary to that of the anneal heating rate.

Figure 8 shows the effect of the heating rate and hold temperature on the grain aspect ratio in the IR and lead-bath-heated materials. As with grain size, the aspect ratio decreases markedly with increased heating rate and

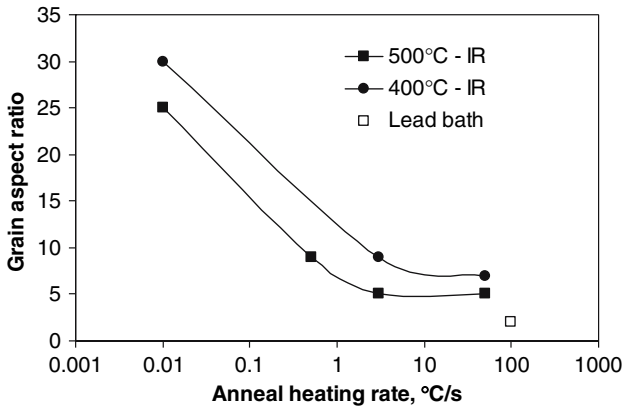

Fig. 8—Effect of anneal heating rate and temperature on grain aspect ratio, computed as the ratio of the mean linear intercept length in the longitudinal and transverse directions of the strip.

higher hold temperature. The increased grain aspect ratio with decreased heating rate is most likely due to the concurrent precipitates preferentially formed at higher angle grain boundaries, which tend to orient themselves parallel to the rolling plane. Doherty[18,19] has previously analyzed this phenomenon. After heavy rolling, materials exhibit pancaked microstructures with high-angle boundaries, for instance, the prior grain boundaries and transition bands, drawn out in the RD and lower angle subgrain boundaries in the ND. Based on both tension and energy models, Doherty analytically showed that the anisotropically deformed microstructure results in an elongated recrystallized grain structure even though the stored energy, the driving force for recrystallization, is isotropic. His idea was that a recrystallization boundary moving in the normal direction would spend only a very short time experiencing the high driving forces of the high-angle boundaries and most of the time experiencing only the low driving force of the low-angle boundaries. Boundaries migrating in the rolling direction will, however, experience a constant medium driving force. In addition, in samples undergoing precipitation at the slower heating rates, the higher angle boundaries in the deformed state are likely to be more potent nucleation sites for dispersoid precipitation, tending to give planar sheets of precipitates on the high-energy boundaries parallel to the rolling plane.[20] Such sheets of dispersoids will accentuate the already anisotropic recrystallization in the studied material. At the very highest heating rate, in molten lead, which took place with negligible precipitation of Mn, not only was the grain size finer still but the grain shape was almost equiaxed (Figures 3, 7, and 8).

Although rapid heating rates are very desirable for reducing recrystallized grain size, it was observed that the avoidance of dispersoid precipitation, beneficial to recrystallization, also allows rapid grain growth after annealing. Figure 9 shows the material annealed at 500 °C with the 50 °C/s heating. It is apparent that grain growth has occurred while holding at temperature for a short period of time, from 5 seconds to 5 minutes. However, grain growth was not observed in material annealed at the lower heating rates, 3 °C/s, 0.5 °C/s, and 0.01 °C/s, even at extended times. These observations suggest that the grain growth at 500 °C is likely to be due to the absence of precipitates during recrystallization in the most rapidly heated material. At lower heating rates, the material had more time to precipitate enough dispersoids to pin the grain boundaries, on slow heating through the temperature range with the fastest precipitation rates, 400 °C to 450 °C (Figure 5). As a result, the as-recrystallized grain structure was stable in material annealed with the slower heating rates, as shown in Figure 10.

The observed fine recrystallized grain size followed by grain growth in material annealed at the highest heating rate indicates optimum industrial production routes to achieve fine-grained TRC 3105 sheet. For instance, heavy cold rolling and rapid heating to a high temperature in a continuous annealing line followed by rapid cooling to room temperature would produce a fine-grained supersaturated alloy, desirable for H temper material. Following the rapid heating with partial cooling and coiling at a temperature at the nose of the TTT curve for precipitation would produce a fine-grained nonsupersaturated alloy, if preferred.

With the insight gained from this study, it appears that the problem of recrystallization to a large grain size with the TRC alloy can be avoided by controlling the relative kinetics of two processes: (1) recrystallization and (2) precipitation of the Mn dispersoids. The TRC avoids the expensive process of lengthy homogenization to precipitate the Mn dispersoids before hot rolling to

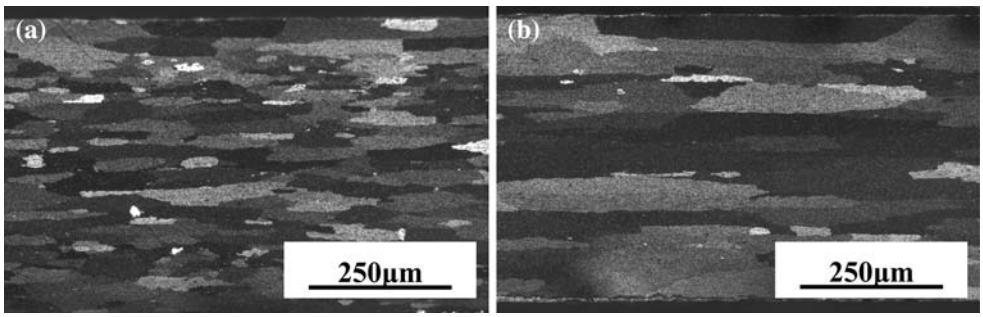

Fig. 9—Grain structure in TRC AA3105 annealed at 500 °C with 50 °C/s heating rate: (*a*) 5 s and (*b*) 5 min hold at temperature. Grain growth occurred during isothermal dwell at temperature.

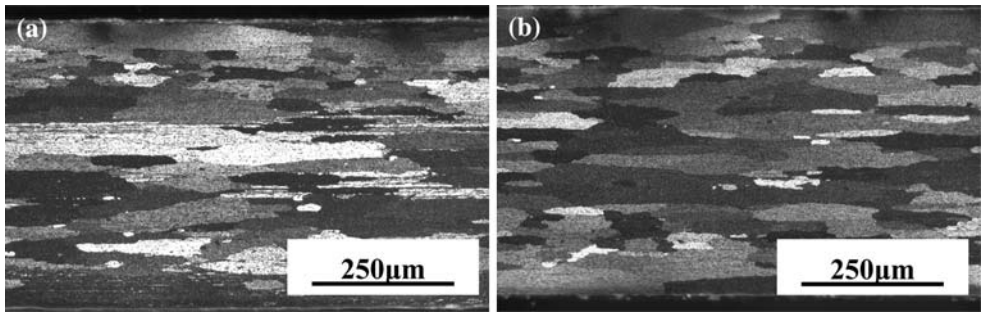

Fig. 10—Grain structure in TRC AA3105 annealed at 500 °C with 3 °C/s heating rate: (*a*) 5 s and (*b*) 5 min hold at temperature. Note that the material has not fully recrystallized yet after 5 s. No apparent grain growth during dwell at temperature.

the TRC thickness. Pre-precipitation of Mn in DC material, giving coarser dispersoids than seen in the TRC samples (Figure 4), allows recrystallization to be less inhibited than with the slowly heated TRC samples.[13,17] However, with the procedure suggested here, rapid annealing of the cold-rolled strip to 500 °C followed by rapid cooling appears to allow the possibility of very fine and nearly equiaxed grain structures that are expected to show the highest formability. In preparing this article for publication, the authors were surprised to find that there appears to be little published information on the empirically well-established need for a fine grain size to achieve good formability in aluminum sheet products. Therefore, quantitative investigations of this relationship would appear to be necessary. The understanding gained from the present study should allow the use of the TRC process for this and other high alloyed aluminum alloys that would also form fine precipitates from the rapidly cooled supersaturated TRC material.

IV. CONCLUSIONS

The following conclusions can be drawn from this study on TRC AA3105.

1. For conventional air furnace heating, annealing at a higher temperature results in a finer recrystallized grain structure. This observed effect is mainly, but not exclusively, due to the effect of a faster heating rate as a result of higher set point temperature than the effect of the anneal temperature itself.
2. An increased anneal heating rate results in a finer recrystallized grain structure and decreased grain aspect ratio, due to reduction of dispersoid precipitation.
3. The recrystallized grain size increases somewhat with decreased annealing hold temperature, even for the same heating rate. The magnitude of this effect increases with increased heating rate and is secondary to the heating rate effect.
4. Grain growth is observed after recrystallization at 500 °C, with the fastest 50 °C/s heating, again due to avoidance of dispersoid precipitation. No grain growth occurred in material annealed at the slower heating rates, 3 °C/s, 0.5 °C/s, and 0.01 °C/s.

ACKNOWLEDGMENTS

The authors gratefully acknowledge research funding by the Department of Energy Grant No. DE-FC36-02ID14401 and the support from the Assistant Secretary for Energy Efficiency and Renewable Energy, Office of Industrial Technologies, Advanced Industrial Materials Program, under Contract No. DE-AC05-00OR22725 with UT–Battelle, LLC.

REFERENCES

1. H. Bessemer: British patent 11,317.
2. M. Yun, S. Lockyer, and J.D. Hunt: *Mater. Sci. Eng. A*, 2000, vol. 280, pp. 116–23.
3. R. Cook, P.G. Grocok, P.M. Thomas, D.V. Edmonds, and J.D. Hunt: *J. Mater. Proc. Technol.*, 1995, vol. 55, pp. 76–84.
4. N. Sun, B.R. Patterson, J.P. Suni, E.A. Simielli, H. Weiland, and L.F. Allard: *TMS Lett.*, 2005, vol. 2, pp. 33–34.
5. N. Sun, B.R. Patterson, J.P. Suni, E.A. Simielli, H. Weiland, and L.F. Allard: *Mater. Sci. Eng. A*, 2006, vol. 416, pp. 232–39.
6. B.A. Parker: in *Aluminum Alloys—Contemporary Research and Applications*, A.K. Vasudevan and R.D. Doherty, eds., Academic Press, New York, NY, 1989, pp. 539–61.
7. W.F. Hosford: in *Formability: Analysis, Modeling and Experimentation*, S.S. Hecker, A.K. Ghosh and H.L. Gegel, eds., TMS, Warrendale PA, 1978, pp. 78–95.
8. G.H. LeRoy and J.D. Embury: in *Formability: Analysis, Modeling and Experimentation*, S.S. Hecker, A.K. Ghosh and H.L. Gegel, eds., TMS, Warrendale, PA, 1978, pp. 183–207.
9. B.R. Patterson, N. Sun, J.P. Suni, E.A. Simielli, H. Weiland, and L.F. Allard: *TMS Lett.*, 2004, vol. 8, pp. 173–74.
10. N. Sun, B.R. Patterson, J.P. Suni, E.A. Simielli, H. Weiland, P. Kadolkar, C.A. Blue, and G.B. Thompson: *Aluminum Wrought Products for Automotive, Packaging, and Other Applications—The James Morris Honorary Symp*, TMS, Warrendale, PA, 2006, pp. 119–24.
11. C.A. Blue, V.K. Sikka, R.A. Blue, and R.Y. Lin: *Metall. Mater. Trans. A*, 1996, vol. 27A, pp. 1–8.
12. N. Sun: Ph.D. Thesis, University of Alabama at Birmingham, Birmingham, AL, 2006.
13. R.D. Doherty and J.W. Martin: *J. Inst. Met.*, 1962, vol. 91, pp. 332–38.
14. E. Nes: *Acta Metall.*, 1976, vol. 24, pp. 391–98.
15. F.J. Humphreys and M. Hatherly: *Recrystallization and Related Annealing Phenomena*, 1st ed., Pergamon, Oxford, United Kingdom, 1995.
16. P.R. Mould and P. Cotterill: *J. Mater. Sci.*, 1967, vol. 2, pp. 241–55.
17. U. Koster: *Met. Sci.*, 1974, vol. 8, pp. 151–60.
18. J.P. Suni, R.D. Doherty, P.A. Hollinshead, T.N. Rouns, and R.T. Shuey: *Aluminum Alloys*, 1998, vol. 2, pp. 1203–11.
19. R.D. Doherty: Drexel University, Philadelphia, PA, unpublished research, 1995.
20. E. Nes, N. Ryum, and O. Hunderi: *Acta Metall.*, 1985, vol. 33, pp. 11–22.

MICROSTRUCTURE EVOLUTION IN TWIN ROLL CAST AA3105

by

NAIYU SUN

BURTON R. PATTERSON, COMMITTEE CHAIR
J. BARRY ANDREWS
KRISHAN K. CHAWLA
ROGER D. DOHERTY
ROBIN D. GRIFFIN
JAAKKO P. SUNI
GREGORY B. THOMPSON
HASSO WEILAND

A DISSERTATION

Submitted to the graduate faculty of The University of Alabama at Birmingham,
in partial fulfillment of the requirements for the degree of
Doctor of Philosophy

BIRMINGHAM, ALABAMA

2006

MICROSTRUCTURE EVOLUTION IN TWIN ROLL CAST AA3105

NAIYU SUN

ABSTRACT

Twin Roll Casting (TRC) is a process by which thin strip is produced directly from molten metal. This process has many advantages over traditional Direct Chill (DC) casting where metal is cast into large slabs or ingots and subsequently hot and cold rolled into strips. While the DC casting involves large capital investment and energy consumption, TRC produces strip with thickness in the range of 10 mm to 2.5 mm in one operation without hot rolling, with less cost, energy usage and equipment requirements.

In TRC AA3105, high solidification and post-solidification cooling rates lead to high manganese supersaturation throughout the as-cast strip and very fine constituent particles near strip surface. After 90% cold rolling, the TRC material shows sluggish recrystallization kinetics and a very coarse grain structure, due to concurrent forming dispersoids and/or fine constituent particles. These particles interfere with the nucleation process by preventing migration of the boundaries associated with potential nuclei, resulting in fewer recrystallization nuclei and slower nucleation rate. In addition, the fine particles can impede grain growth by exerting a pinning pressure on moving boundaries.

The current study investigated the microstructure evolution in TRC AA3105 during different thermo-mechanical treatments. A systematic study of the effects of different homogenization treatments on second phase particles was carried out. The heating rate effect on recrystallization was studies using an infrared heating furnace. The effect of second phase particles on recrystallization behavior was summarized and experimental results were presented.

Different methods for charactering dispersed second phase pinning potential were evaluated analytically and experimentally. A stereological expression, $\frac{S_V}{4}$, was proposed for obtaining the particle pinning potential, *Z*, with neither the assumption of monosized particles nor spherical shape and without the experimental difficulty of unfolding the particle size distribution.

Besides recrystallization, the evolution of abnormal grain growth/coarsening (AGC) was also investigated. A newly-defined dimensionless parameter, the Grain Anchorage Parameter (GAP), the product of the measured matrix grain size and the particle dispersion parameter Z, was shown to control AGC. The longer times needed for AGC in the as-cast material were shown to be due to the fall in Z to achieve the critical value of GAP.

ACKNOWLEDGEMENTS

First, I would like to acknowledge a great debt to my advisor, Dr. Burton R. Patterson, for his inspiration and encouragement throughout my study at the University of Alabama at Birmingham. Without his consistent support, guidance, and patience, I couldn't have accomplished this.

Many thanks also go to the remaining members of my committee – Drs. J. Barry Andrews, Krishan K. Chawla, Roger D. Doherty, Robin D. Griffin, Jaakko P. Suni, Gregory B. Thompson, and Hasso Weiland – for their time, advice and encouragement.

Specially, I want to thank Dr. Eider A. Simielli at Alcoa Technical Center for supplying the experimental materials for this study.

The financial support by Department of Energy (under grant no. DE-FC36-021D14401) and Alcoa Technical Center is graciously acknowledged.

Dr. Lawrence F. Allard, Mr. Larry Walker and Ms. Dorothy Coffey from High Temperature Materials Laboratory at Oak Ridge National Laboratories (ORNL) gave invaluable assistance with electron microscopy. Miss Puja Kadolkar from Materials Processing Group at ORNL gave up her time to help with infrared heating. They deserve my special thanks.

To all of the other faculty, staff, and students of the Department of Materials Science and Engineering who have not been mentioned, your friendship, help, and support are also appreciated.

To my parents, who made everything possible, I can not thank you enough. To my wife, Xiaoyan, it is your unconditional love that keeps me staying in focus and gives me the strength and perseverance in completing this task.

TABLE OF CONTENTS

Page

LIST OF TABLES

Table *Page*

MICROSTRUCTURAL EVOLUTION IN TWIN ROLL CAST AA3105 DURING HOMOGENIZATION

EFFECT OF SECOND PHASE PARTICLE ON RECRYSTALLIZATION IN TWIN ROLL CAST AA3105

HEATING RATE EFFECT ON MICROSTRUCTURE EVOLUTION DURING ANNEALING OF TWIN ROLL CAST AA3105

CHARACTERIZATION OF PARTICLE PINNING POTENTIAL

LIST OF TABLES (Continued)

Figure *Page*

ABNORMAL GRAIN GROWTH IN THE PRESENCE OF EVOLVING PARTICLES

LIST OF FIGURES

Figure *Page*

INTRODUCTION

MICROSTRUCTURAL EVOLUTION IN TWIN ROLL CAST AA3105 DURING HOMOGENIZATION

LIST OF FIGURES (Continued)

Figure *Page*

EFFECT OF SECOND PHASE PARTICLE ON RECRYSTALLIZATION IN TWIN ROLL CAST AA3105

LIST OF FIGURES (Continued)

Figure *Page*

HEATING RATE EFFECT ON MICROSTRUCTURE EVOLUTION DURING ANNEALING OF TWIN ROLL CAST AA3105

LIST OF FIGURES (Continued)

Figure *Page*

CHARACTERIZATION OF PARTICLE PINNING POTENTIAL

ABNORMAL GRAIN GROWTH IN THE PRESENCE OF EVOLVING PARTICLES

LIST OF FIGURES (Continued)

Figure *Page*

LIST OF FIGURES (Continued)

Figure *Page*

LIST OF ABBREVIATIONS

AGC	Abnormal Grain Coarsening
BSE	Backscattered Electron
CLS	Center Line Segregation
CV	Coefficient of Variation
DC	Direct Chill
EC	Electrical Conductivity
FEG	Field Emission Gun
GAP	Grain Anchorage Parameter
HAADF	High Angle Annular Dark Field
HC	Homogenized and Cyclically coarsened
IACS	International Annealed Copper Standard
IR	Infrared heating
ND	Normal Direction
NGC	Normal Grain Coarsening
NH	Non-Homogenized
PSN	Particle Stimulated Nucleation
RD	Rolling Direction
SEM	Scanning Electron Microscopy
STEM	Scanning Transmission Electron Microscopy

TEM	Transmission Electron Microscopy
TRC	Twin Roll Cast
TTT	Temperature Time Transformation

INTRODUCTION

Twin roll casting process

For more than a half century, Twin Roll Casting (TRC) has become increasingly important for producing aluminum sheet and foil product. The driving force for this trend has been the economic advantages of the TRC process when compared to conventional Direct Chill (DC) casting where metal is cast into large slabs or ingots and subsequently hot and cold rolled into strips. TRC has lower capital, energy and labor costs and thus provides a lower conversion cost.

The concept of TRC dates back to the nineteenth century when Sir Henry Bessemer originally conceived the TRC process in his 1846 twin roll caster patent [1]. It took over a hundred years for the aluminum industry to exploit the process. The first successful commercial twin roll caster for aluminum was developed by Joseph L. Hunter in 1954 [2], as shown in Fig. 1.

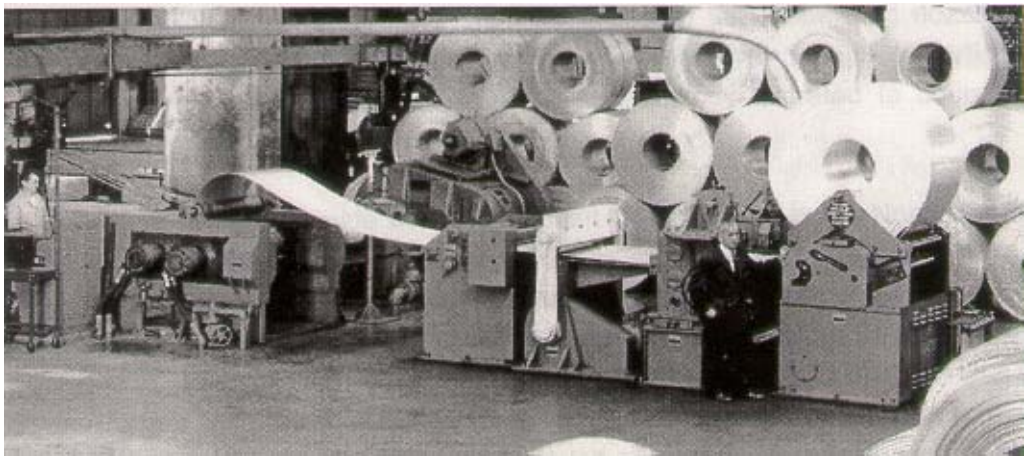

Figure 1, The world's first commercially successful twin roll caster for aluminum [2]

Although TRC technology has progressively improved [3-13], the basic casting process remains unchanged. A planar ceramic pouring nozzle, commonly known as a "tip" introduces the molten metal between two internally water cooled rolls, as shown in Fig. 2. The exit of the nozzle is slightly ahead of the centerline of the rolls, thus the caster solidifies and hot rolls the metal in one process. The simultaneous solidification and hot deformation produces a characteristic microstructure with a fine cell size, fine intermetallic particle distribution, high supersaturation, and residual deformation. Typical as-cast grain structure and second phase morphology in TRC AA3105 are shown in Figs. 3 and 4 respectively. These microstructures are considerably different from those obtained from traditional Direct Chill (DC) casting and hot rolling.

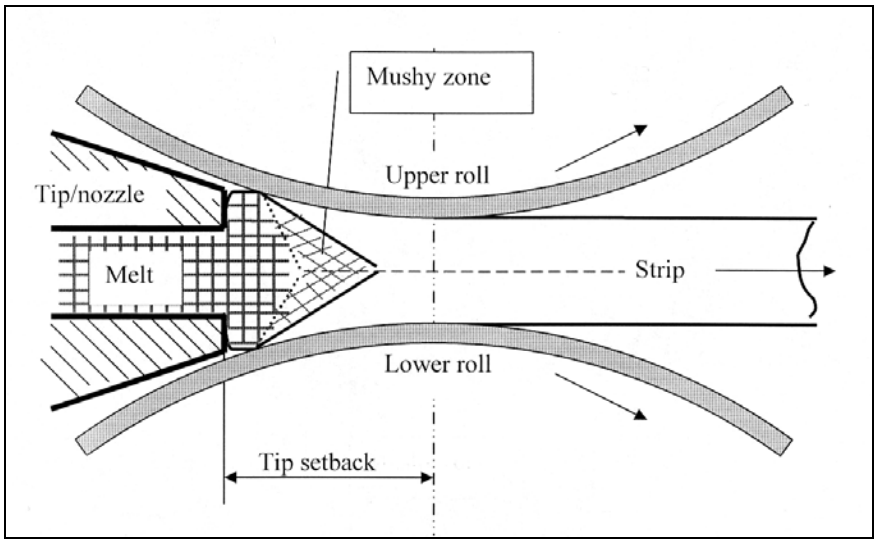

Figure 2, Illustration of the solidification and rolling process during twin roll casting, showing side view of a typical horizontal twin roll caster.

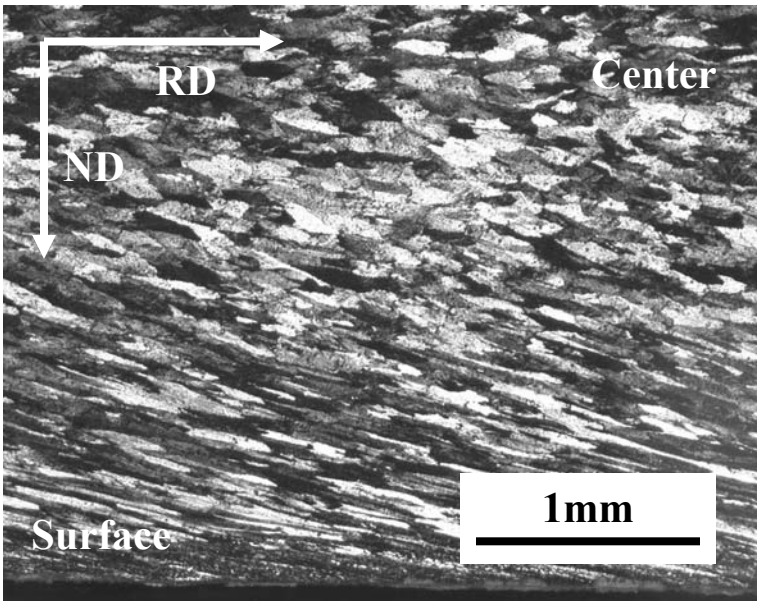

Figure 3, Optical micrograph of as-cast TRC strip of AA3105, showing deformed grain structure. Note that residual deformation decreases with distance from strip surface.

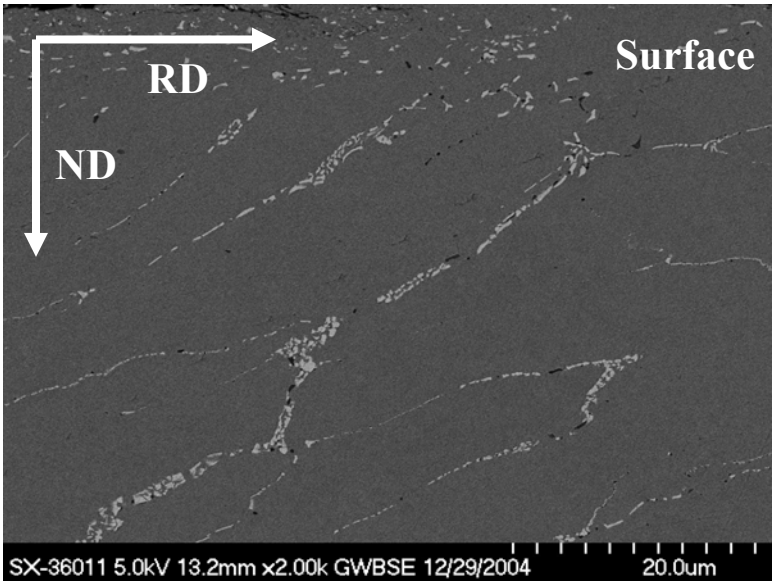

Figure 4, Backscattered Electron (BSE) image showing second phase morphology near an as-cast TRC AA3105 strip surface (top). Notice the approximately 45° orientation of as-cast cells outlined by second phase.

The fine microstructure of TRC strip makes it particularly suitable for some applications, including most fin and foil products [14, 15]. This fine microstructure, however, has traditionally made TRC strip impractical for drawn and ironed applications, for example, can body stock. Due to the "galling" effect and high working hardening rate associated with the fine intermetallic particles, cold-rolled TRC strip has inferior deep drawability than that of hot rolled strip [16]. In order to expand its applications and improve its properties, TRC strip thus requires different downstream rolling and annealing practices than those for DC casting. The present study will investigate the microstructural evolution of TRC AA3105 during different thermo-mechanical treatments.

Review of possible defects in TRC material

A number of defects, both micro- and macro-, can occur in TRC aluminum alloys [3, 17]. Some of them can be controlled very well by employing appropriate casting parameters, but others, mainly internal defects, remain challenging. The casting defects observed in TRC materials can be categorized into surface defects and internal defects.

Surface defects

Level lines are narrow bands at strip surface that are normal to the casting direction. According to Strid et al. [18], this surface feature results from the periodic fracture and reforming of a meniscus between the tip and the roll surface. When the meniscus breaks, liquid metal slumps on to the cold rolls and is rapidly solidified. A new meniscus then forms and is dragged away from the tip, separating the newly arriving

metal from the roll surface and allowing it to solidify more slowly. As a result, the new meniscus is stretched so far that it breaks, causing the cycle to be continued. Avoiding the formation of level lines requires either adjustment of the tip setback or the casting rate.

Under some casting conditions, a strip becomes welded to the roll surface, a phenomenon known as “sticking”. Monaghan [19] reported that alloys with short freezing ranges are more likely to have sticking defects. Sticking can be reduced by applying suitable lubricants to the roll surface or by the addition of low-melting point metals to the aluminum melt to form a liquid film between the aluminum and the roll surface [20].

Surface bleeding is the formation of patches with high concentrations of intermetallic particles on the surface of the TRC strip. Surface bleeding becomes more prevalent as the thickness and load decrease [21-23]. It is believed that surface bleeding is formed by the solute-rich liquid filling in the gap between the strip surface and the roll during the casting process. Surface bleeding can be avoided by controlling the strip gauge and the separating force.

Heat lines are generally described as semi-continuous longitudinal defects, usually only a few centimeters wide, where the cast material leaves the roll bite partially molten [24]. The formation of these defects is related to casting velocity, superheat, interface heat transfer coefficient, and alloy composition [25]. Therefore, alloys with long solidification intervals are more prone to heat line formation. Unfavorable machine settings include short setback distances, high casting speed, high metal temperature and dirty rolls, as well as heavy gauges.

These surface defects can be well controlled by choosing suitable alloy systems and/or by modifying the TRC processing parameters, such as metal temperature, metal level in the head box, casting speed, strip gauge, roll separating force and tip setback.

Internal defects

As a result of segregation and solidification progress in the V-shaped mushy zone, some of the alloying elements have a tendency to end up along, or near, the center line forming Center Line Segregation (CLS). Studies have shown that CLS causes the formation of large, hard, intermetallic particles, which become closer to strip surface during the subsequent cold rolling [22, 23 and 26]. CLS is mainly comprised of eutectic colonies with some metastable phases, as shown in Fig. 5. This occurrence adversely affects mechanical properties of the strip, such as formability. The CLS is accentuated by alloys with larger solidification intervals and by increasing casting speed.

Hot tearing occurs in thin strips, especially in alloys with long freezing ranges, such as AA5182. According to Monaghan [21], hot tearing is the result of differential rolling in adjacent parts (harder/softer materials) of the strip. Often the tears fill with solute-rich material, in which case they are visible on metallographic sections of the sheet.

In addition to the above mentioned defects resulting from the casting process, TRC produces characteristic microstructures different from DC cast materials that can also cause problems during downstream thermo-mechanical treatments. These microstructural characteristics include solute supersaturation, constituent particle size gradient and composition gradient across the thickness of TRC strips. Karlik et al. [27]

found that the presence of surface bands of coarse recrystallized grains and too densely distributed intermetallic particles gave rise to the tearing of thin strip cast AA8006 (1.5Fe-0.4Mn-0.16Si) sheets. Modifying the microstructural inhomogeneity/gradient effects in TRC strips requires not only suitable casting conditions but also particular thermo-mechanical treatments.

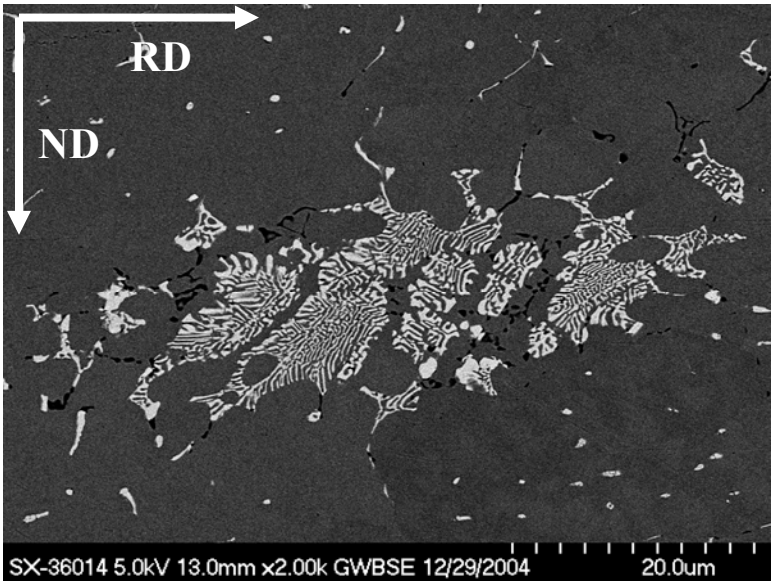

Figure 5, Backscattered Electron (BSE) image showing CLS in as-cast TRC AA3105.

Microstructural evolution during thermo-mechanical treatments

Cold-rolling is one of the most important steps in thermo-mechanical treatments of TRC aluminum alloys. Usually, the as-cast TRC strip is subsequently cold-rolled to a final thickness in three different stages, i.e., primary cold-rolling, intermediate annealing, and final rolling. Puchi-Cabrera [28] investigated the feasibility and benefits of a rolling criterion based on maintaining a constant rolling load rather than a constant thickness reduction. He concluded that the constant load rolling practice has clear advantages in

terms of the productivity of the mill, quality of the rolled products, and extension of the roll life. Other researchers [29-32] have focused on the microstructure and/or texture evolution in TRC aluminum alloys during cold rolling and its effect on material properties and subsequent recrystallization behaviors.

Slamova et al. [33-37] studied the microstructure evolution of strip cast AA8006 and AA8011 (0.7Fe-0.7Si) materials for different heat treatments. They found that the temperature range of transformation processes depends on both alloy composition and heat treatment parameters. The response of the alloys to annealing is markedly different due to different matrix solute content and second phase dispersion level.

Depending on particle size and inter-particle spacing, recrystallization can either be accelerated or retarded [38-42] by particle effects. Low particle dispersion (coarse and not densely dispersed particles) promotes recrystallization via Particle Stimulated Nucleation (PSN), while high particle dispersion (fine and densely dispersed particles) inhibits recrystallization by exerting a dragging/pinning force on subgrain boundaries. Humphreys and Hatherly [43] reported that particle size is an important factor during nucleation of recrystallization. Based on an empirical model of the deformation zone, they obtained the critical particle diameter (d_p), which provides a viable nucleus, as follow:

$$d_p \geq \frac{4\gamma_b}{E_D}$$

where γ_b is grain boundary energy, E_D the matrix stored energy, which is proportional to dislocation density. The stored energy will increase with strain and there will therefore be a critical particle diameter below which PSN will not occur.

The effect of particle spacing on recrystallization was first reported by Doherty and Martin [44] in aluminum-copper Alloys. They concluded that particle dispersion can greatly affect (by a magnitude of five) the recrystallization kinetics as well as grain size (by a magnitude of three). Mould and Cotterill [45] studied the effect of particle spacing on recrystallization in two-phase aluminum-iron alloys, which have particle spacing (~15μm) greater than those (~4μm) reported by Doherty and Martin [44]. Combined with Doherty and Martin's results, Mould and Cotterill [45] postulated that there are two critical inter-particle spacings, $C_1 \approx 4\mu m$ and $C_2 \approx 2\mu m$, in heavily deformed aluminum alloys, which have a deformation cell structure of approximately 1 to 2 μm in diameter. C_1 represents the situation in which a nucleus attached to one particle would be viable in itself but not if nuclei start to form simultaneously at neighboring particles. C_1 corresponds to a spacing of approximately two cell diameter. C_2 defines the distance of the same order as the diameter of the cell structure, at which stage the cells are likely to be pinned by the particles and the ability of subgrains to coalesce to form viable nuclei will be entirely inhibited.

Alloying elements in solid solution also affect recrystallization. Solute atoms have an important effect on dislocation mobility, subgrain and grain boundary migration. Solute atoms can exert a drag on moving boundaries by forming an atmosphere on them. Furu et al. [46] reported that by increasing Fe solid solution content by 0.01 wt% in commercial purity aluminum, the softening process is significantly slowed, i.e. the recrystallization curves are shifted in time by an order of magnitude.

High temperature pre-heat (or homogenization) is one of the most important treatments influencing second-phase particle characteristics in continuously cast and cold

rolled strips [47-55]. A thorough study of the effect of homogenization treatments on evolution of second-phase particles, and their impact on subsequent annealing behaviors of TRC AA3105 has been conducted and presented in Manuscript One. The effects of second phase particles and anneal heating rate on recrystallization behaviors have been summarized in Manuscript Two and Three, respectively.

Quantitative microstructural characterization of second phase particles under different thermo-mechanical treatments has been carried out and summarized in Manuscript Four. The phenomenon of grain growth in TRC AA3105 strip during high temperature anneal has been investigated and is shown in Manuscript Five.

Experimental

The material used in this study, TRC AA3105 (0.50Mn-0.50Mg), was provided by two Alcoa plants, Itapissuma (in Brazil) and Warrick (in Indiana, USA). The as-cast strip has a thickness of approximately 5 mm. Material from Itapissuma plant has a relatively higher Mn and Si content, as shown in Table 1 of Manuscript One, than that of Warrick plant, as shown in Table 1 of Manuscript Four. Itapissuma material was used in the studies reported in Manuscript One through Three and Warrick material was studied in Manuscript Four and Five.

Thermo-mechanical treatments

Prior to annealing, cold work was introduced using a single-stand rolling mill. All materials were cold rolled to 90% reduction after approximately 20 passes with a thickness reduction of 10% for each pass.

Homogenization treatments, including both isothermal and cyclic heating, were given to some specimens prior to cold rolling. All treatments were conducted in a laboratory air furnace with controllable heating and cooling rates. Cyclic heating involved ten cycles between 450 and 620°C with 5h holds at each temperature and 0.3°C/min cooling from the higher to lower temperature and finished with furnace cool from 450°C to room temperature. The cyclic treatments were conducted to maximize second phase coarsening in the material.

Anneals of different temperature and time combinations were conducted in different furnaces: conventional air furnaces, an infrared furnace, and a lead bath furnace.

Microstructural characterization and analysis

Optical microscopy was used to examine and measure the recrystallized grains. A field-emission scanning electron microscope (FEG-SEM) was used to characterize second phase particles. A Hitachi HF-2000 field-emission TEM was used to investigate the interaction between precipitates and moving subgrain/grain boundaries during recrystallization. A Tecnai STEM/TEM/XEDS was used to characterize the morphology and composition of fine precipitates. Two-dimensional image analysis was conducted using Image Pro Plus software. The solute content and amount of precipitation were followed by electrical conductivity measurements.

Organization of the Work

The focus of this study is to characterize the evolution of microstructures in TRC AA3105 under different thermo-mechanical treatments, and to understand some of the fundamental mechanisms associated with these changes.

The experimental and analytical results accompanied by discussions for each aspect of this study are organized into five manuscripts. Each manuscript addresses one important aspect of characterizing the microstructures in the studied material and is consistent with the objectives for the entire study.

Manuscript 1 briefly reviews the twin roll casting process and describles microstructural gradients in the studied material and examines the effect of different high temperature preheating (homogenization) treatments on the evolution of intermetallic particles and recrystallized grain structure.

Manuscript 2 presents the study of second phase particles effect on recrystallization behavior of TRC AA3105. Extensive thermo-mechanical treatments were designed to obtain the different variations in second phase particles, i.e., concurrently forming dispersoids, pre-existing dispersoids and bimodal particle distribution.

Manuscript 3 reports the heating rate effect on microstructure evolution during annealing of TRC AA3105. An infrared heating furnace was employed to obtain the constant heating rates. An experimental Temperature-Time-Transformation diagram was plotted to show the interaction of precipitation with recrystallization.

In Manuscript 4, five methods for characterizing second phase particle pinning potential were evaluated. A stereological expression, $\frac{S_v}{4}$, was demonstrated as a robust

means for characterizing the degree of particle pinning in real material systems with neither the assumption of particle shape nor size distribution and without the experimental difficulty of unfolding the size distribution.

Manuscript 5 investigates Abnormal Grain Growth/Coarsening (AGC), a high temperature annealing phenomenon. A newly-defined dimensionless parameter, the Grain Anchorage Parameter (GAP), the product of the measured matrix grain size and the particle dispersion parameter Z, previously shown to be the shape independent equivalent of the classic Smith –Zener grain size parameter f/r, was shown to control AGC. The longer times needed for AGC in the as-cast material were shown to be due to the fall in Z to achieve the critical value of GAP.

MICROSTRUCTURAL EVOLUTION IN TWIN ROLL CAST AA3105 DURING HOMOGENIZATION

by

NAIYU SUN, BURTON R. PATTERSON, JAAKKO P. SUNI, EIDER A. SIMIELLI, HASSO WEILAND, AND LAWRENCE F. ALLARD

Materials Science and Engineering A, Vol. **416**: 232-539

ABSTRACT

In twin roll cast (TRC) AA3105, high solidification and post-solidification cooling rates lead to high manganese supersaturation throughout the strip and very fine constituent particles near the surface. Rolled and annealed TRC material shows sluggish recrystallization kinetics and a very coarse grain structure, due to concurrent dispersoid precipitation that inhibits formation of recrystallization nuclei. Homogenization from 5 to 120hr at 600°C reduced solute supersaturation and coarsened constituent particles, reducing but not eliminating the particle size gradient. The resulting grain structure was fine throughout most of the strip, but with larger grains at the surface. More extensive cyclical homogenization up to 620°C further coarsened the constituent particles and produced a uniform fine grain structure throughout the strip.

INTRODUCTION

Twin roll casting (TRC) is an energy efficient process for producing several-mm thick sheet directly from molten metal in one operation, eliminating the need for hot rolling [1-3]. Solidification in the TRC process is quite different than that in traditional direct chill (DC) casting, due to the large thermal gradient across the thickness of the strip. Fig. 1 shows the “working zone” of a twin roll caster. The molten metal is directed through a ceramic tip between two internally cooled rolls, with a higher solidification rate at the roll-strip contact surface than at the center of the strip.

To some degree, the microstructure of TRC material is controlled by the various casting parameters, such as casting rate, tip setback, strip gauge, and metal temperature. Higher casting speed increases production efficiency, but can lead to centerline

segregation, as shown in Fig. 2, and macro-defects [4]. Intensive studies have been carried out to optimize the casting parameters and alloy compositions in order to achieve high production and quality in TRC materials [5-9]. However, in some aluminum alloys such as TRC AA3105, microstructural gradients and/or inhomogeneities inherently exist and cannot be eliminated by altering TRC processing parameters.

In particular, there exist gradients in constituent particle size and solute content, with high solute supersaturation throughout the material and very fine constituent particles within 50μm of the surface. After cold rolling and annealing, the recrystallized grain size is much coarser, on the order of mm, than in DC cast AA3105. This coarse structure is detrimental to mechanical properties and surface appearance, and limits the applications for the material to lower end products. The applications for TRC AA3105 would be greatly expanded by developing means to overcome the above problems associated with the roll casting process.

The recrystallization behavior of commercial DC cast aluminum alloys has been the focus of extensive research over several decades, and numerous studies have been made of the effects of second phase particles, both constituent and finer dispersoids [10-16]. It is widely accepted that coarse constituent particles promote nucleation, by the particle-stimulated nucleation (PSN) mechanism. Finer particles, whether constituent or precipitated dispersoids, inhibit growth of subgrains into viable nuclei by boundary pinning, and can restrict growth of nucleated grains. These basic processes and understandings provide insight into the recrystallization problems with TRC AA3105, with inherent constituent particle size gradients and the high solute supersaturation promoting dispersoid formation.

Few detailed recrystallization studies have been performed on TRC aluminum [17, 18]. The above characteristics of TRC AA3105, however, suggest possible solutions to the annealing problems. It is of particular interest to determine the ability of high temperature homogenization, or preheating, on refinement of the recrystallized grain size. High temperature treatment should increase the number of potential PSN nucleation sites by coarsening the overall constituent particle structure and dissolving the finest particles that could hinder formation of viable recrystallization nuclei. Slow cooling from the high temperature soak should also reduce solute supersaturation, depositing the excess manganese on constituent phase, reducing later dispersoid precipitation during annealing. Reduced dispersoid formation would enable more of the nuclei forming at constituent particles to evolve into growing grains, reducing the overall grain size. This paper presents a systematic study of the effects of different homogenization treatments on these processes and the resultant effect on recrystallization of TRC AA3105.

EXPERIMENTAL

Twin roll cast AA3105, with composition given in Table 1, was produced for this study by Alcoa, using normal commercial processing. Homogenization treatments, listed in Table 2, were conducted in a laboratory air furnace with controllable heating and cooling rates. Treatments H1 through H4 involved heating to temperature at 5ºC/min, high temperature holds from 500 to 600ºC for times from 5 to 120hr and cooling to room temperature at a rate of 0.3ºC/min. Treatment H5, suggested by Doherty [19], included ten cycles between 450 and 620ºC with 5hr holds at each temperature and 0.3ºC/min cooling rate from the higher to lower temperature. The single-hold treatments relied on

normal particle coarsening, or Ostwald ripening, to dissolve the finer particles and diffuse the solute to the coarser particles. The cyclic H5 treatment provided accelerated dissolution and coarsening by heating to a higher temperature, 620ºC, to actively dissolve constituent, including the smallest particles, followed by slow cooling to 450ºC to re-precipitate solvent onto the remaining larger particles. All homogenization treatments were concluded by cooling to room temperature at 0.3ºC/min, to simulate the cooling rate of a commercial coil, also reducing residual solvent supersaturation. After homogenization, specimens were cold rolled to 90% reduction in thickness and annealed for recrystallization.

Samples for microstructure examination were prepared on planes parallel to the normal direction (ND) and to the rolling direction (RD). Optical microscopy was used to examine the recrystallized grain structure. Manganese solute precipitation during annealing was monitored by electrical conductivity. A Hitachi S-4700 field-emission SEM and a Hitachi HF-2000 field-emission TEM were used at Oak Ridge National Laboratory to study the constituent and dispersoid particles.

RESULTS AND DISCUSSION

Homogenization effect on solute precipitation

Figure 3 shows the electrical conductivity of both homogenized (H3) and non-homogenized materials annealed at different temperatures for various times. The homogenized material showed much higher initial conductivity than non-homogenized material, with only slight change with time due to solute removal. The non-homogenized material showed a marked increase in conductivity with annealing time, from relatively

low initial values. The degree of manganese removal from solution during annealing, Fig. 4, could be computed from the nearly linear relationship between manganese removal and decrease in resistivity in this material. It is apparent that there is substantial precipitation of Mn-bearing dispersoid in the non-homogenized material during annealing but little, if any, precipitation in the homogenized material. For the non-homogenized material, more than 0.4wt% Mn left solution by precipitating as dispersoids. The H3 homogenization treatment was found to produce almost precipitate-free material after annealing, greatly increasing the recrystallization kinetics and resulting in a fine recrystallized grain structure.

Homogenization effect on constituent phase

Figure 5 shows backscattered-electron micrographs of the constituent morphology in as-cast TRC AA3105 before and after homogenization. In the as-cast state, the constituent exists at grain boundaries with an essentially continuous network structure, as shown in Fig. 5 (a). After homogenization, the second phase is broken up forming chain structures of discrete particles, as shown in Fig. 5 (c). This chain structure of particles is completely replaced by well-spaced large individual particles after H5 homogenization due to more aggressive coarsening, Fig. 5 (e). At the strip mid-thickness, homogenization changes the constituent from a lamellar eutectic structure, as shown in Fig. 5 (b), to colonies of individual particles, as shown in Fig. 5 (d), which are further coarsened during H5 homogenization, as shown in Fig. 5 (f).

Figure 6 shows the constituent particle morphology after 90% cold rolling. As shown in Fig. 6 (a), the particles in the non-homogenized material tend to exist in

clusters, with a size gradient from the strip surface toward the center, i.e. smaller particles at the surface, and larger particles towards the center. After H3 homogenization and cold rolling, the constituent particles do not tend to form clusters but still show the size gradient, Fig. 6 (b). This distribution of more discrete particles is inherited from the homogenized structure prior to cold rolling.

With the more extensive H4 homogenization, i.e. 120hr at 600ºC, the overall particle size is coarser and the severity of size gradient is reduced, as shown in Fig. 6 (c). After the higher temperature, cyclic H5 treatment, the particles are seen to be much more rounded and uniformly distributed, with a larger size and mean spacing, as shown in Fig.6 (d).

Particle analysis

Particle size and distribution changes during different homogenization treatments were quantitatively characterized using particle analysis techniques. Particle sections were classified into two size groups, greater than 1μm diameter and less than 1μm, and quantified as particle number per area, N_A. Figures 7 and 8 show the variation in N_A from strip surface to center.

Figure 7 shows the small particle number density gradient from strip surface to the center for the different homogenization treatments, H3, H4 and H5. For H3 homogenized material, the particle density shows a maximum of approximately 1.7×10^5 sections/mm^2 near the surface, rapidly decreasing towards the center until reaching a stable level of ~4.0×10^4 sections/mm^2 at a depth of approximately 50μm. The maximum overall particle density for H4 homogenized material is ~1.1×10^5 sections/mm^2 at strip

surface, decreasing to ~$2.5x10^4$ sections/mm^2 at approximately 50μm below the surface. As for H5 homogenized material, the particle density shows only a small decrease from $3.0x10^4$ to about $1.5x10^4$ sections/mm^2 from strip surface to center.

The density of large particles shows the opposite trend, as shown in Fig. 8. For H3 homogenized material, the large particle density sees a minimum of ~4 $x10^3$ sections/mm^2 near the strip surface, increasing with depth to a stable level of ~$1.3x10^4$ sections/mm^2 at approximately 50μm below the strip surface. For H4 and H5 homogenized materials, the density of large particles is fairly stable at ~$1.3x10^4$ sections/mm^2 across the strip thickness, showing only a small fluctuation with depth.

The above results show that from H3 to H5, the small particle density decreases by a factor of 6 at the strip surface and a factor of 3 at the center, while the density of large particles remains constant except for the very surface layer. It is clear that coarsening occurs during H3, H4 and H5 homogenization, with H5 giving the most extensive coarsening and reduction in particle gradient, which plays a very important role in recrystallized grain structure as shown below.

Homogenization effect on recrystallization

Figure 9 shows the recrystallized grain structures for both non-homogenized and homogenized TRC AA3105 after 90% cold roll and annealing. In Fig. 9 (a) for non-homogenized material, most grains are very coarse and elongated in the rolling direction. Although this material contains many large constituent particles, there are apparently few effective nucleation sites. As shown in Fig. 5(a), constituent tends to form a continuous network along grain boundaries during casting. The subsequent cold rolling process does

not completely break up the as-cast second phase network into widely spaced discrete particles as in the case of homogenized material, forming instead colonies of particle clusters, greatly reducing the potential to be nucleation sites. Moreover, concurrent precipitation of dispersoid from the supersaturated matrix further hinders nuclei forming near large particles, which makes it even more difficult for a large constituent particle to act as a PSN site in the non-homogenized material.

Cold rolling tends to align grain boundaries longitudinally, compressed closer together in the normal direction forming a denser barrier to growth of recrystallizing grains than in the rolling direction. As a result, the boundaries of newly recrystallized grains and/or nuclei encounter less inhibition when growing in the rolling direction than in the normal direction, resulting in elongated recrystallized grains. In addition to the resulting very coarse and elongated grain structure, the recrystallization kinetics for non-homogenized material is much slower compared to homogenized material.

Figures 9 (b) - (d) are optical micrographs of the recrystallized grain structures resulting from the different homogenization treatments prior to cold rolling and annealing. Compared with non-homogenized material, recrystallized grain structures are much finer and more equiaxed after homogenization. Higher homogenization temperature results in a finer recrystallized grain structure, comparing Figs. 9 (b) and (c). Note that these homogenized materials contain a grain size gradient, with a larger grain size at the strip surface and finer grains in the center. The structure in Fig. 9 (d) has a mean linear grain intercept of approximately 70μm at the surface and 20μm at the center along the rolling direction.

The grain size gradient appears to be closely related to the second phase particle gradients in this material, as shown in Figs. 7 and 8. It is well established that finely dispersed small particles inhibit recrystallization by pinning moving boundaries while large particles promote recrystallization by acting as nucleation sites. According to Humphreys et al. [20], PSN is usually found to occur only at particles of diameter greater than approximately 1μm. In Fig. 6 (b) the density of the small particles is extremely high at the strip surface, rapidly decreasing to a stable level at a depth of 50μm. Meanwhile, the density of potential PSN particles is very low at the surface, approximately $4x10^3$ sections/mm^2, increasing rapidly to about $1.3x10^4$ sections/mm^2 at a depth of 50μm from the surface, which is approximately the thickness of large grain size layer in recrystallized material, as shown in Figs. 9 (c) and (d).

In order to eliminate the grain size gradient in recrystallized material, more aggressive homogenization treatments, H4 and H5, were investigated. The recrystallized grain structures of these are shown in Fig. 10. The grain size gradient is greatly reduced in the H4 material, as shown in Fig. 10 (a). This improvement can be understood by examining the data shown in Figs. 7 and 8, showing reduced particle density gradients for both small and PSN particles. No grain size gradient exists in H5 material, which also shows a very fine grain size of approximately 15μm across the strip thickness, as shown in Fig. 10 (b). As seen in Fig. 7, H5 greatly reduces the density of overall particles and essentially eliminating the gradients. These factors all contribute the fine and uniform recrystallized grain structure in this material.

Figure 11 shows the effect of H3 homogenization on recrystallization kinetics in TRC AA3105. It is clear that homogenized material has much faster recrystallization

kinetics than that of non-homogenized material, where the non-homogenized material was annealed at even a higher temperature. The sluggish recrystallization kinetics of non-homogenized material is due to the concurrent precipitation of large quantities of dispersoids on subgrain boundaries, greatly hindering their motion and preventing formation of viable recrystallization nuclei at potential PSN sites, as shown in Fig. 12 (a). However, homogenization removes surplus manganese solute, resulting in larger constituent particles and no further precipitation, as shown in Fig. 12 (b).

CONCLUSIONS

The following conclusions can be made from this study:

1. TRC AA3105 has a marked gradient in constituent particle size, with very fine, closely spaced particles within approximately 50μm of the 90% cold rolled strip surface and larger particles with greater spacing toward the strip center.
2. As roll cast, AA3105 has a high manganese supersaturation, capable of precipitating many fine dispersoids during annealing.
3. Non-homogenized material shows a very coarse recrystallized grain structure, suggesting that nucleation is hindered by fine constituent and dispersoid pinning.
4. Homogenization reduces the supersaturation, coarsens constituent particles and reduces the total number of particles in TRC AA3105.

5. Homogenization prior to cold rolling and annealing results in marked reduction in recrystallized grain size and faster recrystallization kinetics in TRC AA3105.
6. Extensive isothermal homogenization treatments result in a recrystallized grain size gradient zone at the strip surface with a thickness of approximately 50μm.
7. More extensive cyclic homogenization treatments greatly coarsen constituent particles, producing a uniform fine grain structure.

ACKNOWLDGEMENTS

The authors gratefully acknowledge funding of this research by the Department of Energy, award number: DE-FC36-021D14401. The electron microscopy studies were sponsored by the Assistant Secretary for Energy Efficiency and Renewable Energy, Office of Transportation Technologies, as part of the High Temperature Materials Laboratory User Program, Oak Ridge National Laboratory, managed by UT-Battelle, LLC, for the U.S. Department of Energy under contract number DE-AC05-00OR22725. The authors also thank Dr. R. D. Doherty for his very helpful discussions and suggestions.

REFERENCES

[1] Sir H. Bessemer, British Patent 11317

[2] M. Yun, S. Lokyer, J. D. Hunt, Materials Science and Engineering A280 (2000) 116-123

[3] R. Cook, P.G. Grocok, P.M. Thomas, D.V. Edmonds and J. D. Hunt, Journal of Materials Processing Technology 55 (1995) 76-84

[4] S. A. Lockyer, Ming Yun, J. D. Hunt and D. V. Edmonds, Materials Characterization 37 (1996) 301-310

[5] A. V. Kuznetsov, Int. J. Heat Mass Transfer 40 (1997) 2949-2961

[6] M. Slamova, P. Dvorak and Z. Juricek, Microstructural Science 27 (2000) 20-28

[7] Toshio Haga and Shinsuke Suzuki, Journal of Materials Processing Technology 118 (2001) 165-168

[8] T. Haga, Journal of Materials Processing Technology 111 (2001) 64-68

[9] M. Slamova, Z. Juricek and V. Ocenasek, Materials Science Forum 331 (2000) 161-186

[10] Erik Nes, Acta Metallurgica 24 (1976) 391-398

[11] P. Furrer and H. Warlimont, Aluminum 54 (1978) 135-142

[12] N. Hansen and B. Bay, Journal of Materials Science 7 (1972) 1351-1362

[13] P. Furrer and G. Hausch, Metal Science 13 (1979) 155-162

[14] U. Koster, Metal Science 8 (1974) 151-160

[15] R. D. Doherty and J. W. Martin, Journal of the Institute of Metals 91 (1962) 332-338

[16] Y. J. Li and L. Arnberg, Acta Materialia 51 (2003) 3415-3428

[17] B. R. Patterson, N. Sun, J. P. Suni, E. A. Simielli, H. Weiland and L. F. Allard, TMS letters 8 (2004) 173-174

[18] B. Patterson, N. Sun, J. Suni, E. Simielli, H. Weiland, Proceedings of Materials Solutions Conference 2003: 1st International Symposium on Metallurgical Modeling for Aluminum Alloys (2003) 209-212

[19] R. D. Doherty, Private communication, November, 2004

[20] F. J. Humphreys and M. Hatherly, Recrystallization and Related Annealing Phenomena, First ed., Pergamon, Oxford, 1995

Table 1, Chemical composition of the experimental AA3105, wt%

Mn	Fe	Mg	Si	Cu	Al
0.59	0.55	0.44	0.28	0.04	Bal.

Table 2, Homogenization parameters

Variables / Designation	Temperature ºC	Duration hr	Cooling rate ºC/min	Heating cycles
H1	500	5	0.3	1
H2	550	5	0.3	1
H3	600	5	0.3	1
H4	600	120	0.3	1
H5 [19]	620/450	5	0.3	10

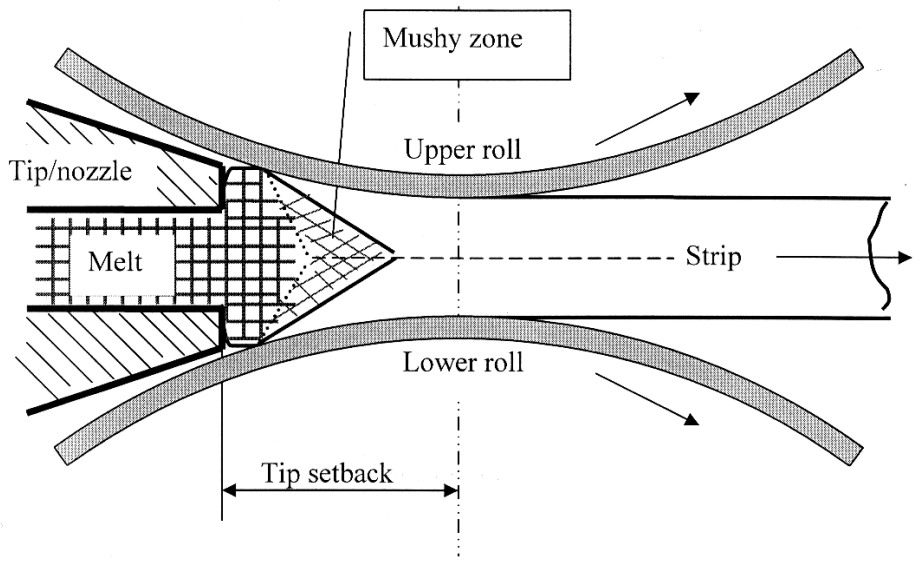

Figure 1, Illustration of the solidification and rolling process during TRC

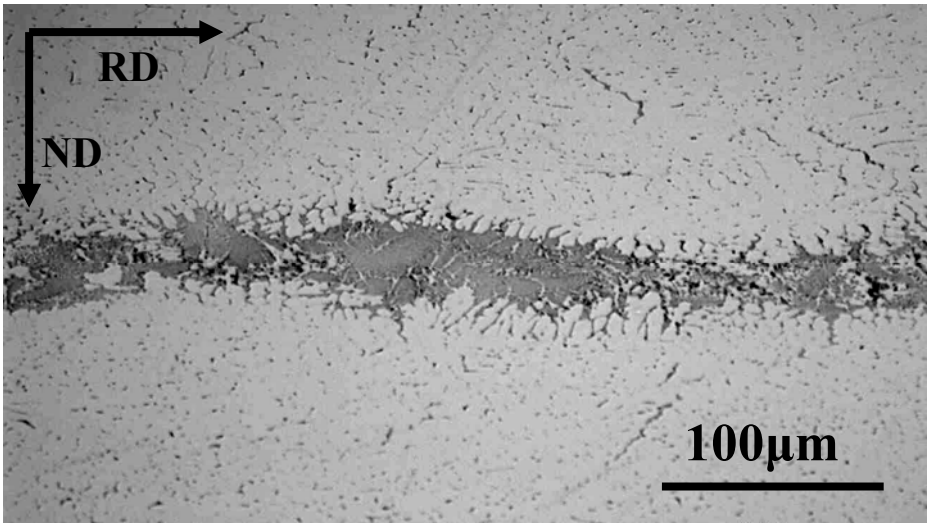

Figure 2, Optical micrograph of centerline segregation in an as-cast AA3105 strip

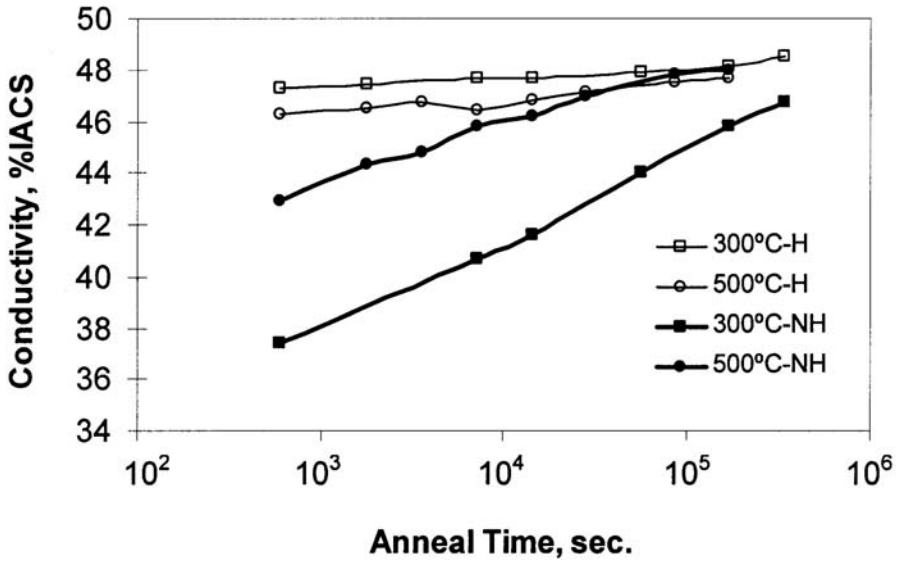

Figure 3, Electrical conductivity of homogenized (H) and non-homogenized (NH) materials during annealing

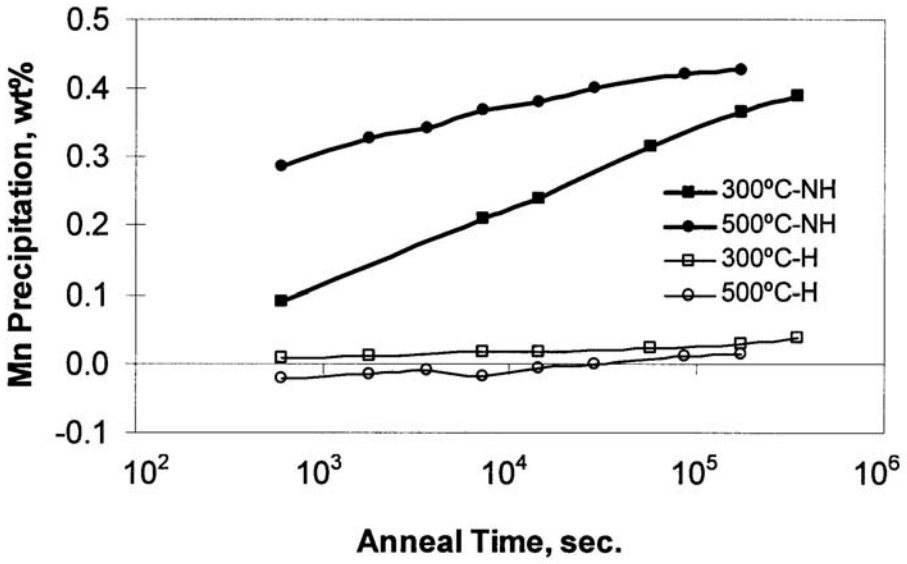

Figure 4, Mn precipitation in H3 homogenized (H) and non-homogenized (NH) materials during annealing

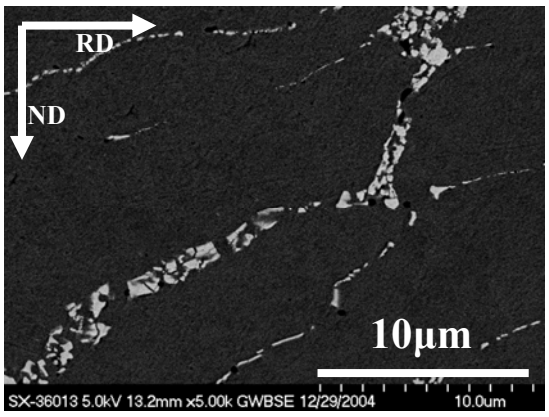
RD
ND
10µm
SX-36013 5.0kV 13.2mm x5.00k GWBSE 12/29/2004
10.0um

(a)

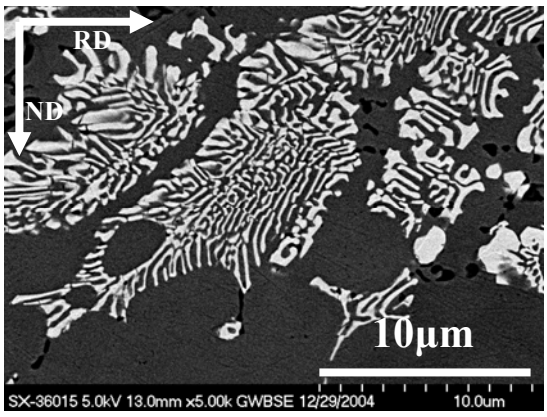
RD
ND
10µm
SX-36015 5.0kV 13.0mm x5.00k GWBSE 12/29/2004
10.0um

(b)

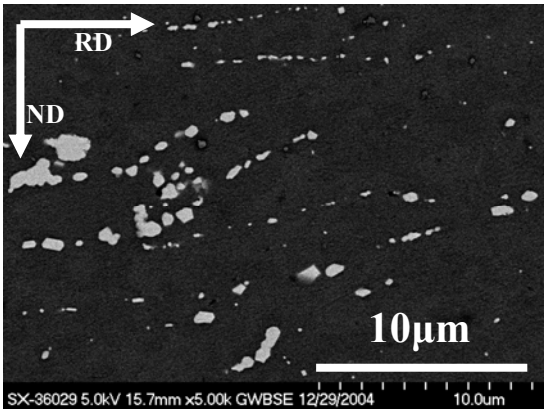
RD
ND
10µm
SX-36029 5.0kV 15.7mm x5.00k GWBSE 12/29/2004
10.0um

(c)

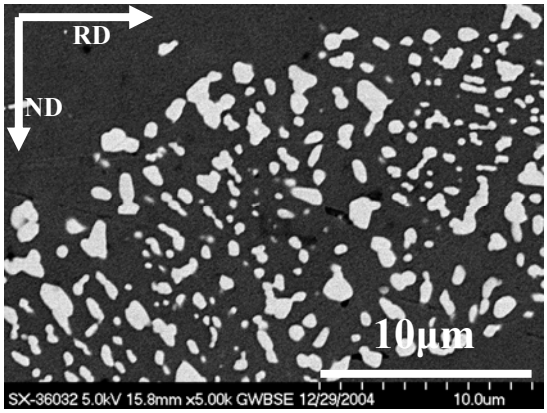
RD
ND
10µm
SX-36032 5.0kV 15.8mm x5.00k GWBSE 12/29/2004
10.0um

(d)

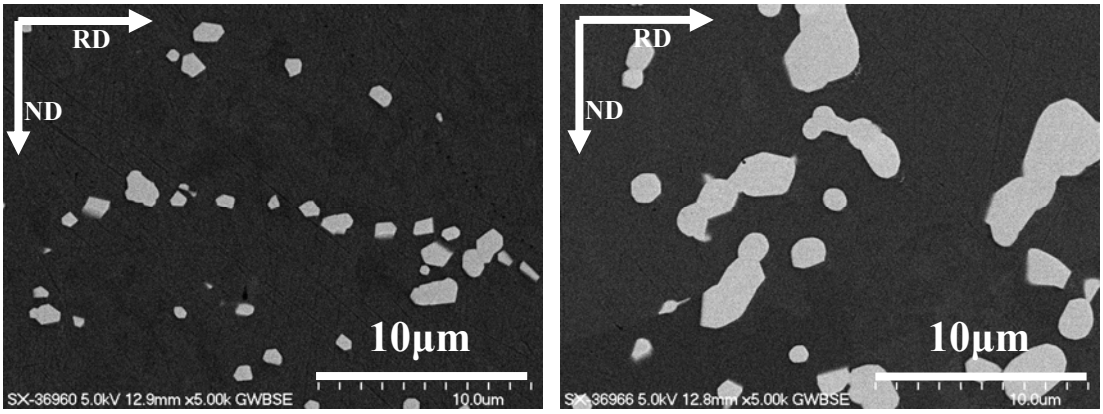

(e) (f)

Figure 5, Backscattered electron images showing constituent phase morphology of a TRC AA3105 strip before and after homogenization. (a) as-cast, strip surface, (b) as-cast, strip center, (c) after H3, strip surface, (d) after H3, strip center, (e) after H5, strip surface, and (f) after H5, strip center.

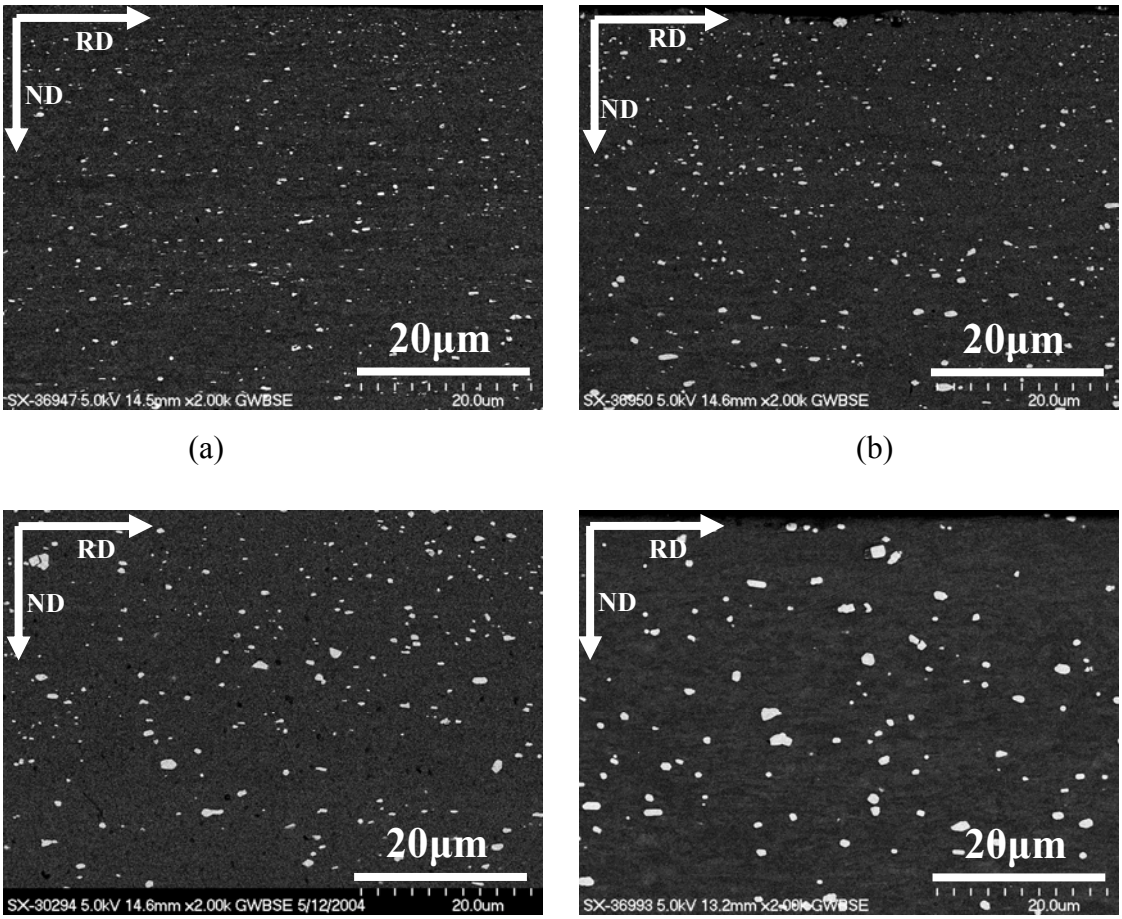

Figure 6, Backscattered electron images showing homogenization effect on second phase particles in TRC 3105 strip after 90% cold roll. (a) non-homogenized, and after (b) H3, (c) H4, and (d) H5 homogenization.

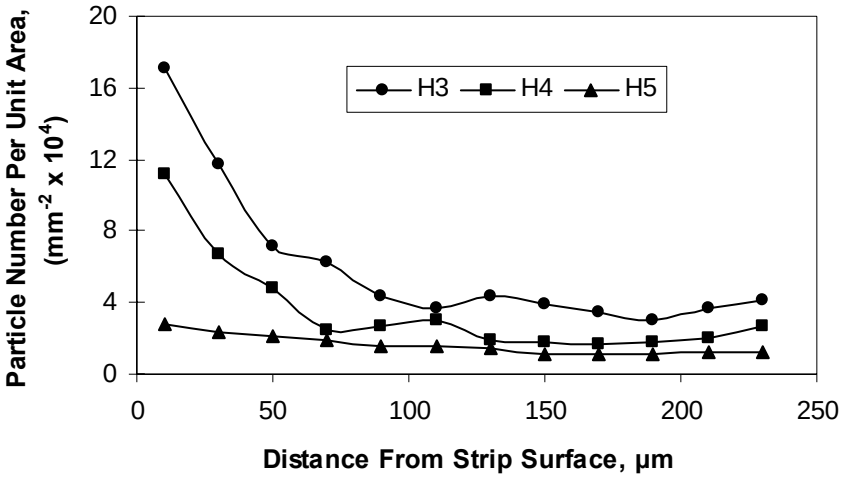

Figure 7, Small particle (<1μm) number distribution from strip surface to center after different homogenization treatments: H3, H4 and H5. Materials are cold rolled 90%.

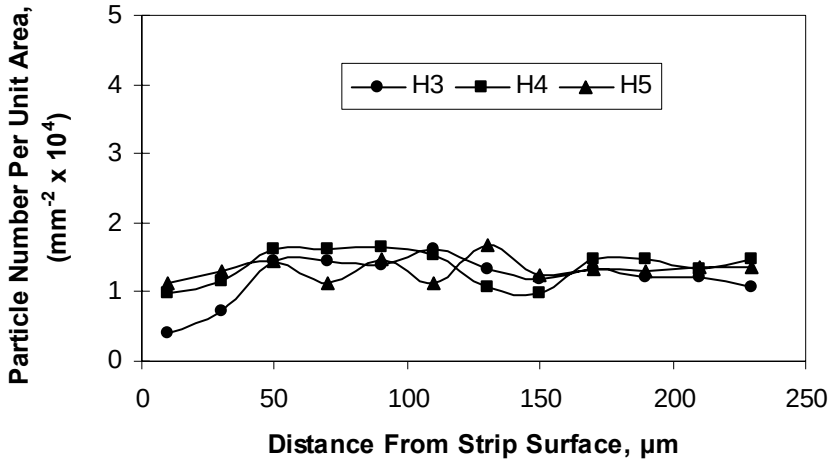

Figure 8, Large particle (>1μm) number distribution from strip surface to center after different homogenization treatments: H3, H4 and H5. Materials are cold rolled 90%.

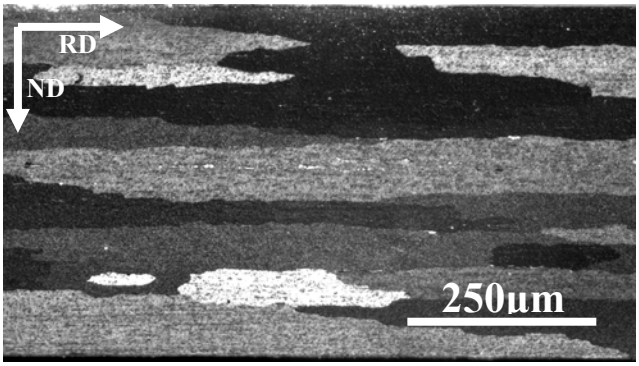

(a)

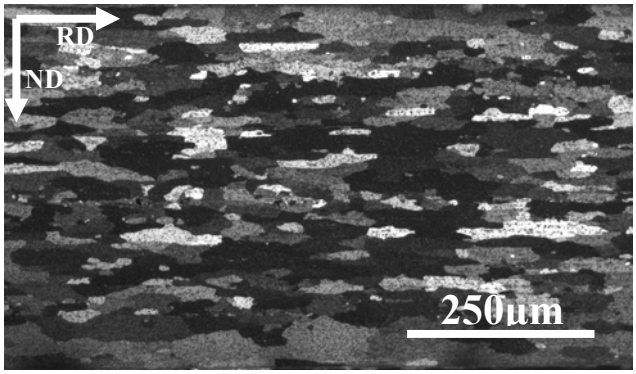

(b)

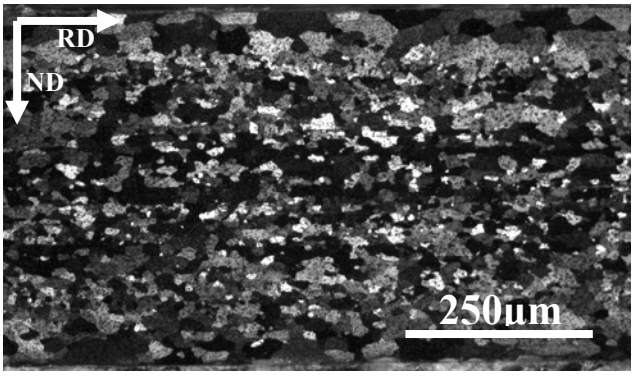

(c)

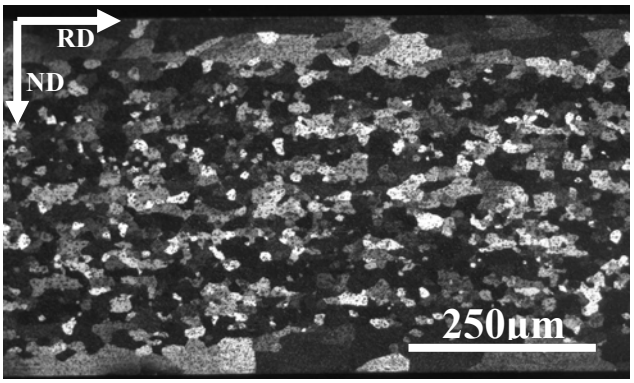

(d)

Figure 9, Optical micrographs of cold rolled and recrystallized TRC AA3105. (a) non-homogenized, after (b) H1, (c) H2, and (d) H3 homogenization

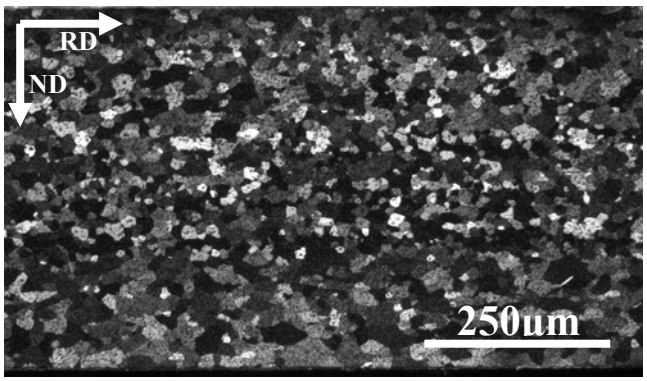

(a)

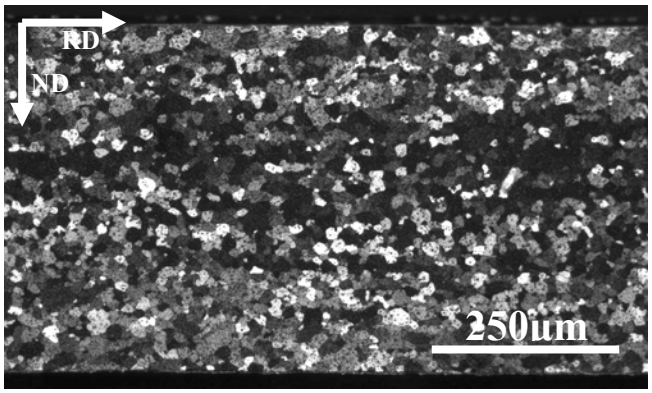

(b)

Figure 10, Optical micrographs of cold rolled and recrystallized material. After (a) H4, and (b) H5 homogenization

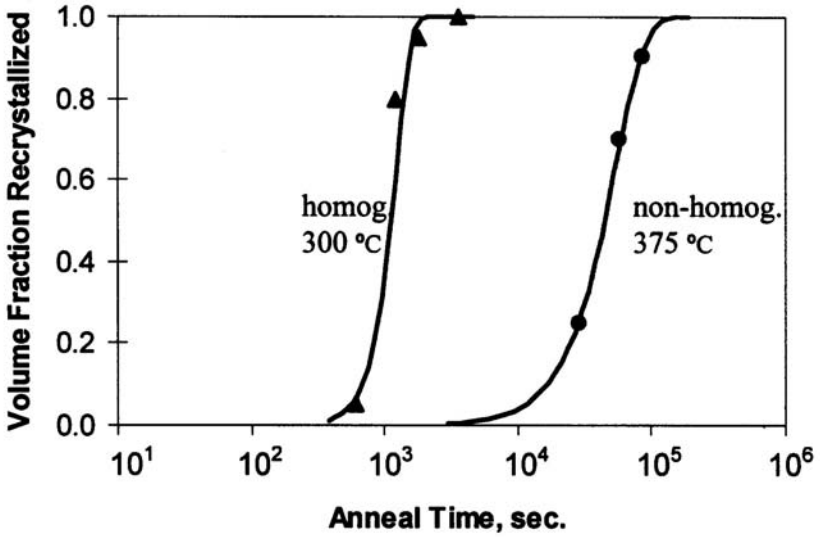

Figure 11, Recrystallization kinetics for H3 homogenized and non-homogenized (NH) materials. Notice that homogenized material exhibits faster recrystallization kinetics than non-homogenized material.

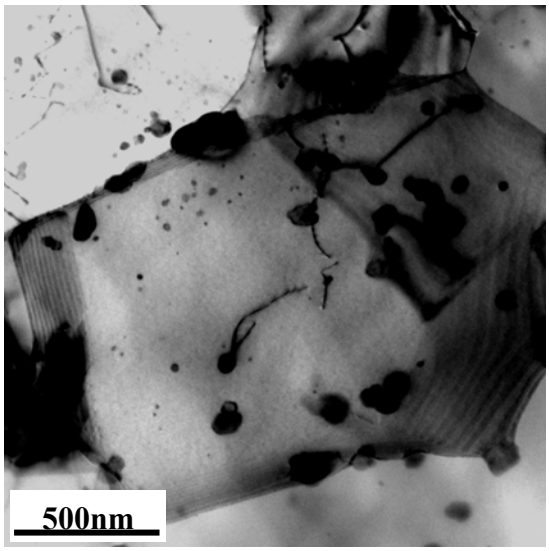

(a)

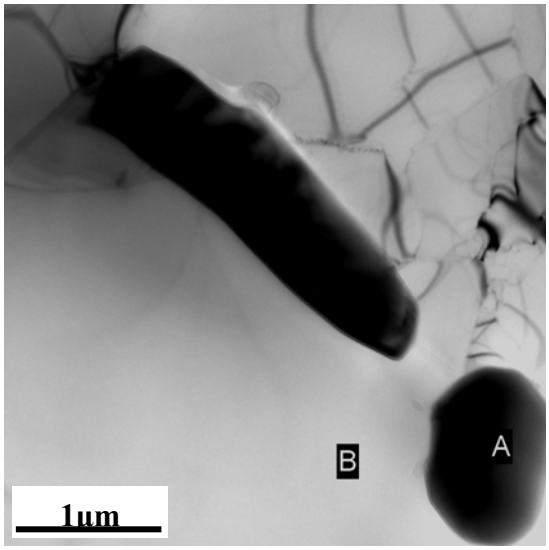

(b)

Figure 12, Bright-field TEM images of early recrystallization. (a) non-homogenized material, note particle pinning at subgrain boundaries, and (b) H3 homogenized material, note absence of small particles in matrix, B, only large constituent particles present, such as A.

EFFECT OF SECOND PHASE PARTICLES ON RECRYSTALLIZATION IN TWIN ROLL CAST AA3105

by

NAIYU SUN, BURTON R. PATTERSON, JAAKKO P. SUNI, HASSO WEILAND, AND LAWRENCE F. ALLARD

In preparation for *Materials Science and Engineering A*

Format adapted for dissertation

ABSTRACT

The effect of different aspects of second phase particles, i.e., concurrently forming dispersoids, pre-existing dispersoids, and bimodal particles, on recrystallization behavior in twin roll cast AA3105 were investigated. With concurrently forming dispersoids, this material exhibits much slower recrystallization kinetics, but with a similar grain size, than material with pre-existing dispersoids. For pre-existing dispersoids, as the size and/or spacing increases, the recrystallized grain size decreases and recrystallization kinetics increases. The efficiency of Particle Stimulated Nucleation (PSN) during recrystallization was shown to be affected by fine dispersoids, which, in a large amount, can prevent PSN in the studied material.

INTRODUCTION

The importance of second phase particles has long been recognized in controlling the recrystallization behavior in two-phase alloys. Depending on the particle size and/or spacing, recrystallization can be either promoted or retarded [1-6].

The effect of particle spacing on recrystallization was first reported by Doherty and Martin [1] in aluminum-copper Alloys. They concluded that particle dispersion can greatly affect (by a magnitude of five) the recrystallization kinetics as well as grain size (by a magnitude of three). Mould and Cotterill [2] studied the effect of particle spacing on recrystallization in two-phase aluminum-iron alloys, which have particle spacing (~15μm) greater than those (~4μm) reported by Doherty and Martin [1]. Combined with Doherty and Martin's results, Mould and Cotterill [2] proposed three characteristic inter-particle spacings that control the nucleation and growth in recrystallization. The three

characteristic spacings are closely related to the deformation cell structure and partitioned by one cell diameter and two cell diameters, that is, smaller than one cell diameter, larger than two cell diameters, and in-between [2].

Humphreys and Hatherly [3] show that in addition to inter-particle spacing, particle size is also very important in controlling material recrystallization behavior. Quite a few studies have reported Particle Stimulated Nucleation (PSN) of recrystallization in materials containing particles of diameter greater than approximately 1μm [3, 4, 6, and 7]. According Humphreys and Hatherly [3], the critical particle diameter, d_{crit}, for PSN is a function of strain, given as:

$$d_{crit} \geq \frac{4\gamma_b}{E_D} \tag{1}$$

where γ_b is the boundary energy, E_D is the stored energy. For a bimodal particle distribution, the effect of fine dispersoid on PSN can be incorporated into Equation 1 as [3]:

$$d_{crit} \geq \frac{4\gamma_b}{E_D - \frac{3f\gamma_b}{2r}} \tag{2}$$

where *f* and *r* are the volume fraction and the radius of the smaller particles.

Nes et al. [4, 8 and 9] reported the effect of a bimodal particle distribution on recrystallization. Based on an abnormal grain growth model, Nes [4] proposed a semi-analytical method for calculating the number of recrystallization nuclei in a material with a bimodal particle distribution. He further justified his model in a commercial Al-Mn alloy.

Jones et al. [10] investigated the precipitation and recrystallization interaction in a series of aluminum-scandium alloys with different concentration of Sc. They reported that fine equiaxed microstructure was obtained when recrystallization precedes precipitation. When recrystallization interacts with precipitation, irregular microstructures such as faceted boundaries and strain induced boundary migration occurred. Kang et al. [11] studied the effects of different stages of precipitation, i.e., nucleation, growth and coarsening, on recrystallization during annealing of niobium micro-alloyed steel.

The effects of particles on recrystallization are rather complicated due to the variations in particle size, particle formation mechanisms, and the mutual interaction between fine and coarse particles. Most studies have been focused on the effect of one or two of the many inter-related characteristics of particles. This is partially due to the difficulty of preparing a material that compassing all the important aspects of particles.

In this study, the effects of concurrently forming precipitates, pre-existing dispersoids, and a bimodal particle array on recrystallization have been investigated in TRC AA3105 strip, which, due to the high solidification and after solidification cooling rates, possesses many variations in microstructures [12] needed for the current study.

EXPERIMENTAL

Twin Roll Cast (TRC) AA3105, with chemical compositions given in Table 1, was produced for this study by Alcoa. Materials were pre-heated under different conditions and cold rolled 90% before the final anneal. The detailed pre-heat treatments and specimen designations are listed in Table 2. Specimen A was as-received/as-cast

material, which forms concurrent dispersoids during final annealing. Specimens B, C and D were obtained by preheating as-cast material at different temperatures for 120 hours followed by ageing at 350°C for 48 hours before water quenched. The goal is, for these specimens, to obtain different precipitate dispersion levels while maintain the same solute level in the matrix [1]. Specimen E was preheated at 375°C for 120h followed by slow cooling at a rate of 0.3°C/min to achieve a fine dispersion of particles and a lean matrix (with no/little precipitation during the final anneal). Specimens F and G were preheated at 600°C for 120 hours followed by slow cooling at 0.3°C/min and water quenching, respectively to produce microstructures of similar coarsened constituent particles but different solute level in the matrix.

Matrix solute level or amount of precipitation during annealing was monitored by Electrical Conductivity (EC) measurements. All optical and Scanning Electron Microscopy (SEM) micrographs were taken in the longitudinal cross section and presented such that the Rolling Direction (RD) is horizontal, and the Normal Direction (ND) is vertical. Scanning Transmission Electron Microscopy (STEM) specimens were prepared such that the viewing field is parallel to/within the rolling plane.

RESULTS AND DISCUSSION

1. Concurrently forming dispersoids vs. pre-existing dispersoids

Figure 1 shows the recrystallization kinetics for materials A and E. It can be seen that material with pre-existing dispersoids, as shown in Fig. 1(b), had much faster recrystallization kinetics than material with concurrently forming dispersoids, as shown in Fig. 1(a), annealed even at a higher temperature. The greater retardation of

concurrently forming dispersoids on recrystallization kinetics can be attributed to the segregation of solute or preferential precipitation of particles at dislocations and subgrain boundaries, as shown in Figure 2. For material E, dispersoids formed before cold rolling and thus distributed rather uniformly, as shown in Fig. 3. Although these pre-existing dispersoids will result in higher dislocation density, the dynamic recovery associated with high strains reduces the dislocation density to an approximately same level as a single phase alloy [3].

Figure 4 shows the EC changes for materials A and E during isothermal annealing at 375°C. It is clearly shown there was no precipitation in material E – EC was stabilized at 51.4%IACS after an early increase of EC due to softening, as shown in Fig. 4 (b). For material A, however, EC kept increasing as time and finally approached the value of 51.4 %IACS after approximately 192 hours long after recrystallization had finished, as shown in Fig. 4 (a). This implies that there was actually fewer overall dispersoids present during recrystallization in material A than in material E. However, due to the preferential segregation and precipitation nature, concurrent dispersoids exerted more effective dragging on the boundaries resulting in a greater inhibition on recrystallization kinetics (by a magnitude of two, as shown in Fig. 1) than the pre-existing ones.

Figures 5 and 6 show the particle morphology in materials A and E before and after annealing, respectively. Comparing Fig. 5 (a) with Fig. 6 (a), a large amount of dispersoids formed concurrently in material A during annealing, which was conformed by the EC results as shown in Fig. 4 (a). There was no further dispersoids forming in material E during anneal, which was confirmed by the EC results shown in Fig. 4 (b).

Figure 7 shows recrystallized grain structure for materials A and E. As we can see, both materials exhibited similar coarse grain structure, which elongated along the rolling direction. Compared to the marked difference on recrystallization kinetics, the pre-existing and concurrent dispersoids had a rather similar effect on recrystallized grain size. A plausible explanation will be that both materials underwent continuous (in-situ) instead of discontinuous recrystallization due to the fine particle dispersion. The final grain size was thus controlled by the original grain structures, which were similar for materials A and E.

2. Effect of dispersoid size and spacing

Figure 8 shows the typical FEG-SEM backscatter electron micrographs of second phase particles in materials with different pre-heating treatments. The few larger particles are constituent particles and the many finer dispersoids particles are mainly precipitates that formed during pre-heating. For better resolution, the high angle annular dark field (HAADF) STEM images of the dispersoids were taken, as shown in Fig. 9. It is clear that as pre-heating temperature increased from 375/400°C to 450°C, the dispersoid size and spacing increased and their number decreased. The difference of particle size and spacing between material B and C is not as significant as that between material B/C and D. As it will be shown later that the recrystallized grain structure in materials B and C were coarser than that of material D, which agrees well with the particle dispersion characteristics. Unlike the concurrent dispersoids preferring boundaries and dislocations, the pre-exist dispersoids were distributed rather uniformly with sizes ranging from approximately 10nm to 150nm.

Figure 10 shows the dispersoids number density for materials B, C, and D obtained via a similar procedure reported elsewhere [13]. It should be pointed out that due to the electron-specimen interaction effect (for a 5 keV electron beam, the Kanaya-Okayama range for aluminum is 0.41μm [14]), the data in Figure 10 is not rigorous but valid for comparison purpose.

Figure 11 shows the grain structure of materials B, C and D after annealing at 375°C for 1 hour. Material B was only partially recrystallized, as shown in Fig. 11 (a), while, materials C and D were fully recrystallized, as shown in Figs. 11 (b) and (c), respectively. The recrystallized grain structure was much finer in material D than that of material C. Both the FEG-SEM micrographs and EC results in Table 3 indicated that there was no further precipitation for materials B, C and D during annealing at 375°C. It is clear that the recrystallization kinetics increased and the recrystallized grain size decreased as the dispersoid particle size/spacing. The finer grain size in specimen D can be qualitatively explained by Mould and Cotterill's [2] recrystallization nucleation theory in the presence of dispersed particles. They proposed that viable nuclei associated with each particle can form independently when the inter-particle spacing is larger than two cell diameters; the nuclei will interact with each other when their spacing is smaller than two cell diameters; recrystallization nucleation should be inhibited completely if the particle spacing is equal or smaller than a cell.

3. Effect of Dispersoid on the efficiency of PSN

Figure 12 shows the typical constituent particle structures in materials F and G. Compared to non-homogenized and low temperature pre-heated materials (Figs. 6 - 8),

particles in materials F and G were greatly coarsened after 120 hours at 600°C. Figure 13 shows the effect of different after-homogenization cooling rates on precipitation in materials F and G during annealing. Specimen G, with water quench, showed concurrent precipitation during annealing, while specimen F with slow cooling at 0.3°C/min showed negligible amount of precipitation.

In a previous study [12], the authors showed that PSN is the major nucleation mechanism of recrystallization in homogenized TRC AA3105. Figure 14 shows the grain structure in materials F and G after 30 min annealing at 325°C. As we can see, material F showed faster recrystallization kinetics than material G. According to Humphreys [6], although the dislocation density in the deformation zone near a large particle is an order of magnitude higher than in the matrix, it takes sub-boundary migration and Y junction movement to form a nucleus. During this course, the concurrently forming dispersoids can impose a dragging force on these sub-boundaries and thus slow the kinetics of nucleation, resulting in slower recrystallization kinetics. An example of the pinned subgrain structures/dislocations by concurrent dispersoids is given in Figure 2.

Figure 15 shows the recrystallized grain structure of materials F and G. As it is clearly shown, material G had coarser grain structure than material F. The coarser grain structure in material G can be explained by recalling Equation 2. The presence of fine dispersoids increases the critical size for a particle to be a viable recrystallization nucleation site. Thus the total number of viable PSN sites will decrease due to concurrent precipitates resulting in fewer recrystallization nuclei and thus a larger recrystallized grain size.

CONCLUSIONS

1. Compared with pre-existing dispersoids, concurrently forming dispersoids/supersaturated solutes retard the recrystallization kinetics much more effectively. However, their effects on grain size are similar.
2. Larger dispersoid size/spacing results in faster recrystallization kinetics and finer recrystallized grain structure.
3. Concurrently forming dispersoids can lower the efficiency of PSN by slowing the nucleation kinetics and by increasing the critical size of potential nucleation sites.

ACKNOWLDGEMENTS

The authors gratefully acknowledge funding of this research by the Department of Energy, award number: DE-FC36-021D14401. The electron microscopy studies were sponsored by the Assistant Secretary for Energy Efficiency and Renewable Energy, Office of Transportation Technologies, as part of the High Temperature Materials Laboratory User Program, Oak Ridge National Laboratory, managed by UT-Battelle, LLC, for the U.S. Department of Energy under contract number DE-AC05-00OR22725. The authors also thank Dr. R. D. Doherty for his very helpful discussions and suggestions.

REFERENCES

[1] R. D. Doherty and J. W. Martin, Journal of the Institute of Metals 91 (1962) 332-338

[2] P. R. Mould and P. Cotterill, Journal of Materials Science 2 (1967) 241-255

[3] F. J. Humphreys and M. Hatherly, Recrystallization and Related Annealing Phenomena, first ed., Pergamon, Oxford, 1995

[4] E. Nes, Acta Metall. 24 (1976) 391-398

[5] U. Koster, Metal Science 8 (1974) 151-160

[6] F. J. Humphreys, Acta Metall. 25 (1977) 1323-1344

[7] N. Hansen and B. Bay, Scripta Metall. 8 (1974) 1291-1296

[8] E. Nes, Scripta Metall. 10 (1976) 1025-1028

[9] E. Nes and J. D. Embury, Z. Metallk. 66 (1975) 589-593

[10] M. J. Jones and F. J. Humphreys, Acta Mater. 51 (2003) 2149-2159

[11] K. B. Kang, O. Kwon, W. B. Lee and C. G. Park, Scripta Mater. 36 (1997) 1303-1308

[12] N. Sun, B. R. Patterson, J. P. Suni, E. A. Simielli, H. Weiland and L. F. Allard, Materials Science and Engineering A 416 (2006) 232-239

[13] N. Sun, B. R. Patterson, J. P. Suni, E. A. Simielli, H. Weiland and L. F. Allard, Acta Metall. (2006) in press

[14] J. I. Goldstein, A. D. Romig, Jr., D. E. Newbury, C. E. Lyman, P. Echlin, C Fiori, D. C. Joy and E. Lifshin, Scanning Electron Microscopy and X-ray Microanalysis, Second Edition, Plenum Press, New York, 1992

Table 1, Chemical composition of the experimental TRC AA3105, wt%

Mn	Fe	Mg	Si	Cu	Al
0.59	0.55	0.44	0.28	0.04	Bal.

Table 2, Specimen ID and preheat treatments for the studied TRC AA3105

Specimen ID	Preheat treatment, °C/h	Ageing treatment, °C/h	After treatment cooling rate
A	No	No	No
B	375/120	350/48	Water Quench
C	400/120	350/48	Water Quench
D	450/120	350/48	Water Quench
E	375/120	No	0.3°C/min
F	600/120	No	0.3°C/min
G	600/120	No	Water Quench

Table 3, Electrical conductivity data for materials under different thermo-mechanical treatments, IACS%

Specimen	B	C	D
As cold rolled	50.2	50.6	50.1
375°C anneal, 1h	51.4	51.7	51.2
375°C anneal, 5h	51.4	51.7	51.3

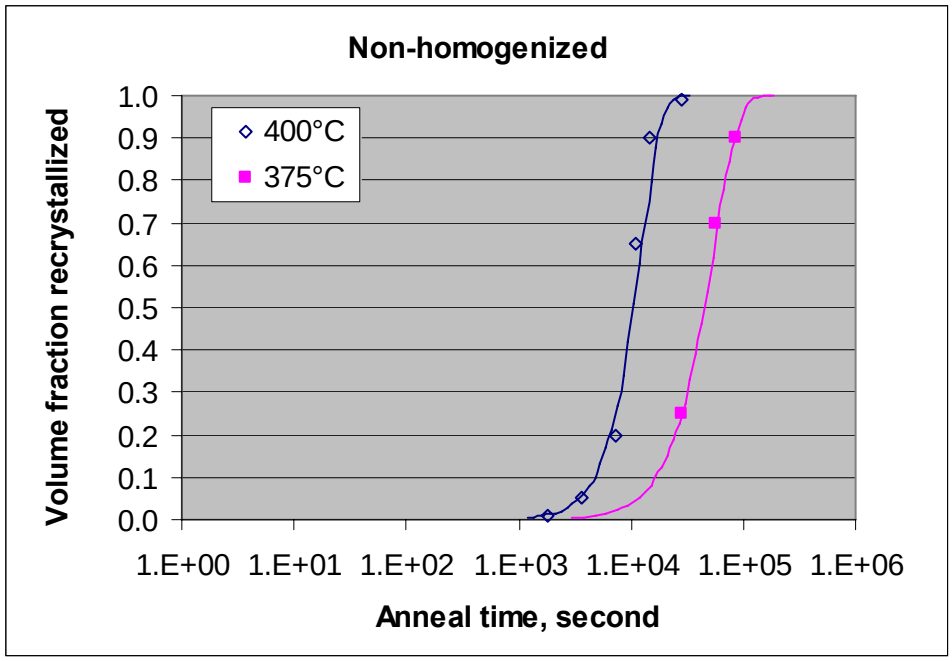

(a)

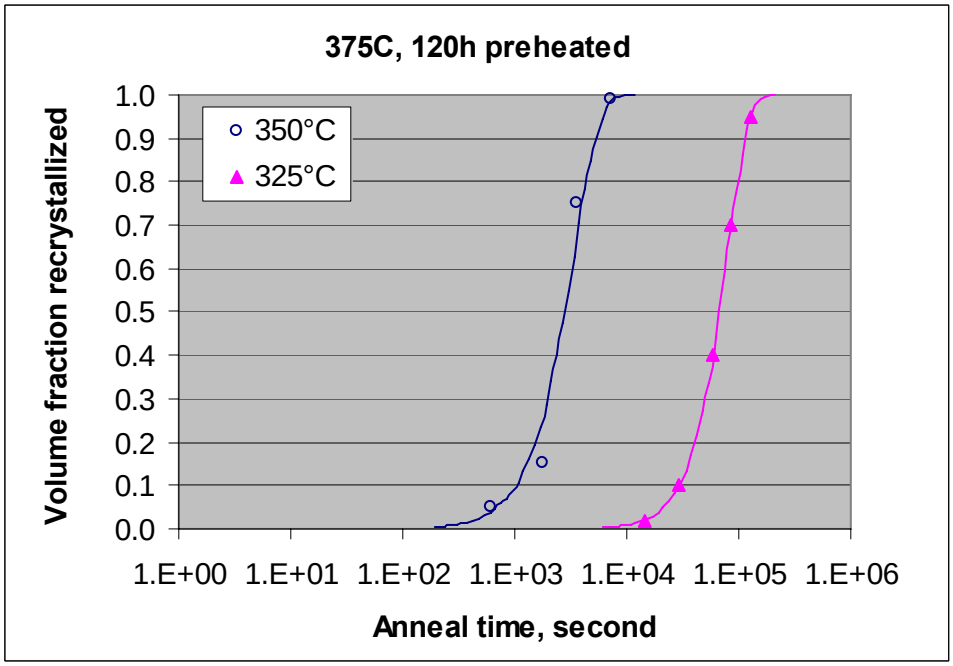

(b)

Figure 1, Recrystallization kinetics for: (a) material A, and (b) material E

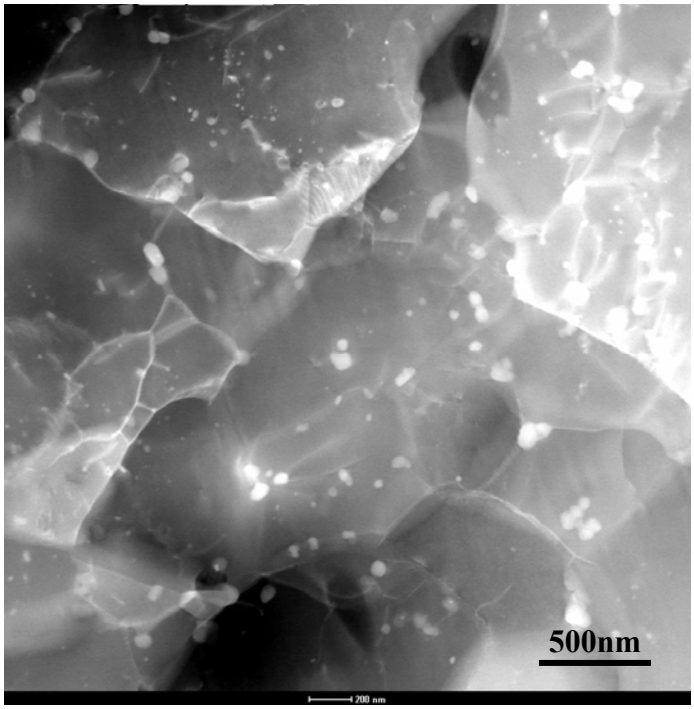

Figure 2, Dark-field STEM image showing subgrain boundaries and dislocations pinned by concurrently forming dispersoids in TRC AA3105.

Figure 3, FEG-SEM backscatter electron image showing second phase particles in material E. Note that precipitates are uniformly dispersed.

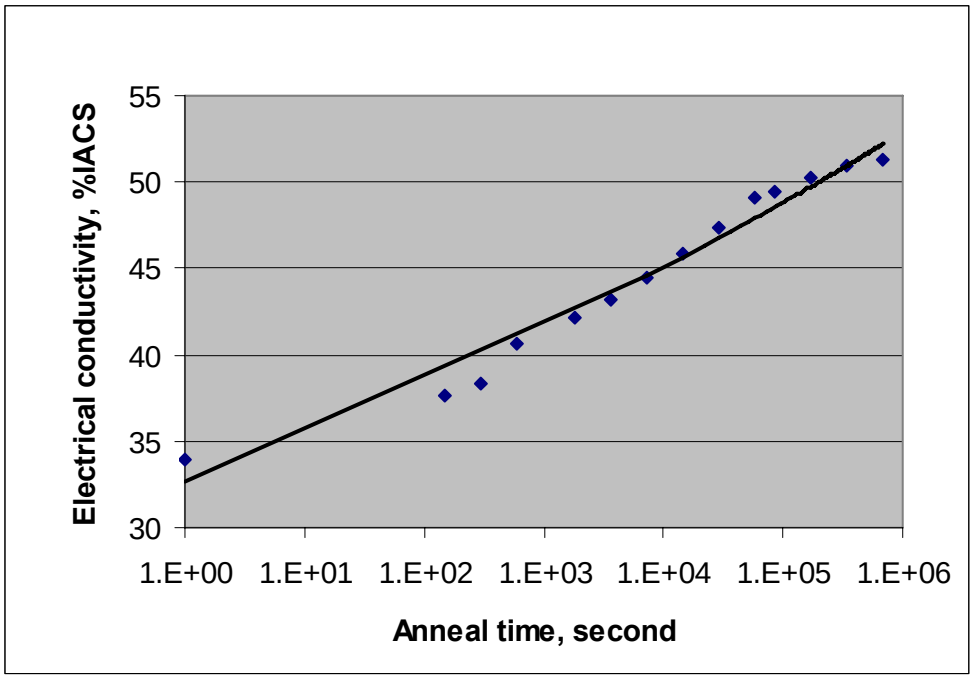

(a)

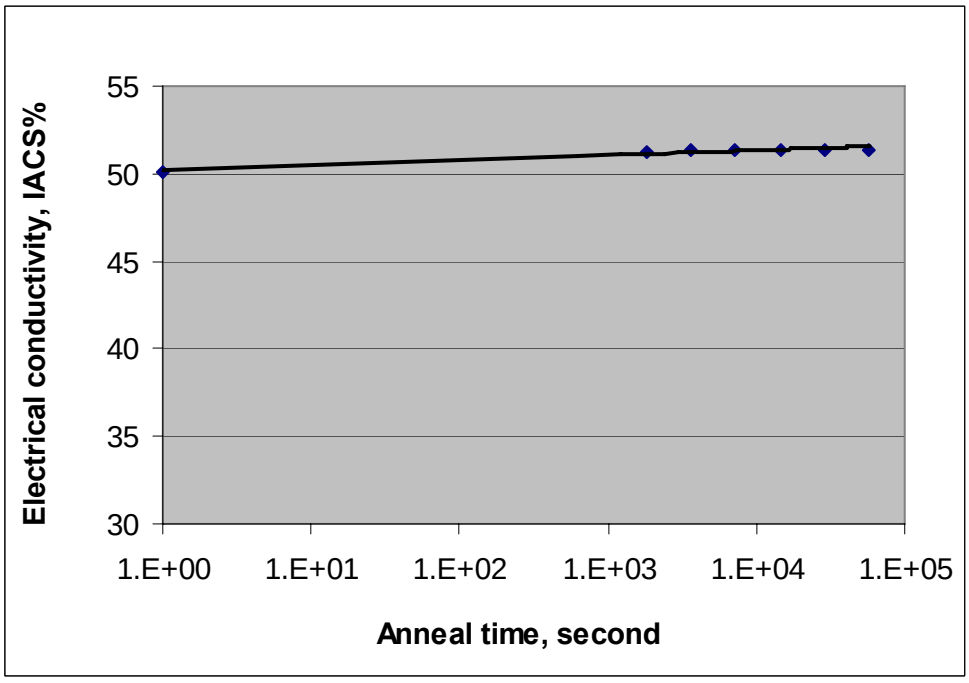

(b)

Figure 4, Electrical conductivity evolution for materials annealed at 375°C: (a) material A, and (b) material E

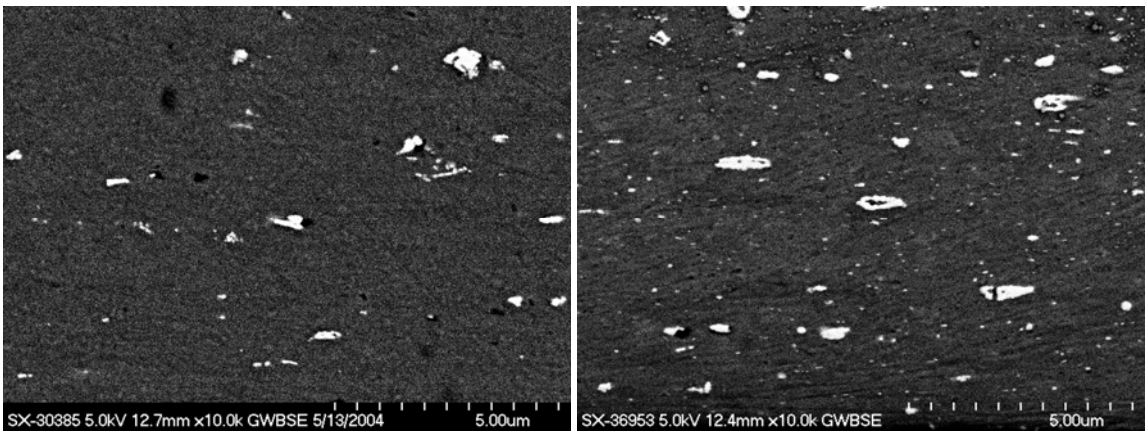

(a) (b)

Figure 5, Backscatter electron images showing second phase particles in as-cold rolled TRC AA3105: (a) material A, and (b) material E

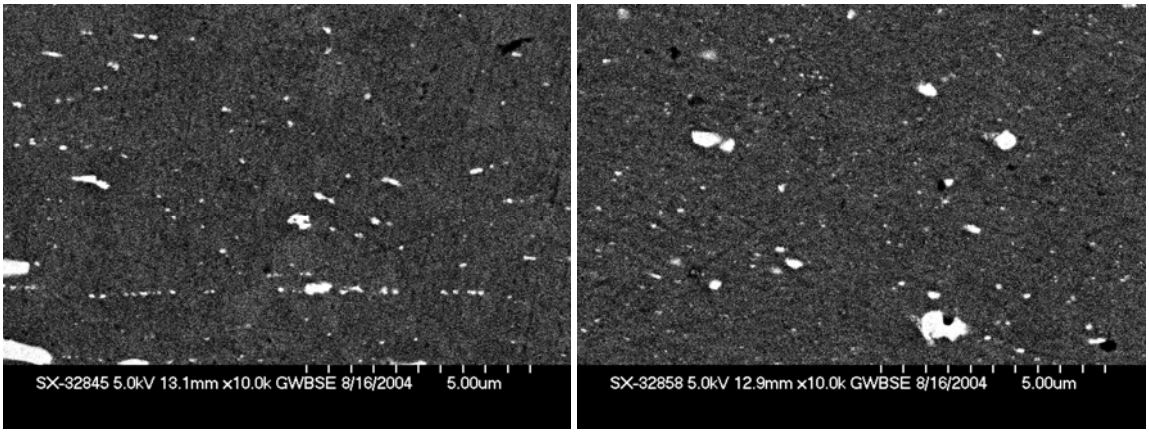

(a) (b)

Figure 6, Backscatter electron micrographs showing second phase particles in TRC AA3105 annealed at 375°C: (a) material A, and (b) material E

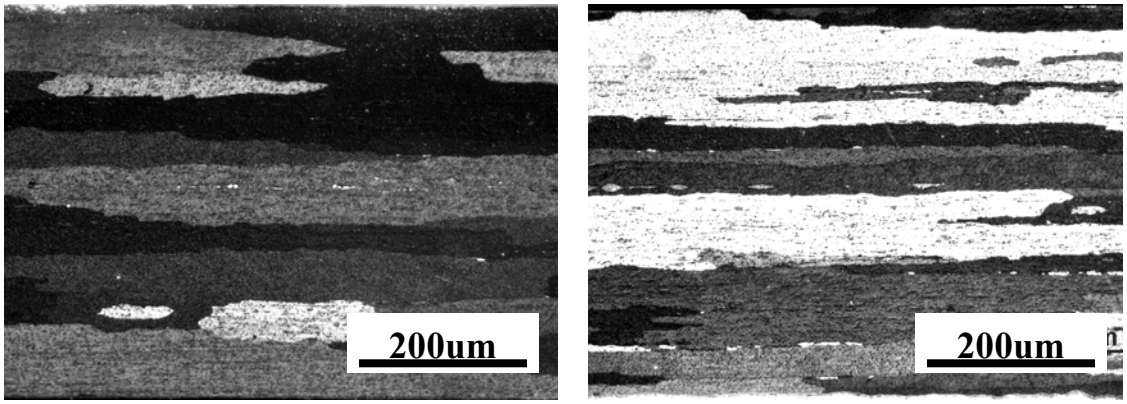

(a) (b)

Figure 7, Optical micrographs showing recrystallized grain structure after annealing at 375°C: (a) material A after 48 hrs, (b) material E after 30min.

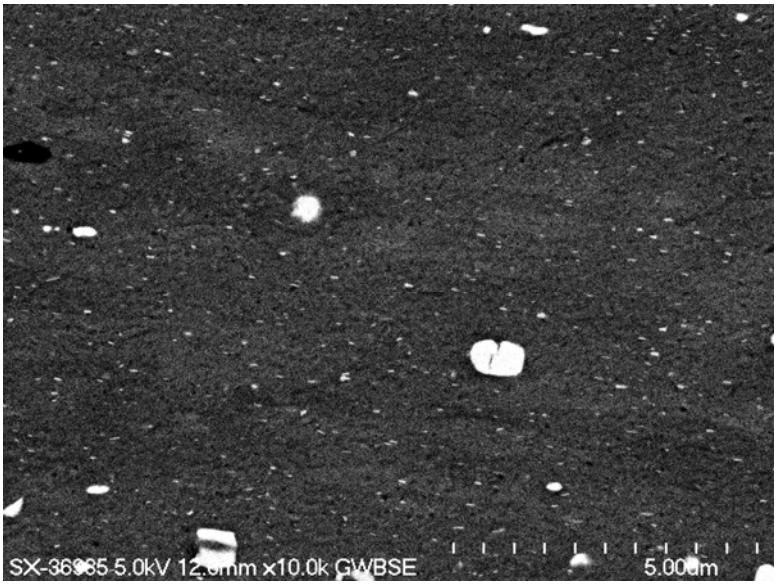
SX-36985 5.0kV 12.6mm x10.0k GWBSE
5.00um

(a)

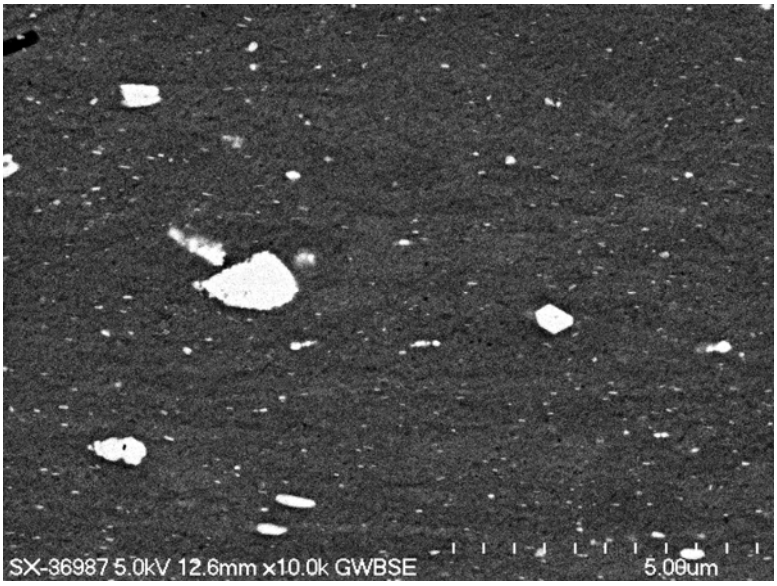
SX-36987 5.0kV 12.6mm x10.0k GWBSE
5.00um

(b)

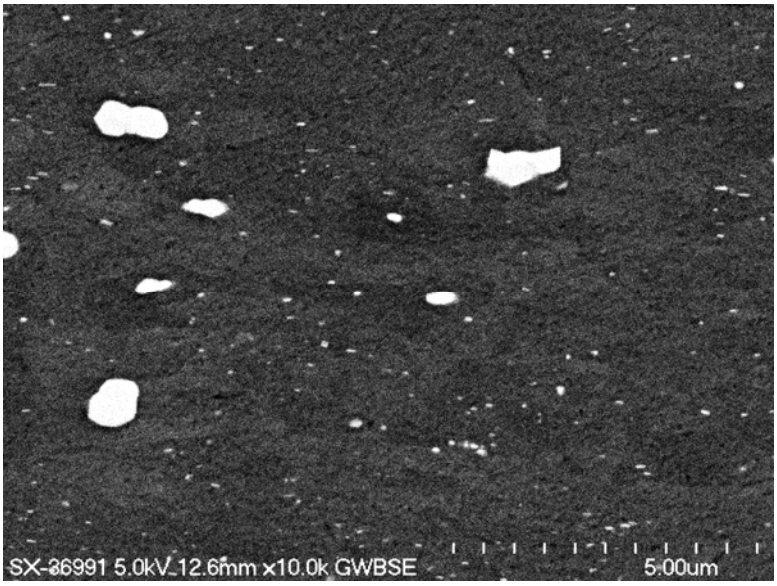

(c)

Figure 8, FEG-SEM backscatter electron micrographs showing second phase particles in as-cold rolled TRC AA3105: (a) material B, (b) material C, and (c) material D

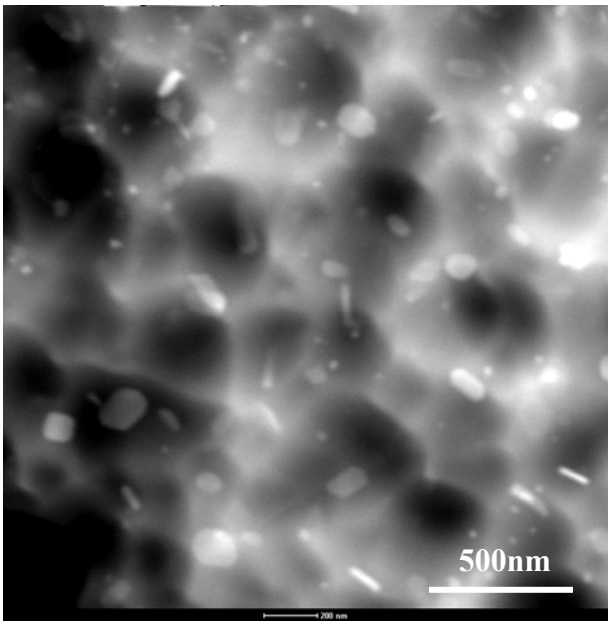

(a)

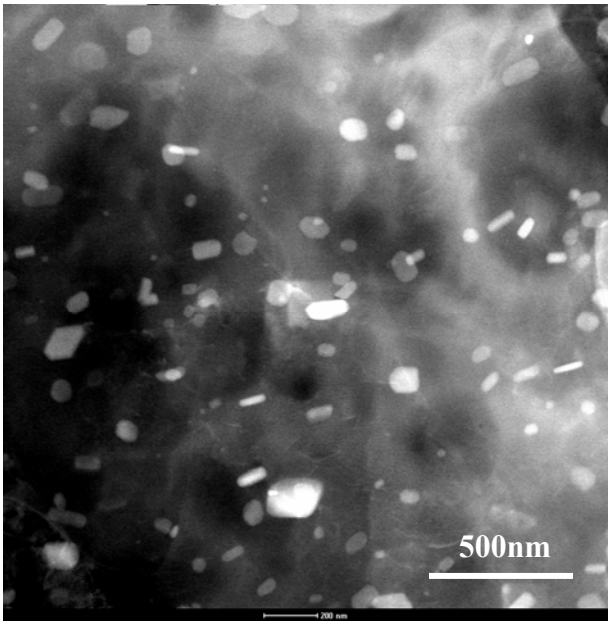

(b)

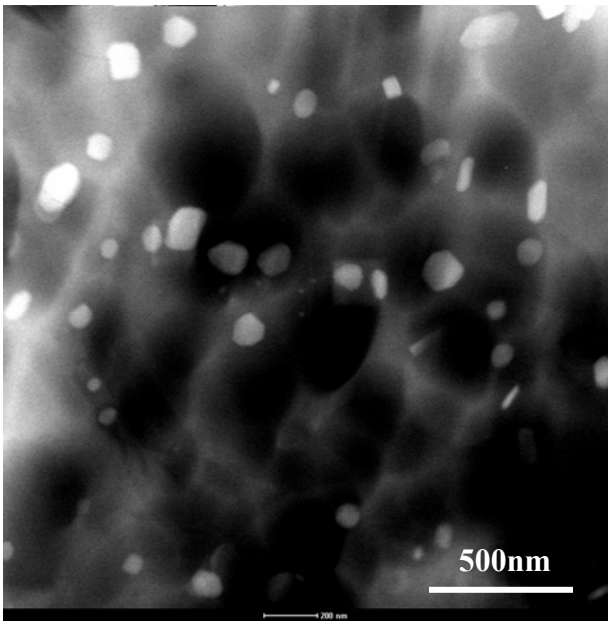

(c)

Figure 9, HAADF STEM micrographs showing second phase particles in as-cold rolled TRC AA3105: (a) material B, (b) material C, and (c) material D

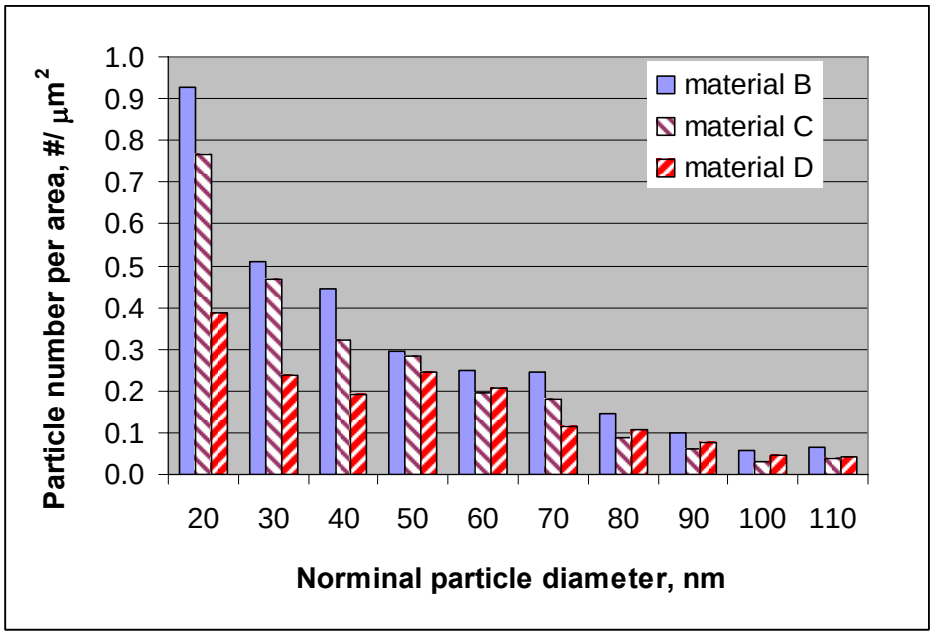

Figure 10, Dispersoids, arbitrarily chosen as particles smaller than approximately $0.01\mu m^2$ in area in Figure 8, number per area for specimens: B, C and D

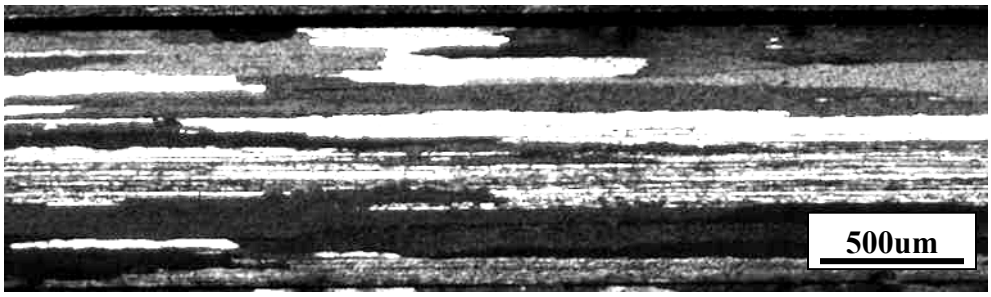

(a)

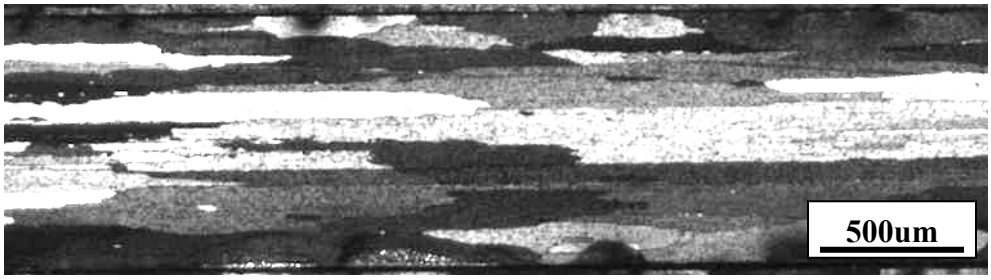

(b)

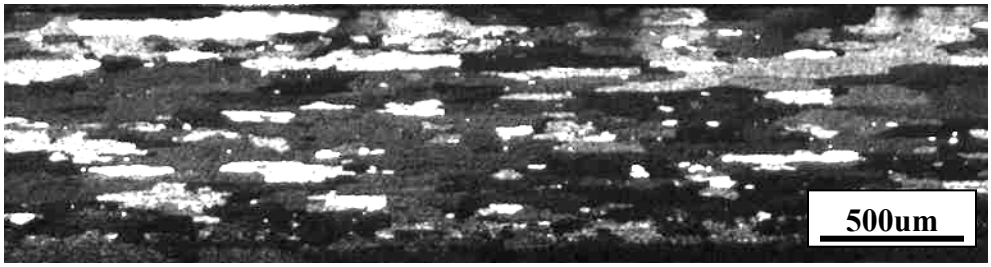

(c)

Figure 11, Optical micrographs showing grain structure in materials annealed at 375°C for 1h: (a) sample B, (b) sample C, and (c) sample D

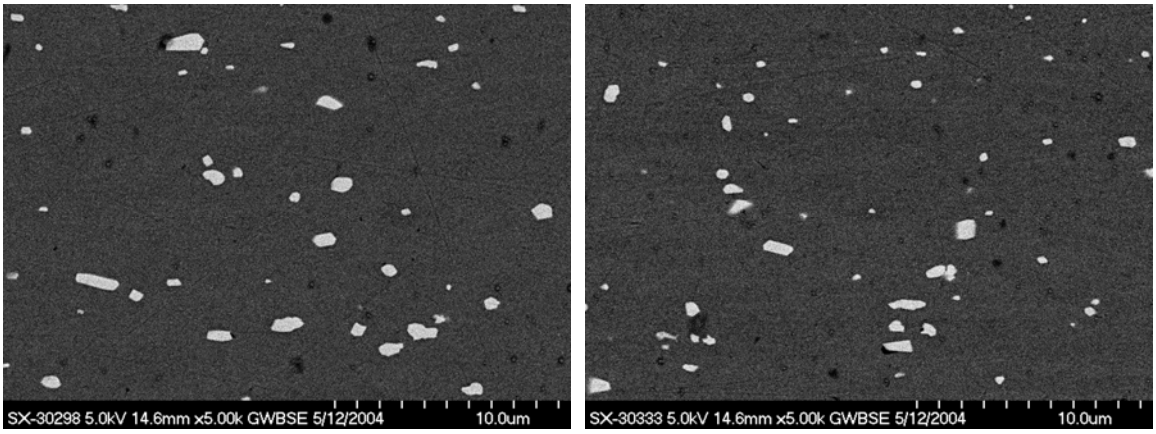

(a) (b)

Figure 12, Backscatter electron micrographs showing second phase particles in TRC AA3105: (a) material F, and (b) material G

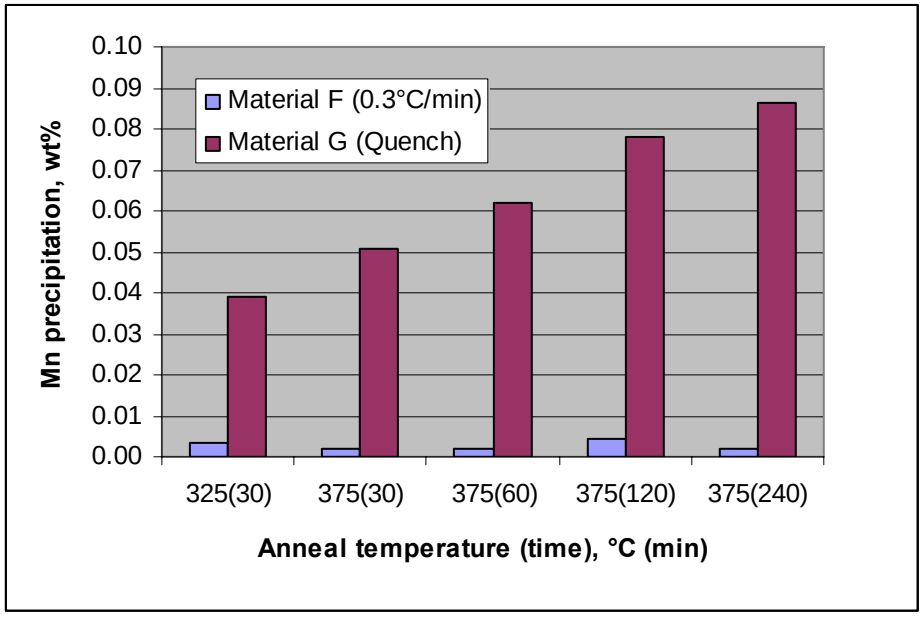

Figure 13, Mn precipitation in material F and G during annealing

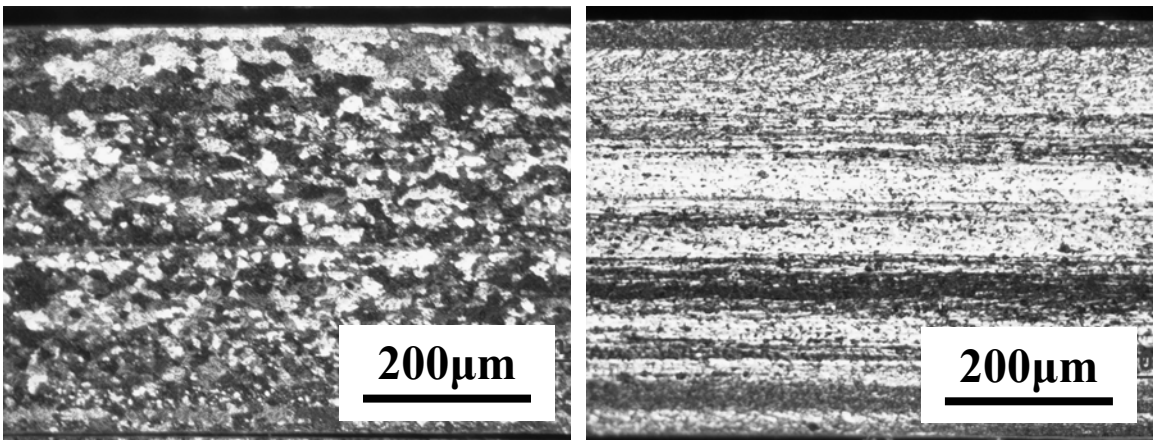

(a) (b)

Figure 14, Optical micrographs showing grain structure in TRC AA3105 annealed at 325°C for 30min: (a) material F, and (b) material G

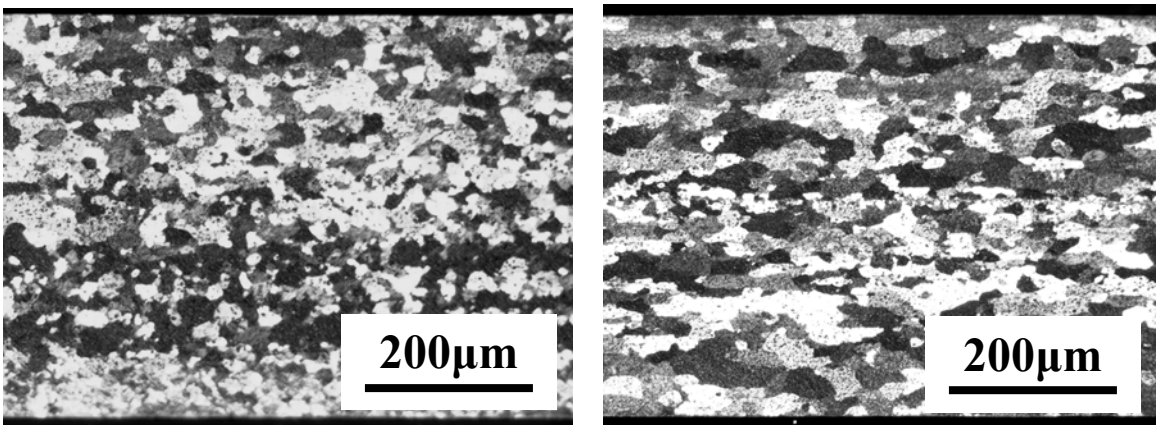

(a) (b)

Figure 15, Optical micrographs showing grain structure in TRC AA3105 annealed at 375°C for 30min: (a) material F, and (b) material G

HEATING RATE EFFECT ON MICROSTRUCTURE EVOLUTION DURING ANNEALING OF TWIN ROLL CAST AA3105

by

NAIYU SUN, BURTON R. PATTERSON, JAAKKO P. SUNI, HASSO WEILAND, PUJA KADOLKAR AND CRAIG BLUE

In preparation for *Materials Science and Engineering A*

Format adapted for dissertation

ABSTRACT

The effect of heating rate on precipitation and recrystallization behavior in twin roll cast (TRC) AA3105 has been investigated using controlled infrared heating. Experimental results show that as-recrystallized grain size decreases as heating rate increases. Time-temperature-transformation (TTT) curves for both precipitation and recrystallization were obtained. At a heating rate of 50°C/s, the material undergoes grain growth after recrystallization at 500°C. No sign of grain growth was observed in materials heated with lower heating rates, 3, 0.5 and 0.01°C/s.

INTRODUCTION

Rapid solidification and cooling during twin roll casting of AA3105 retains manganese supersaturation that precipitates as fine $Al_{12}(Mn,Fe)_3Si$ dispersoids during annealing. These particles inhibit recrystallization by Zener pinning of subgrain boundaries, resulting in a coarse, elongated grain structure [1, 2]. Prior studies have shown that a higher annealing temperature produces a finer recrystallized grain structure [3]. However, the heating rate of material placed in a conventional air furnace at temperature varies with both furnace temperature and time, as shown in Figure 1(a). As a result, in a conventional air furnace, the effect of annealing temperature on recrystallization is combined with the effect of heating rate, i.e., higher furnace temperatures produce higher workpiece heating rates and the two effects on recrystallization are difficult to separate.

Infrared (IR) heating provides an excellent means for investigating the effect of heating rate on precipitation and recrystallization in a material with supersaturated

matrix. The IR furnace employs a high intensity tungsten filament to transfer radiant energy to the part. The extremely high source temperature of the tungsten filament leads to high thermal transfer and extremely fast heating [4, 5]. The low thermal mass of the tungsten filament gives good control of the heat output and process temperature. Full output can be obtained within seconds of applying power. Also, power can be turned off almost immediately at the end of the process. Thus, workpiece heating rate can be well controlled and is independent of temperature, as shown in Figure 1(b).

EXPERIMENTAL

TRC AA3105 was produced by Alcoa, with the chemical composition given in Table 1. The material was cold rolled 90% prior to annealing. The three highest constant heating rates, 50, 3 and 0.5°C/s, were achieved in an electric IR furnace at the ORNL Materials Processing Lab, while the slowest constant heating rate, 0.01°C/s, was obtained with a conventional programmable air furnace. For comparison, some material was also annealed at different temperatures in a conventional air furnace. Optical microscopy was used to examine the recrystallized grain structure. Solute precipitation during annealing was monitored via electrical conductivity measurement.

RESULTS AND DISCUSSION

Figure 2 shows recrystallized grain structure for TRC AA3105 annealed in an air furnace at different temperatures, 500°C and 400°C. Material annealed at 500°C shows finer recrystallized grain structure than at 400°C, as shown in Figures 2 (a) and (b). This apparent effect of recrystallization temperature on grain size is actually a combined effect

of both annealing temperature and heating rate. Dispersoid particles precipitating during heating and at the annealing temperature are known to interact with subgrains that form the nuclei for recrystallization [2, 6-9]. Slower heating allows more dispersoid precipitation on subgrain boundaries, preventing nucleation of recrystallizing grains, resulting in a coarser recrystallized grain size. In Figure 3, a typical Scanning Transmission Electron Microscopy (STEM) image depicts the interaction between precipitates and subgrain boundary at the early stage of recrystallization in TRC AA3105.

Figure 4 shows the TTT diagram determined for TRC AA3105, overlaying the start and finish of recrystallization with the times for different amounts of dispersoids precipitation at different temperatures, the latter determined from electrical conductivity measurements. It is apparent that high heating rates to high temperatures should allow rapid recrystallization prior to formation of nucleation of inhibiting dispersoids, and should result in a fine recrystallized grain size. Also, slower heating rates should allow significant dispersoid precipitation prior to the start of recrystallization, greatly hindering nucleation and resulting in a much coarser grain size. The following study was designed to explore this predicted effect of heating rate on recrystallized grain size.

The rapid, controlled heating rate of the IR furnace enables separation of the effects of heating rate and annealing temperature on recrystallization. Figure 5 shows as-recrystallized grain structure, i.e., prior to any grain growth, for materials annealed with different IR heating rates. It is apparent that, the average recrystallized grain size increases as the heating rate decreases. For the fastest heating rate, 50°C/s, the material was heated up to target temperature within approximately 10 seconds from room temperature. As a result, very little manganese precipitation occurred, less than 0.05 wt%,

as shown in Figure 4. As heating rate decreases, materials require a longer heating time to temperature, resulting in greater precipitation. As it is widely accepted that precipitates tend to pin subgrain boundaries and inhibit nucleation process during recrystallization, as shown in Figure 3. Thus, material with fewer precipitates can form more nuclei during recrystallization, and obtain a finer recrystallized grain structure.

Figure 6 shows material annealed at 500°C with a 50°C/s heating rate. It is apparent that the material underwent grain growth after holding at temperature for a short period of time, from 5 seconds to 5 minutes. However, grain growth was not observed in material annealed at the lower heating rates, 3, 0.5 and 0.01°C/s. This observation suggests that the grain growth at 500°C may due to the absence of precipitates during recrystallization in the most rapidly heated material. At lower heating rates, the material had more time to precipitate a large amount of dispersoids that pin the grain boundaries. As a result, the as-recrystallized grain structure is stable in material annealed with the slower heating rates, as shown in Figure 7.

CONCLUSION

The following conclusions can be drawn from this study on TRC AA3105:

1. For conventional air furnace, annealing at a higher temperature results in a finer recrystallized grain structure.
2. Higher anneal heating rate results in a finer recrystallized grain structure.
3. Grain growth is observed after recrystallization at 500°C with the fastest 50°C/s heating.

4. No grain growth is found in material annealed at the slower heating rates, 3, 0.5 and 0.01°C/s.

ACKNOWLEDGMENTS

The authors gratefully acknowledge research funding by Department of Energy grant no. DE-FC36-02ID14401 and the support from the Assistant Secretary for Energy Efficiency and Renewable Energy, Office of Industrial Technologies, Advanced Industrial Materials Program, under contract DE-AC05-00OR22725 with UT-Battelle, LLC.

REFERENCES

[1] N. Sun, B. R. Patterson, J. P. Suni, E. A. Simielli, H. Weiland and L. F. Allard, TMS Letters 2 (2005) 33-34

[2] N. Sun, B. R. Patterson, J. P. Suni, E. A. Simielli, H. Weiland and L. F. Allard, Materials Science and Engineering A 416 (2006) 232-239

[3] B. R. Patterson, N. Sun, J. P. Suni, E. A. Simielli, H. Weiland and L. F. Allard, TMS Letters 8 (2004) 173-174

[4] Craig A. Blue, Vinod K. Sikka, Randall A. Blue and Ray Y. Lin, Metallurgical and Materials Transactions A 27 (1996) 1-8

[5] C. A. Blue, V. K. Sikka, E. K. Ohriner, P. G. Engleman and D. C. Harper, JOM-e 52 (2000)

[6] R. D. Doherty and J. W. Martin, Journal of the Institute of Metals 91 (1962) 332-338

[7] Erik Nes, Acta Metallurgica 24 (1976) 391-398

[8] F. J. Humphreys and M. Hatherly, Recrystallization and Related Annealing Phenomena, First ed., Pergamon, Oxford, 1995

[9] P. R. Mould and P. Cotterill, Journal of Materials Science 2 (1967) 241-255

Table 1, Chemical Composition of TRC AA3105

Element	Mn	Mg	Fe	Si	Cu
Wt %	0.59	0.44	0.55	0.28	0.04

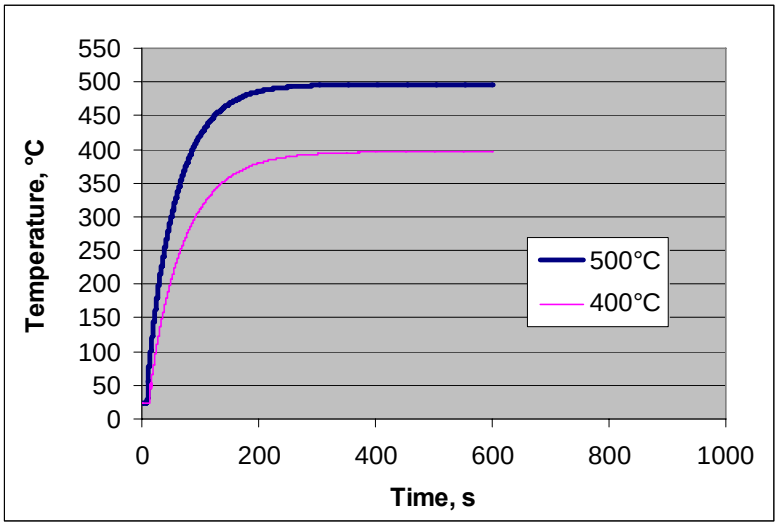

(a)

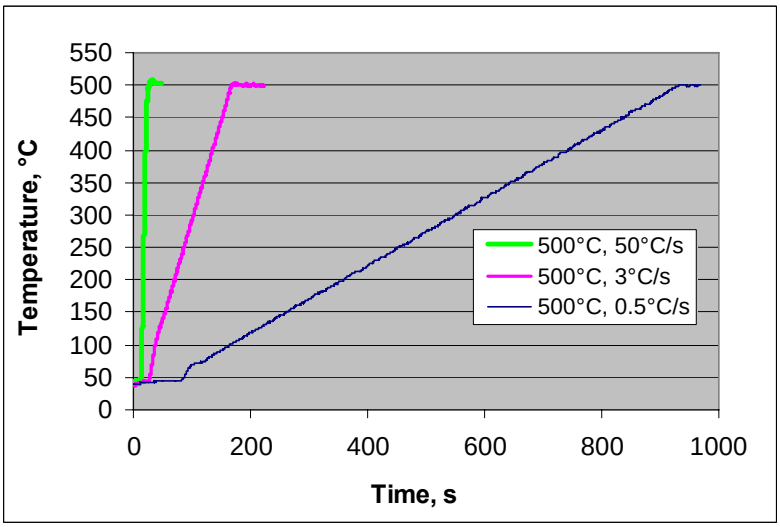

(b)

Figure 1, Heating curves for TRC AA3105: (a) conventional air furnace, (b) IR furnace

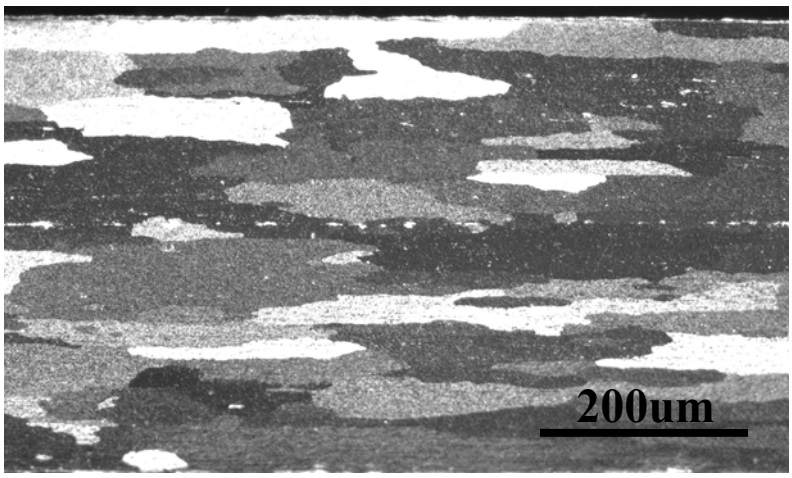

(a)

(b)

Figure 2, As-recrystallized grain structure for material annealed in an air furnace at different temperatures: (a) 500°C, and (b) 400°C

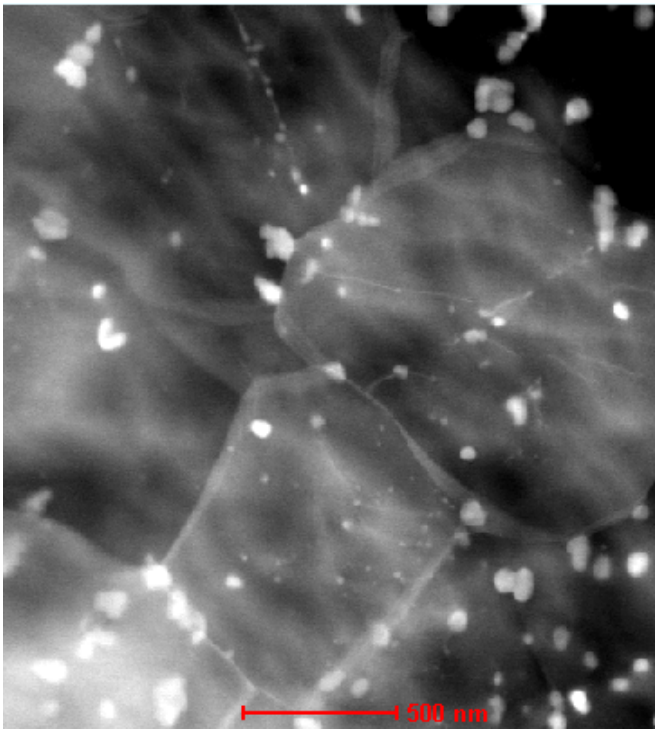

Figure 3, STEM HAADF image of early recrystallization in TRC AA3105

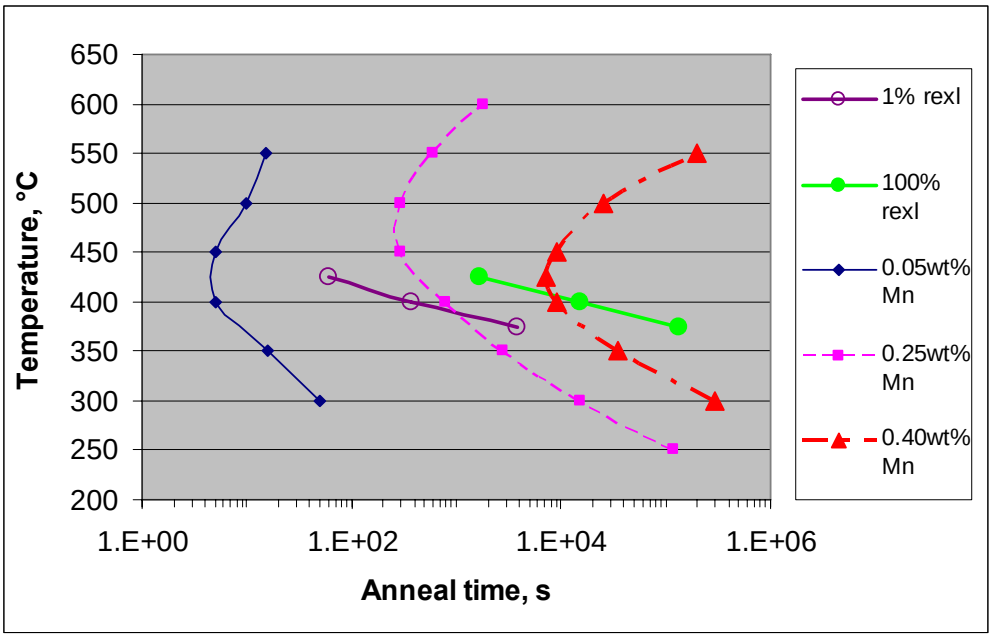

Figure 4, Recrystallization and precipitation TTT curves for TRC AA3105

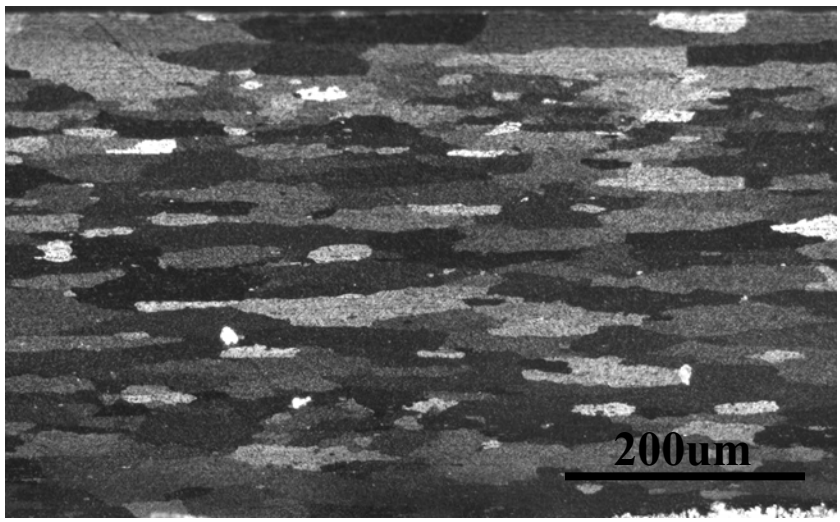

(a)

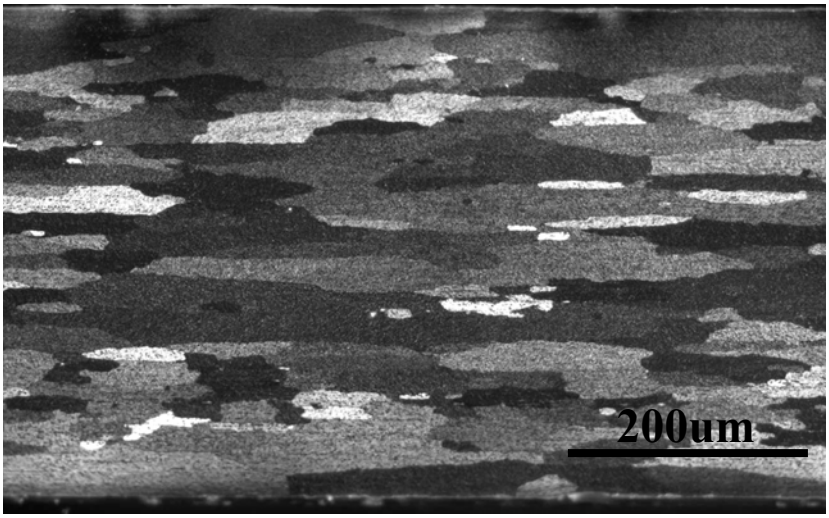

(b)

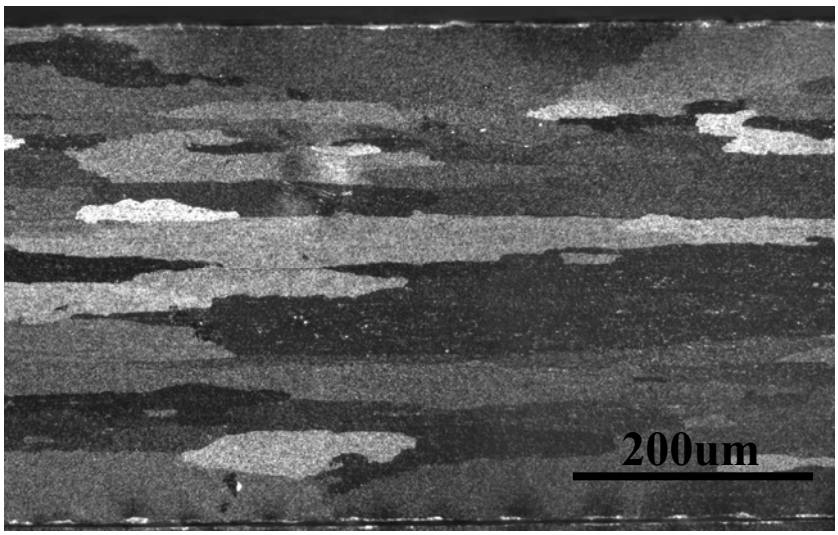

(c)

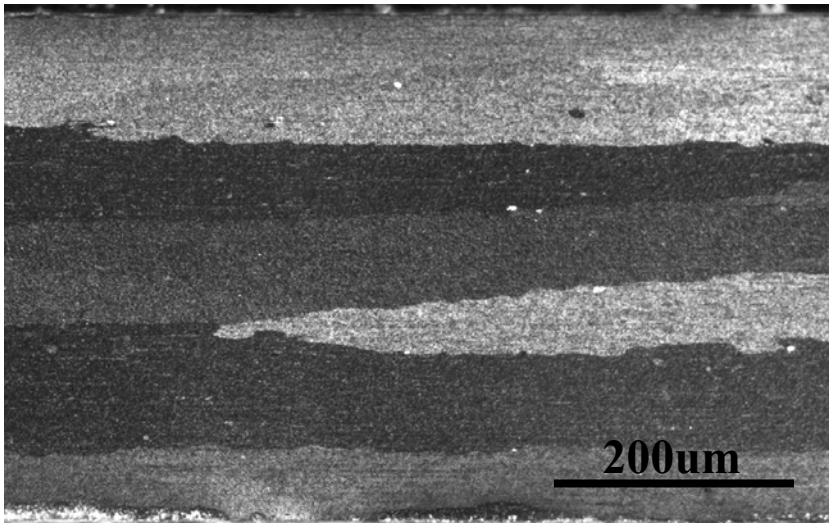

(d)

Figure 5, As-recrystallized grain structure for materials annealed at 500°C with different heating rates: (a) 50, (b) 3, (c) 0.5, and (d) 0.01°C/s

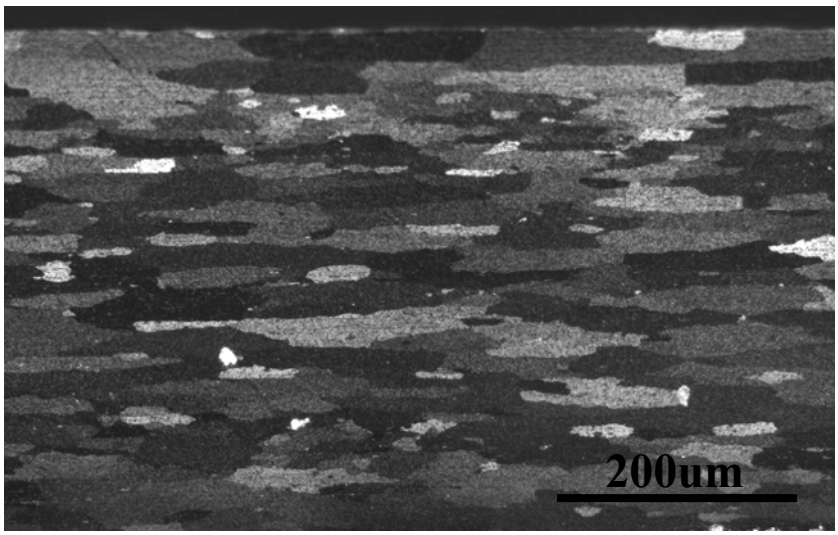

(a)

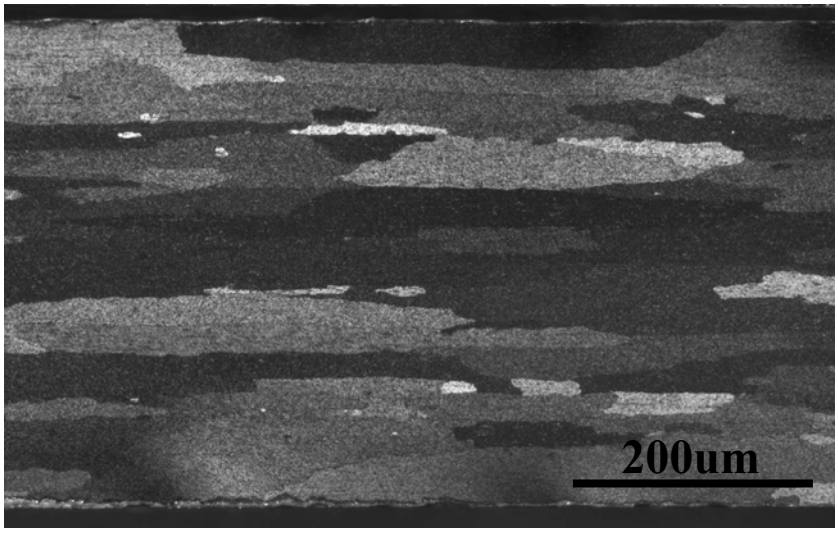

(b)

Figure 6, Grain structure in TRC AA3105 annealed at 500°C with 50°C/s heating rate:

(a) 5s hold at temperature, and (b) 5min at temperature

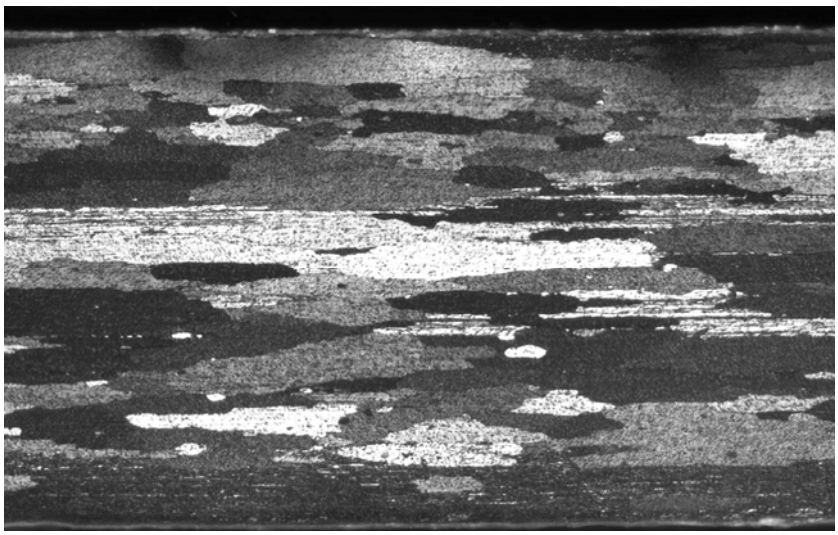

(a)

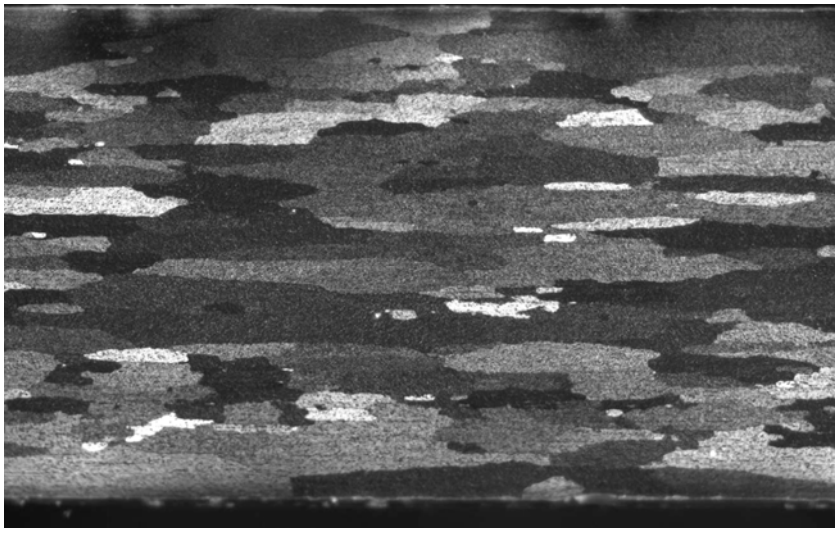

(b)

Figure 7, Grain structure in TRC AA3105 annealed at 500°C with 3°C/s heating rate: (a) 5s hold at temperature, and (b) 5minute at temperature. Note: material has not fully recrystallized yet after 5 seconds

CHARACTERIZATION OF PARTICLE PINNING POTENTIAL

by

NAIYU SUN, BURTON R. PATTERSON, JAAKKO P. SUNI, HASSO WEILAND,
AND LAWRENCE F. ALLARD

Accepted for publication by *Acta Materialia*

Format adapted for dissertation

ABSTRACT

Five methods for characterizing second phase particle pinning potential in twin roll cast AA 3105 have been evaluated experimentally and analytically. A stereological expression, $\frac{S_v}{4}$, has been demonstrated as a robust means for characterizing the degree of particle pinning in real material systems with neither the assumption of particle shape nor size distribution and without the experimental difficulty of unfolding the size distribution.

INTRODUCTION

The grain growth behavior of particle-containing materials is dependent on the volume fraction, size, shape and spatial distribution of second phase particles. Many models, beginning with Zener [1], have been developed to describe these effects on grain growth inhibition [2-20]. Although these models differ in various aspects, essentially all contain the ratio of the particle volume fraction, *f*, to some measure of particle size, typically radius, *r*. This well-known ratio $\frac{f}{r}$, often referred to as *Z*, the Zener pinning factor, results from a variety of descriptions of restraining pressure or energy dissipated during grain boundary motion and includes the computation of the number of particles interacting with the boundary.

The fact that most models of grain growth inhibition are based on the assumption of monosized spherical particles of radius *r* presents a problem with model testing due to the unrealistic nature of the assumption. Not only are particles often non-spherical but the presence of a size distribution leads to ambiguity of *which* size parameter to employ.

Different characterization methods measure different averages of the mean size, such as by number or volume weighting. The relative ease of some measurements may favor those that are not necessarily the most appropriate. Difficult and time consuming methods that appear theoretically sound may be employed when easier measurements give equivalent results.

Based on an energy model of describing particle pinning in grain growth, Rios [18] first introduced a stereological parameter, S_V, the surface area of particles per unit volume, to characterize the energy dissipated when a grain boundary moves across particles. Liu and Patterson later employed this parameter in their study [12] of grain growth inhibition by porosity. More recently, Rios and Fonseca developed this idea further by relating S_V to grain boundary curvature and validated their models in a high purity Al-1wt%Mn alloy [19, 20]. From the fundamental stereological relationships [21],

$$\bar{\lambda} = \frac{4f}{S_V} \quad (1)$$

It is clear that S_V has similar properties as $\frac{f}{r}$ in that it includes the ratio of volume fraction to a length scale, $\bar{\lambda}$, which is the mean linear intercept of second phase. To compare the different approaches for determining *Z*, it is necessary to use a single basic definition, Eq.(2), consisting of the simplest core common to all such models - the ratio of particle volume fraction to a length scale, the shape independent $\bar{\lambda}$.

$$Z = \frac{f}{\bar{\lambda}} \quad (2)$$

Use of the common format of Eq.(2) enables fundamental comparison of the different measures without confounding effects from other constants or components of the

different models. Understanding the differences in this component of the pinning force gives a better understanding of the biases present in the different methods.

This study will compare values of *Z* computed from S_V with four other more common approaches employing *f* and *r*, experimentally and analytically. It will be shown that the different experimental methods for obtaining *Z* result in different *averages* of the particle size that are not necessarily apparent from the measurement. The various measures and their expressions for *Z* will then be analyzed with respect to these differences.

EXPERIMENTAL

Twin roll cast (TRC) aluminum alloy AA3105 was employed for the measurements of Zener pinning factor in this study. The composition of this material, provided by Alcoa, is given in Table 1. This alloy contains aluminum-manganese constituent particles that are typically much finer near the rapidly solidified surface than in the interior, and that coarsen during homogenization or high temperature annealing. These particles impart considerable influence on recrystallization and grain growth and this material has been the subject of extensive studies of the effects of homogenization, annealing temperature and heating rate on recrystallization, and the transition between the pinned state and normal and abnormal grain growth [22-25].

The experimental material was roll cast as 5mm thick sheet and given different thermo-mechanical treatments for recrystallization and grain growth. Homogenization treatments, given to some specimens prior to rolling, involved ten cycles between 450 and 620°C with 5h holds at each temperature and 0.3°C/min cooling from the higher to

lower temperature [26]. Both as-cast and homogenized materials were cold rolled to 90% reduction and annealed for 19 different temperature/time combinations, ranging from 550 to 640 °C and 5min to 3 weeks. The variety of thermal treatments provided a wide range of particle structures for evaluating the different measures of the Zener pinning factor. Specimens for microstructural examination were prepared on the longitudinal cross section, parallel to the normal (ND) and rolling directions (RD).

Figures 1 and 2 show typical variations in particle size and morphology among different locations and materials. Figures 1 (a) and (b) show the typically finer particle structure at strip surface than in the center that often leads to gradients in recrystallized grain size and strong pinning during grain growth. Figures 2(a) shows still coarser constituent typically present after annealing at higher temperature. Figures 2(b) shows the coarsest constituent particles that result from the extensive homogenization treatment. The volume fraction of constituent particles resulting from the variety of heat treatments varied from approximately 1.0% to 2.0% among the specimens, as shown in Table 2.

Considerable particle characterization, including volume fraction, length of particle boundary, and distribution of 2D particle section area, was performed by automated image analysis on field-emission SEM images taken at 2,000X magnification. A very low accelerating voltage, 5 kV, was employed to minimize the electron-specimen interaction volume effect. Measurements were performed, at six randomly selected locations along the strip length, in both the surface and interior regions of the strip cross section respectively. Measurements typically included a total of 250 to 1500 particle sections from the six fields. The relative errors associated with the measurements in this

study were evaluated by the coefficient of variation of the measurements, which ranged from 0.03 to 0.09, typically 0.06.

Five different approaches, described below, were used to experimentally determine the particle pinning potential in the above specimens. Analytical descriptions for the five methods, illustrating the effect of the particle size distribution width on the measured *Z* values, are also presented for comparison. It should be noted that the methods described in this paper are general and apply to any material with second phase particles.

COMPUTATION OF PARTICLE PINNING POTENTIAL, *Z*

1. Monosized Sphere Assumption

The simplest, although unrealistic, assumption of particle structure is that of monosized spheres. For this case, Fullman [27] developed stereological relationships between the 3D particle radius, *r*, and the mean linear intercept, $\overline{\lambda}$, and mean particle section area, $\overline{A}$:

$$\overline{\lambda} = \frac{4}{3} r \quad (3)$$

$$\overline{A} = \frac{2}{3} \pi r^2 \quad (4)$$

Combining Eqs. (2)-(4) yields the particle pinning potential for the monosized sphere assumption, Z_m, in terms of $\overline{A}$, the number weighted mean section area:

$$Z_m = \frac{3f}{\sqrt{(\frac{24}{\pi})\overline{A}}} \quad (5)$$

This approach computes the pinning potential equivalent to Eq.(2), with the assumption that the relationship between the mean section area and the mean intercept is

that for monosized spheres, which is often not the case in real materials. Table 2 tabulates values of Z_m measured for the matrix of specimens. Figure 4 compares these values with those computed by the other four methods.

To understand the relationship between this measure of *Z* and others it is necessary to re-express Z_m in terms of particle, rather than section size. Also, since there is generally a distribution of particle sizes in real materials, it is useful to examine the effect of width of the particle size distribution on the experimentally measured Zener pinning factor. In the following analysis, Z_m is then re-formulated using the coefficient of variation (CV) of the distribution of particle radii.

From Eq.(4), the average section area from particles of the i^{th} 3D particle size class given by:

$$\overline{A}_i = \frac{2}{3}\pi r_i^2 \quad (6)$$

The average section area contributed from all particle classes is:

$$\overline{A} = \sum_i \left[(\overline{A}_i) \cdot \left(\frac{(N_A)_i}{N_A} \right) \right] \quad (7)$$

where $(N_A)_i$ is the number of sections from the i^{th} particle class per unit area of examination plane, and is related to the number of particles per unit volume, $(N_V)_i$, and their size, r_i. In turn, $(N_V)_i$ can be expressed as the ratio of the volume fraction of particles in the i^{th} class to their individual volumes, V_i:

$$(N_A)_i = 2r_i (N_V)_i = 2r_i \left(\frac{f_i}{V_i} \right) = \frac{2r_i f_i}{4\pi r_i^3 / 3} = \frac{3 f_i}{2\pi r_i^2} \quad (8)$$

Combining Eqs.(6)-(8) yields the expression for the mean section area in terms of particle radii:

$$\overline{A} = \frac{2\pi}{3}\left[\frac{f}{\sum_i (f_i / r_i^2)}\right] = \frac{2\pi}{3}\left[\frac{1}{\overline{(r^{-2})}_v}\right] \quad (9)$$

where $\overline{(r^{-2})}_v$ is the volume weighted average of the *inverse square* of 3D particle size, defined as:

$$\overline{(r^{-2})}_v = \frac{\sum_i (f_i / r_i^2)}{f} \quad (10)$$

Inserting Eq. (9) for $\overline{A}$ into Eq. (5) yields:

$$Z_m = \left(\frac{3f}{4}\right)\overline{(r^{-2})}_v^{1/2} \quad (11)$$

Expressing S_V and f in terms of moments of the distribution:

$$S_V = N_V \cdot (4\pi\mu_2^n) \quad (12)$$

$$f = N_V \cdot (\frac{4}{3}\pi\mu_3^n) \quad (13)$$

yields:

$$f = \left(\frac{S_V}{3}\right)\left(\frac{\mu_3^n}{\mu_2^n}\right) \quad (14)$$

Where, μ_2^n and μ_3^n are the second and third number weighted moments of the particle radius, about the origin. Inserting Eq. (14) into Eq. (11) and re-writing $\overline{(r^{-2})}_v$ as the moment μ_{-2}^v yields:

$$Z_m = \left(\frac{S_V}{4}\right)\left(\frac{\mu_3^n}{\mu_2^n}\right)\left(\mu_{-2}^v\right)^{1/2} \quad (15)$$

Where, μ_{-2}^v is the volume weighted second moment of the inverse particle size, about the origin.

The following Eqs. (16) – (19) give the basic relationships for the moments of the lognormal distribution [28, 29]:

$$\mu_k^n = \exp[k \cdot \overline{(\ln D)}_n + \frac{k^2}{2}(\ln^2 \sigma_D)] \quad (16)$$

$$\mu_k^v = \exp[k \cdot \overline{(\ln D)}_v + \frac{k^2}{2}(\ln^2 \sigma_D)] \quad (17)$$

$$CV^2 + 1 = \exp(\ln^2 \sigma_D) \quad (18)$$

$$\overline{(\ln D)}_v = \overline{(\ln D)}_n + 3\ln^2 \sigma_D \quad (19)$$

where, μ_k^n and μ_k^v are the k[th] number weighted and volume weighted moments of the particle size about the origin, $\overline{(\ln D)}_n$ and $\overline{(\ln D)}_v$ are the number and volume weighted geometric means of the particle diameters, and $\ln \sigma_D$ is the geometric standard deviation of the particle diameters. Employing Eqs. (16) - (19) with Eq. (15) yields:

$$Z_m = \left(\frac{S_V}{4}\right)\left(CV^2 + 1\right)^{1/2} \quad (20)$$

In Equation (20), Z_m consists of two components, a stereological core, $\frac{S_V}{4}$, which will be shown to be the unbiased Zener pinning potential, and a particle size distribution term, $\left(CV^2 + 1\right)^{1/2}$, that biases the experimental measurement to higher apparent values. As will be shown below, the analytical formulae of all the five methods for computing Z

contain the same fundamentally correct core, but some measures also contain these variations of the size distribution term that bias them above or below the actual pinning potential. Here, for the case of monosized particles, CV=0 and the size distribution term is unity, leaving Z_m equal to the basic term, $\frac{S_V}{4}$. Wider distributions with CV>0 have size distribution terms greater than unity, with larger computed values of Z_m. A compilation of all of the analytical *Z* expressions is shown in Table 3.

2. Unfolding 3D Size Distribution

Several approaches for computing the pinning factor involve determining the 3D particle size distribution from measurements on the 2D plane. Unfolding methods, requiring measurement of particle section size distribution and assumption of constant geometric shape, can be experimentally difficult and prone to error, especially with micron or submicron sized particles. The obtained size distribution information can be incorporated into *Z* by either (a) directly inserting number or volume weighted average values of *r*, or (b) summing values of Z_i, obtained from r_i and the computed f_i for each size class, over all classes. The appropriateness of the former method depends on the weighting of the average particle size. The latter method is a logical extension of the basic Zener derivation. With the assumption of constant geometric shape, in this case spherical particles, the summation method is analytically equivalent to the stereological approach, $\frac{S_V}{4}$, which relies upon no assumptions in computing the Zener pinning potential, as will be shown below.

Other methods for estimating *r* include the number or volume weighted mean particle volume, which can be obtained without unfolding and independent of shape [30, 31]. Assuming spherical particles enables computation of radii of these mean volumes. Obtaining the number weighted mean volume requires serial sectioning [32], potentially difficult for fine particles. Obtaining volume weighted mean volume requires selected 2D chord measurements and is more feasible, but again, would be difficult with the usual case of fine particles. These experimental methods have not been included in this study.

2.1 Unfolding method

For the Schwartz-Saltykov method used here, the distribution of section areas obtained by image analysis was converted to equivalent section diameters, classified into ten size groups and unfolded to the distribution of 3D diameters using Eq.(21):

$$N_V(j) = \frac{\alpha(i)N_A(i) - \alpha(i+1)N_A(i+1) - \alpha(i+2)N_A(i+2) - \cdots - \alpha(k)N_A(k)}{\Delta} \quad (21)$$

where $N_V(j)$ *and* $N_A(i)$ are the number of 3D particles per unit volume and number of 2D sections per unit area, respectively, in size classes *i* and *j*, which vary from 1 to *k*, the total number of classes, Δ is defined as the ratio of the maximum diameter $D_{\max}$ to the number of size classes. The values of the coefficients α (*i*), α (*i*+1), ..., α (*k*) have been tabulated by Saltykov [21].

Figure 3 illustrates 3D particle size distributions computed by this technique, demonstrating the wide range in particle size in both the surface and center regions of rolled AA3105 strip annealed at 630°C for 12h.

2.2 Number weighted average radius

The most simple use of the unfolded 3D particle size distribution involves computation of the average particle radius, specifically the number weighted mean radius, $\bar{r}_n$:

$$\bar{r}_n = \sum_{i=1} \left[r_i \cdot \left(\frac{(N_V)_i}{N_V} \right) \right] \quad (22)$$

where the number per volume ratio is the number frequency of 3D particles in the i^{th} size class. The equivalent particle pinning potential is then obtained from Eqs.(2) and (3), as Z_n , indicating that this Z is weighted by number fraction of particles:

$$Z_n = \frac{3f}{4\bar{r}_n} = \left(\frac{3f}{4} \right) (\bar{r}_n)^{-1} \quad (23)$$

Use of the number weighted mean radius in Z_n biases the averaged r towards relatively smaller values, resulting in a relatively larger computed pinning factor than with Z_m. The experimental values for Z_n are, in fact, markedly higher than those from any of the other methods, as predicted. The values of Z_n determined from the experimental materials with a wide range of coarsened sizes are listed in Table 2 and included in the comparison plots of Fig. 4.

The effect of the particle size distribution on Z_n , can be determined by inserting Eq. (14) into (23) and substituting the first number weighted moment of particle radius about the origin, μ_1^n , for $\bar{r}_n$:

$$Z_n = \left(\frac{S_V}{4} \right) \left(\frac{\mu_3^n}{\mu_2^n} \right) (\mu_1^n)^{-1} \quad (24)$$

Again, restating these distribution terms using relationships for the moments of the lognormal distribution, Eqs. (16) and (18), one obtains:

$$Z_n = \left(\frac{S_V}{4}\right)\left(CV^2 + 1\right)^2 \quad (25)$$

Comparing this expression to Eq. (20) it is apparent that both are of the same form except for the size distribution term. Here, the distribution term is again unity for monosized particles and increases with increasing distribution width, biasing Z_n to higher values than the fundamental term, $\frac{S_V}{4}$.

2.3 Volume weighted average radius

Alternate to the above number weighted particle size, the *volume* weighted mean particle radius, $\bar{r}_v$, can also be determined from the unfolded 3D size distribution:

$$\bar{r}_v = \sum_{i=1}\left[r_i \cdot \left(\frac{f_i}{f}\right)\right] \quad (26)$$

where the volume fraction ratio is the volume frequency of 3D particles in the i^{th} size class. The pinning potential is then obtained from Eqs.(2) and (3), as Z_v, indicating the weighting by particle volume:

$$Z_v = \frac{3f}{4\bar{r}_v} = \left(\frac{3f}{4}\right)\left(\bar{r}_v\right)^{-1} \quad (27)$$

The volume weighting biases the averaged *r* towards larger sizes, resulting in a relatively smaller computed pinning factor than with Z_m or Z_n. The values of Z_v determined from the specimens are given in Table 2 and plotted in Fig. 4. The experimental values for Z_v are, in fact, markedly smaller than those from any of the other methods, as predicted.

Inserting Eq.(14) into (27) and substituting μ_1^v for $\bar{r}_v$ yields:

$$Z_v = \left(\frac{S_V}{4}\right)\left(\frac{\mu_3^n}{\mu_2^n}\right)\left(\mu_1^v\right)^{-1} \quad (28)$$

Employing Eqs. (16) - (19) with Eq. (28) yields:

$$Z_v = \left(\frac{S_V}{4}\right)\left(CV^2+1\right)^{-1} \quad (29)$$

This expression is again similar in structure to Eqs. (20) and (25) except for the size distribution term, $\left(CV^2+1\right)^{-1}$. Note that this term *decreases* below unity for wider distributions, decreasing Z_v below the fundamental pinning term. It is apparent that using different averages of *r* (Z_n and Z_v) or assuming monosized spherical particles (Z_m) introduces variable biases into the experimentally measured values of *Z* . If the particles were actually monosized sphere all of the above measures would yield the same correct value of the pinning factor, $\frac{S_V}{4}$. The analytical descriptions of the experimental equations show that the distribution of particle size, that is inevitably present in real materials, increases the magnitude of error in the measured *Z* values.

2.4 Summation method

A more fundamentally sound method of computing *Z* from the unfolded 3D size distribution determines the pinning potential for each size class, Z_i , and computes the overall potential as the sum of the effects from each size class.

Combining Eqs.(2) and (3) gives the pinning potential of particles in size group *i* as:

$$Z_i = \frac{3 f_i}{4 r_i} \quad (30)$$

The pining potential of the overall particle distribution is the sum of Z_i over all size groups, here termed Z_s:

$$Z_s = \frac{3}{4} \sum_i \left(\frac{f_i}{r_i} \right) = \left(\frac{3 f}{4} \right) \overline{(r^{-1})}_v \quad (31)$$

where $\overline{(r^{-1})}_v$ is the volume weighted average of the *inverse* of particle size:

$$\overline{(r^{-1})}_v = \frac{\sum_i \left[f_i \cdot (r_i^{-1}) \right]}{f} \quad (32)$$

The values of Z_s for all experimental materials, computed from the summation of Z_i, are tabulated in Table 2 and used as the abscissa against which the other *Z* computations are plotted in Fig. 4.

Inserting Eq.(14) into (31) and substituting μ_{-1}^v for $\overline{(r^{-1})}_v$ yields:

$$Z_s = \left(\frac{S_V}{4} \right) \left(\frac{\mu_3^n}{\mu_2^n} \right) \left(\mu_{-1}^v \right) \quad (33)$$

Again, using the moments of the lognormal distribution and converting the volume weighted moment to number weighted moment, Eq. (33) reduces to:

$$Z_s = \frac{S_V}{4} \quad (34)$$

Compared to Eqs. (20), (25) and (29), Eq. (34) consists of only the stereological core, $\frac{S_V}{4}$. The size distribution term is lost because Eq. (31) already sums the pinning effect from all particle classes, and is, thus, independent of the size distribution. It will be

shown that for constant geometric shape this result is analytically equivalent to that obtained from the stereological measurement of S_V.

3. Stereological Parameter, L_A

This method involves measuring only the surface area of particles per unit volume, S_V, which is easily obtained from direct measurement of the length of boundary between the particles and matrix per unit area, L_A, by automated means, or can be obtained easily from manual line intercept measurement, P_L. The basic stereological equations [21] give the following relationships:

$$S_V = 2P_L = \frac{4}{\pi} L_A \quad (35)$$

Recalling Eqs. (1) and (2) and combining them with Eq. (35) yields:

$$Z_{st} = \frac{S_V}{4} = \frac{L_A}{\pi} \quad (36)$$

where the stereological pinning factor, Z_{st}, contains only the particle surface area per unit volume, S_V. Equation (36), identical to Eq.(34), inherently contains the particle size, shape and volume fraction information, regardless of size distribution, and is valid for particles with complex morphology in real material systems.

The measurements required for Equation (36) are much simpler and more accurately obtainable than the unfolding measurements for Z_s. The particle pinning potential calculated from Eq. (36) employs direct image analysis measurements of L_A, with no post-measurement processing. Measured values of Z_{st} for the different

specimens, shown in Table 2, are in very good agreement with those from Z_s. In Fig. 4 these values are plotted versus Z_s with a slope of unity, illustrating their equivalence.

DISCUSSION

Figure 4 shows the experimentally determined relationships among the five methods for computing *Z*. The data, listed in Table 2, were obtained from specimens with a wide range of particle structures covering a four-fold range of *Z*. It should be noted that Z_m, Z_n, Z_v, and Z_s were computed from the basic experimental expressions for each method, Eqs. (5), (23), (27), and (31), compiled in Table 3, rather than the respective analytical descriptors containing the size distribution term. For Z_{st}, the experimental and analytical expressions are identical since there is no shape or size distribution assumption involved in the basic definition. The non-homogenized specimens in Fig. 4 (a) and surface regions of the strip, Fig. 4 (c), had relatively finer particles and high *Z* values while the homogenized specimens, Fig. 4 (b), and strip interior regions, Fig. 4 (d), had relatively coarser particles and lower *Z*. In each plot, the values of Z_m, Z_n, Z_v and Z_{st} were plotted versus Z_s, chosen here as the most basic and recognizable descriptor of *Z*. As shown in these figures, Z_{st}, the pinning potential calculated from S_V was in excellent agreement with Z_s, especially the homogenized specimens with more equiaxed particles. The number weighted term, Z_n, showed much higher values than Z_s, by a factor of two, due to the bias towards finer particles. Conversely, the volume weighted term, Z_v, showed much smaller values than Z_s, falling well below the comparison line. The Z_m

values were generally close to Z_s, but slightly higher, and again closer for homogenized specimens.

The trends of the data in Fig. 4 can be explained through the analytical expressions for the different measures, Eqs.(20), (25), (29), (34) and (36), condensed in Table 3. Figure 5 shows the effect of particle size distribution on the Zener pining factor, *Z*, computed by these five methods, with CV varying from 0 to 1. Here the ordinate represents the size distribution term, that multiplied by $\frac{S_V}{4}$ yields the total *Z*. It is clear that the number weighting in Z_n produces the greatest positive bias, by a factor of $(CV^2+1)^2$ relative to the unbiased values of Z_s or Z_{st}. The volume weighting in Z_v results in a negative bias, by a factor of $(CV^2+1)^{-1}$. The monosized sphere assumption, Z_m, exhibits a slight positive bias, by a factor of $(CV^2+1)^{1/2}$. The Z_s and Z_{st} terms are analytically equivalent, as described above, and are not influenced beyond their basic expression by CV. The degree of bias of the different expressions increases with particle size distribution width. Thus, for an actual material with a particle size distribution width, CV ranging from 0.5 to 0.7 for the studied specimens, Z_m, Z_n and Z_v are variably biased in computing the Zener pinning factor. For CV=0.6, the respective values of Z_m, Z_n and Z_v are approximately 1.2, 1.8 and 0.7 Z_{st}, in general agreement with the slopes of the experimental data in Fig. 4.

The advantages for using the stereological means versus the summation method are evident when dealing with real material systems. In many materials, particles not only exhibit a size distribution but also possess different shapes. Because the summation

method is reliant upon particle shape assumption, it is prone to error in description of the size distribution, while the stereological method needs no shape assumption. Secondly, the stereological means is experimentally more robust than the summation method by avoiding the considerable effort and tendency for errors in the unfolding process. Use of a single parameter obtained from simple line intercept or automated field measurements requires significantly less experimental effort than those of measuring several parameters, whose ratio increases the statistical error of the final Z term.

SUMMARY

Five methods for characterizing the Zener pinning factor have been compared through experimental measurements on second phase particles in TRC AA3105 and evaluated analytically. Based on a general expression for the Zener pinning potential, $Z = \frac{f}{\bar{\lambda}}$, the analytical expressions of the five approaches are structurally similar, with a common fundamental core, $\frac{S_V}{4}$, but with different size distribution terms, which biases them above or below the correct core value. The stereological method, yielding the fundamental pinning factor, $\frac{S_V}{4}$, is experimentally very close and analytically identical to the summation method, however, with neither the need for unfolding the 3D particle size distribution nor assumption of spherical particles. For a real material system, the stereological means is demonstrated to be the simplest experimentally and with the least error.

ACKNOWLEDGEMENTS

The authors gratefully acknowledge funding of this research by the Department of Energy, award number: DE-FC36-021D14401. The electron microscopy studies were sponsored by the Assistant Secretary for Energy Efficiency and Renewable Energy, Office of Transportation Technologies, as part of the High Temperature Materials Laboratory User Program, Oak Ridge National Laboratory, managed by UT-Battelle, LLC, for the U.S. Department of Energy under contract number DE-AC05-00OR22725. The authors especially appreciate the critical reviews and suggestions by Professors R. T. DeHoff and R. D. Doherty and extensive assistance of Mr. Larry Walker of the HTML Materials Analysis Group with the FEG-SEM operation.

REFERENCES

[1] Smith CS. Trans Am Inst Min Eng 1948;175:47

[2] Hillert M. Acta Metall 1965;13:227

[3] Rios PR. Acta Metall 1992;40:649

[4] Rios PR. Acta Metall 1992;40:2765

[5] Rios PR. Acta Metall 1994;42:839

[6] Rios PR. Acta Metall 1997;45:1785

[7] Rollett AD, Srolovitz DJ, Anderson MP. Acta Metall 1989;37:1227

[8] Doherty R, Hoffman E, Hovanec C, Lens A. Materials Science Forum 2004;467:843

[9] Rios PR. Scripta Mater 1996;34:1185

[10] Nes E, Ryum N, Hunderi O. Acta Metall 1985;33:11

[11] Liu Y, Patterson BR. Scripta Mater 1992;27:539

[12] Liu Y, Patterson BR. Acta Metall 1993;41:2651

[13] Liu Y, Patterson BR. Metall Trans A 1993;24:1497

[14] Liu Y, Patterson BR. Scripta Mater 1993;29:1101

[15] Liu Y, Patterson BR. Metall Trans A 1994;25:81

[16] Liu Y, Patterson BR. Acta Metall 1996;44:4327

[17] Couturier G, Doherty R, Maurice C, Fortunier R. Acta Mater 2005;53:977

[18] Rios PR. Acta Metall 1987;35:2805

[19] Rios PR, Fonseca GS. Scripta Mater 2004;50:71

[20] Rios PR, Fonseca GS. Scripta Mater 2004;50:1373

[21] Dehoff RT, Rhines FN, editors. Quantitative Microscopy. McGraw-Hill; 1968

[22] Sun N, Patterson BR, Suni JP, Simielli EA, Weiland H, Allard LF. Mater Sci Eng A 2006;416:232

[23] Patterson BR, Sun N, Suni JP, Simielli EA, Weiland H, Allard LF. TMS Letters 2004;1:173

[24] Sun N, Patterson BR, Suni JP, Simielli EA, Weiland H, Allard LF. TMS Letters 2005;2:33

[25] Patterson BR, Sun N. Unpublished research, University of Alabama at Birmingham, USA, 2006

[26] Mould PR, Cotterill P. J Mater Sci 1967;2:241

[27] Fullman RL. Trans AIME 1953;197:447

[28] Aitchison J, Brown JAC. The Lognormal Distribution. Cambridge University Press; 1957

[29] Goldman A, Lewis HD, Moore RH. On the Proper Use of Transformations of Log Normal Functions in Small Particle Statistics. Los Alamos Scientific Laboratory, LA-3262; 1965

[30] Howard CV, Reed MG. Unbiased Stereology. Garland Science/Bios Scientific Publishers; 2005

[31] Kurzydlowski KJ, Ralph B. The Quantitative Description of the Microstructure of Materials. CRC Press; 1995

[32] Patterson BR, Rhines FN. Microstructural Science 1979;7:457

Table 1, Chemical composition of the experimental TRC AA3105, wt%

Mn	Mg	Fe	Si	Cu	Al
0.40	0.51	0.52	0.14	0.15	Balance

Table 2, Particle volume fraction and pinning potential, Z, ($x10^{-2}$ μm^{-1})

Treatments (°C /Hours)	f (Vol %)	Z_m Sur. /Cen.	Z_n Sur. /Cen.	Z_v Sur. /Cen.	Z_s Sur. /Cen.	Z_{st} Sur. /Cen.
620 / 504	1.4	2.6 / 2.2	4.7 / 4.3	1.6 / 1.5	2.4 / 2.0	1.9 / 1.8
630 / 1.5	1.4	5.3 / 3.1	6.7 / 4.9	2.3 / 1.9	4.1 / 2.7	3.9 / 2.7
630 / 12	1.3	3.7 / 2.6	5.1 / 3.5	1.8 / 1.6	2.9 / 2.3	3.2 / 2.4
630 / 132	1.3	2.6 / 1.7	4.8 / 2.9	1.4 / 1.2	2.2 / 1.7	2.0 / 1.5
630 / 168	1.3	2.5 / 2.1	3.7 / 3.3	1.5 / 1.4	2.3 / 1.9	2.2 / 1.8
640 / 8	1.2	2.8 / 2.2	3.9 / 3.1	1.6 / 1.4	2.4 / 2.0	2.6 / 2.1
640 / 16	1.1	2.6 / 1.9	4.1 / 2.7	1.4 / 1.2	2.1 / 1.7	2.3 / 1.9
650 / 0.5	1.3	5.0 / 3.1	6.4 / 4.7	2.2 / 1.7	3.8 / 2.5	3.9 / 2.9
650 / 2	1.2	2.1 / 1.1	4.4 / 2.3	1.5 / 0.9	2.0 / 1.1	2.1 / 1.2
500 / 2 (H)	1.4	2.6 / 1.6	4.5 / 3.0	1.8 / 1.3	2.3 / 1.6	2.3 / 1.5
550/ 0.5 (H)	1.5	2.4 / 1.7	4.7 / 3.6	1.8 / 1.4	2.3 / 1.6	2.0 / 1.5
550 / 24 (H)	2.0	2.8 / 2.2	4.8 / 4.8	2.1 / 1.8	2.5 / 2.1	2.5 / 1.9
600 / 0.1 (H)	1.5	2.5 / 1.6	3.7 / 2.4	1.9 / 1.3	2.4 / 1.6	2.4 / 1.5
600 / 0.2 (H)	1.5	2.3 / 1.8	3.5 / 3.8	1.8 / 1.5	2.3 / 1.8	2.1 / 1.6
600 / 1 (H)	1.4	2.1 / 1.4	3.0 / 3.0	1.7 / 1.2	2.1 / 1.4	2.0 / 1.2
620 / 0.2 (H)	1.4	2.0 / 1.6	2.8 / 2.4	1.5 / 1.4	1.9 / 1.7	1.9 / 1.5
620 / 2 (H)	1.6	2.3 / 1.7	2.9 / 2.2	1.8 / 1.5	2.2 / 1.8	2.3 / 1.6
640 / 0.2 (H)	1.4	2.2 / 1.4	3.4 / 2.7	1.7 / 1.2	2.1 / 1.4	2.1 / 1.4
640 / 2 (H)	1.2	1.8 / 1.2	2.7 / 1.9	1.4 / 1.0	1.8 / 1.1	1.8 / 1.2

(H) = Homogenized

Table 3, Expressions for particle pinning potential, Z, for different methods

Z	Experimental		Analytical	
Z_m	$\frac{3f}{\sqrt{(24/\pi)\overline{A}}}$	(5)	$\left(\frac{S_V}{4}\right)\left(CV^2+1\right)^{1/2}$	(20)
Z_n	$\frac{3f}{4\bar{r}_n}$	(23)	$\left(\frac{S_V}{4}\right)\left(CV^2+1\right)^{2}$	(25)
Z_v	$\frac{3f}{4\bar{r}_v}$	(27)	$\left(\frac{S_V}{4}\right)\left(CV^2+1\right)^{-1}$	(29)
Z_s	$\frac{3}{4}\sum_i\left(\frac{f_i}{r_i}\right)$	(31)	$\frac{S_V}{4}$	(34)
Z_{st}	$\frac{L_A}{\pi}$	(36)	$\frac{S_V}{4}$	(36)

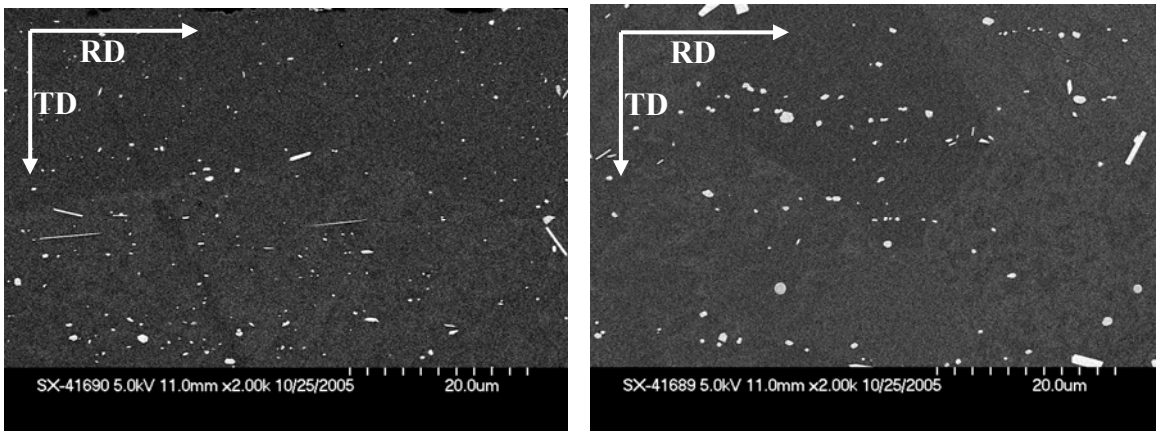

(a) (b)

Figure 1, Backscattered electron (BSE) images showing second phase particles of a TRC AA3105 strip annealed at 630°C for 12h. (a) strip surface, (b) strip interior. Note that particles are finer near the strip surface, with some acicular shapes present

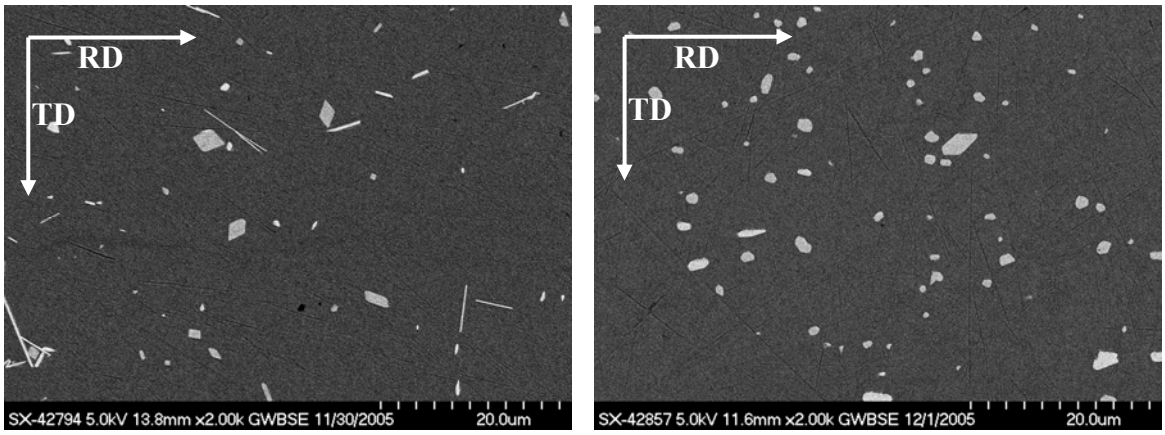

Figure 2, BSE images showing particles in the interior region of the annealed strip. (a) non-homogenized material annealed at 650°C for 2h, (b) homogenized material annealed at 550°C for 24h

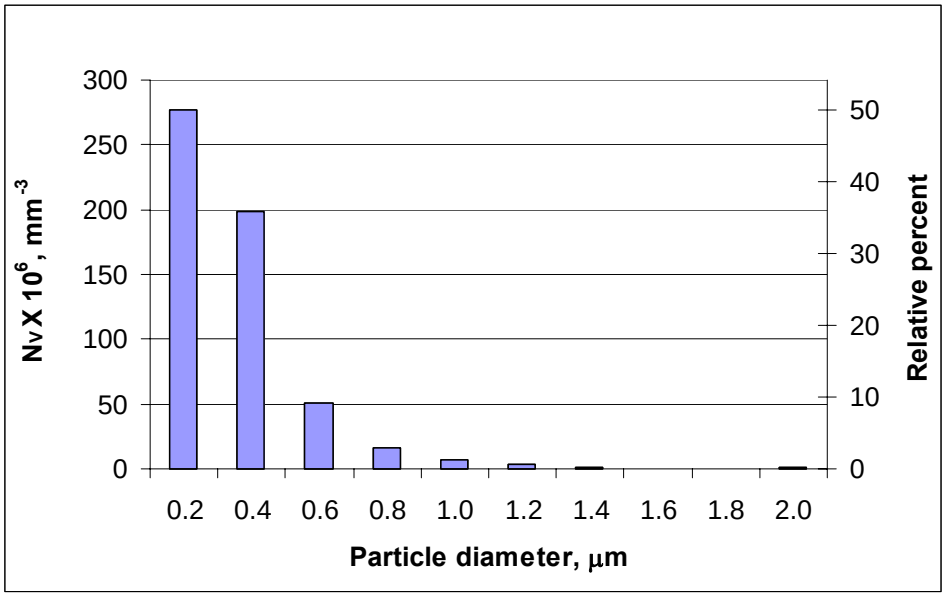

(a)

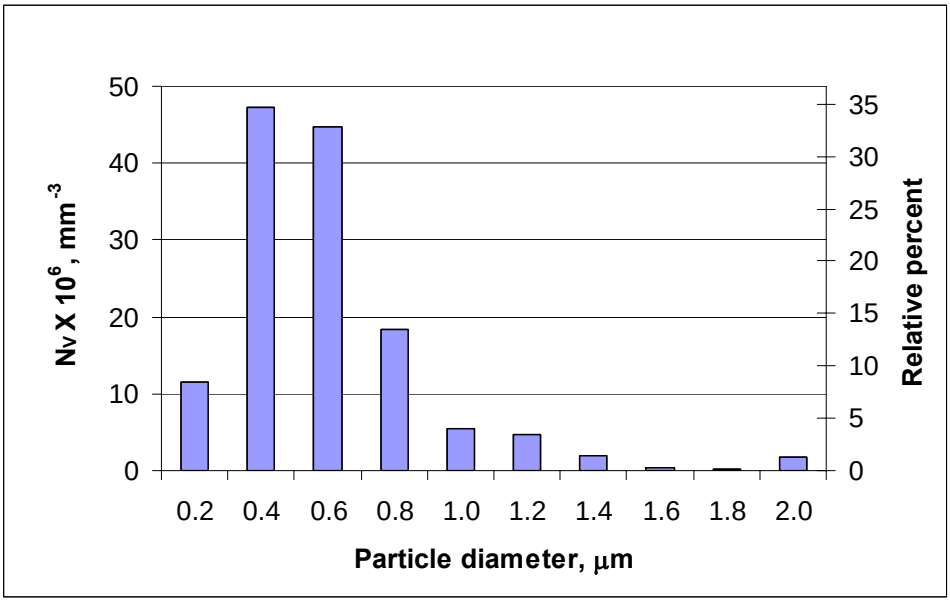

(b)

Figure 3, Distribution of 3D particle diameter computed by the Schwartz-Saltykov method in TRC AA3105 after 12h at 630°C, at (a) surface and (b) interior region of the strip. Typical micrographs of these areas are shown in Figs. 1(a) and (b)

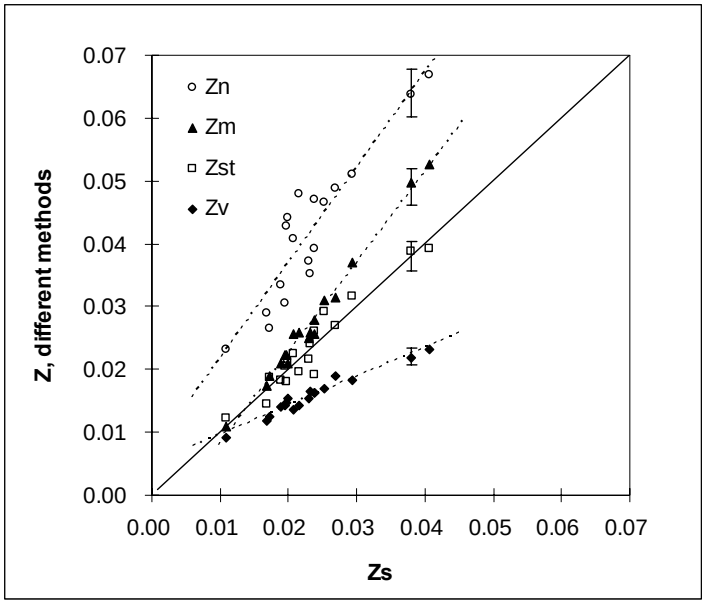
0.07
0.06
0.05
0.04
0.03
0.02
0.01
0.00
Z, different methods
Zn
Zm
Zst
Zv
0.00
0.01
0.02
0.03
0.04
0.05
0.06
0.07
Zs

(a)

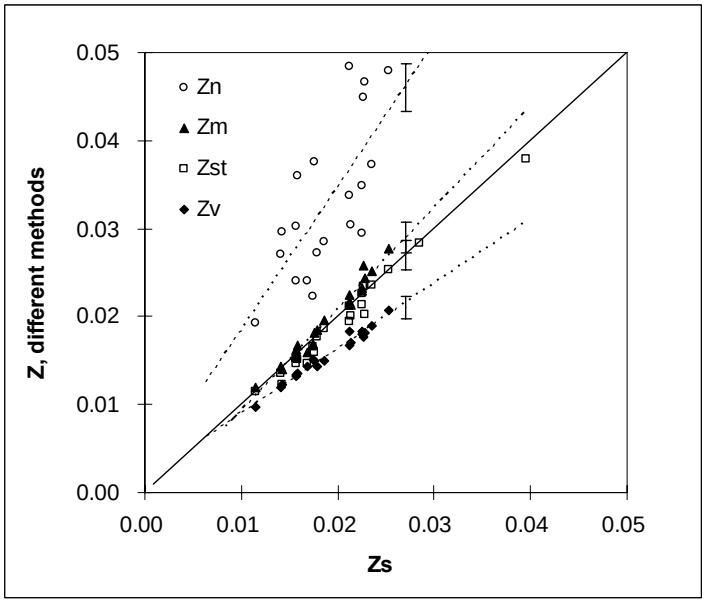
0.05
0.04
0.03
0.02
0.01
0.00
Z, different methods
Zn
Zm
Zst
Zv
0.00
0.01
0.02
0.03
0.04
0.05
Zs

(b)

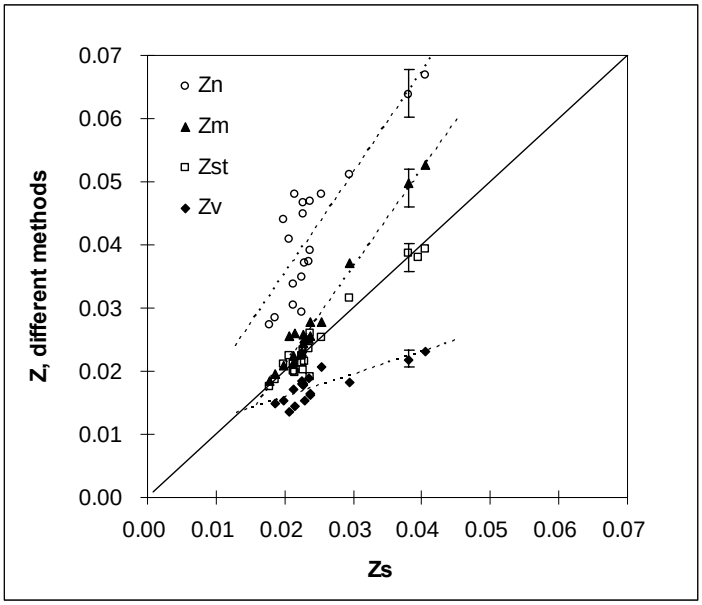

(c)

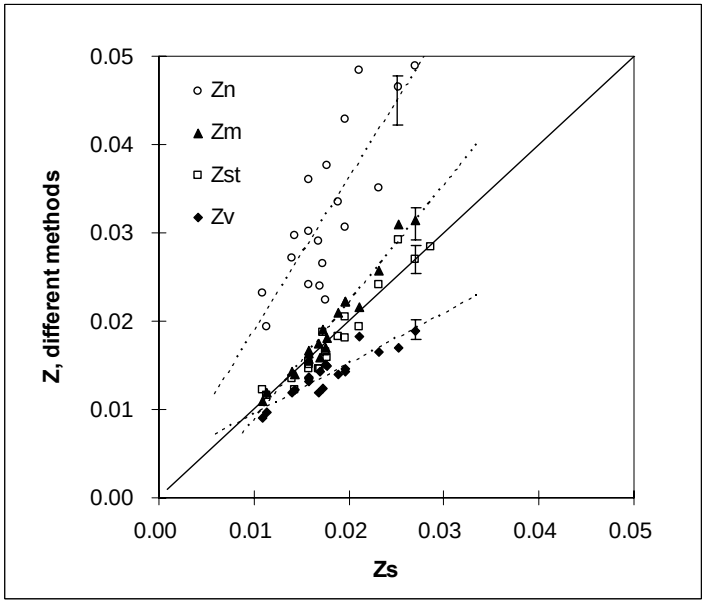

(d)

Figure 4, Experimental results of particle pinning potential, *Z*, measured by different methods, (a) non-homogenized, (b) homogenized, (c) strip surface, and (d) strip interior. Error bars for each data set indicate ± 1 SE

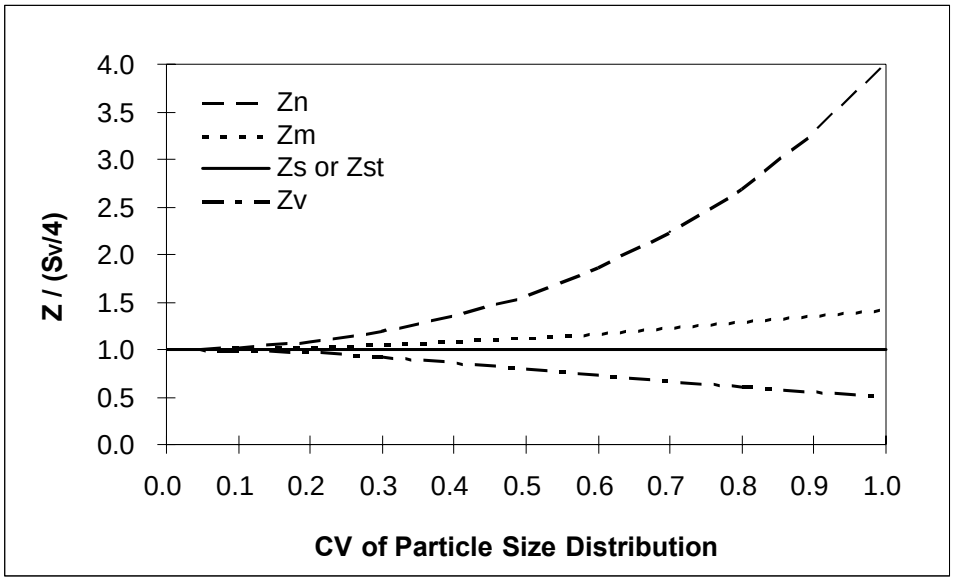

Figure 5, Analytical prediction of particle pinning potential, *Z*, computed by the different methods, for different particle size distributions

ABNORMAL GRAIN GROWTH IN THE PRESENCE OF EVOLVING PARTICLES

by

NAIYU SUN, BURTON R. PATTERSON, ROGER D. DOHERTY, JAAKKO P. SUNI, HASSO WEILAND AND LAWRENCE F. ALLARD

In preparation for *Acta Materialia*

Format adapted for dissertation

ABSTRACT

The evolution of abnormal grain coarsening (AGC) has been investigated in twin roll cast AA3105, with coarsening/dissolving intermetallic particles – Al_6Mn and $Al_{12}(Mn, Fe)_3Si$. In the as-cast state with a high supersaturation of Mn, on annealing at 600 to 640°C, after rapid recrystallization to a fine grain size, AGC occurred after extended times, as long as 800 hr at 600°C but falling to only 12 hr at 640°C. For material carefully homogenized first to precipitate the excess solute and then cyclically annealed between 450 and 620°C to coarsen the intermetallic phase, AGC occurred in the 90% cold rolled samples annealed at 550 to 620°C in times of less than 1 hr. A newly-defined dimensionless parameter, the Grain Anchorage Parameter (GAP), the product of the measured matrix grain size and the particle dispersion parameter Z, previously shown to be the shape independent equivalent of the classic Smith –Zener grain size parameter f/r, was shown to control AGC. The longer times needed for AGC in the as-cast material were shown to be due to the fall in Z to achieve the critical value of GAP. The results also appear to provide support for the particle shape change hypothesis previously proposed by Doherty et al.

INTRODUCTION

For many metallic/ceramic materials, the grain microstructure, produced by prior processing such recrystallization of deformed metals, is often found to be metastable. Further growth of the mean grain size may occur in order for the sample to lower its grain boundary area and thus the interfacial energy due to the grain boundaries. Since this process is equivalent to the growth of mean particle size that is known as particle

coarsening we prefer to describe the growth of grains as ***grain coarsening*** rather than the commonly used term ***grain growth*** in order to distinguish grain coarsening from the growth of recrystallizing grains driven by the energy of the deformation induced dislocations--a mechanism invariably described as nucleation and growth [1, 2].

In practice, one distinguishes two kinds of grain coarsening: normal/continuous and abnormal/discontinuous. During normal grain coarsening (NGC), the mean grain size grows by the loss of the smallest grains with their volume being transferred to larger grains maintaining a compact, usually near log-normal grain size distribution. In the absence of any general impediment to grain boundary migration, NGC is invariably observed [2]. However, if grain boundary motion can be strongly inhibited, for example by a dispersion of stable second phase particles, abnormal grain coarsening (AGC) can sometimes occur. Here a limited number of grains grow rapidly consuming all the other grains. In a classic study, almost 60 years ago, Beck et al. [3] had a thorough review of previous studies on AGC and as confirmed by the authors' own investigation of grain stability in high purity Al-Mn alloys, AGC frequently occurred with very low volume fractions of second phase particles. In a remarkable demonstration it was shown that AGC could be used to trace out the locus of the solvus of the Al_6Mn phase. Just below the solvus temperature in any binary alloy the structure will always have a negligibly small amount of the second phase. Ten years later Calvet and Renon [4] duplicated the Beck et al. solvus criterion for AGC in a range of Al-Cu alloys. However in a later study of two-phase Al –Al_2O_3 alloys by Tweed et al. [5] with very low values of f, despite lengthy anneals of samples of this alloy AGC was not detected. The grain structure after a very limited amount of grain coarsening after recrystallization then remained anchored.

As was noted in a recent review by Doherty et al [6] the physical origin of this phenomenon is not yet understood so that no reliable method of predicting when AGC will or will not occur in two phase microstructures yet exists. In a recent study of the processing of Twin Roll Cast (TRC) AA3105, with different dispersions of the second phase particles [7], AGC was unexpectedly found. The present study was then undertaken to clarify the conditions giving AGC in this industrial alloy. AGC is not only of major scientific interest but also of great importance for a wide range of industrial applications, most significantly the development of Goss texture needed for the magnetic properties of transformer steels [8]. So it seems important to gain as much insight as possible into this phenomenon.

PRIOR STUDIES OF AGC

It is known that AGC appears to occur only when NGC is inhibited usually by second phase particles, texture, or free surface effects. Detailed theoretical/statistical studies of grain coarsening have been carried out first by Hillert [9] and then developed further by others [10-16]. In his classic grain coarsening paper [9], Hillert conceived, based on a 2D defect model, that there are two grain size limits during grain coarsening in the presence of second phase particles. NGC takes place below the lower limit. Between the two limits a large grain would be able to coarsen abnormally. Above the upper limit, all grains are pinned by particles and no grain coarsening occurs.

The pinning of grain boundary motion by second phase particles was analyzed by Smith [17] who acknowledged the contribution of Zener to the model and ever since the topic has been attributed solely to Zener, see for example Manohar et al [18], where the

authors also reviewed the many later developments of the "Zener" model. However Hillert recently reported that Smith in private discussions noted that the model was developed by both Smith and Zener and as such Hillert recommended that the model in future be called the "Smith –Zener" model. As frequently noted, see for example [6, 18], the Smith-Zener model has three components. These concern the *maximum* drag force, F_P, exerted by a spherical particle on a migrating grain boundary, the random density, N_A, expected for spherical particles all of the same radius r in a microstructure where the second phase particles occupy a volume fraction, f, (the product of F_P and N_A then provides the drag pressure P_r) and the limiting, mean, grain size <D> in which the drag pressure exerted by particles can limit surface energy driven grain coarsening.

$$F_P = \pi r \gamma \quad (1)$$

$$N_A = 3 f / 2\pi r^2 \quad (2)$$

$$P_r = 3 f \gamma / 2 r \quad (3)$$

$$\langle D \rangle = 4 r / 3 f \quad (4)$$

Here, γ is the grain boundary interfacial tension.

Doherty et al. [6] recently noted that while Eq. 3 was initially developed for the limiting size of NGC and almost universally used to predict the grain size at which NGC will be anchored, see for example [18], the classic Smith-Zener analysis should not be applied to NGC. However, it does seem appropriate, within the limitations of the original analysis, to be the expected grain size limit for AGC. The reasoning for these two conclusions was that in AGC, once a giant grain has somehow formed, it will have a pressure for growth that is approximately, $2\gamma / \langle D \rangle$. In NGC grain whose size is close to the average, will neither grow nor shrink. The process of NGC of grain like that of

coarsening of second phase particles is the loss of the smallest grains, which must be smaller than <D> and so in contrast to Hillert's prediction, the limiting grain size for NGC, $<D>_{NGC}$, will be ***smaller*** than the limiting matrix grain size, $<D>_{AGC}$, that can stop the growth of the largest grain. That conclusion was found for the situation, analyzed by Smith-Zener, for spherical particles all of the same radius.

In an attempt to account for the frequent observation that AGC can occur [3, 4] in a grain structure where NGC had been anchored by particles Doherty et al. proposed that a critical event is the expected relaxation of the spherical particle shape on stationary or very slowly moving grain boundaries to the equilibrium "convex lens" shape allowing triple point equilibrium between the tension, γ , of the boundary between the two grains and the tension, $\gamma_{\alpha\beta}$, of the interface between the α matrix and the β second phase particle. For the case where the particle was assumed incoherent with both grains the shape change is readily shown to lead to a significant increase, by about twice when $\gamma \approx \gamma_{\alpha\beta}$, in the drag force per particle. Such a shape change will require some finite solute mobility, the product of the diffusion coefficient and the solubility of the solute, and is thus expected in an alloy and at a temperature where the particles can themselves coarsen. The shape change hypothesis for AGC was supported by its compatibility with the observations of (a) that AGC occurs most easily for very small values of the volume fraction [3, 4] since then at a critical value of f/r the particles will be much smaller than the grains so the kinetics of the proposed shape change will occur most quickly and (b) for the apparent absence of AGC in the Al-Al_2O_3 system studied by Tweed et al. [5]. Below the melting point of Al the solubility of Al_2O_3 will be negligible, giving effectively no solute mobility and thus no detectable oxide coarsening.

Besides second phase particles, AGC can be induced by strong crystallographic orientations/textures. By means of a Monte Carlo computer simulation, Rollett [19] studied the AGC behavior in a matrix of grains with anisotropic grain boundaries. He reported that anisotropic grain boundary energies and mobilities result in different AGC mechanisms, namely melting and secondary recrystallization morphology respectively. It is shown that in the presence of textures grain coarsening generally leads to strong texture changes. Abbruzzese [20] modeled the texture effects on grain coarsening more realistically by introducing discrete grain size and orientation classes instead of continuously varying functions. He concluded that, for each orientation, there is a different critical radius dividing the growing and shrinking grains.

Another factor that has been reported to affect AGC is free surfaces in thin films [21-23]. The driving pressure for AGC in thin films comes from the orientation related surface energy. The velocity of AGC was shown experimentally by Palmer et al. [21] to be inversely proportional to the thickness of thin sheet materials.

Quite a few two- and three-dimensional simulations have been performed to validate many physical and statistical models of different AGC mechanisms [19, 22-26]. Unfortunately, direct experimental studies of AGC have been falling behind the corresponding theoretical and simulation developments since Beck et al. [3] and Calvet and Renon [4]. Not much research has been conducted to experimentally quantify AGC in a material containing evolving second phase particles.

In this paper, an experimental study of AGC in TRC AA3105 was carried out. Due to the TRC process, no significant texture evolution was found during recrystallization and grain coarsening. Moreover, nuclei of AGC often originated from

the center of the strip indicating the absence of free surface effect. Thus, for the studied material, the dominating factor in grain coarsening is the evolving second phase particles, which is the focus of this paper.

EXPERIMENTAL

AA3105 strip was twin roll cast as 5mm thick sheet and with composition given in Table 1. The TRC alloy was produced for this study by Alcoa. The alloy contains Al-Mn-Fe constituent particles that are typically much finer near the rapidly solidified surface than in the interior, and these coarsen during homogenization or high temperature annealing [27]. In addition, the rapidly solidified TRC strip exhibits significant supersaturation of the slowly diffusing elements, Mn and Fe, which results in fine dispersoids during downstream thermo-mechanical treatments [28]. Unlike Manganese, Iron has very low solubility in Al, so most of subsequently precipitated dispersoids will be Mn rich. However unlike ingot cast aluminum alloys, where the constituents at 1-2μm are much larger than the dispersoids that are typically 0.01 to 0.2μm in size, here the types of particle are closer in size. A large variation in particle sizes and morphology for different thermal treatments gives a large range of particle dispersion levels. Two types of sample were processed: (a) as-cast and thus non-homogenized (NH) with the potential for additional precipitation of dispersoids, and (b) Homogenized and cyclically coarsened (HC) material. The HC treatment involved ten cycles between 450 and 620°C with 5 hr holds at each temperature and 0.3°C/min cooling rate from the higher to lower temperature and a faster heating rate of 5°C/min. This was based on an accelerated coarsening treatment developed for Al-Fe alloys [29].

Both NH and HC materials were cold rolled to 90% reduction and annealed as small samples in a pre-heated air furnace for different temperatures and times. The values of time and temperature of annealing listed in Table 2, are for those samples where the particle dispersion had been carefully characterized [7]. Specimens for microstructural examination were prepared on the longitudinal cross section, parallel to the normal (ND) and rolling directions (RD). The detailed methods used for evaluating the particle dispersions have been previously described [7]. In the present work the grain structures were evaluated by optical microscopy using polarized light on anodized samples. The samples were ground with silicon carbide paper (240/320/600 grit) and then polished with diamond pastes (3μm/1μm) and finished with a final polish with colloidal silica. The as-polished samples were anodized with a Barker's reagent at 30 Volts dc for approximately 100 seconds.

The matrix grain size was estimated by averaging the mean linear intercept length in both the longitudinal and the transverse directions of the strip. The evolution of second phase particles was followed by electrical conductivity (EC) and volume fraction measurements [7] and diffusivity calculations.

RESULTS AND DISCUSSION

All the samples listed in table 2 were found to be fully recrystallized after the shortest times of annealing. The HC material was fully recrystallized after only 5mins at 400°C. The recrystallized grains exhibited a size gradient from strip surface to center for NH material and a uniform finer grain structure for HC material.

3.1 AGC in non-homogenized material

Figure 1 shows grain structure before and after AGC in NH material annealed at 620°C. AGC only emerged in the material after three weeks at temperature. At a higher temperature, 630°C, AGC occurred after one week, as shown in Fig. 2. However at 600°C it took over 800 hrs for AGC to occur, with no detectable change in the matrix grain size during these extended times. Interestingly, surface layers of approximately 50 to 100μm thick remained as-recrystallized grain structure long after AGC started. Such AGC resistant surface layers appeared in all NH materials that underwent AGC. The presence of the surface layers can be attributed to the higher particle dispersion level and the larger as-recrystallized grain size associated with strip surface compared with those at strip interior. Prior to AGC, the recrystallized grain size remains relatively constant with an average size of approximately 50μm near strip surface and 30μm at interior. The corresponding particle morphology of material in Fig. 2 (a) is shown in Fig. 3 and the particle size distribution shown in Fig. 4. As we can see that particles are finer at strip surface than the center, however, their number is approximately 5 times as many. As expected, longer annealing time results in coarser particle dispersion and finer particle dispersion for shorter time, as shown in Figs. 5 and 6, respectively.

Figure 7 shows the grain structure in material annealed at 640°C for different times. Here AGC started after only 12 hours at temperature and progressed as time, as shown in Figs. 7(b)-(f). The surface layers became evident after a few large grains consumed most grains at strip interior, as shown in Fig. 7(c) and (d). As time at 640°C increased, the surface layers were slowly consumed by growth of the giant grains that developed from the grain interior, as shown in Figs. 7(e) and (f). Eventually this resulted

in a single grain occupying the whole strip thickness. The particle morphology and size distribution of the material in Fig. 7(c) are shown in Figs. 8 and 9, respectively. The particle dispersion level is given in Table 2 along with others.

At higher temperatures 650°C and at almost 660°C, thin (at 650°C) and thicker (at 660°C) liquid films developed at the grain boundaries and NGC was seen to occur. Figure 10 shows grain structure in materials annealed at 650°C for different times and Fig. 11 shows that despite the melting of the grain boundaries the constituent particles survived - the eutectic temperature in both Al-Mn and Al-Fe is greater than 650°C. At 660°C, the liquid fraction is much larger and, as seen in Fig. 12, much more rapid NGC occurred than at 650°C and this appears to correlate with the melting of the eutectic constituent particles as seen after re-solidification on cooling to room temperature in Fig. 13.

3.2 AGC in cyclically homogenized material

Figure 14 shows grain structures in HC material annealed at temperatures from 400 to 640°C. At temperatures below 525°C there was no sign of AGC, even for extended times. The grain structures at the lower temperatures remained unchanged from 5 mins till at least 24hrs, as shown in Fig. 15. It is striking that the as-recrystallized grain size after 5 mins at 400°C is somewhat finer (about 15μm) than that at the higher temperatures (25μm). Recrystallization at 300°C, requiring one hour annealing, showed an even finer grain size, approximately 10μm. These finer grain size samples recrystallized either at 300°C or at 400°C on further anneals of 5 minutes at 500°C then showed a detectable increased of grain size to approximately 25μm.

The HC material, showed very early onset of AGC at all temperatures at or above 550°C, as shown in Figs 14 (d-g) and in more detail Fig. 16 for 600°C for times from 5 mins to 8 hrs with similar results for the grain structures at 550, 620 and 640°C. There appears to be a long period of incomplete AGC after its quick emergence at short times. At 620 and more clearly at 640°C there was some general grain coarsening as well, Figs 14 (f) and (g).

At 650°C, like NH material, HC material showed NGC/Ostwald ripening instead of AGC, as shown in Fig. 17, again this is apparently related to the onset of melting producing thin mobile liquid metal films, again with unmelted constituent particles, at the grain boundaries.

3.3 Evolution of particles.

The simple Smith-Zener analysis [17] of Eqs.1 and 2 has been revised in many ways both theoretically and experimentally, see for example [18, 30-33]. Recently Sun et al. [7] developed a new method of evaluating the particle contribution to the pressure drag. They introduced a Z parameter, $Z = f/\lambda$, where λ is a particle size parameter. For the case of a random distribution of spherical particles all of the same radius, the Smith-Zener assumption, they noted that Z would then be given by:

$$Z = 3f / 4r \qquad [5]$$

Different methods of evaluating Z were explored [7] and a simple stereological method, Eq.6, was developed and used to evaluate many of the particle microstructures in samples whose grain structure has been reported here.

$$Z = S_V / 4 = L_A / \pi \qquad [6]$$

S_V is the area of particle/matrix interface in unit volume of the alloy, a parameter that is readily determined in modern image analysis procedures by measuring L_A.

As analyzed [7], Eq.6 appears to be able to account for a wide range of particle shapes and size distributions. At constant volume fraction of the second phase particles, f, Z will fall during particle coarsening but if a significant fraction of particles are on the grain boundaries, then the predicted shape change, discussed by Doherty et al. [6], as previously near spherical particles relax to the equilibrium lens shape on the boundaries will lead to *an increase* in Z. Table 2 reports these Z values in units of μm^{-1}. In Table 2 clear coarsening effects can be seen, for example in NH material at 630°C but with some evidence for the postulated particle shape change – the samples where, despite the loss of small particles by coarsening, Z was found to have increased with longer times. It is important to note that this is occurring while the particle volume fraction is remaining essentially constant, apparently close to the equilibrium value.

Values of Z measured at the center and surface were found to be different arising from the different solidification conditions during TRC at these locations. Different surface and center particle microstructures can be seen directly in Figs. 3, 5, 6, 8 and 18 for the NH material and Fig. 19 for HC material. After the HC processing and/or after extended annealing times at high temperatures in the NH material the Z values at the surface and center, while, not identical, are much closer to each other than they are in the NH material after shorter high temperature annealing times.

Values of the volume fraction f, measured by area fraction using Image Pro Plus, are also included in Table 2. From the change in f and, with higher sensitivity, from the change in eddy current measured EC as % of the International Annealed Copper Standard

(IACS), as shown in Fig. 20, it can be seen some dissolution of the Mn dispersoids appears to be occurring at higher temperatures. High temperature dissolution can be seen more clearly in the HC material, with its much higher pre-rolling EC but it also appears in NH material at the highest temperatures. At low temperatures, precipitation of Mn rich dispersoids from supersaturated solid solution is occurring in both NH and HC materials. The solubility of the iron-rich dispersoids is so small even at the highest temperatures that the observed changes in f and EC are expected to be very largely determined by the diffusion of Mn. Table 3 gives estimates of the diffusion coefficients of Mn and Fe, these values are based on unpublished data from Alcoa.

It is striking that after intermediate annealing times (for example 24 – 48 hrs), at high temperatures (for example at 600 – 640°C), the NH material had lower EC values indicating a slightly higher Mn solute contents than the HC material, even though the EC values were essentially unchanged indicating no significant continued precipitation, as shown in Figures 20 (a) and (b). This somewhat unexpected result is due to the NH material having fine dispersoid particles, precipitated on annealing after rolling, that have very low Fe content compared to the constituents. Figure 21 shows the typical particle morphology for NH material annealed at 600°C for different times. As we can see, the fine dispersoid particles slowly dissolved as time, comparing Fig. 21 (a) with (b). In the HC material the Mn will have precipitated mainly onto the constituents. The lower EC values in NH will then reflect the higher local solubility in regions with these fine Mn rich dispersoids compared to a lower Mn solubility in equilibrium with the iron containing constituents. On extended annealing to give AGC in the NH material 800 hrs

at 600°C (Fig. 22), the EC value of NH then approaches to that of HC after the dispersoids have dissolved up.

The very long times, 800hr at 600°C for the dissolution of the fine Mn rich dispersoids and re-precipitation of the Mn on the Fe containing constituents can be qualitatively understood by a simple model proposed by Doherty and Rajab [34] for the growth of the thickness of a GP zone free region around growing plates of a more stable Ag2Al phase in Al-Ag. In this model though the thickness of the GP zone depleted layer grew with the expected kinetics, proportional to the square root of annealing time, for diffusion controlled growth of the plates - the times need for a thickness X, of GP zone depletion, were very much larger than the usual $X \approx \sqrt{Dt}$ result expected for solute depletion distance around precipitates during growth from supersaturated solution. The reason for this increased time is that while the amount of solute that needs to move is the same, with the solute pre-precipitated, as GP zones in the Al-Ag system [34] or as dispersoids in the present study, the concentration gradients are much less when the dispersoids are present. 800 hours at 600°C gives a diffusion distance, $\sqrt{Dt}$ for Mn (table 3), of 80μm. This distance is very much larger than the spacing between the constituents, seen in Fig. 18, to be only a few μm! This analysis appears to account for the very long times needed for AGC in the NH material.

3.4 Interaction of particles and grain boundaries.

It has long been recognized that the derivation of the simple particle drag pressure of Eq. 3 as the product of the ***maximum force*** exerted by each particle and the ***random density*** of particles of unit area of the boundary cannot be more than a first

approximation. In deriving Eq. 2, the boundary was assumed to be either flat or smoothly curved, so Eq. 3 cannot be valid, as the model, used for Eq. 2 would have as many particles pulling the boundary forward as pulling it back. There have been various experimental investigations, see for example [31-33], in which the density of particles on the grain boundaries was shown to be higher by a non randomness factor, N*, than the value of the density given by Eq. 2.

By use of the methods previously described [31-33], N* was measured and the experimental values, ranging from approximately 3 to 5, match fortuitously well the values of N* of 4 ± 0.3 recently reported by Couturier et al. [30] by a finite element simulations of a single grain boundary. The origin of N* being > 1 was shown by the finite element model [30] to arise from the ***flexibility*** of the boundary. That is, the particles remain in contact with the boundary even when the average position of the boundary plane is several times the particle radius. The higher than random density of particles will increase the particle drag by the factor N*, so yielding the following expressions for (a) spherical particles all of the same radius r or (b) a dispersion characterized by the Sun-Patterson Parameter Z.

$$P_r = 3\,N^*\,f\,\gamma / 2\,r \qquad (7a)$$

$$P_r = 2\,N^*\,Z\,\gamma \qquad (7b)$$

A further result from the finite element model [30], still with all particles spherical and of the same radius, was that the average force per particle, $\langle F_P \rangle$ was less by a factor *a* than that predicted by the Smith – Zener Eq. 1. For anchored boundaries where N* ≈ 4, the particle drag factor $a \approx 0.55$, so reducing the predicted drag pressure

by about 50% from that given in Eqs. 7a and 7b. For simplicity it is convenient to combine the N* and *a* into a single parameter, C.

$$C = N^* a \approx 2.2 \quad (8)$$

The final versions of the particle drag pressure are then:

$$P_r = 3 C f \gamma / 2 r \quad (9a)$$

$$P_r = 2 C Z \gamma \quad (9b)$$

As noted above in section 2, the drag pressure exerted by particles can be expected to be overcome by the growth of a grain that has by some means become much larger than the other grains which have a mean grain size <D> since the pressure for capillarity driven boundary migration generates a pressure $2 \gamma / Rc \approx 2 \gamma / \langle D \rangle$. By equating this with the two predictions of particle drag we obtain as the critical condition for AGC, the continued growth of a giant grain whose size has somehow become >> <D> by:

$$\langle D \rangle f / r \leq 4/3C \approx 0.6 \quad (10a)$$

$$\langle D \rangle Z \leq 1/C \approx 0.45 \quad (10b)$$

Only the values in Eq. 10b are relevant to the current microstructures where Z has been carefully characterized. The values in Eq. 10a have been quoted since the parameter f/r is very well known but the f/r formulation is only relevant to models not to real microstructures where particles are rarely spherical and never all of the same size.

On the basis of Eq.10b we propose that the necessary condition for AGC in a particle containing grain structure is that the product <D> Z that we call the GAP for abnormal coarsening G_A, must be less than 1/C for a giant grain to be able to continue to grow. That is for AGC:

$$G_A = \langle D \rangle Z \leq 1/C \approx 0.45 \qquad (11)$$

It should be noted that while G_A is a necessary it may not be a sufficient condition since the model only gives the condition for the *continued growth* of an abnormally large grain. The conditions for the "nucleation" of the abnormally large grain, by initial enlargement of a grain from within the distribution of grain sizes is a more difficult problem [6].

Table 4 lists the matrix grain size <D>, the measured minimum value of Z (in the center of the strip), and the resulting values of G_A for microstructures in both NH and HC materials where AGC was found to clearly established. The close agreement with the simple model developed here is striking, with the NH material has a critical value somewhat greater than predicted by Eq. 11. In order for Z to decrease sufficiently small for G_A to be reached in the NH material, very extensive times for particle coarsening were required, see Figs. 5 and 23 as well as Table 2. The decrease of Z occurred in a stable grain structure with no apparent NGC, see Figs. 2 and 7, during the extended annealing required before AGC occurred. The need for extensive particle coarsening is in qualitative agreement with the particle shape model of Doherty et al. [6] and the small local increases of Z seen in some examples in Table 2.

Doherty et al. [6] also showed that by balancing the curvature removed by particle drag, using the Couturier et al. [30] values for C, against the curvature driving boundary migration, determined for each grain by its number of grain faces that the resultant limit to NGC, $\langle D \rangle_N$, closely matched the wide range of experimental data, for $f < 0.03$, reviewed by Manohar et al [18].

$$\langle R \rangle \approx \langle D \rangle_N \approx (1/3) \langle D \rangle_A \approx (4/9)\ (1/C)\ r/f \qquad (12a)$$

The model was developed assuming spherical particles all of the same size, so this result can be immediately translated after relaxing those assumptions by use of the Sun and Patterson parameter:

$$<D>_N \approx (4/9)(1/C)(3/4Z) \approx (1/3)(1/C)(1/Z) \quad (12b)$$

This is the maximum size that can be achieved by normal grain growth in the presence of a particle dispersion Z by the loss of the smallest grains in a log normal grain size distribution with the smallest grains <D>/3 that continue to vanish after the largest grains in the distribution, 3<D>, have stopped growing. So in terms of Z the GAP for NGC, G_N, is given by:

$$G_N = <D>_N Z = (1/3)\ (1/C) \approx 0.15 \quad (13)$$

The experimental results of Grain Anchorage Parameter for both NGC and AGC are shown in Figure 24, also included are the two AGC limits denoted with dashed lines. For NH material the experimental $G_A \approx 0.56$, higher than the model value of 0.45, may be due to the difficulty of nucleation for AGC from a pinned state. Thus, $G_A \approx 0.56$ defines the upper limit of AGC, which is the transition from completely pinned state to AGC. For HC material the experimental $G_A \approx 0.38$, lower than the model value of 0.45, can be attribute to the fact that AGC occurred from unpinned state or as a continuation of NGC. Thus $G_A \approx 0.38$ gives the lower limit of AGC, which defines the transition from NGC to AGC. Moreover, for HC material, the starting particle dispersion is not large enough to pin NGC, which emerged before AGC. The experimental $G_N \approx 0.15$ is in a fair agreement with the experimental values of G_{AP}, where the material underwent NGC.

CONCLUSION

1. By use of the particle dispersion term Z, it can be predicted, that a critical parameter G_A defined as the product <D> Z, is 1/C (based on Zener-Couturier model) where <D> is the matrix grain size and C is the Couturier parameter found to be about 2.2. That is $G_A \leq 0.45$
2. TRC AA3105 either as-cast that is non-homogenized, NH, or as cyclically homogenized, HC, show two experimental values of G_A of 0.56 and 0.38 respectively, which represents the upper and lower limit of AGC.
3. Upon annealing, the supersaturated NH material undergoes first precipitation of the supersaturated Mn and only after extended coarsening to reduce the drag term Z to the critical value of $G_A \approx 0.56$ does AGC occur and grow to completion from the enter of the strip.
4. The surfaces of the NH strip with larger values of Z, resist being consumed by the established and growing large grains, until additional coarsening has occurred.
5. Upon annealing, the HC material undergoes first NGC, and then quickly AGC ($G_A \approx 0.38$), which significantly slows down. At lower temperatures the very slow kinetics of AGC may due to some further precipitation of Mn rich particles and at higher temperatures by NGC aided by particle dissolution.
6. The nucleation of AGC in the NH material may be able to occur by the particle shape change model proposed by Doherty et al., since that requires extensive particle coarsening as observed here. However the rapid kinetics of the onset of AGC in the HC material cannot be explained by that model.

ACKNOWLDGEMENTS

The authors gratefully acknowledge funding of this research by the Department of Energy, award number: DE-FC36-021D14401. The electron microscopy studies were sponsored by the Assistant Secretary for Energy Efficiency and Renewable Energy, Office of Transportation Technologies, as part of the High Temperature Materials Laboratory User Program, Oak Ridge National Laboratory, managed by UT-Battelle, LLC, for the U.S. Department of Energy under contract number DE-AC05-00OR22725. The authors especially appreciate the extensive assistance of Mr. Larry Walker of the HTML Materials Analysis Group at Oak Ridge National Laboratory with the FEG-SEM operation.

REFERENCES

[1] J.W.Martin, R.D.Doherty and B.Cantor, Stability of Microstructure in Metallic Systems, Cambridge University Press, Cambridge Second Edition 1997

[2] F.J.Humphreys and M Hatherly, Recrystallization and Related Annealing Phenomenon, Pregamon Press, Oxford, Second Edition 2004

[3] P. A. Beck, M. L. Holzworth and P. Sperry, Trans. AIME 1949;180:163

[4] J. Calvet and C. Renon, Mem. Sci. Rev. Met. 1960;57:345

[5] C. J. Tweed, B. Ralph and N. Hansen, Acta Metall. 1984;32:1407

[6] Roger Doherty, E. Hoffman, C. Hovanec and A. Lens, Materials Science Forum 2004;467:843

[7] Naiyu Sun, B. R. Patterson, J.P.Suni, H.Weiland and L.F.Allard, Acta Materialia 2006;in press

[8] H. Afer, N. Rouag and R. Penelle, Journal of Crystal Growth 2004;268:320

[9] M. Hillert, Acta metall. 1965;13:227

[10] P. R. Rios, Acta metall. 1992;40:649

[11] C. V. Thompson, H. J. Frost and F. Spaepen, Acta metall. 1987;35:887

[12] P. R. Rios, Acta metall. 1992;40:2765

[13] P. R. Rios, T. Yamamoto, T. Kondo and T. Sakuma, Acta metall. 1998;46:1617

[14] P. R. Rios, Acta metall. 1994;42:839

[15] P. R. Rios, Acta metall. 1997;45:1785

[16] G. Abbruzzese, I. Heckelmann and K. Lucke, Acta metall. 1992;40:519

[17] C.S. Smith. Trans Am Inst Min Eng 1948;175:47

[18] P.A. Manohar, M Ferry and T. Chandra, ISIJ Intern 1998;38:913

[19] A. D. Rollett, D. J. Srolovitz and M. P. Anderson, Acta metall.1989;37:1227

[20] G. Abbruzzese and K. Lucke, Acta metall. 1986;34:905

[21] J. E. Palmer, C. V. Thompson and H. I. Smith, J. Appl. Phys. 1987;62:2492

[22] H. J. Frost and C. V. Thompson, Journal of Electronic Materials 1988;17:447

[23] S. Ling and M. P. Anderson, Journal of Electronic Materials 1988;17:459

[24] G. S Grest, M. P. Anderson, D. J. Srolovitz and A. D. Rollett, Scripta metall. 1990; 24:661

[25] D. J. Srolovitz, G. S Grest and M. P. Anderson, Acta Metall. 1985;33:2233

[26] H. J. Frost and C. V. Thompson, Acta Metall. 1987;35:529

[27] N. Sun, B. R. Patterson, J. P. Suni, E. A. Simielli, H. Weiland and L. F. Allard, Materials Science and Engineering A 2006;416:232

[28] B. R. Patterson, N. Sun, J. P. Suni, E. A. Simielli, H. Weiland and L. F. Allard, TMS Letters 2004;1:173

[29] P. R. Mould, P. Cotterill, Journal of Materials Science 1967;2:241

[30] G. Couturier, R. D. Doherty, C. Maurice, R. Fortunier, Acta Metall. 2005;53:977

[31] Y. Liu and B. R. Patterson, Metall. Trans. A 1993;24:497

[32] B. R. Patterson, Y. Liu and J. A. Griffin, Metall. Trans. A 1990;21:2137

[33] B. R. Patterson and Y. Liu, Jour. Amer. Ceram. Soc. 1990;73:3703

[34] R. D. Doherty and K. E. Rajab, Acta Metall. 1989;37:2723

Table 1, Chemical composition of the experimental TRC AA3105, wt%

Mn	Mg	Fe	Si	Cu	Al
0.40	0.51	0.52	0.14	0.15	Balance

Table 2, Particle dispersion for TRC AA3105 annealed under different conditions, μm^{-1}

Treatments		$Z = \frac{L_A}{\pi}$		Volume fraction, %
Temperature (°C)	Time (h)	surface	center	
620	504*	0.019	0.018	1.4
630	1.5	0.039	0.027	1.4
	12	0.032	0.024	1.3
	132	0.020	0.015	1.3
	168*	0.022	0.018	1.3
640	8	0.026	0.021	1.2
	16*	0.023	0.019	1.1
650	0.5	0.039	0.029	1.3
	2	0.021	0.012	1.2
400 (H)	1	0.025	0.017	1.6
500 (H)	2	0.025	0.020	1.8
	24	0.025	0.021	1.9
525 (H)	1	0.025	0.017	1.7
	96	0.025	0.020	1.9
550 (H)	0.5*	0.020	0.015	1.5
	24	0.025	0.019	2.0
600 (H)	0.1*	0.024	0.015	1.5
	0.2	0.021	0.016	1.5
	1	0.020	0.012	1.4
620 (H)	0.2*	0.019	0.015	1.4
	2	0.023	0.016	1.6
640 (H)	0.2*	0.021	0.014	1.4
	2	0.018	0.012	1.2

* Indicates time at which AGC has become established.

Table 3, Calculated diffusion coefficient for Mn and Fe in TRC AA3105, $\mu m^2/s$

	600°C	610°C	620°C	630°C	640°C	650°C
Mn	0.0024	0.0034	0.0048	0.0066	0.0091	0.0125
Fe	0.0158	0.0227	0.0323	0.0456	0.0640	0.0891

Table 4, Calculation of the AGC limits in terms of Grain Anchorage Parameter

Treatments, °C/h	Average grain size (λ), µm	Particle dispersion level (Z), μm^{-1}	Grain anchorage parameter for AGC, G_A	Growth limit
620/504(NH)	30	0.018	0.55	Upper limit
630/168 (NH)	31	0.018	0.57	
640/16 (NH)	32	0.019	0.58	
Average(NH)	31	0.018	**0.56**	
550 / 0.5 (HC)	25	0.015	0.38	Lower limit
600 / 0.1 (HC)	25	0.015	0.38	
620 / 0.2 (HC)	25	0.015	0.38	
Average(HC)	25	0.015	**0.38**	

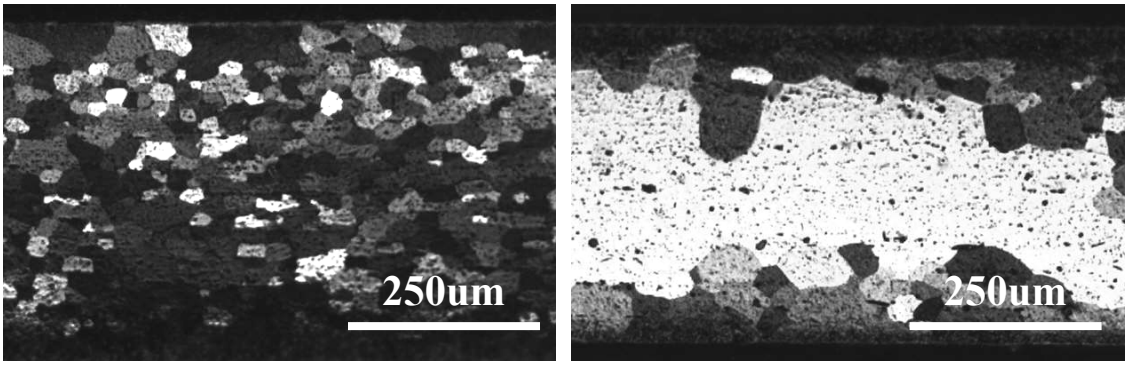

(a) (b)

Figure 1, Optical micrographs showing the grain structure in a NH TRC AA3105 strip annealed at 620°C for: (a) 1week, and (b) 3weeks

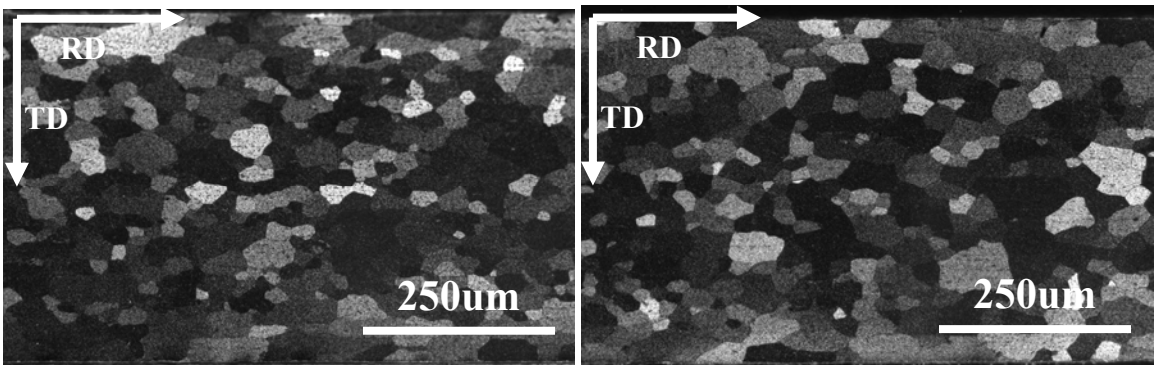

(a) (b)

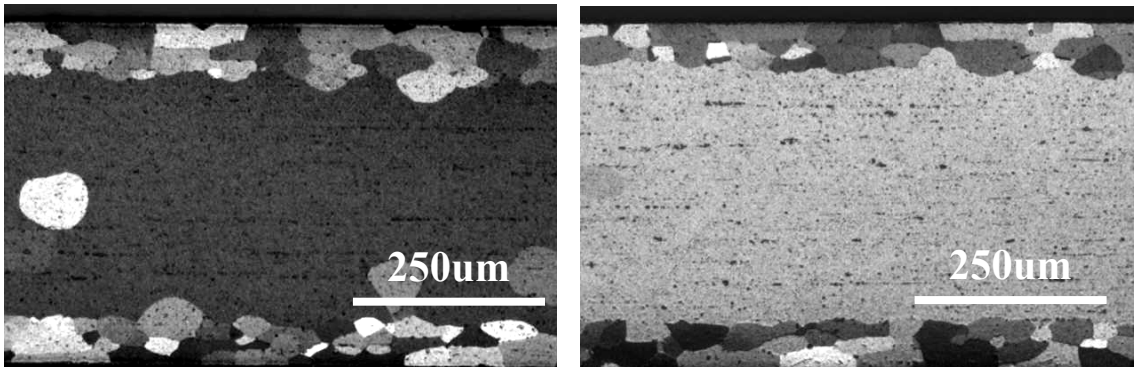

(c) (d)

Figure 2, Optical micrographs showing the grain structure in a NH TRC AA3105 strip annealed at 630°C for: (a) 12h, (b) 132h, (c) 1week, and (d) 2weeks

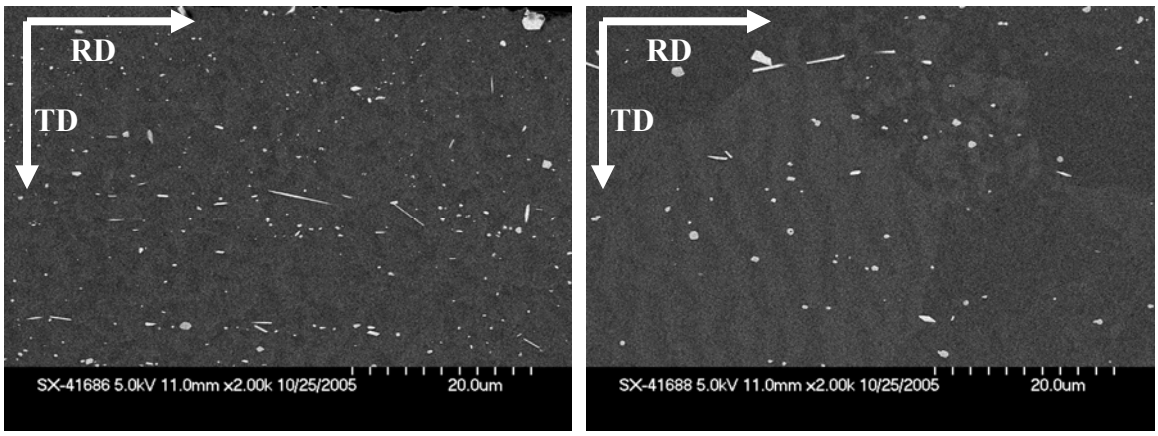

(a) (b)

Figure 3, FEG-SEM backscattered electron images showing second phase particles in a NH TRC AA3105 strip annealed at 630°C for 12h: (a) strip surface, and (b) strip interior

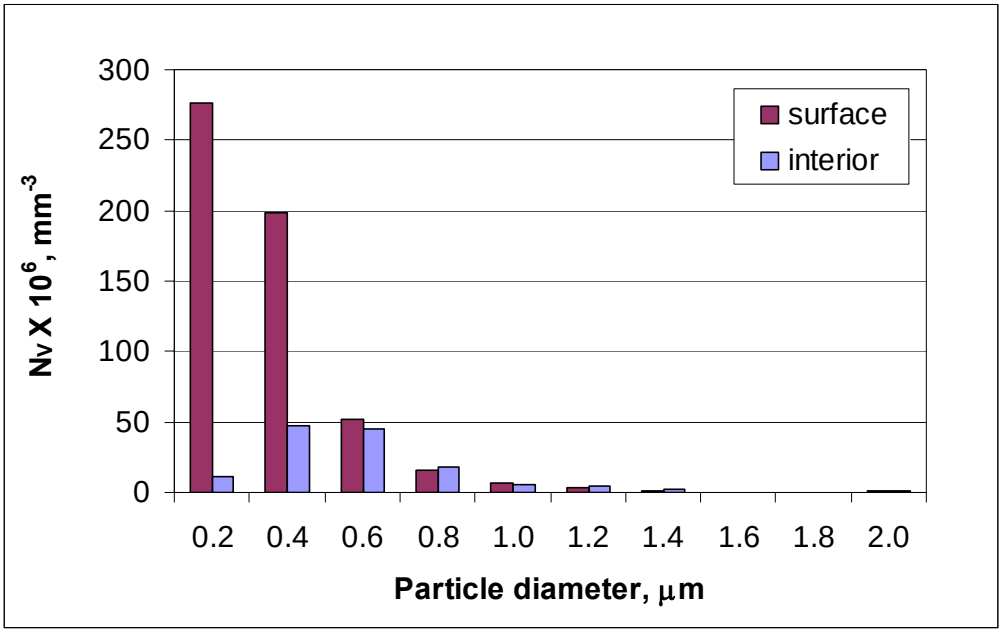

Figure 4, 3D particle size distribution computed by the Schwartz-Saltykov method in TRC AA3105 after 12h at 630°C, at both strip surface and interior. Typical micrographs of these areas are shown in Fig. 3

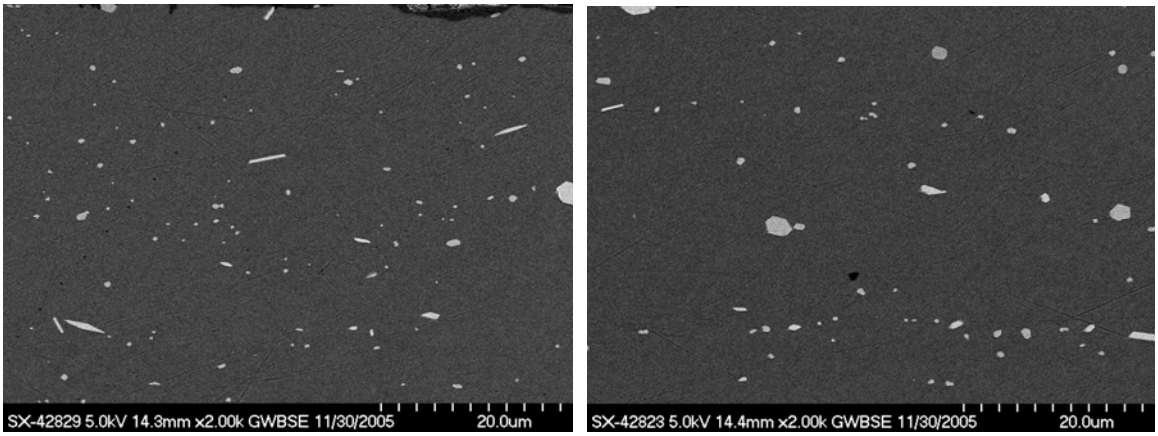

(a) (b)

Figure 5, Backscattered electron images showing second phase particles in a NH TRC AA3105 strip annealed at 630°C for 168h: (a) strip surface, and (b) strip interior

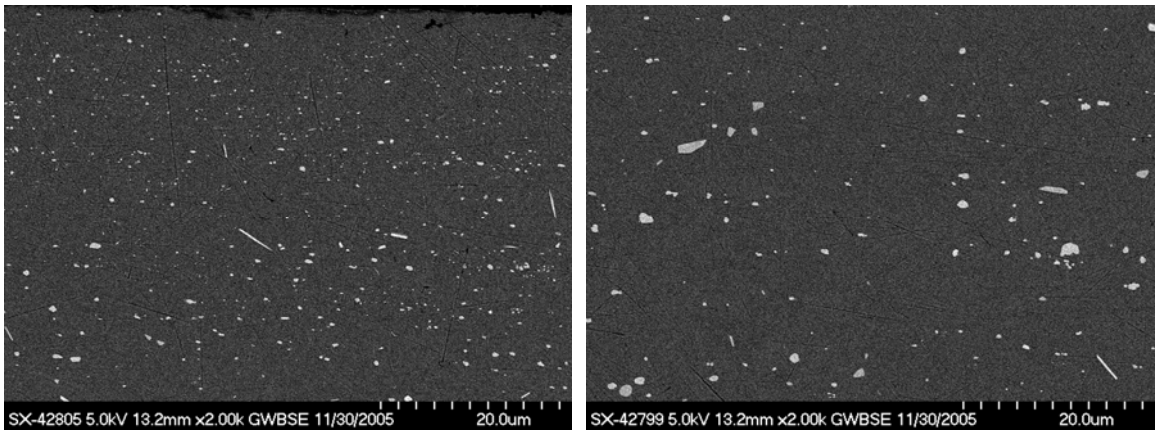

(a) (b)

Figure 6, Backscattered electron images showing second phase particles in a NH TRC AA3105 strip annealed at 630°C for 1.5h: (a) strip surface, and (b) strip interior

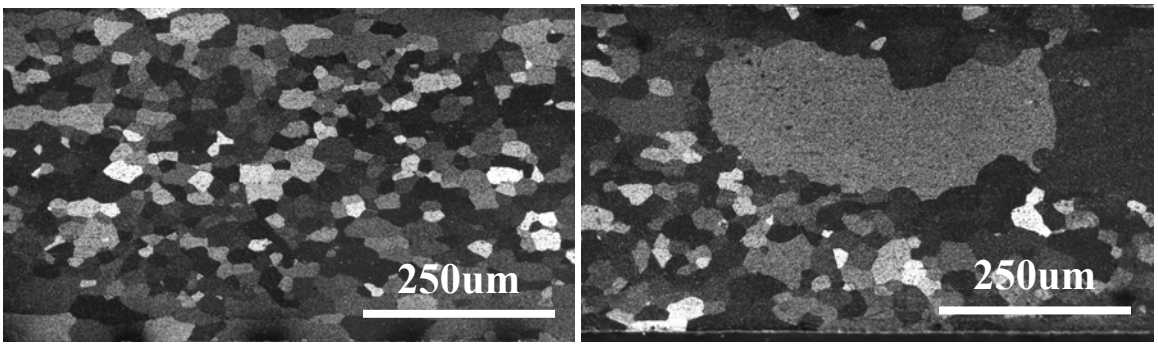

(a) (b)

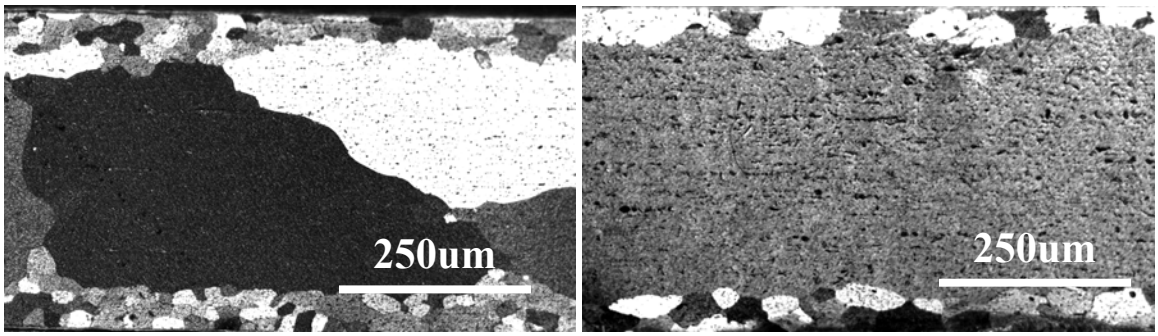

(c) (d)

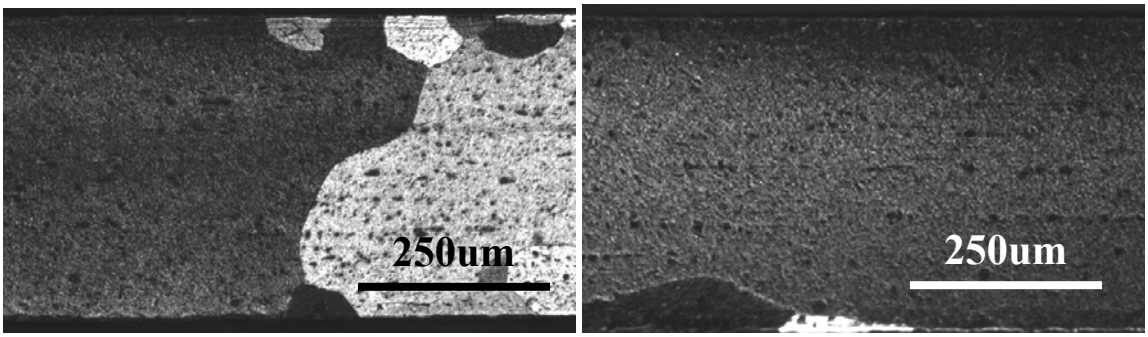

(e) (f)

Figure 7, Optical micrographs showing the grain structure in a NH TRC AA3105 strip annealed at 640°C for: (a) 4h, (b) 12h, (c) 16h, (d) 48h, (e) 2weeks, and (f) 4weeks

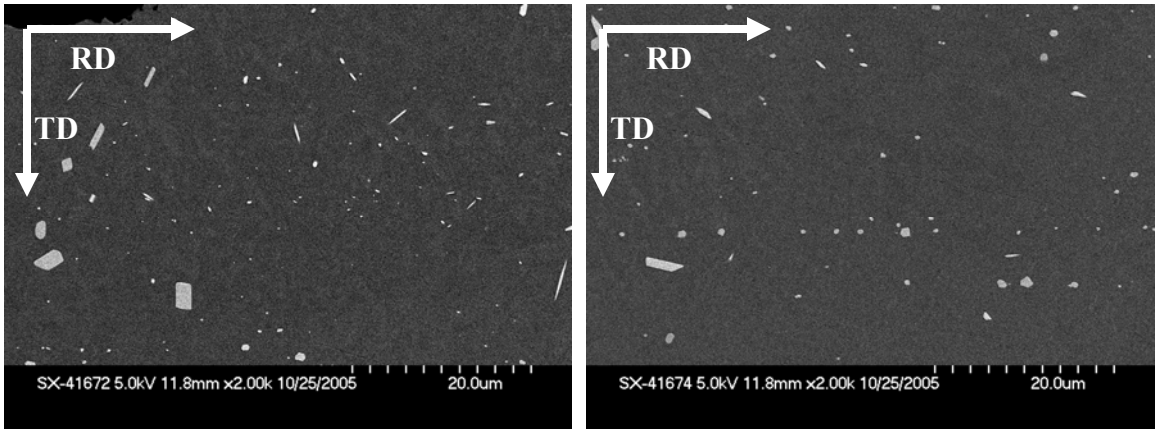

(a) (b)

Figure 8, Backscattered electron images showing second phase particles in a NH TRC AA3105 strip annealed at 640°C for 16h: (a) strip surface, and (b) strip interior

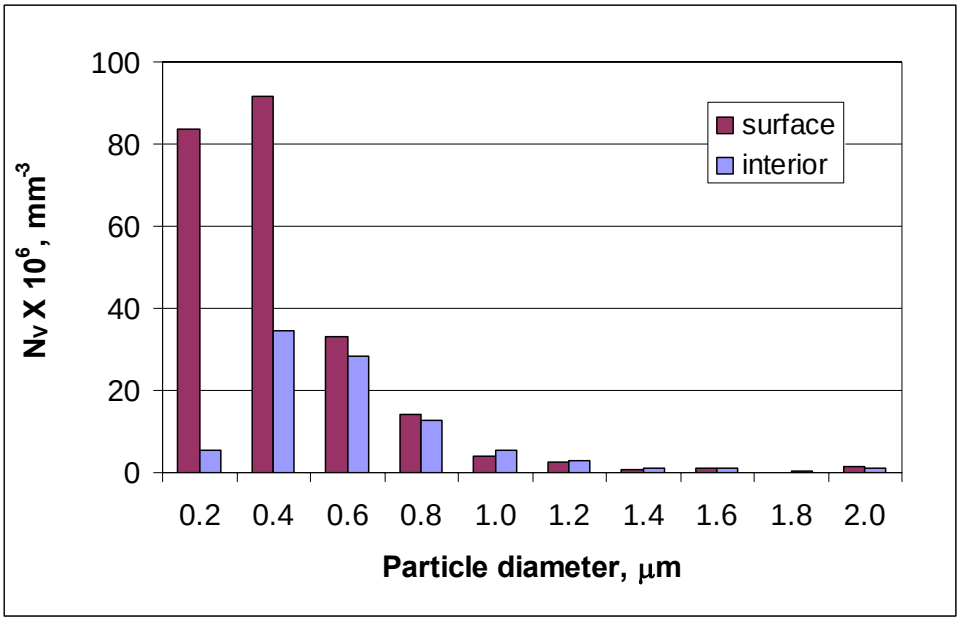

Figure 9, 3D particle size distribution computed by the Schwartz-Saltykov method in TRC AA3105 after 16h at 640°C, at both strip surface and interior. Typical micrographs of these areas are shown in Fig. 8

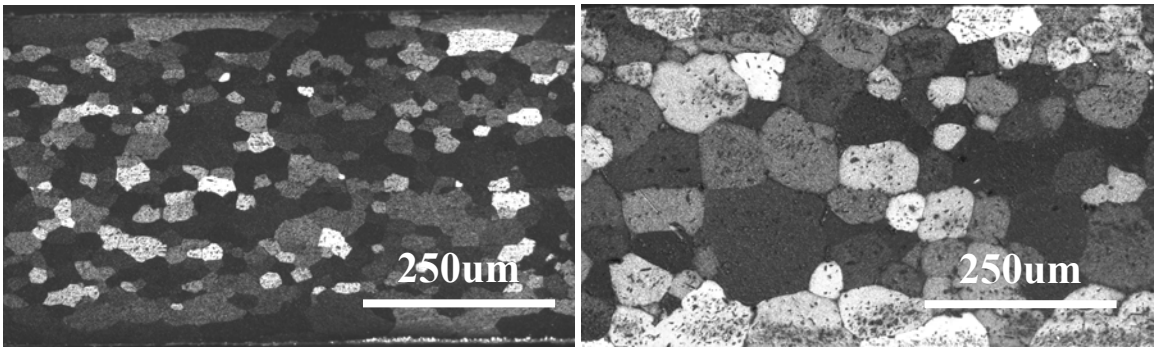

(a) (b)

Figure 10, Optical micrographs showing the grain structure in a NH TRC AA3105 strip annealed at 650°C for different times: (a) 30min, and (b) 2h

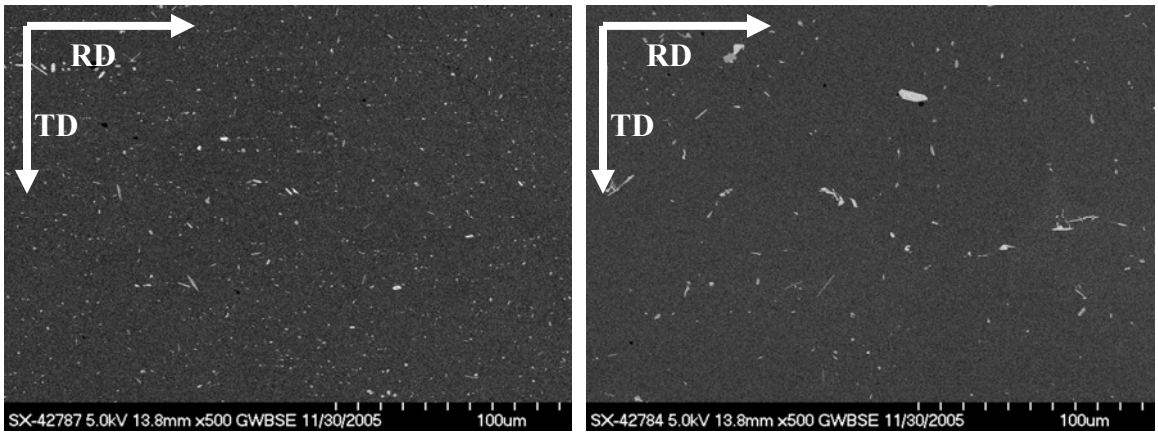

(a) (b)

Figure 11, Backscattered electron images showing second phase morphology in a NH TRC AA3105 strip annealed at 650°C for different times: (a) 30min, and (b) 2h

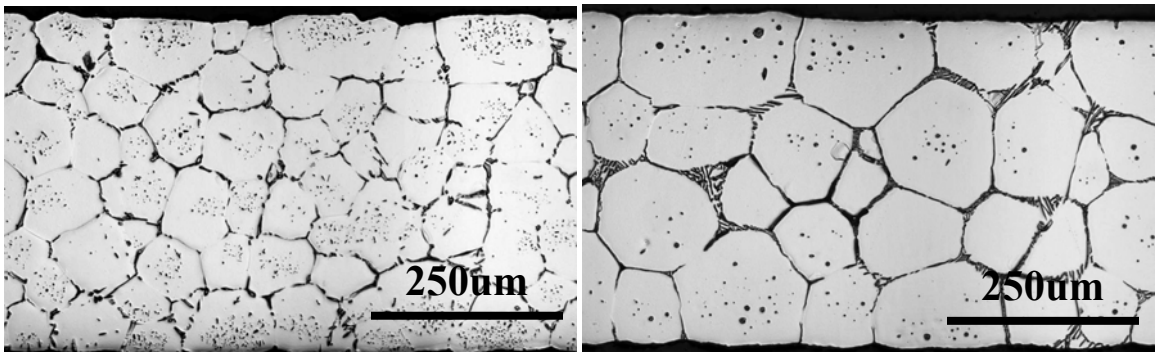

(a) (b)

Figure 12, Optical micrographs showing the grain structure in a NH TRC AA3105 strip annealed at 660°C for different times: (a) 10min, and (b) 30min

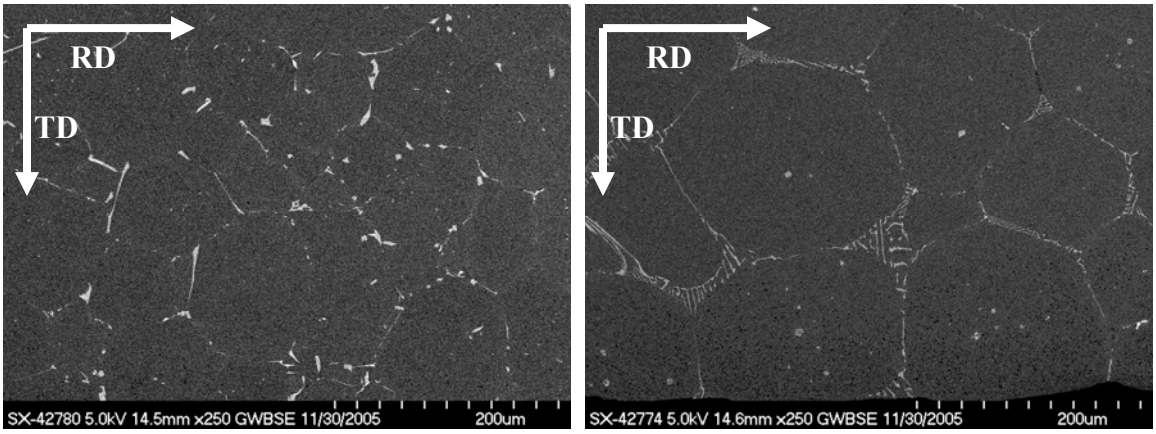

(a) (b)

Figure 13, Backscattered electron images showing second phase morphology of a NH TRC AA3105 strip annealed at 660°C for different times: (a) 10min, and (b) 30min

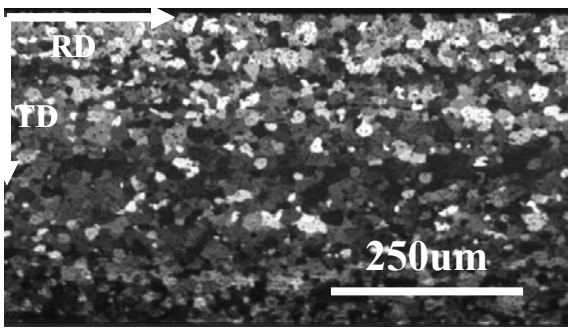

(a)

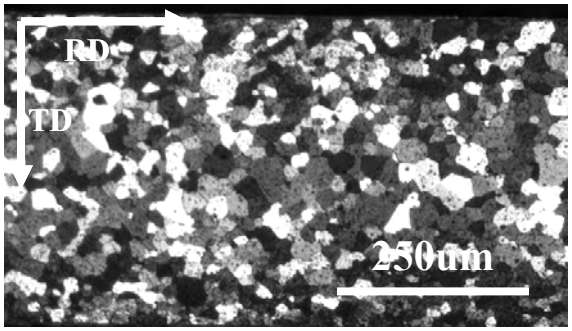

(b)

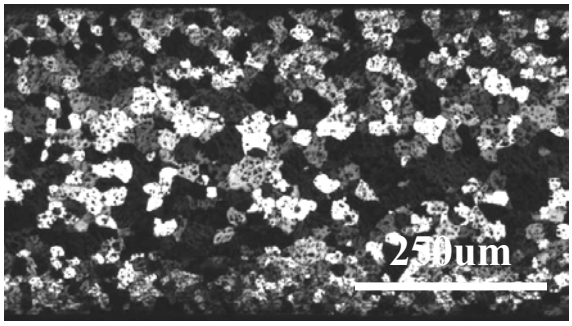

(c)

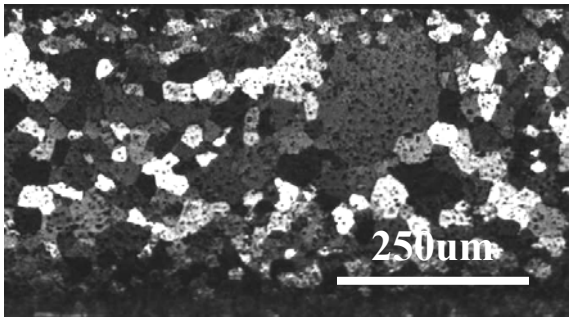

(d)

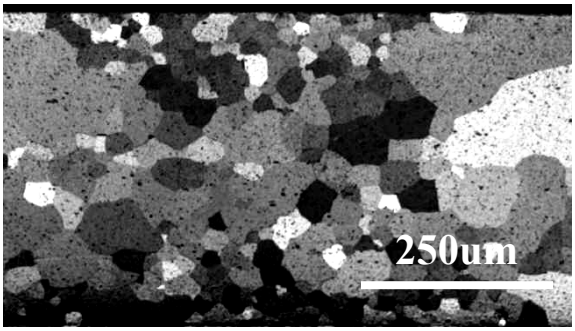

(e)

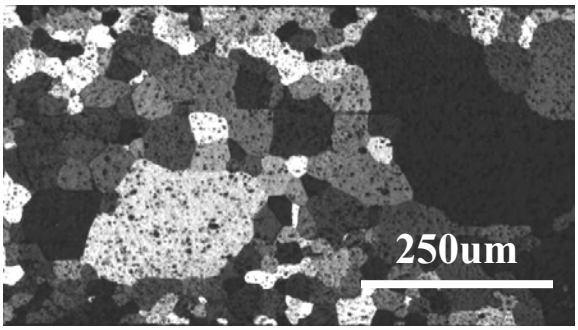

(f)

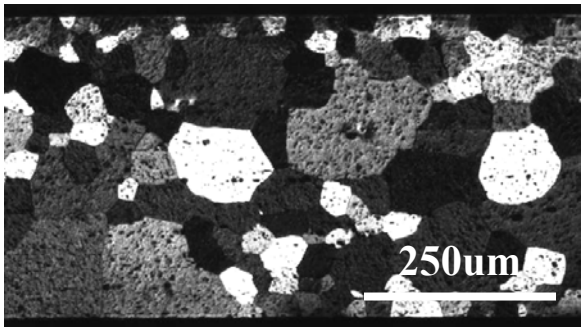

(g)

Figure 14, Optical micrographs showing the grain structure in annealed HC material. (a) 400°C for 1h, (b) 500°C for 1h, (c) 525°C for 1h (no sign of AGG even for 4 days), (d) 550°C for 1h, (e) 600°C for 1h, (f) 620°C for 1h, and (g) 640°C for 30min.

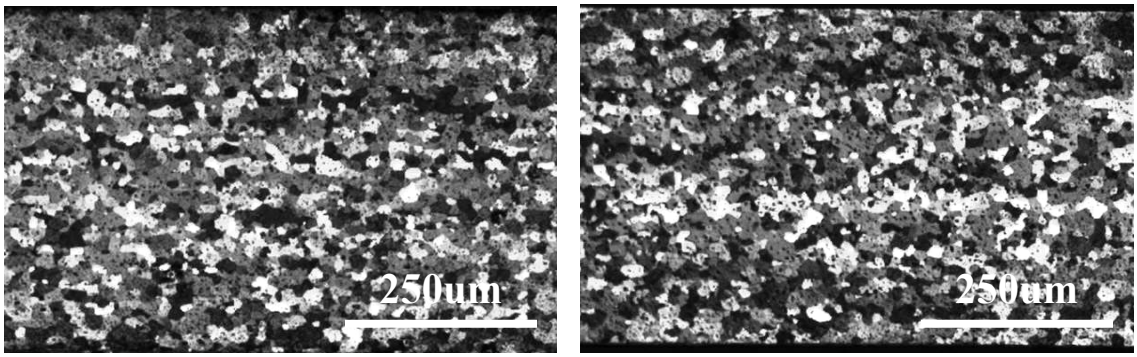

(a) (b)

Figure 15, Optical micrographs showing the grain structure in HC material annealed at 400°C for: (a) 5min, and (b) 24h

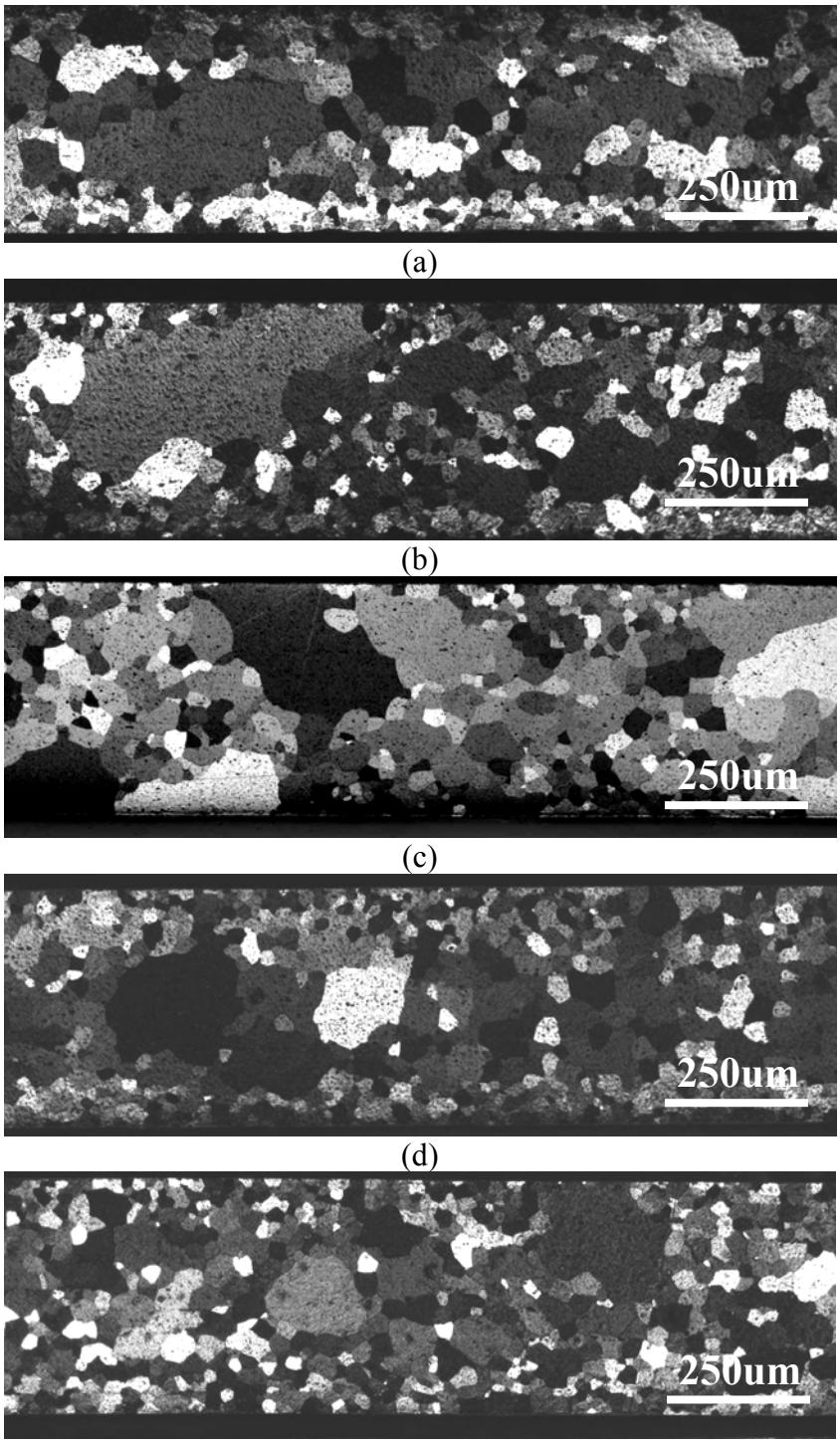

Figure 16, Optical micrographs showing the grain structure in HC material annealed at 600°C: (a) 5min, (b) 10min, (c) 1h, (d) 4h, and (e) 8h

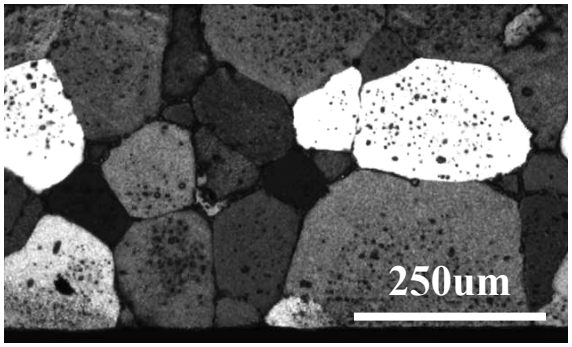

Figure 17, Optical micrographs showing the grain structure in HC material after 30 min anneal at 650°C

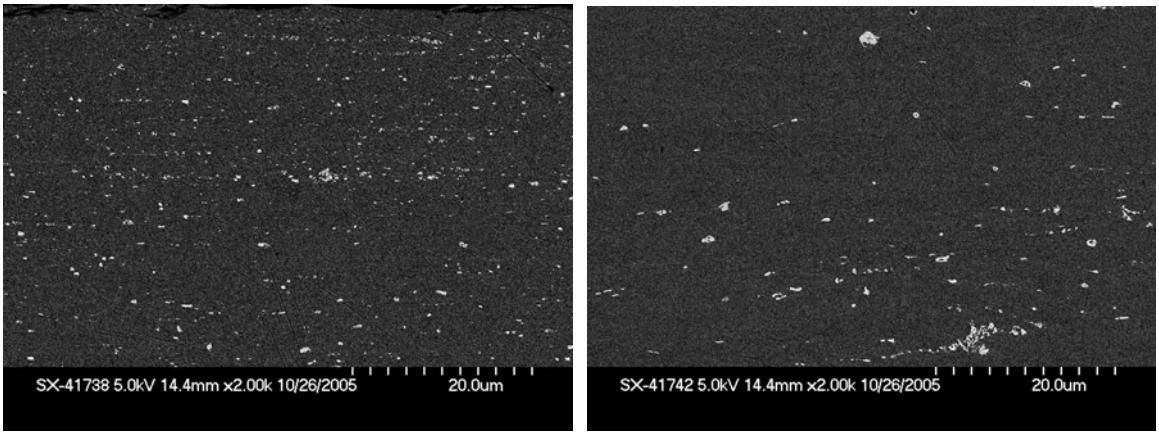

(a) (b)

Figure 18, Backscattered electron images showing second phase particle morphology in as-cold rolled NH material: (a) strip surface, and (b) strip interior.

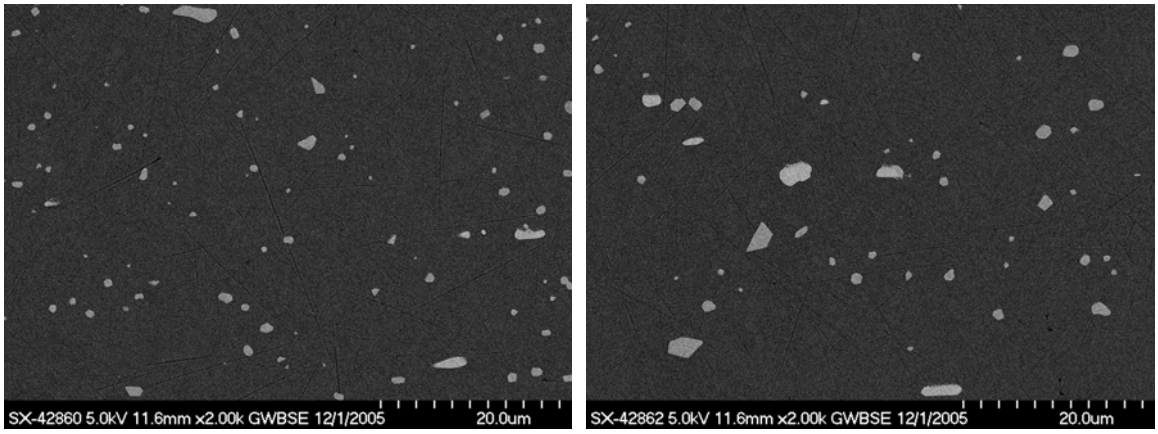

(a) (b)

Figure 19, Backscattered electron images showing second phase particle morphology in HC material annealed at 550°C: (a) strip surface, and (b) strip interior

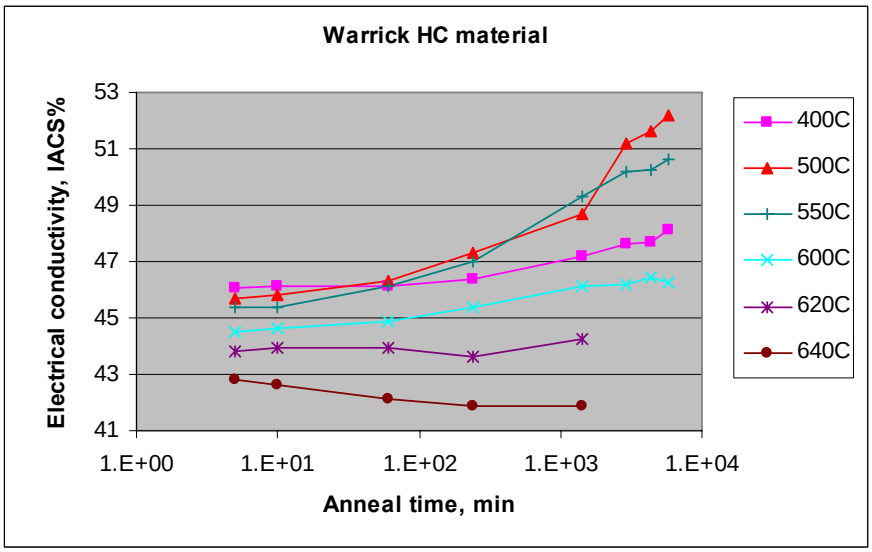

(a)

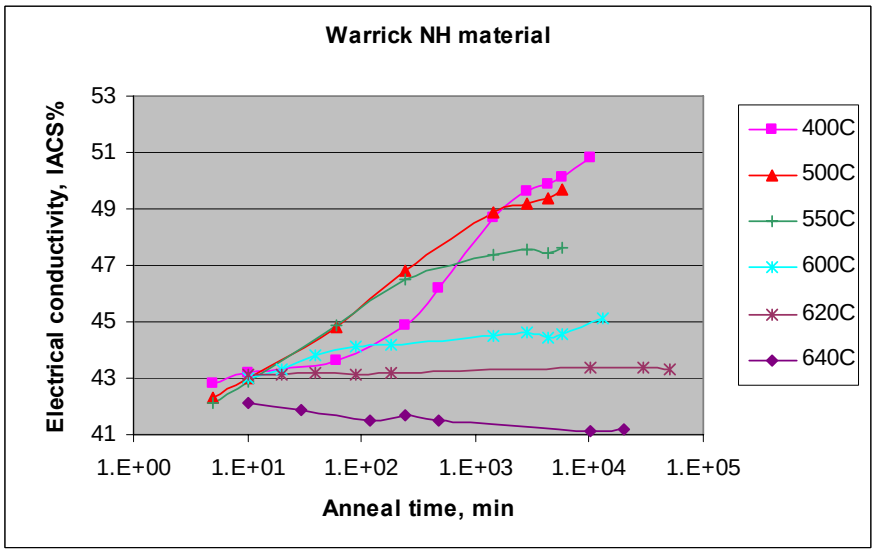

(b)

Figure 20, Electrical conductivity changes in (a) HC material, and (b) NH material annealed at different temperatures and times

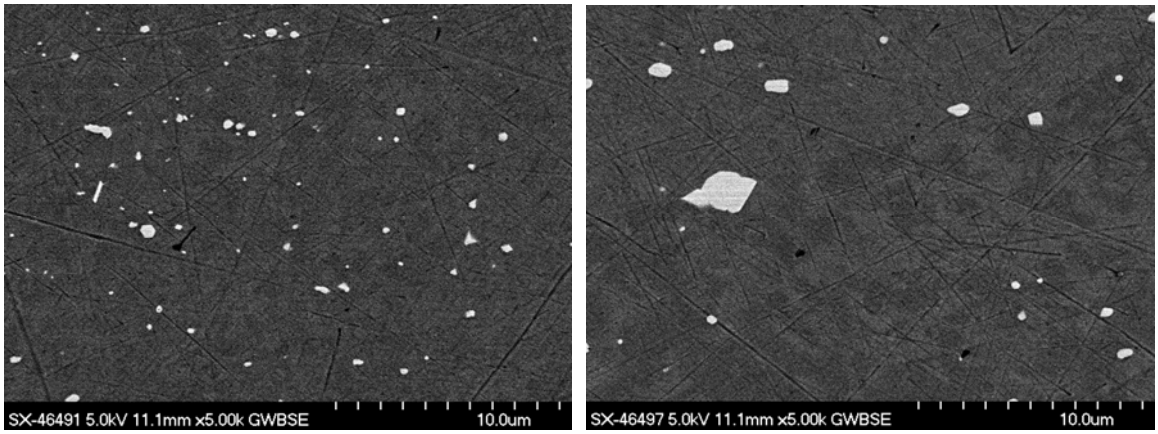

(a) (b)

Figure 21, FEG-SEM backscattered electron images showing second phase particle morphology in NH material annealed at 600°C: (a) 24 hours, and (b) 220 hours

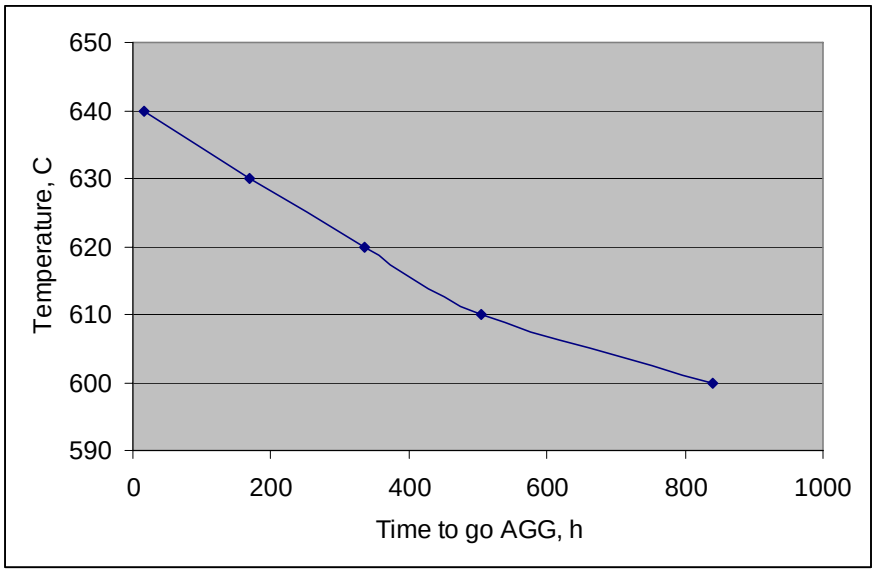

Figure 22, Incubation times of AGC in NH material annealed at different temperatures

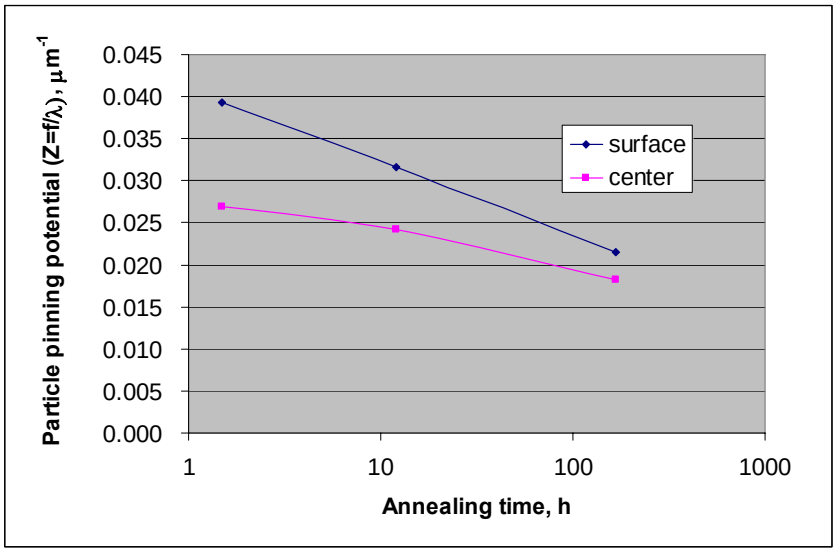

Figure 23, Evolution of particle pinning potential in a NH TRC AA3105 strip annealed at 630°C

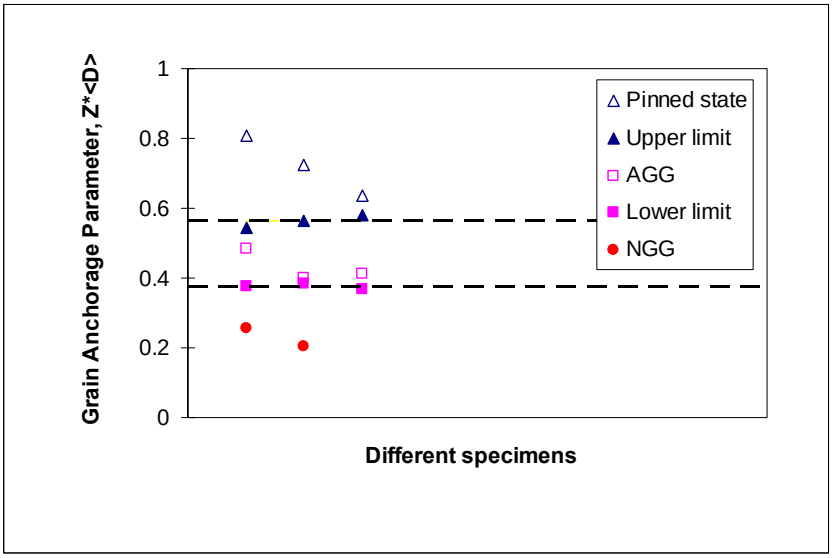

Figure 24, Diagram of Grain Anchorage Parameter in TRC AA3105. Note: the two dashed lines represent the upper and lower limit of AGC

GENERAL SUMMARY

In TRC AA3105, high solidification and post-solidification cooling rates lead to high manganese supersaturation throughout the as-cast strip and very fine constituent particles near strip surface. TRC AA3105 has a marked gradient in constituent particle size, with very fine, closely spaced particles within approximately 50μm of the 90% cold rolled strip surface and larger particles with greater spacing toward the strip center. Non-homogenized material shows a very coarse recrystallized grain structure, suggesting that nucleation is hindered by fine constituent and dispersoid pinning. Homogenization prior to cold rolling and annealing reduces the supersaturation, coarsens constituent particles and results in marked reduction in recrystallized grain size and faster recrystallization kinetics in TRC AA3105. An extensive cyclical homogenization treatment was demonstrated to greatly coarsen the constituent particles and eliminate the recrystallized grain size gradient presented in TRC AA3105 strips.

Compared with pre-existing dispersoids, concurrently forming dispersoids retard the recrystallization kinetics much more effectively. However, their effects on grain size are similar. Larger dispersoid size/spacing results in faster recrystallization kinetics and finer recrystallized grain structure. Solute/concurrently forming dispersoids can lower the efficiency of PSN by pinning subgrain boundary motion and increasing the critical size of potential PSN sites. Faster anneal heating rate results in a finer recrystallized grain structure in TRC AA3105 by reducing precipitation interaction with recrystallization.

A stereological method was proposed for characterizing the dispersion of second phases in TRC AA3105. It has been justified by extensive experimental results and by analytical derivations that the stereological approach is a robust means for characterizing the degree of particle pinning in real material systems.

AGC was observed in TRC AA3105. The AGC behavior in the studied material was investigated. Two grain growth limits have been observed and quantified via a newly-defined dimensionless parameter, the GAP, the product of the measured matrix grain size and the particle dispersion parameter Z.

FUTURE WORK

The current study has investigated the evolution of microstructures during cold rolling, low temperature pre-heating, homogenization, recrystallization and grain growth. The following are some areas that could be further investigated:

- The fundamental mechanism of the elongated recrystallized grain structure in non-homogenized material.
- The effect of alloy composition on annealing behaviors: Warrick plant material versus Itapissuma material.
- Shape evolution of second phase particles on grain boundaries during grain growth.

GENERAL LIST OF REFERENCES

1. Sir H. Bessemer, British Patent No. 11317.
2. Shaun Hamer, Bruno Taraglio and Chris Romanowski, FATA Hunter report.
3. R. Cook, P.G. Grocok, P.M. Thomas, D.V. Edmonds and J. D. Hunt, Journal of Materials Processing Technology 55 (1995) 76-84
4. T. Haga, K. Tkahashi, M. Ikawaand, and H. Watari, Journal of Materials Processing Technology 153 (2004) 42-47
5. M. Yun, S. Lokyer and J. D. Hunt, Materials Science and Engineering A280 (2000) 116-123
6. B. Forbord, B. Andersson, F. Ingvaldsen, O. Austevik, J. A. Horst and I. Skauvik, Materials Science and Engineering A415 (2006) 12-20
7. T. Haga, T. Nishiyama and S. Suzuki, Journal of Materials Processing Technology 133 (2003) 103-107
8. T. Haga, and S. Suzuki, Journal of Materials Processing Technology 118 (2001) 165-168
9. T. Haga, Journal of Materials Processing Technology 111 (2001) 64-68
10. T. Haga, and S. Suzuki, Journal of Materials Processing Technology 113 (2001) 291-295
11. A. V. Kuznetsov, Int. J. Heat Mass Transfer 40 (1997) 2949-2961
12. X. M. Zhang, Z. Y. Jiang, X. H. Liu and G. D. Wang, Journal of Materials Processing Technology 162 (2005) 591-595
13. H. Watari, K. Davey, M. T. Rasgado, T. Haga and S. Izawa, Journal of Materials Processing Technology 155 (2004) 1662-1667
14. M. Slamova, Z. Juricek and V. Ocenasek, Materials Science Forum 331 (2000) 161-166
15. M. Slamova, V. Ocenasek, M. Cieslar, B. Chalupa and P. Merle, Materials Science Forum 331 (2000) 829-834

16. S. Zhou, J. Zhong, D. Mao and P. Funke, Journal of Materials Processing Technology 134 (2003) 363-373

17. S. A. Lockyer, M. Yun, J. D. Hunt and D. V. Edmonds, Materials Characterization 37 (1996) 301-310

18. J. Strid, T. Furu, R. Orsund and E. Nes, Continuous Casting of Non-Ferrous Metals and Alloys, Edited by H. D. Merchant and E. M. Chia, Chicago (1988)

19. David Monaghan, Twin-roll Cast Aluminum Alloys, PhD dissertation, University of Oxford, 1993

20. British Patent No. 9111476.9

21. D. J. Monaghan, M. B. Henderson, J. D. Hunt and D. V. Edmonds, Materials Science and Engineering A 173 (1993) 251-254

22. Ch. Gras, M. Meredith and J. D. Hunt, Journal of Materials Processing Technology 167 (2005) 62-72

23. Ch. Gras, M. Meredith and J. D. Hunt, Journal of Materials Processing Technology 169 (2005) 156-163

24. Ming Yun, A Numerical and Experimental Study of the Twin-roll Casting Process, PhD dissertation, University of Oxford, 1992

25. M. J. Basgshaw, J. D. Hunt and R. M. Jordan, Cast Metals 1 (1988) 16-23

26. N. Sun, B. R. Patterson, J. P. Suni, E. A. Simielli, H. Weiland and L. F. Allard, Materials Science and Engineering A416 (2006) 232-239

27. M. Karlik, J. Siegl, M. Slamova and Y. Birol, Materials Science Forum 331 (2000) 619-624

28. E. S. Puchi-Cabrera, Journal of Engineering Materials and Technology 123 (2001) 149-154

29. J. Liu, J. G. Morris, Materials Science and Engineering A357 (2003) 277-296

30. H. Zhu, A. K. Ghosh, and K. Maruyama, Materials Science and Engineering A419 (2006) 115-121

31. J. T. Liu, Y. S. Liu and J. G. Morris, Materials Science and Technology 19 (2003) 1498-1506

32. S. X. Zhou, J. Zhong, D. Mao and P. Funke, Materials Processing Technology 134 (2003) 363-373

33. M. Slamova and Paneske Brezany, Aluminum 77 (2001) 801-808

34. M. Slamova, V. Ocenasek, P. Dvorak and Z. Juricek, Aluminum Alloys 2 (1998) 1287-1292

35. M. Slamova, M. Cieslar, B. Chalupa and P. Merle, Physical Metallurgy and Fracture of Materials (1999) 227-230

36. M. Slamova, P. Dvorak and Z. Juricek, Microstructure Science 27 (1999) 20-28

37. M. Slamova, V. Ocenasek, P. Dvorak, and Z. Juricek, Aluminum Alloys 2 (1998) 897-902

38. F. J. Humphreys, Acta Materialia 45 (1997) 5031-5039

39. F. J. Humphreys, Scripta Materialia 43 (2000) 591-596

40. E. Nes, Acta Metallurgica 24 (1976) 391-398

41. E. Nes and J. D. Embury, Z. Metallkunde 66 (1975) 589-593

42. H. M. Chan and F. J. Humphreys, Acta Metallurgica 32 (1984) 235-243

43. F. J. Humphreys and M. Hatherly, Recrystalization and related annealing phenomena, Pergamon, 1995

44. R. D. Doherty and J. W. Martin, Journal of the Institute of Metals 91 (1962) 332-338

45. P. R. Mould and P Cotterill, Journal of Materials Science 2 (1967) 241-255

46. T. Furu, R. Orsund and E. Nes, Acta Metall. Mater. 43 (1995) 2209-2232

47. O. S. Es-Said, A. Zeihen, M. Ruprich, J. Quattrocchl, M. Thomas, K. H. Shin, M. Obrien, D. Johansen, W. H. Tijoe and D. Ruhl, Journal of Materials Engineering and Performance 4 (1995) 346-357

48. Suzuki Yoshikazu, Hashimoto Takeyoshi and Muramstsu Toshiki, Advances in the Metallurgy of Aluminum Alloys (2001) 330-336

49. Ekstrom Hans-Erik, Hagstrom Joacim and Ostensson Lars, Materials Science Forum 331 (2000) 179-184

50. Suzuki Yoshikazu, Hashimoto Takeyoshi and Muramstsu Toshiki, Materials Science Forum 331 (2000) 811-816

51. X. Li, M. E. Kassner and S. C. Bergsma, Journal of Materials Engineering and Performance 9 (2000) 416-423

52. R. A. Jeniski Jr., Materials Science and Engineering A 237 (1997) 52-64

53. T. J. Cockfield and J. D. Hunt, Microstructure Modeling and Prediction during Thermomechanical Processing (2001) 211-220

54. M. Aghaie-Khafri, Journal of Materials Science 39 (2004) 6467-6472

55. J. P. Suni and T. N. Rouns, Materials Science Forum 396 (2002) 687-692